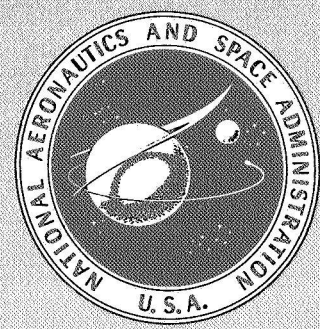


SIGNIFICANT ACCOMPLISHMENTS IN TECHNOLOGY

Goddard Space Flight Center, 1972

CASE FILE COPY

A symposium held at
GODDARD SPACE FLIGHT CENTER
November 7-8, 1972



NATIONAL AERONAUTICS AND SPACE ADMINISTRATION

SIGNIFICANT ACCOMPLISHMENTS IN TECHNOLOGY

Goddard Space Flight Center, 1972

The proceedings of a symposium held at the NASA
Goddard Space Flight Center, November 7-8, 1972

Prepared by Goddard Space Flight Center



Scientific and Technical Information Office

NATIONAL AERONAUTICS AND SPACE ADMINISTRATION

Washington, D.C.

1973

FOREWORD

This is an almost-verbatim transcript of a symposium held at Goddard Space Flight Center (GSFC) on November 7 and 8, 1972. No attempt has been made to introduce editorial or stylistic uniformity: on the contrary, an effort has been made to retain the informality of the proceedings. The text of the papers are substantially as given; but in some instances where a more detailed paper has been prepared for publication, this paper has been substituted for the transcript.

A major change results from NASA policy, which now requires in all formal publications the use of international metric units according to the Systeme International d'Unites (SI). However, in certain cases, utility requires the retention of other systems of units in addition to the SI units. The conventional units stated in parentheses following the computed SI equivalents are the basis of the measurements and calculations reported here.

CONTENTS

Foreword	ii
Introduction	1
SECTION I: SPACECRAFT AND VEHICLE TECHNOLOGY	
Overview	
<i>Robert E. Bourdeau</i>	5
The OSO-7 Mission	
<i>John M. Thole</i>	7
Delta Vehicle Improvements	
<i>Robert J. Goss</i>	11
Delta Launch Vehicle Inertial Guidance System	
<i>Kenneth I. Duck</i>	14
STRAP IV Sounding Rocket Attitude Control System	
<i>David J. Shrewsberry</i>	16
Inertial Reference Unit	
<i>Frederick J. Kull</i>	20
Fine Pointing Control, OAO-3	
<i>James V. Moore</i>	22
The Data Processor from the Small Scientific Satellite	
<i>Harry G. McCain</i>	25
The Onboard Processor on OAO-3	
<i>Thomas D. Taylor</i>	28
Gravity-Gradient Dynamics Experiments Performed in Orbit Utilizing the Radio Astronomy Explorer (RAE-1) Spacecraft	
<i>Harvey Walden</i>	32

CONTENTS (Continued)

Heat Pipe Flight Experiments <i>Stanford Ollendorf</i>	37
Two-Dimensional Digital Computers <i>David H. Schaefer</i>	42
Secondary Mirror Support (LST) <i>Ewald E. Schmidt</i>	45
Momentum Wheel with Magnetic Bearings <i>Leo J. Veillette</i>	49
An Ironless Armature Brushless Torque Motor <i>Phillip A. Studer</i>	53
SECTION II: SENSOR TECHNOLOGY	
Overview <i>Henry W. Price</i>	59
Multispectral Scanner (MSS), ERTS-1 <i>Joseph Arlauskas</i>	60
Two-Inch Return Beam Vidicon (RBV) Multispectral Three-Camera Subsystem <i>Oscar Weinstein</i>	63
ERTS Wideband Tape Recorder <i>John M. Hayes</i>	67
Visible Infrared Spin-Scan Radiometer <i>James E. Phenix</i>	71
Multispectral Image Dissector Camera Flight Test <i>Bernard L. Johnson</i>	74
Very High Resolution Radiometer <i>Joseph R. Schulman</i>	77

CONTENTS (Continued)

The GSF C Cosmic Radiation Experiment for the Pioneer F/G Jupiter Mission <i>James H. Trainor</i>	82
The International Ultraviolet Explorer <i>Albert Boggess</i>	86
Scientific Instrument Package, LST <i>George Levin</i>	89
Glancing Incidence Telescopes for Space Astronomy <i>Jose Alonso, Jr.</i>	93
SECTION III: GROUND OPERATIONS	
Overview <i>Albert G. Ferris</i>	99
Adaptive Ground Implemented Phased Array <i>Robert E. Spearing</i>	103
Optical Tracking Telescope Compensation <i>James W. Gilbert</i>	109
High Efficiency Ground Data Transmission <i>William B. Dickinson</i>	113
Very Long Baseline Interferometry <i>Irving M. Salzberg</i>	116
Results of Mariner Mars Tracking Calibration Experiment <i>James W. Ryan</i>	121
The Calculation of Efficient High Precision Orbits by Optimum Matching of the Formulation and Numerical Integrator <i>Carmelo E. Velez</i>	125
ERTS Orbit Maintenance <i>Arthur J. Fuchs</i>	129

CONTENTS (Continued)

Attitude Computation System <i>Roger D. Werking</i>	132
Misalignment Estimation Software System <i>Richard L. desJardins</i>	136
Spacecraft Reorientation via Slewing About Nonorthogonal Axes <i>Paul B. Davenport</i>	140
Computer Assisted Interactive Resource Scheduling System <i>Carl E. Gustafson</i>	143
Interactive Experimenters' Planning Procedures and Mission Control <i>Richard L. desJardins</i>	147
Electron Beam Recorder Image Correction for ERTS <i>Paul Heffner</i>	155
A Photographic Processing Control Method for ERTS Imagery <i>Bernard Peavey</i>	159
SECTION IV: COMMUNICATIONS AND NAVIGATION	
Overview <i>James L. Baker</i>	165
Ionospheric Fading Effects on the Equatorial Zone <i>Thomas S. Golden</i>	167
ATS-5 Millimeter Wave Propagation Measurements <i>Louis J. Ippolito</i>	171
Coordination Procedure for Radio Relay and Communication Satellite Services <i>Jerome Eckerman</i>	175
Balloon Atmospheric Propagation Experiment Measurements <i>Peter O. Minott</i>	179

CONTENTS (Continued)

Theoretical and Experimental Comparison of an Ultra-High-Speed Laser Data Transmission System <i>Mona Tycz</i>	183
The Waveguide CO ₂ Laser <i>John J. Degnan, III</i>	187
The CO ₂ Laser Frequency Stability Measurements <i>Edward H. Johnson, Jr.</i>	191
Voice Intelligibility in Satellite Mobile Communications <i>Sheldon Wishna</i>	195
A Zero-Error Operational Video Data Compression System <i>Richard L. Kutz</i>	199
Health/Education Telecommunications Experiment <i>Albert A. Whalen</i>	204

INTRODUCTION

This document presents the collection of papers summarizing 1972 achievements in technology delivered during the annual science and technology review at the Goddard Space Flight Center, November 7 and 8, 1972. The overall objective of the review was to report a representative sampling of significant accomplishments across the broad spectrum of Center activity. The particular subjects presented were selected competitively from a much larger body of candidate achievements of equal or slightly less significance. One of the primary constraints was the number of five-minute papers that could be presented in the time allocated.

The papers were presented in four groups: Spacecraft and Vehicle Technology, with Robert Bourdeau (Chairman of the November 8 session) presenting an overview; Sensor Technology, with an overview by Henry Price; Ground Operations, with an overview by Albert Ferris; and Communications and Navigation, with an overview by James Baker.

The audience consisted of scientists and engineers who had interest in and responsibility for the direction of space applications research and development. In addition to the many GSFC scientists and engineers, members of the audience came from NASA Headquarters, other NASA Centers, and other Government agencies.

SECTION I
SPACECRAFT AND VEHICLE TECHNOLOGY

OVERVIEW

Robert E. Bourdeau

During this year, Goddard has had, amongst others, mission successes on OAO, the most advanced astronomical observatory ever launched. We have launched the first earth observatory satellite, ERTS-1; put IMP in a challenging 30-earth radii orbit; and started a new generation of operational satellites with the ITOS/NOAA series. I would like to put this session in the context of what you heard yesterday, and what you are about to hear for today.

Goddard is a total system, as indicated in Figure 1. It can generate requirements, it can produce results, and it can provide the implementation between those two factors. Yesterday you heard results from the space sciences group at Goddard. This afternoon you will hear the output of our applications disciplines in terms of results.

Right now, we'll concentrate on the implementation box, which you see in Figure 1. The theme we would like to produce is that through the last decade Goddard has preached functional redundancy to enhance our mission successes. By functional redundancy we mean functional redundancy not only within each element, but between elements.

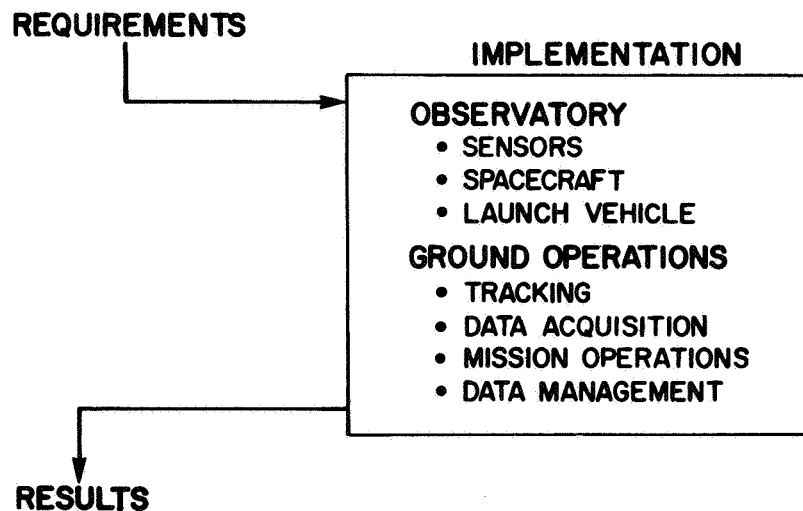


Figure 1. The Goddard system.

For example, often times we will have an anomaly on a spacecraft, which requires that we program around the fault, using previous ground simulations. Similarly, if we have an outage on our ground operations, we have designed our spacecraft so that they can take care of themselves until the ground faults are corrected.

In order to set the theme of functional redundancy through that whole box, the first paper by John Thole will concentrate on one mission. In this mission we had an anomaly in one of the elements, but because we paid attention to the total system within the box, we were able to recover the mission.

THE OSO-7 MISSION

John M. Thole

OSO-7, the Orbiting Solar Observatory-7, was the seventh in a series, as the name implies. It was the most challenging of the original series; its mission objective is shown in Figure 1.

The payload for OSO-7, which was composed of six experiments, had a total weight of 204 kilograms (450 lb). Early in the program it was obvious to many of us that we had great incompatibility between the existing spacecraft and the selected payload. Recognizing that the science to be accomplished was challenging and that it was unreasonable to expect this science from a lesser payload, we had to make some changes in the spacecraft. The required changes to the basic spacecraft amounted to roughly doubling its physical parameters.

That sounds like a big deal, but it really wasn't.

We used the system approach here of using fully the launch vehicle. We had plenty of launch vehicle capability. We didn't impose weight constraints. We just let it happen to a great extent and this saved considerable money.

We added a gyro and a star sensor to the wheel section, to provide a nighttime pointing capability for the three experimenters who needed night reference.

And for the first time this payload forced us to think clean, build it clean, and keep it clean through injection. This imposed several system requirements on the launch vehicle people since, for the first time, they had to really clean everything up, get rid of all the particles and they did a terrific job in this regard.

MISSION OBJECTIVE:

- TO OBTAIN HIGH-RESOLUTION SOLAR-CORONA DATA
IN THE XUV AND VISIBLE SPECTRAL REGIONS

CHANGES REQUIRED TO DO MISSION:

- PHYSICAL PARAMETER OF S/C DOUBLED
- GYRO AND STAR SENSOR ADDED
- BUILD THRU LAUNCH-CLASS 10,000 CLEAN

Figure 1. OSO-7 mission objectives and spacecraft compatibility.

I will show you the reference launch trajectory in Figure 2. In this standard Delta launch trajectory, about half way up you see the fairing jettison. When that happened, we caused the sail portion to rotate by a motor which is in the wheel. The wheel is the bottom part and the sail is the upper part. When the shroud came off, the motor caused the sail to spin up with respect to the wheel, thus storing momentum in the sail.

The launch vehicle control system easily accommodated this torque until we separated. At the time of separation the plan was that the momentum stored in the sail would be transferred to the wheel to provide a stable momentum vector about the spin axis. We, of course, did all of the regular things with regard to the mission planning in preparation for this launch. We made sure the data links were correct; the data processing plan was viable; that the spacecraft and experiment were built and tested properly; the format for experimenter data was proper; and the ground stations and control center support was properly planned. At that point we had, in the classical sense, met all the requirements; except as it transpired, the mission would have been a failure. And in Figure 3 you see what we like to think of as the first principle of system engineering stated rather simply. "If you can't afford to lose your pants, wear your belt and suspenders, too."

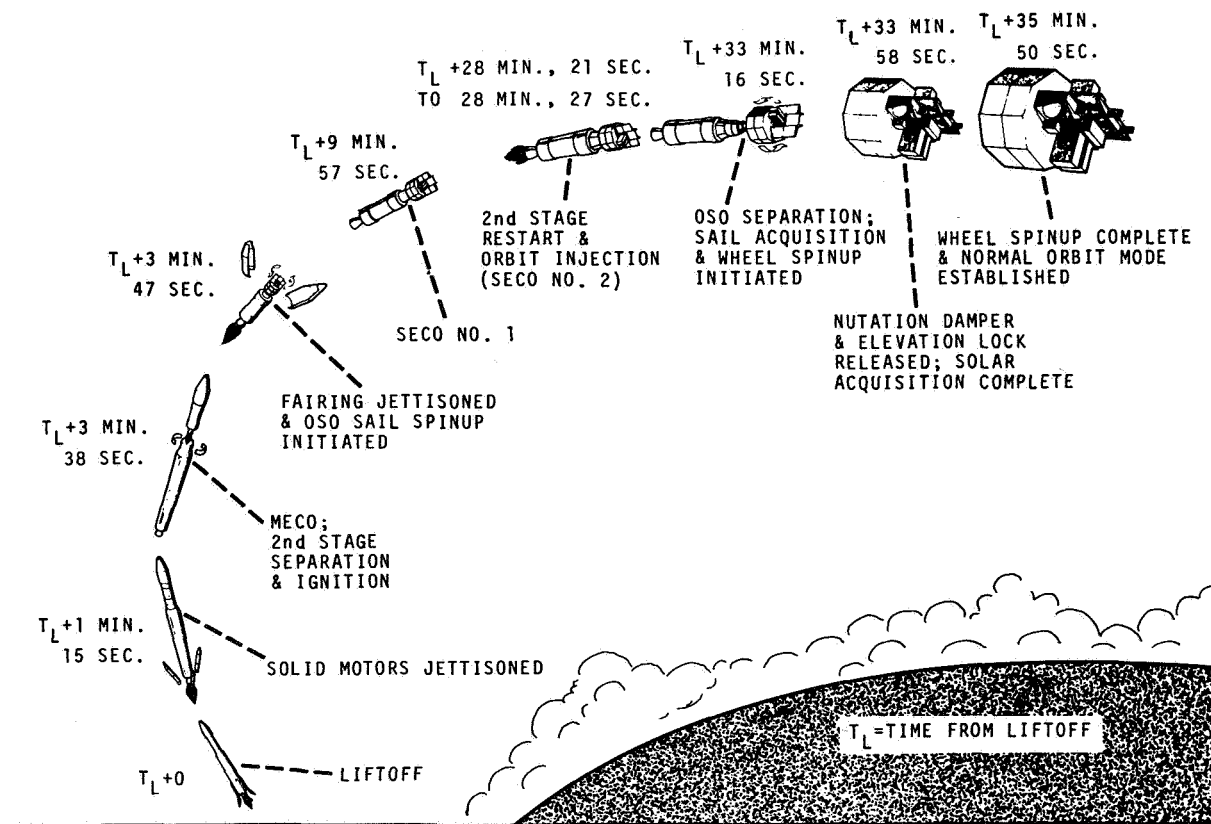


Figure 2. OSO-H launch sequence.

FIRST PRINCIPLE OF SYSTEM ENGINEERING:

“IF YOU CAN’T AFFORD TO LOSE YOUR PANTS,
WEAR YOUR BELT AND SUSPENDERS, TOO.”

CONSEQUENCE OF THIS TO OSO-7:

- ADD 3-MINUTE SPINUP TIMER
- LARGE-ANGLE SUN SENSOR
- SHORTED-CELL MONITOR
- CONTINGENCY PLAN

Figure 3. OSO-7 system engineering.

What this means is that after you have got the original configuration pretty well tied down, it is necessary to really take a look at the whole mission from end to end, and try to ferret out those particularly sensitive points and put in functional redundancy where you can.

In the case of OSO-7 we added four things. They are shown on the bottom of the figure — none of these are very cosmic — we added a three-minute timer, which would dump gas in a spinup direction for three minutes after separation. This would be quite important in the event that the transfer of momentum that was indicated in the previous figure did not really come off as programmed.

We added a large-angle sun sensor. We had flown this mission six times before without this sun sensor. This time, because of the importance of the mission, the fact that it cost \$36 million, and some other things which I don’t have the time to go into, we put one on. This device gave us the capability of determining the angle between the sun line and the spin axis within plus or minus 90 degrees and backed up the standard sun sensor which had only a plus or minus 15 degree field of view. We never had a shorted-cell monitor before, but in this particular case we were flying batteries that were five or six years old, and we wanted the capability of being able to determine if we were going to generate gas and perhaps blow the side off the spacecraft. We really needed this device later in the mission.

We always had a contingency plan before, but we never really had a contingency plan like this one. The OSO-7 contingency plan tied together the ground stations, the control center, the engineers, everybody had rehearsed this launch until it was coming out of their ears.

We did this because, if we had trouble, we had to have people that were skilled, that really knew what they were going to do. The day of launch arrived, and to be quite frank about it, I really felt that it would be a routine launch, and there wouldn't really be any trouble.

I figured that I would never have to tell anybody that we spent \$135,000 for those last four items. And those are the only four we added, and the contractor really didn't like them because they were a pain to him, and he felt they weren't really necessary and a "waste of taxpayers' money." And I figured that we would never have to tell anybody about how we "wasted the taxpayers' money," but we put them in and didn't need them at all until September 29, 1972, the day of launch, when we had a launch vehicle anomaly.

This anomaly put the combined OSO spacecraft and launch vehicle into a flat spin at 60 rpm. It killed off the spin momentum we had stored in the spacecraft, and meant that when we came off the delta launch vehicle, we were spinning about the wrong (transverse) axis at 60 rpm.

All our instrumentation was set up for spinning about the correct axis. When we saw the telemetry data in the control center, we saw nothing but zeros for about two minutes. Then we began to see some data that made sense. The spacecraft was actually starting to nutate and three minutes after separation it had erected about the right axis. This nutation and subsequent erection was caused by the three minute timer functioning as described above. In this condition we had some chance of bailing out the mission by using the other features listed in Figure 2. So, the inclusion of those last four items, which were sort of the second-effort functional redundancy, meant we were able to successfully get OSO-7 straightened out 8 hours and 29 minutes after liftoff. Because of this successful spacecraft recovery the scientific mission of OSO-7 was a success, and some of its scientific firsts which you heard about yesterday, are recapped in Figure 4.

- THE DISCOVERY OF GAMMA-RAY EMISSION LINES, WHICH DEMONSTRATE THE OCCURRENCE OF NUCLEAR REACTIONS ON THE SURFACE OF THE SUN, WERE OBSERVED BY THE UNIVERSITY OF NEW HAMPSHIRE EXPERIMENT.
- THE EJECTION OF LARGE PLASMA CLOUDS FROM THE OUTER CORONA (IN RESPONSE TO SOLAR FLARES AT LOWER LEVELS IN THE SOLAR ATMOSPHERE) AS OBSERVED BY THE NAVAL RESEARCH LABORATORY WHITE-LIGHT CORONAGRAPH EXPERIMENT.
- THE OBSERVATION BY THE GSFC (NEUPERT) EXPERIMENT OF THE 262-SECOND OSCILLATION OF EXTREME ULTRAVIOLET EMISSION LINES WHICH GIVES VALUABLE INFORMATION ON THE HEATING OF THE CORONA.

Figure 4. Major OSO-7 scientific results.

DELTA VEHICLE IMPROVEMENTS

Robert J. Goss

The history of Delta has been characterized by configuration changes which have periodically increased the performance of the vehicle, while maintaining a high reliability and relatively low cost.

Shown in Figure 1 are the performance increases associated with the 14 major configuration changes to date in terms of spacecraft weight into synchronous transfer orbit – from 45 kilograms (100 lb) in 1960 to 680 kilograms (1500 lb) when the H-1 booster becomes operational next year. Also shown is the per-mission cost history, which very nearly follows the 5 percent inflation curve. Note that all costs are included except range cost and amortization of development.

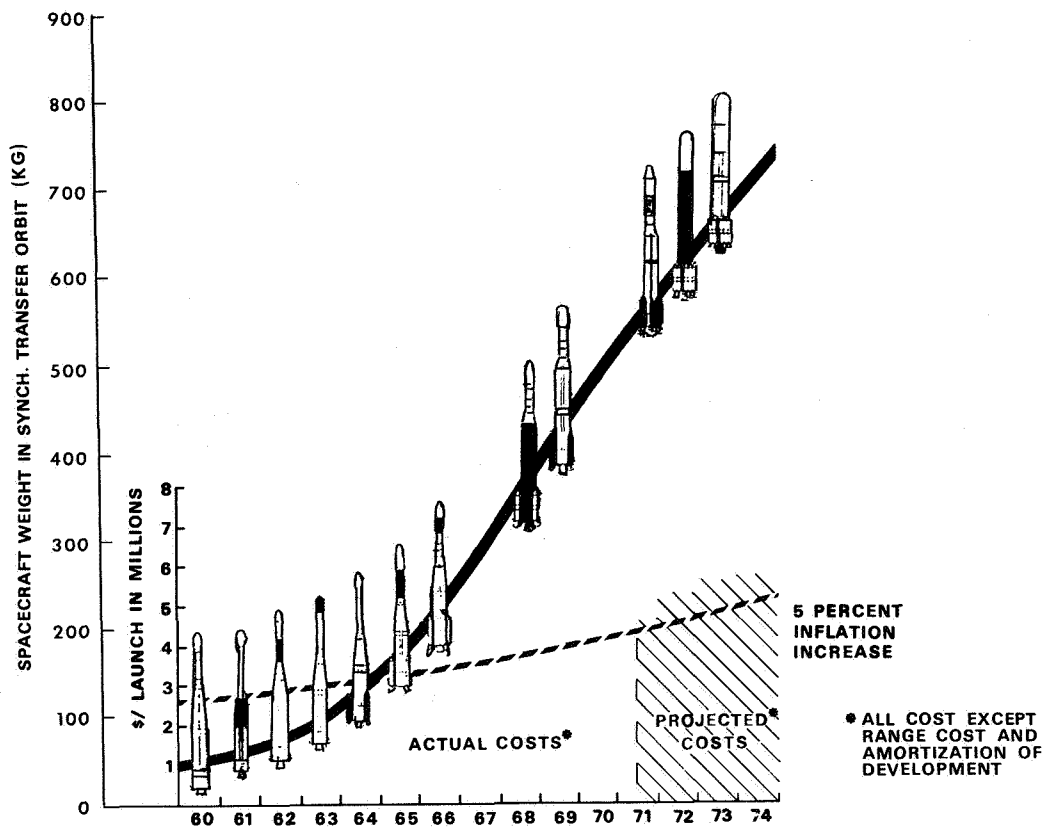


Figure 1. Delta performance and cost history.

Now I would like to highlight Delta's activities of the past 12 months.

In November 1971 we were preparing to ship the last two vehicles of the 1965-68 design and were in the design and early manufacturing phase of extensive vehicle configuration changes. The baseline vehicle as the year began was the long-tank Thor first stage, introduced in 1968, the 1.65-meter (65 in) diameter second stage with radio guidance introduced in 1965, and the FW-4 or T-364-3 third stages, 1965 and 1968 respectively (Figure 2). The initial change was the incorporation of the (UBT) Universal Boat Tail section of the Thor. The UBT is basically a structural beefup of the aft end of the first stage to permit carrying as many as nine thrust augmentation solids. The first UBT was flown on the TD-1A mission.

Next was the first flight of the T-364-4 third stage, which is a lengthened version of the 1.13-meter (37 in) Surveyor spherical motor. The -4 was introduced on the Atlas Centaur Pioneer F flight as the Delta project provided third stage. The launch of ERTS-1 was the first use of nine solids. It was also the first flight of the new higher-performing second stage engine, which was originally developed for the Titan-III Transtage vehicle. More important, however, it was the maiden flight of the Delta Inertial Guidance system, DIGS, which will be discussed in detail in the next presentation. These changes increased

HEOS-A2	TD-1A	PIONEER-F	ERTS-A	IMP-H	TELESAT-A
					
LONG TANK THOR AJ 10-118E RADIO GUIDANCE FW-4 165 CM FAIRING BASELINE	UNIVERSAL BOATTAIL	TE-364-4	NINE CASTOR II SOLID MOTORS AJ 10-118F DELTA INERTIAL GUIDANCE + 544.3 KG FOR ERTS TYPE MISSION (RELATIVE TO BASELINE)	EXTENDED LONG TANK THOR TE-364-4	2.44 M INTERSTAGE 2.44 M FAIRING SUSPENDED SECOND STAGE + 181.4 KG FOR SYNCHRONOUS TRANSFER MISSION (RELATIVE TO BASELINE)

Figure 2. Delta improvement schedule, 1972.

the allowable spacecraft weight in an ERTS type orbit by about 545 kilograms (1200 lb) relative to the baseline vehicle.

Next was the launch of IMP-H, which was the first flight of the extended long-tank first stage. This is basically 3.1 meter (10 ft) extension of the propellant tanks, and features a revolutionary isogrid construction of the tank walls. IMP-H was also the first Delta use of the -4 third stage. Capping the 1972 introductions was delivery of the first 2.4-meter (8ft) diameter second stage, with an improved first-to-second stage separation system, and the 2.4 meter diameter all-metal fairing. The combined improvements have increased the allowable spacecraft weight for a synchronous transfer mission by about 180 kilograms (400 lb) relative to the baseline vehicle.

Reviewing briefly the launch record for 1972 (Figure 3), the year started with two launches for the European Space Research Organization. HEOS A-2 was placed in a near-nominal, highly elliptical orbit. It is an IMP-type particles and field satellite. TD-1A, an astronomical observatory, achieved a very accurate circular orbit. The ERTS-A launch vehicle, with its three major changes previously noted, and scores of minor improvements, performed flawlessly. All aspects of the IMP-H launch, with its significant innovations, and the ITOS-D launch, were completely successful. And finally, we are one day from the scheduled launch of Delta-92, our first straight eight vehicle. Surely, 1972 has been a year of spectacular achievement for NASA's busiest launch vehicle.

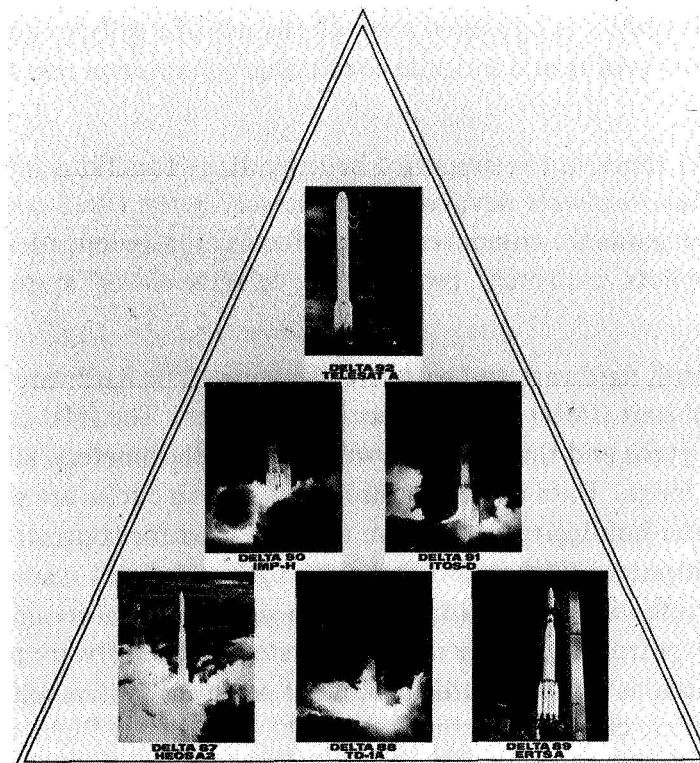


Figure 3. Delta launches – 1972.

DELTA LAUNCH VEHICLE INERTIAL GUIDANCE SYSTEM (DIGS)

Kenneth I. Duck

The Delta launch vehicle inertial guidance system (DIGS) which has been under development for several years, has now been successfully demonstrated in the launching of Deltas number 89, 90, and 91. This system is one of the improvements made by the Delta Project Office to increase vehicle performance, flexibility, and reliability in order to meet the launch objectives of the 1970s. The decision to convert from the radio guidance system previously used by Delta to a pure inertial strap-down system, was heavily influenced by the advances made in inertial guidance technology in recent years, and the inherent advantages associated with the use of an inertial system. Advantages associated with the use of DIGS in the Delta program are as follows:

- The extensive field support operation required by the radio guidance system can be eliminated, which will ultimately result in a reduced overall program cost
- Spacecraft injection accuracy is improved by at least a factor of two for two-stage missions
- Vehicle mission flexibility is improved through the use of a self-contained guidance system in that boost profile and attitude constraints for antenna pointing are eliminated
- The vehicle ground check-out is simplified because many functions formerly performed by individual hardware devices are performed by the DIGS computer. Devices whose function the guidance computer now performs are: independent first and second stage autopilots, sequencer, programmer, velocity cut-off system, and radio guidance system

The DIGS consists of both hardware and software elements. The hardware is made up of an inertial measurement unit (IMU) and an airborne computer. The IMU consists of three strap-down integrating gyros and three strap-down linear accelerometers, all of which have pulse torque rebalance loops. Data from 20 sensor torque loop cycles are summed and transferred to a computer-holding-register where they are used for controls and guidance computations. The computer utilizes a 24-bit word length and direct readout memory. It has available input discrete sense lines, output discrete signals, digital-to-analog converted signals, and a software controlled priority interrupt system. The software performs both preflight and flight functions. In the preflight mode it performs system alignment, engine slew checks, and a dynamic closed loop simulated flight test. In the flight mode the software performs open-loop sequencing, autopilot control, navigation, closed-loop guidance, and PCM data formatting.

The DIGS has been successfully flown on the last three Delta missions (ERTS-1, IMP-H, and ITOS-D). Extensive data analyses have been completed for the ERTS-1 and IMP-H flights. In examining the flight data, no events were observed that could not be explained. All flights have used the same flight program even though the mission profiles and vehicle configurations were significantly different. For example, the ERTS-1 launch used a two-stage vehicle with nine strap-on solid propellant thrust augmentors to achieve a near polar sun synchronous orbit. The IMP-H launch used a three-stage vehicle, six solid propellant thrust augmentors, and a lengthened first stage to achieve a near-escape orbit. The ITOS-D spacecraft was injected into an orbit similar to the ERTS-1 and had the same vehicle configuration except that it used three thrust augmentors instead of nine.

Typical injection accuracies are shown in the following table for the ERTS-1 and IMP-H missions, respectively. The table shows the apogee, perigee, and inclination deviation from nominal for selected second-stage burn-out points and the expected three-sigma dispersions. The significance of the points chosen for discussion are as follows: For ERTS-1 the second-stage burn-out (SECO-2) is the point at which the spacecraft is injected into orbit; IMP-H had a single second-stage burn and the point that was chosen as the third stage is unguided and predominates as a source of error.

Table 1
Typical DIGS Flight Performance Data

Delta 89 (ERTS-A) At SECO-2			
	Error	3-Sigma	Units
Apogee	2.213	- 5.942, +6.252	km
Perigee	-2.958	-12.87, +12.214	km
Inclination	-0.016	±0.044	degrees
Delta 90 (IMP-H) At SECO-2			
	Error	3-Sigma	Units
Apogee	6.714	-7.948, + 8.604	km
Perigee	1.551	-3.481, + 3.263	km
Inclination	0.005	±0.011	degrees

It is seen in examining the data that the orbit errors observed are of the order of one-sigma for ERTS-1 and two-sigma for IMP-H. The dispersions observed are of the magnitude of the errors expected from thrust tailoff and navigation uncertainties.

In conclusion, the Delta Inertial Guidance System, part of the Delta launch vehicle improvement effort, has become a reality. The system has been flown on three launches and was found to perform as expected for a variety of mission profiles and vehicle configurations.

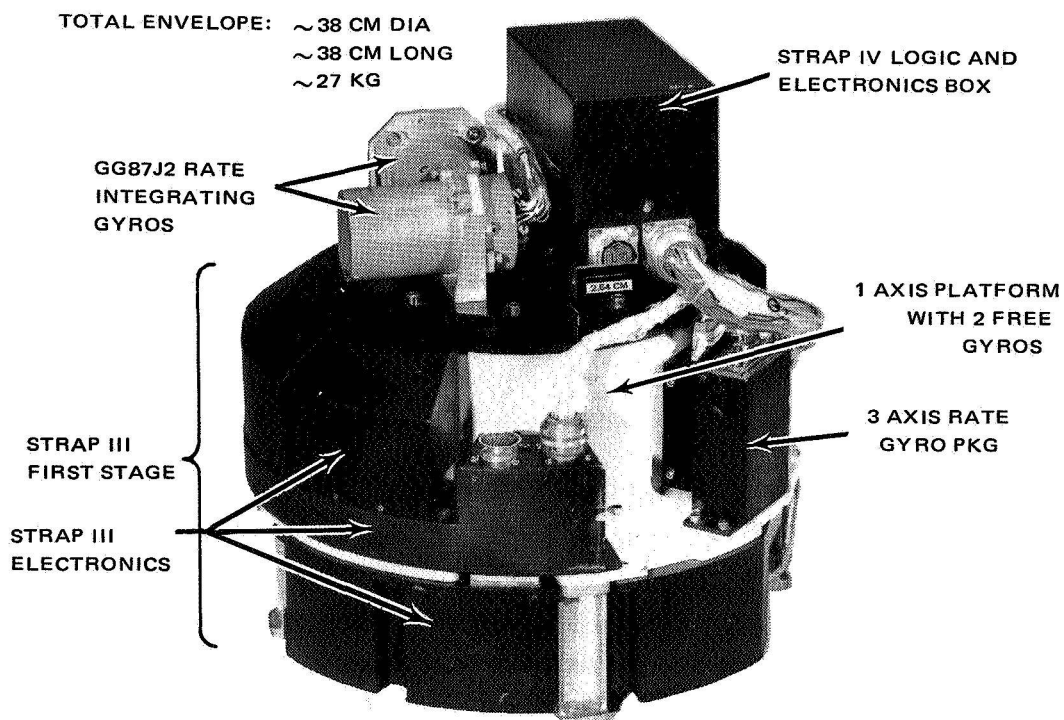
STRAP IV SOUNDING ROCKET ATTITUDE CONTROL SYSTEM

David J. Shrewsberry

I will discuss the STRAP IV sounding rocket attitude control system (Figure 1), which is used on Aerobee class and larger rockets. STRAP IV now provides our experimenters, for the first time, high accuracy pointing – better than ± 10 minutes absolute with ± 10 arc second stability – at nontrackable scientific objectives such as X-ray sources and diffuse star fields. Bear in mind that sounding rocket attitude control takes place during the coast phase of the flight, after motor burnout.

In the past, the STRAP III system with an experimental boresighted startracker, has been successfully used to stabilize and point the rocket payload to a stellar target within 30 seconds of control initiation.

X-ray astronomy is becoming increasingly active, and since many X-ray sources have been precisely located by rockets and satellites, it is now desirable to study their characteristics by pointing an instrument at them for an extended period of time. To reduce background noise the instruments necessarily must have a narrow field of view, which requires accurate



NOTE: THIS SYSTEM HAS FLOWN FOUR TIMES; TWO AS A STRAP III, TWO AS A STRAP IV

Figure 1. STRAP IV sounding rocket attitude control system.

payload pointing. Currently there are no X-ray source tracking devices similar to a startracker for rocket use. Consequently STRAP IV has been designed, built, and successfully flown as an in-house project of the Sounding Rocket Division to meet the requirement of the X-ray experimenters for high accuracy pointing at X-ray sources.

Because of STRAP III free gyro uncertainties about the coarse axis – mainly drift and torquing rate – it is usually not possible to physically offset either the experiment or the startracker so that a star could be tracked while the experiment viewed a target offset from the star, say by 10 degrees or so. The coarse axis uncertainty would cause a corresponding error to be translated to the experiment boresight axis, if either the startracker or the experiment axis were not parallel to the coarse axis.

STRAP IV utilizes a STRAP III first stage in conjunction with high quality rate integrating gyros (RIGS) operated in both closed loop and open loop modes. The RIGS have accurate torquers and a very low drift rate of less than one arc second of time. In normal operation the RIGS are zeroed on a nearby star and torqued to the proper location in the closed loop mode; that is, the rate output is electronically integrated to provide a position displacement signal. Once RIG closed loop torquing is completed, the caging loop is opened and the RIG is operated as an angular displacement sensor to provide limit cycle control while viewing the target.

The uncertainties about the coarse axis are reduced by first acquiring and tracking an overhead star, then moving to a second star near the first X-ray target. In moving from the first star to the second star an error is generated on the STRAP III free gyros which is proportional to the coarse axis error prior to the maneuver. This signal is used to update the coarse axis gyro and subsequently the vehicle itself, so that coarse axis error will not contribute to experiment pointing error when the vehicle is maneuvered under RIG control to the nearby X-ray target.

A typical flight profile of STRAP IV (shown in Figure 2) is as follows:

- An overhead star is acquired and the free gyros are caged
- A second star is acquired and the coarse axis error is reduced; the RIGS are caged to the star
- The vehicle is maneuvered to the desired location by torquing the RIGS closed loop
- The RIG torquing loop is opened and the fine limit cycle and experiment viewing is begun
- Other targets are acquired in a similar manner
- The payload is recovered by parachute

I want to emphasize the fact that we recover and reflly our ACS. The system shown in Figure 1 has been flown four times, and will be flown again in the spring.

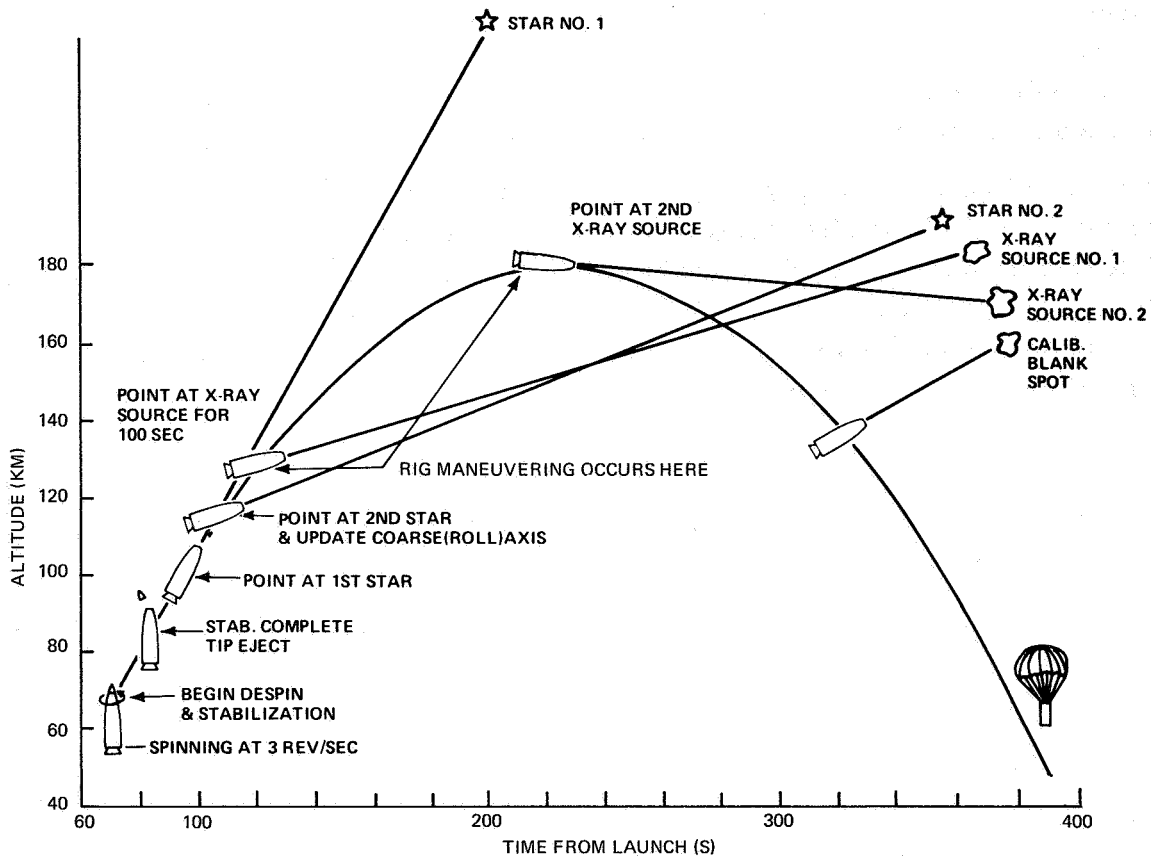


Figure 2. STRAP IV flight profile.

Figure 3 is an actual flight telemetry record from the first launch of STRAP IV in May of this year. For this shot the two fine axes were roll and yaw. The sequence of events is:

- Coarse axis update occurs
- The fine mode startracker signal is received, during which time the RIGs are caged to the star
- The first RIG maneuver is accomplished
- When yaw is within 0.5 arc minute, the second RIG maneuver occurs
- When roll is within 0.5 arc minute, the fine limit cycle is enabled and experiment viewing begins

The magnitude of the fine limit cycle can be seen here to be around 20 arc seconds peak to peak with very low body rates. On this launch, we pointed the payload to within four arc minutes on both X-ray targets.

The ACS Branch has several more STRAP IV launches scheduled in the next year.

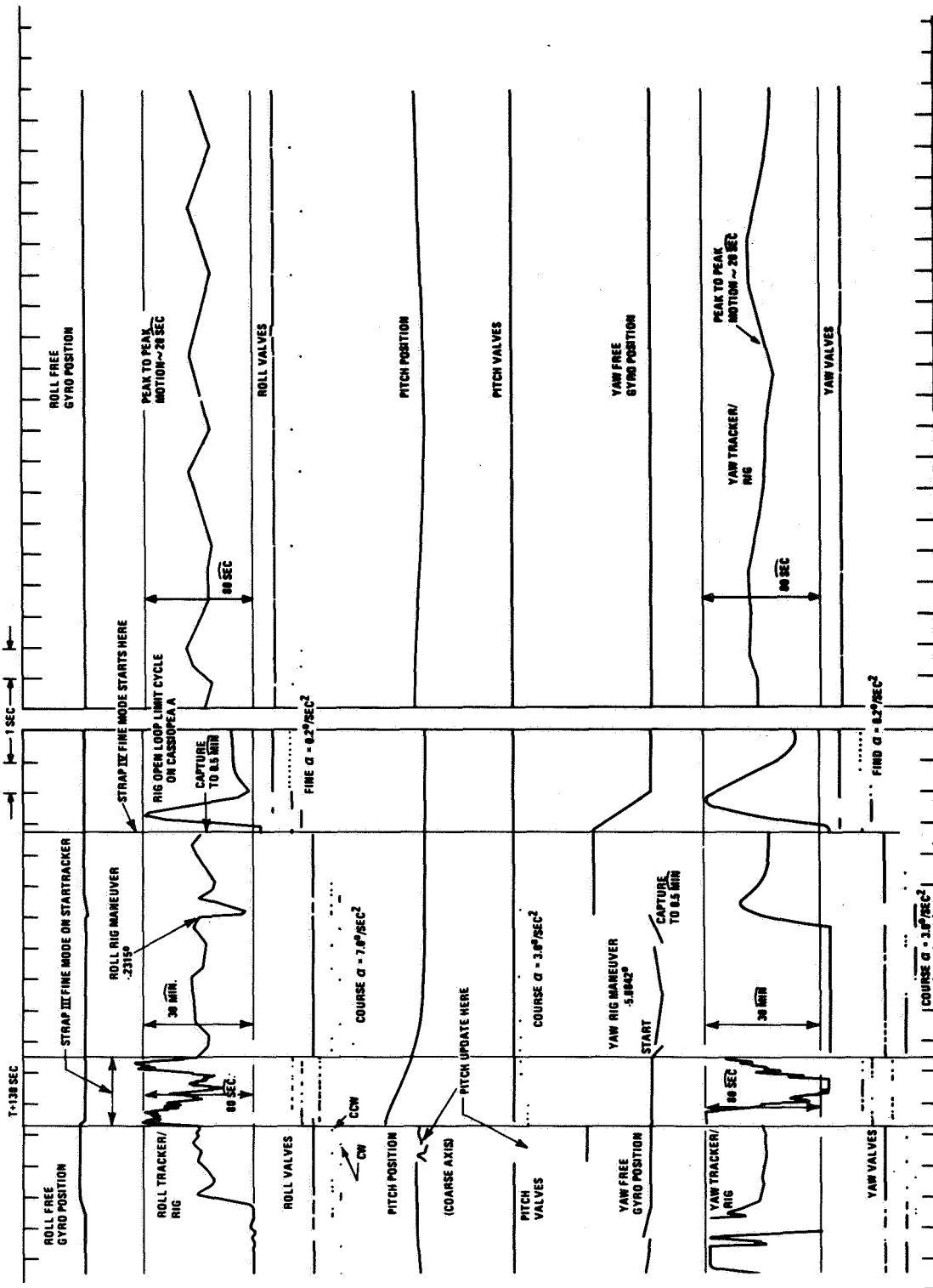


Figure 3. STRAP IV flight telemetry, Aerobee 13.009GG.

INERTIAL REFERENCE UNIT

Frederick J. Kull

The Inertial Reference Unit, referred to as the IRU, is a high performance gyro attitude reference system designed and built by the C.S. Draper Laboratory at MIT for use on the OAO Spacecraft. The IRU is a three axis system, which provides both rate and attitude information for spacecraft control.

The purpose of the IRU is to reduce the dependency on gimballed startrackers and, in turn, simplify the OAO ground operations by eliminating the need for the continual programming of gimballed startracker assignments in accordance with computed occultation schedules. During normal operations, it is used to control the pitch and yaw axes during experiment occultations and during spacecraft reorientations. The roll axis is continuously under control of the IRU except during brief periods for attitude update.

To provide for these capabilities the IRU must be able to perform two basic functions. One is to maintain an inertially fixed reference for spacecraft control and the second is to accurately reorient the reference upon command.

The accuracy of a spacecraft reorientation is primarily a function of the accuracy and stability of the torquer pulse weighting factor and gyro alignment relative to the spacecraft control axes. The performance goal established prior to launch was to have the capability of reorienting the spacecraft up to thirty degrees, and acquiring a target star within the field of view of the Princeton Experiment, which is ± 4 minutes of arc. This capability was demonstrated in orbit prior to the conduct of the slew calibrations. The degree to which this goal will be exceeded, especially after the slew calibration and alignment data are available, is not known at this time.

The capability of the IRU to maintain a fixed inertial reference is limited by the effective drift level. The high performance drift characteristics achieved by the IRU are based on the use of gyros and torque rebalance loop electronics which have extremely stable characteristics and the capability for in-orbit commandable drift compensation. The performance goal was to achieve a compensated drift rate of less than 10 arc seconds per hour. This goal has been exceeded by more than an order of magnitude. The IRU has demonstrated the capability for maintaining an inertially fixed reference with an accumulated error of less than one arc second per hour. This level of performance has proved extremely valuable on the OAO spacecraft and provides a basis for the expanded use of precision gyro reference systems. Improvements in this drift performance are limited by both the ability to accurately measure drift at this level and the granularity of the in-orbit compensation term.

An interesting by-product of the IRU drift determinations, and one which demonstrates the problems associated with the measurement of these low levels of drift, is the direct measurement by the IRU of the velocity aberration phenomena.

Figure 1, which relates to the pitch axis, indicates the IRU attitude error while the spacecraft is pointing at a specific star under control of the Princeton Fine Error Sensor. The breaks in the data are due to occultation of the experiment and ground contacts when the spacecraft is controlled by the IRU.

The curve defines the deviation between the IRU reference and the Princeton Fine Error Sensor reference. The ramp component of the curve is the IRU drift, which in this case is less than one tenth of an arc second per hour, or about $\frac{1}{4}$ degree per year. The sinusoidal component of the curve is the spacecraft motion resulting from the response to an apparent sinusoidal motion of the target star. Although the star is inertially fixed, its apparent position varies as a function of the velocity of the spacecraft normal to the line of sight to the star source. This is the velocity aberration phenomena. The magnitude of the maximum velocity aberration error is within a few percent of that theoretically predicted for the OAO orbital characteristics.

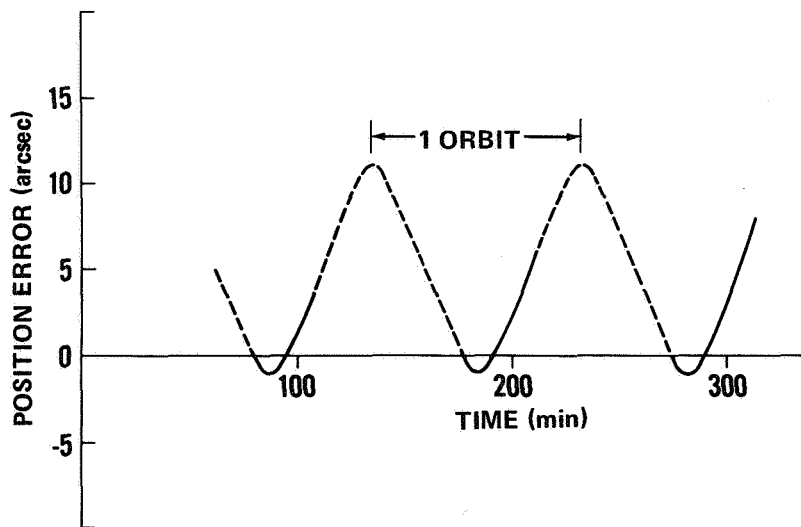


Figure 1. IRU/PEP differential error.

FINE POINTING CONTROL, OAO-3

James V. Moore

During periods of experimentation with the Princeton Experiment Package (PEP), the sensor used for spacecraft control was the fine error sensor located within the PEP. This fine error sensor, in conjunction with the balance of the control loop, was designed to acquire a star within the field of view of the fine error sensor; and hold the spacecraft within plus or minus one-tenth of an arc second in pitch, and plus or minus three-arc seconds about the yaw axis.

My first figure defines the result of a test that was conducted in orbit to measure the transfer function of the PEP.

This test consisted of driving the fine error sensor across the target star, about the pitch axis, at a stable rate of one-tenth of an arc second per second, and plotting the error signal as a function of the vehicle angle.

The resulting transfer function defines a maximum gain of about 36 volts per second of arc at null.

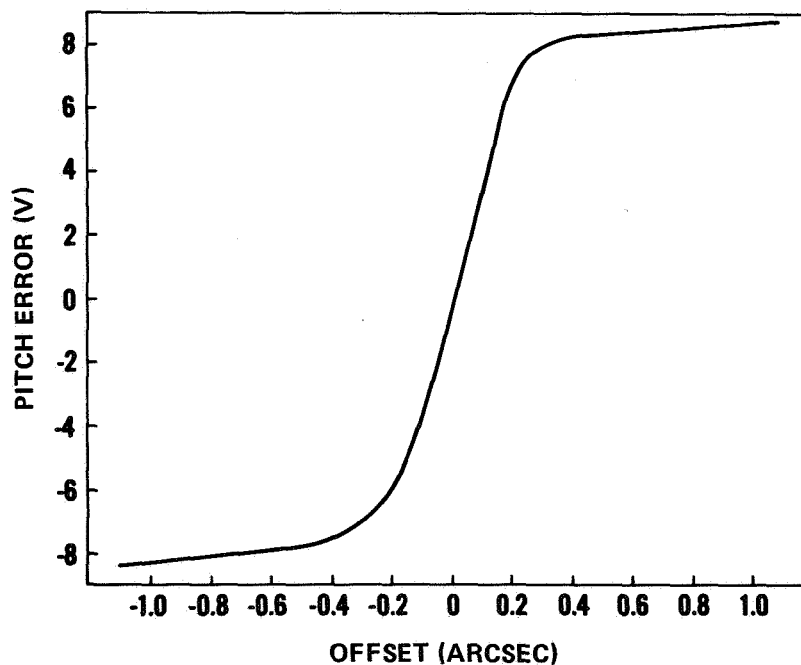


Figure 1. PEP fine error signal, pitch transfer function.

With regard to pointing accuracy and stability, the performance under control of the PEP fine error sensor has been exceptional, and far exceeds the plus or minus 0.1 arc second requirement.

This precise pointing has resulted in extremely high quality experiment data. It has been noted that the pointing stability varies as a function of the spacecraft attitude and orbital position. This phenomena is not completely understood at this time and is presently under study. The level of stability also varies as the spacecraft moves from "day" to "night." Additional variations have been tentatively attributed to noise sources. Figure 2 describes the settling and holding characteristics of the PEP control loop for a specific observation. During the initial period after settling, the spacecraft is in the light. During this period, the maximum of spacecraft jitter is encountered. This maximum jitter, however, is only plus or minus five-hundredths of an arc second.

During the dark portion of the orbit, the PEP stability is variable. For this particular observation, the maximum jitter is plus or minus three-hundredths of an arc second with relatively long periods of time when the jitter is less seven thousandths of an arc second.

To put this number in perspective, if the spacecraft were pointed at the earth, seven-thousandths of an arc second would be equivalent to one inch on the earth's surface. As stated previously, this defines a specific observation. There were observations when the jitter remained at relatively high levels of plus or minus three-arc seconds for the entire viewing time. There were also observations where the very quiet condition was maintained throughout the contact. The variation and jitter that were demonstrated in this figure approach the normal condition.

The performance goals for the OAO program have been more stringent with each launch.

(OBSERVATION - ORBIT 581)

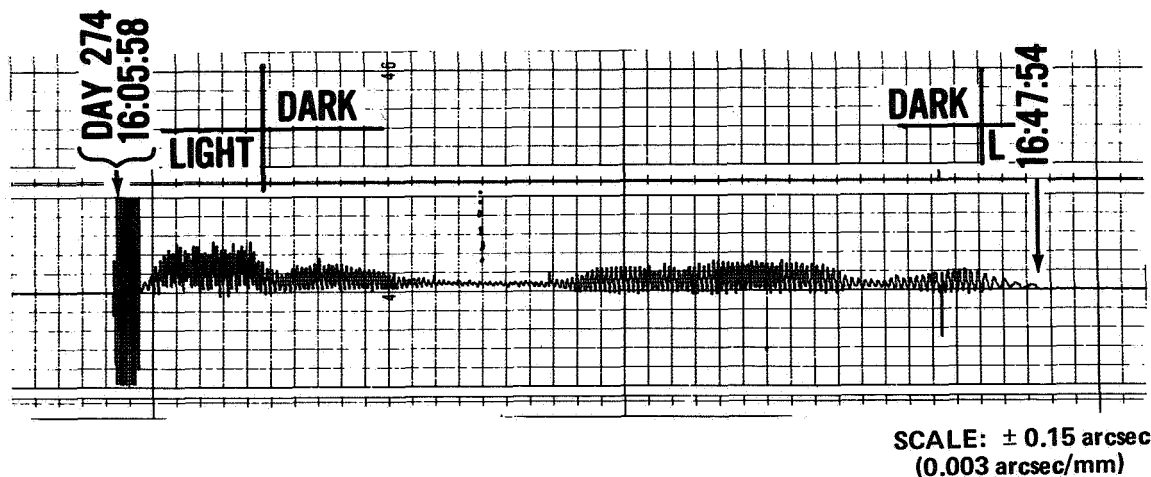


Figure 2. PEP fine error sensor signal.

My final figure summarizes the stability requirements for each spacecraft as dictated by the objectives of the on-board scientific instrument. This summary shows that the performance exceeds the original goals of the OAO program. In addition actual in-orbit data from OAO-C indicates an unprecedented pointing accuracy.

OAO SPACECRAFT	STABILITY GOAL (arcsec)	DEMONSTRATED PERFORMANCE (arcsec)
A2	± 15.0	± 3.0
B	± 1.0	NO ORBIT
C	± 0.1	$\pm .007$

Figure 3. Performance summary.

THE DATA PROCESSOR FROM THE SMALL SCIENTIFIC SATELLITE

Harry G. McCain

The Small Scientific Satellite, called S³, was launched on November 15, 1971.

The mission of S³ is to investigate the inner-magnetosphere of the earth. After a year in orbit, the satellite has been declared an official success, and the experimenters have been extremely happy with the data they have received.

One of the main reasons for this success has been the reprogrammable data system aboard the spacecraft.

Figure 1 shows the approximate duties of a typical spacecraft data system. These duties include sampling the experiments one by one, taking the data in, formatting that data, and preparing it for transmission to the ground.

A typical hard-wired encoder will sample these experiments in order one by one, and then repeat the sequence again and again.

A reprogrammable system such as the one onboard S³ can rearrange this order in any way desired, so that an experiment which is not giving significant data at the moment can be ignored or can be skipped in a sequence. The sequence can be changed around or an experiment which is giving particularly interesting data at the moment can be sampled repetitively.

In addition to this feature on the S³ system, experiments are sampled in synchronization with the spin of the spacecraft. This allows the experimenter to know the spin orientation of the spacecraft, and to sample his data at any desired position in the spin.

As shown here, the S³ system is an in-line system, and it is not a backup system for any other encoder system.

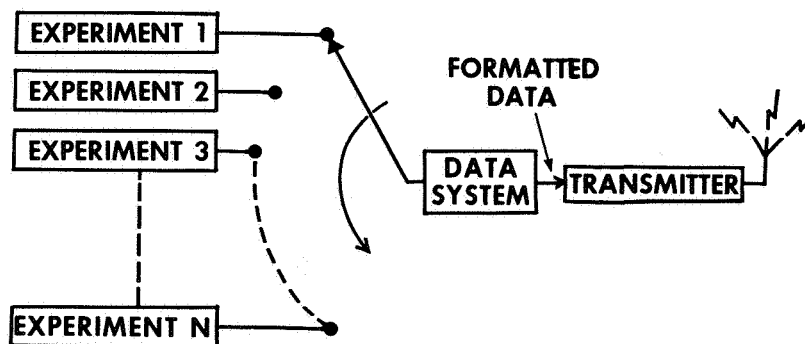


Figure 1. Function of typical spacecraft data system.

You may well ask what makes the S³ system different from other reprogrammable systems? The main difference results from the small size of the spacecraft. Also, it is designed for multiple missions, which I will explain in more detail later.

The weight of the spacecraft is only 50 kilograms. Therefore, power, weight, and volume constraints were very strict on the data system, as shown in Figure 2 – only 5.65 watts, 3.8 kilograms, and 0.056 cubic meters, respectively.

Figure 3 shows the basic configuration of the S³ system, which is made up of four boxes. The program memory, where the programs are stored, which is reprogrammable from the

- REPROGRAMMABLE
- DESIGNED FOR MULTIPLE MISSIONS
- DESIGNED FOR SMALL SPACECRAFT
 - LOW POWER 5.65 W
 - LOW HEIGHT 3.81 KG
 - LOW VOLUME 0.006 M³

Figure 2. S³ data processing system characteristics.

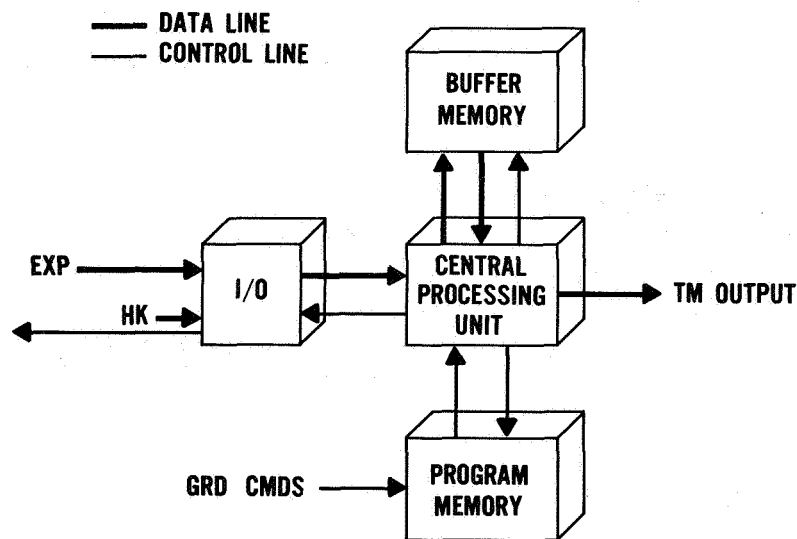


Figure 3. Block diagram S³ data handling system.

ground. A data memory, which provides buffering because the spacecraft clock times the telemetry output and the spin-synchronous clock times the data coming in. There is an input/output module, which interfaces with the various signal types of the experiments; and a central processing unit which controls the entire system.

To provide flexibility for multiple missions, this system was built modularly so that these three boxes (BM, PM, CPU) would not have to be changed. Only the signal conditioning for the experiments need be changed if a similar type mission were to be flown.

At launch, the reprogrammability of this system proved very valuable to the spacecraft. Right after launch it was discovered that the spacecraft was wobbling, or nutating, and it was found by the spacecraft dynamics people that it was necessary to obtain the magnetic crossing times with a great degree of accuracy in order to correct this nutation problem. Reprogramming the system enabled these people to obtain the information they needed.

It was found after the nutation problem had been solved that in order to maintain a small, stable nutation angle, the spacecraft had to be spinning at almost twice the originally anticipated rate.

Since the original programs had been written so that the experimenters could look at their data synchronized to the spin, it was necessary again to reprogram the system in order to correct for this increased spin rate. As a result of reprogramming, there was no degradation of the data.

In addition to these two examples, the data system has been reprogrammed more than 165 times as of October 25, to accomplish other specific goals. The experimenters feel that this reprogrammability has enabled them to perform several experiments rather than just the one which a hard-wired encoder would have allowed them to do.

Presently, the spacecraft is investigating a magnetic storm by using six different programs on one storm in order to thoroughly drain the scientific data available.

As a result of this type of adaptability, the reprogrammable data system is considered to be the largest contributing factor to a successful S³ mission.

MEMBER OF THE AUDIENCE:

What is the size of the data memory?

MR. McCAIN:

It is 4096 words, four bits each.

THE ONBOARD PROCESSOR ON OAO-3

Thomas D. Taylor

Figure 1 is a picture of the onboard processor, or OBP, which was developed here at Goddard by the Spacecraft Data Management Branch. This computer was developed specifically for flight applications, and I would like to address myself to the first application of this computer on OAO-3, or Copernicus, which was launched on August 21 of this year.

Before talking about the boxes, I would like to mention that the computer was turned on the day after launch, and has been executing instructions at the rate of 2½ billion a day. We have executed 2×10^{11} instructions since launch. This is an 18-bit, parallel, medium-scale computer. The four boxes on the right are four memory units. Each memory unit is 4096 words. There is a central processor unit, an IO unit, and off to the left is the power converter for the computer. It is a 40-watt machine. Its capability lies somewhere between that of an XDS-920 and 930, to compare it with the capability of a ground computer. It has a ten-microsecond add time and a hardware multiply/divide capability.

In interfacing the computer on the OAO spacecraft, we could only connect to signals which were on connectors, but we were still able to gain access to the spacecraft telemetry, and

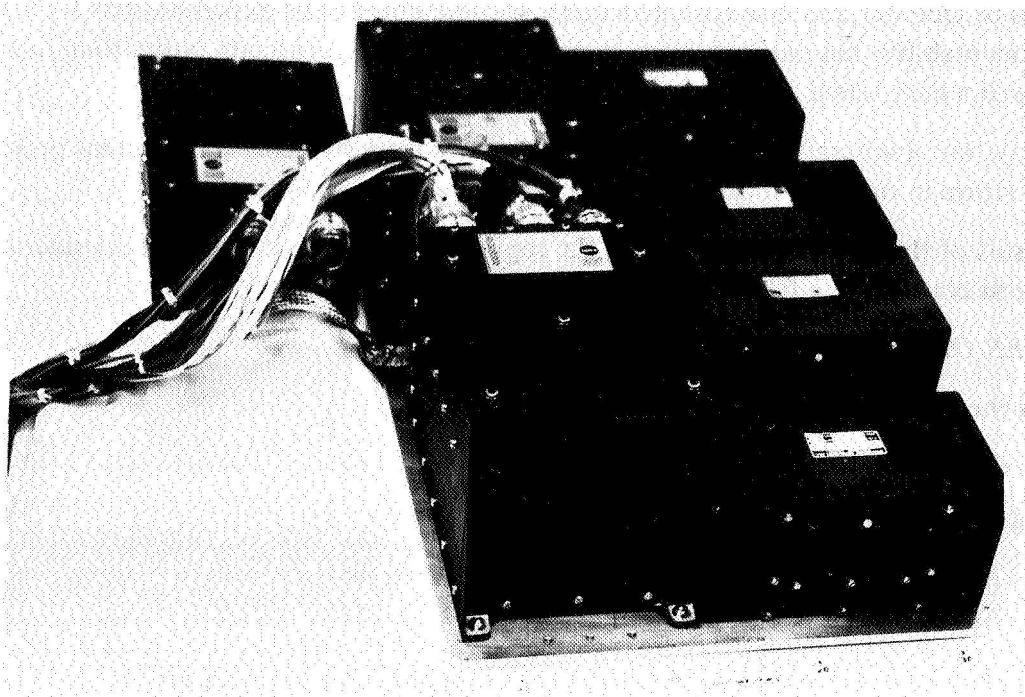


Figure 1. The OAO-3 onboard processor (OBP).

so have access to all spacecraft status data. There are four analog signals out of the computer, three of which control the fine wheels and one controls the power regulator unit on the spacecraft. The computer can also issue commands, and therefore, the computer has powerful interface with access to all spacecraft telemetry and the ability to send any OAO command.

Next, I will discuss the applications of the computer, but I wanted to say in passing that the design of this computer was tailored for space applications and it is a very worthy design. Such features as hardware memory protect, the ability to load and dump the memory without program execution, and the very powerful interrupt structure have proved useful and made it easy to program. These features have increased its utility as well as its security.

There are three main application areas: commanding, data processing, and as in Figure 2, worker programs, or subsystem programs. In the commanding area, the hard-wired command handler on OAO stores 256 commands. One day's operation requires the execution of about 1000 commands. The computer provides an additional 1024 command storage capacity, so that the spacecraft can be loaded with commands once a day, sending 256 to the wired command handler, an additional 1024 to the computer, and then in the back orbit the computer transfers commands in blocks of 128 to the hard-wired command handler. This has reduced the need for ground station coverage for OAO. Commands are loaded at only Rosman. There is no need to load commands at remote sites and ground station requirements have been reduced by 40 percent with this feature.

COMMANDING

- **AUXILIARY COMMAND STORAGE**
- **SCRATCH-PAD COMMAND STORAGE**

DATA PROCESSING—STATUS BUFFER

- **DUMPED ONCE/ORBIT**
 - OBP COMMAND ACTIVITY**
 - S & C MODE CHANGES**
 - ATTITUDE-FIX DATA FOR GROUND**
 - POWER SNAPSHOTS AT D/L/D**
 - PERIODIC SNAPSHOTS**
 - ALARMS**
- **VALUABLE FOR TRENDS AND ALARM**

Figure 2. OBP applications.

There is also what is called a scratch-pad command storage. This essentially augments the command execution of the command handler on the spacecraft. Commands may be sent to the computer rather than being sent to the command handler. The computer imitates the command handler, in that it compares the execute time of the command with the spacecraft time. When a time equality exists, the computer formats the command as though it were coming from the ground and sends it to the command handler for immediate execution. This affords the interleaving of commands from preprogrammed command memory with the computer. It is a very important feature which has been used successfully many times in orbit.

The scratch command feature is used for engineering tests in which the engineering test commands are loaded in the computer and it performs the engineering test and does not interfere in any way with normal experiment operations. Also, it is a good emergency feature so that should a problem be detected during a ground station contact, corrective commands which must be issued in the back orbit can be sent to the computer and it will execute them in the back orbit without interfering with the normal command memory load.

In the data processing area, there is a 320-word block of memory, which is continually stored into during the back orbit of the OAO. In there, the computer records its command activity, and stabilization and control mode changes, some attitude data for the ground to assist in attitude determination of the spacecraft, and snapshots of the power system at dark-light and light-dark transitions.

The 320-word block of memory has a very good synopsis of the condition of the spacecraft, and also a list of the significant events of the spacecraft in the back orbit. This data is dumped once an orbit, and a realtime printout is given to the ground controllers. It has virtually eliminated the need for tape recorder playback and analysis which has a two- to three-week turnaround time.

In the subsystem area we were fortunate in having access to all telemetry data in the computer, because this contains data from all the subsystems on the spacecraft, coupled with the ability of the computer to send any spacecraft command. With that interface, the computer is able to perform a broad range of functions in the various subsystem areas (Figures 2 and 3).

For example, in the case of the Princeton Experiment Package spectrometer temperature control, the computer can provide a thermostatic function better than a thermostat, because even though it is a trivial function, the threshold is adjustable and the hysteresis can be diminished as much as thermodynamics allows.

Heat pipe control is a program which turns heaters on and off to maintain a constant power to the bay in which there are heat pipes on the spacecraft. It is a complicated algorithm. The computer duty cycles the heaters to maintain a constant power, and all that's needed is a program to do this function. The interface allows it and it would require considerable hardware to do the function on the spacecraft.

WORKERS (COMMANDING)

- **THERMAL**
 - PEP SPECTROMETER TEMP CONTROL
 - HEAT PIPE CONTROL
- **POWER**
 - MAX POWER
- **S & C**
 - HOLD WHEEL SPEED
- **WORK-AROUND PROGRAMS**
 - BST STAR SEARCH
 - FINE GUIDANCE BACKUP
 - RELIEF VALVE (GAS LINE)
 - UNDER VOLTAGE DETECT
 - SUN AVOIDANCE
 - I-STAR INSTABILITY

Figure 3. OBP applications (continued).

In the power area there is a max-power algorithm in which the computer controls the voltage regulator. The computer essentially sets the operating point of the array to maintain the maximum power from the array.

There are several workaround programs which will be called into use should that need arise. One of them, the undervoltage detect, is going to be committed to operations this week, because the level is adjustable if the function is done from a computer. It has turned out on OAO that the undervoltage level does not permit the optimum charging of the batteries, so the project is going to commit to computer operation of this point.

So we feel that the computer on OAO has enhanced ground operations, and has made them simpler. We feel that the computer has improved the performance of the spacecraft. And we feel that we have proved that a central computer on a spacecraft can do subsystem jobs in a cost and performance effective way.

MEMBER OF THE AUDIENCE:

Have you used the arithmetic unit portion of the computer?

MR. TAYLOR:

Yes. The heat pipe control program has been our main use. That is a complicated algorithm. We are multiplying, dividing — in fact, we do the logic in double-precision arithmetic.

**GRAVITY-GRADIENT DYNAMICS EXPERIMENTS PERFORMED IN
ORBIT UTILIZING THE RADIO ASTRONOMY
EXPLORER (RAE-1) SPACECRAFT**

Harvey Walden

Between December 1970 and December 1971, a series of six dynamics experiments was performed in earth orbit utilizing the RAE-1 spacecraft as an experimental apparatus. This satellite, launched into a near-circular earth orbit at nearly 6000-kilometer altitude on July 4, 1968, measures radio emissions from extraterrestrial sources at frequencies which are obscured from ground-based instruments due to ionospheric interference.

As shown in Figure 1, the spacecraft consists of four highly flexible antenna booms mounted in a double-vee configuration with a rigid cylindrical spacecraft hub at the center. The four main radio frequency sensing antenna booms each extend 230 meters from the hub center, making the RAE-1 spacecraft the largest array in longitudinal dimensions ever placed in space. In addition to monitoring long-wavelength emissions from cosmic sources,

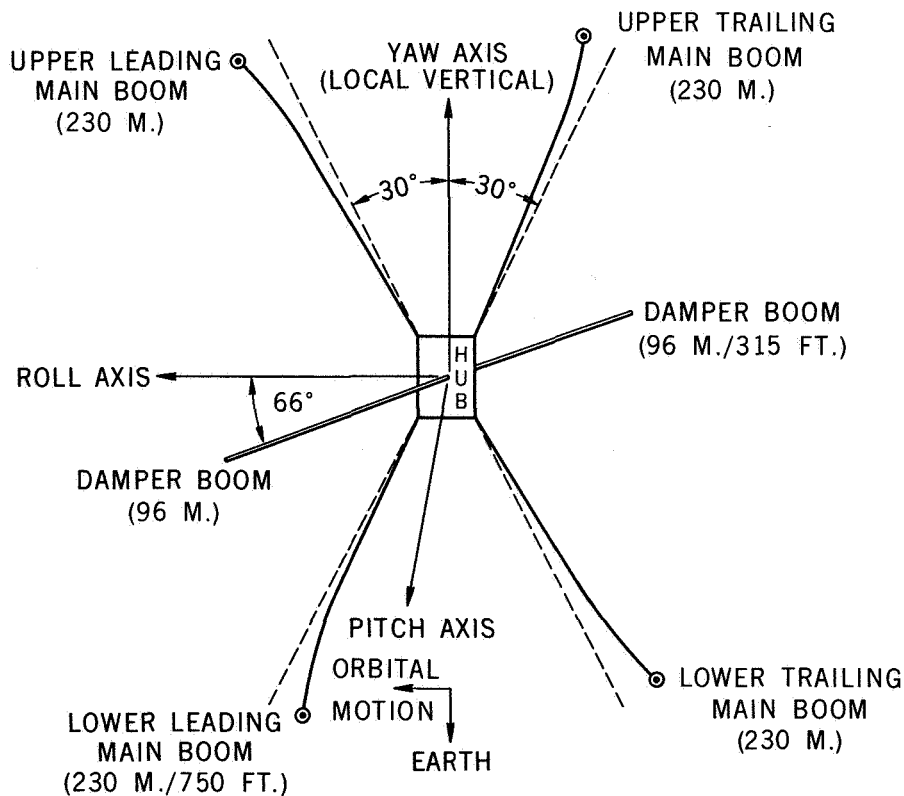


Figure 1. Basic configuration of the RAE-1 satellite.

the vee-antennas serve to stabilize the spacecraft in a nonspin mode about the local vertical axis by the passive three-axis gravity-gradient method. In this way, one vee-antenna is continuously directed toward the earth, while the other antenna scans the celestial sphere under the combined effects of orbital motion and orbital precession in inertial space. Rotational oscillations of the spacecraft hub and the resulting indirect vibration of the primary antennas are attenuated by a magnetic hysteresis damper mechanism consisting of two additional damper booms, each 96 meters from hub center to tip.

In the 26 months following full deployment of the primary antenna booms in October 1968, the RAE-1 satellite remained stabilized by gravity-gradient forces about the roll, pitch, and yaw axes to within a few degrees of local orientation. Altitude stabilization was entirely passive, with the basic control torques provided solely by gravity-gradient and inertial forces. Damping was provided by the magnetic hysteresis libration damper system and by whatever structural damping was present in the primary booms. The well stabilized attitude motions about the three axes were so small and erratic, in fact, that it was often impossible to distinguish between actual oscillations and sensor system noise and inaccuracies.

In light of the numerous difficulties encountered in attitude control of previous flexible gravity-stabilized spacecraft, and in order to advance current understanding of the dynamics of gravity-gradient stabilization, the six in-orbit experiments (as shown in Figure 2) were conducted. These dynamics experiments were developed to test the accuracy of the mathematical model of the RAE dynamics, which was formulated prior to the 1968 launch and used subsequently to predict and describe the spacecraft in-orbit dynamical behavior.

- **DAMPER CLAMPING**
 - FULL SUNLIGHT CONDITIONS (DEC. 1–7, 1970)
 - PARTIAL SOLAR SHADOWING (JUNE 14–21, 1971)
19- TO 25-MIN SHADOW PER 225-MIN ORBITAL PERIOD
- **SINGLE LOWER LEADING BOOM OPERATIONS**
 - PARTIAL RETRACTION TO 165-M LENGTH (JAN. 18, 1971)
DAMPER ACTIVE THROUGHOUT
 - FULL REDEPLOYMENT TO 230-M LENGTH (JAN. 25, 1971)
DAMPER CLAMPED FOR 29 HR INITIALLY
- **DOUBLE LOWER BOOM OPERATIONS**
 - PARTIAL RETRACTION TO 200-M LENGTH (DEC. 7, 1971)
DAMPER CLAMPED FOR 24 HR INITIALLY
 - FULL REDEPLOYMENT TO 230-M LENGTH (DEC. 15, 1971)
DAMPER ACTIVE THROUGHOUT

Figure 2. RAE-1 gravity-gradient dynamics experiments.

The RAE-1 spacecraft was, thus, deliberately perturbed in precise and well-calculated fashion so that flight data relating to the spacecraft dynamics under mildly adverse situations could be gathered.

In the first pair of experiments shown in Figure 2, the damper was clamped, or rendered inactive – once for a six-day period when the satellite was in full sunlight, and later again for a similar period when it was experiencing partial solar shadowing during each orbit. These experiments were designed to determine how great a role the damper system had been playing in maintaining the excellent spacecraft attitude stability under steady-state sunlight and time-varying solar pulsing conditions. The second pair of experiments involved creating an asymmetrical spacecraft configuration in order to perturb the satellite away from equilibrium, and observe the resultant transient attitude motions and subsequent damper effectiveness. The lower leading boom was partially retracted some 54 meters to a shortened length of 165 meters with the damper mechanism remaining active. After seven days in this state of mismatched boom lengths, the retracted boom was fully redeployed, but, during this experiment, the damper was kept clamped for the initial 29 hours after deployment. This experiment was intended to investigate the spacecraft's dynamical behavior when initially considerably removed from the steady-state equilibrium condition for the nominal symmetric configuration and when deprived of damper action. In the final pair of experiments, two lower booms were partially retracted simultaneously some 30 meters to 200 meter lengths, and then eight days later, redeployed back to full lengths. In this pair, however, the damper was clamped for a 24-hour interval after the boom retraction operation and, conversely, the damper was allowed to remain in active status upon redeployment. These last two experiments were designed to investigate the spacecraft dynamics under a third distinct configuration, known as a semisymmetric array (two pairs of vee-antennas at unequal length), both with, and without benefit of damper action.

The performance of the entire series of six dynamics experiments was completed successfully over the course of 13 months. No hardware failures aboard the spacecraft, or major operational difficulties were experienced. Figure 3 provides a sample of in-orbit attitude measurements observed and a comparative match with the results of a computer simulation of the flexible-body spacecraft dynamics. These data were recorded during the second dynamics experiment, performed on January 18, 1971, beginning at the time at which a single lower boom was partially retracted and extending for 25 hours thereafter with the damper active throughout. Although the motions in roll remain fairly small in amplitude, it is seen that the retraction excited a very noticeable pitch libration, with an initial amplitude of ± 10 degrees, about an average value of -4 degrees. The fact that the equilibrium value is biased negative by 4 degrees, as compared to the pre-experiment zero equilibrium value, is a direct result of the asymmetry caused by the boom retraction. A significant reduction in the pitch motions is observed during the first eight hours or so after retraction; further attenuation in amplitude was slow and irregular. The retraction operation also excited an initial yaw libration of ± 14 degrees, centered about an

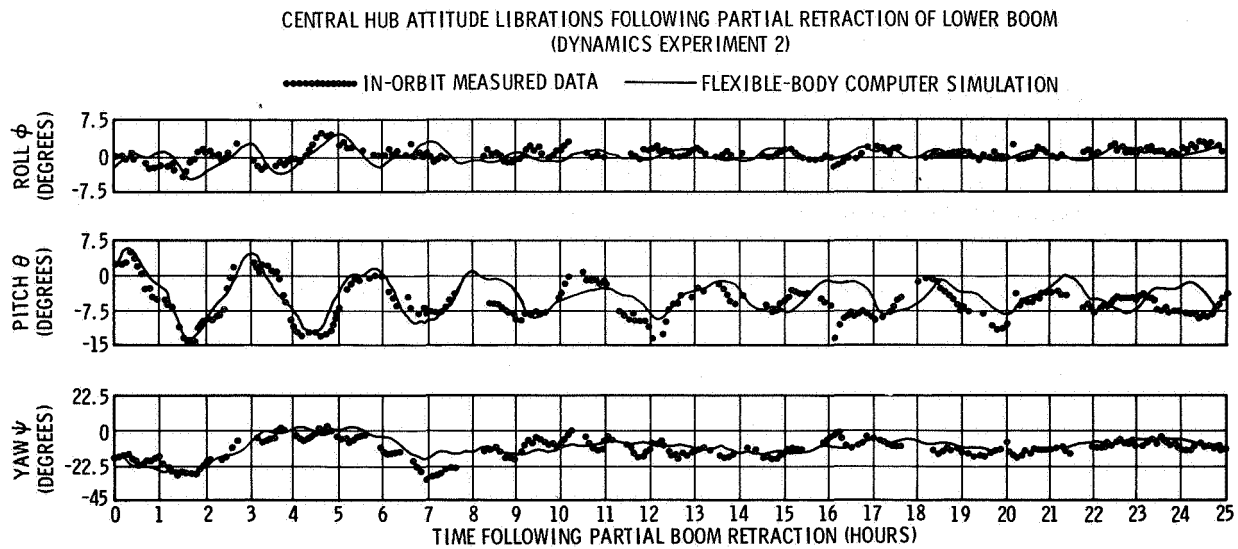


Figure 3. Central hub attitude librations following partial retraction of lower boom.

equilibrium value of -12 degrees (which is approximately the equilibrium value under a symmetric configuration, with the negative bias caused by the fact that the damper booms are skewed at an angle of 66 degrees from the plane of the primary double-vee antennas; see Figure 1). The yaw motions observed immediately after retraction reduced fairly rapidly to ± 5 degrees and less. The cause of the pitch libration immediately following the signal boom retraction is the resultant reduction of the spacecraft moment of inertia about the pitch axis. This, according to the principle of conservation of angular momentum, caused the pitch rate, relative to both inertial space and to the rotating local vertical, to increase. The conservative restoring torque due to gravity gradient counteracted the resulting pitch motion, and hence, the spacecraft began to oscillate. The results of the computer simulation of the flexible-body spacecraft dynamics are seen to provide an excellent duplication of the flight data.

The primary results and conclusions of the full series of in-orbit dynamics experiments are displayed in Figure 4. Based upon the excellent correlation that was observed between the in-orbit measurements and the results of the computer simulations throughout the series of experiments, increased confidence in the accuracy of the analytical techniques used to model the RAE dynamical behavior has been generated. The dynamics experiments also provided an opportunity to investigate the in-orbit capabilities of the damper system aboard the RAE-1 spacecraft. The effectiveness of the damper system was significant in reducing large angular attitude disturbances and in alleviating adverse dynamical situations, as was indicated in Figure 2. However, the absence of a substantial increase in attitude oscillations during the two damper clamping experiments verified that external disturbances produce only minor effects on the spacecraft. Therefore, the damper system is only marginally useful in maintaining dynamical stability (at least over time intervals not

- **INCREASED CONFIDENCE IN VALIDITY AND ADEQUACY OF**
 - **COMPUTER SIMULATIONS** } **USED TO MODEL RAE DYNAMICS**
 - **ANALYTICAL TECHNIQUES** }
- **RAE-1 ON-BOARD DAMPER SYSTEM CAPABILITIES IN ORBIT**
 - **SIGNIFICANT FOR REDUCING LARGE-AMPLITUDE ATTITUDE OSCILLATIONS**
 - **ONLY MARGINALLY USEFUL IN MAINTAINING DYNAMICAL STABILITY NEAR EQUILIBRIUM**
 - **MORE EFFECTIVE FOR ASYMMETRIC SPACECRAFT CONFIGURATION**
- **IN-ORBIT OBSERVATION OF PITCH-YAW NONLINEAR COUPLING PHENOMENON THAT HAD BEEN THEORETICALLY PREDICTED**
- **EXTERNAL IN-ORBIT DISTURBANCES ON SPACECRAFT ARE VIRTUALLY NEGLIGIBLE**
- **ON-BOARD MECHANICAL AND ELECTRICAL SYSTEMS PERFORM RELIABLY EVEN AFTER 3½ YEARS IN SPACE ENVIRONMENT**
- **INCREASED CONFIDENCE IN ACHIEVING SUCCESSFUL RAE-B LUNAR MISSION (SPRING 1973)**

Figure 4. Primary results of in-orbit gravity-gradient dynamics experiments.

greatly exceeding one week) after the spacecraft is brought close to equilibrium conditions. These results, in fact, confirm the design criteria adopted for the damper prior to launch. The surprisingly rapid damping of large pitch and yaw motions, as shown in Figure 3, indicates that the damper is more effective for an asymmetric spacecraft configuration (such as mismatched boom lengths) than for the nominal symmetric configuration, and this result reflects a point of new knowledge about the system.

During the single boom redeployment experiment, when the damper was inactive, a non-linear coupling phenomenon was observed between the pitch and yaw modes of oscillatory motion. During the interval of damper clamping, the pitch motions excited by the redeployment operation remained fairly constant, but the yaw librations increased dramatically and then decreased at about the same rate. Apparently, the RAE-1 is the first satellite known conclusively to have demonstrated this instability in orbit, although such a resonance phenomenon had been predicted previously on theoretical grounds.

Finally, the wholly successful performance of the series of dynamics experiments, without adverse impact to either the spacecraft structure or to its scientific mission, was due largely to the fact that the mechanical and electrical systems aboard the satellite performed satisfactorily and reliably, even after exposure to the hostile space environment for more than three years. In sum, these results will aid the design and planning of the forthcoming RAE-B mission (now scheduled for launch in spring 1973 into lunar orbit with a nearly identical spacecraft to RAE-1) and provide increased confidence in achieving a successful lunar mission.

HEAT PIPE FLIGHT EXPERIMENTS

Stanford Olendorf

The discussion that follows will be on heat pipe flight experiments as part of a Goddard evaluation program. The heat pipe is a general, all-purpose thermodynamic heat transfer device. It is rather simple in its theory.

The pipe, as seen in Figure 1, consists of a working fluid, usually ammonia methanol or acetone, with a wicking system. At the evaporator section where the heat enters, the working fluid is evaporated. The vapor travels down the tube to the condenser region, where it is condensed out and brought back by a wicking system. This device is generally used to transport large quantities of heat around the spacecraft. It is also used for isothermalizing optical instruments as in the Princeton Experiment on OAO, which I will discuss later.

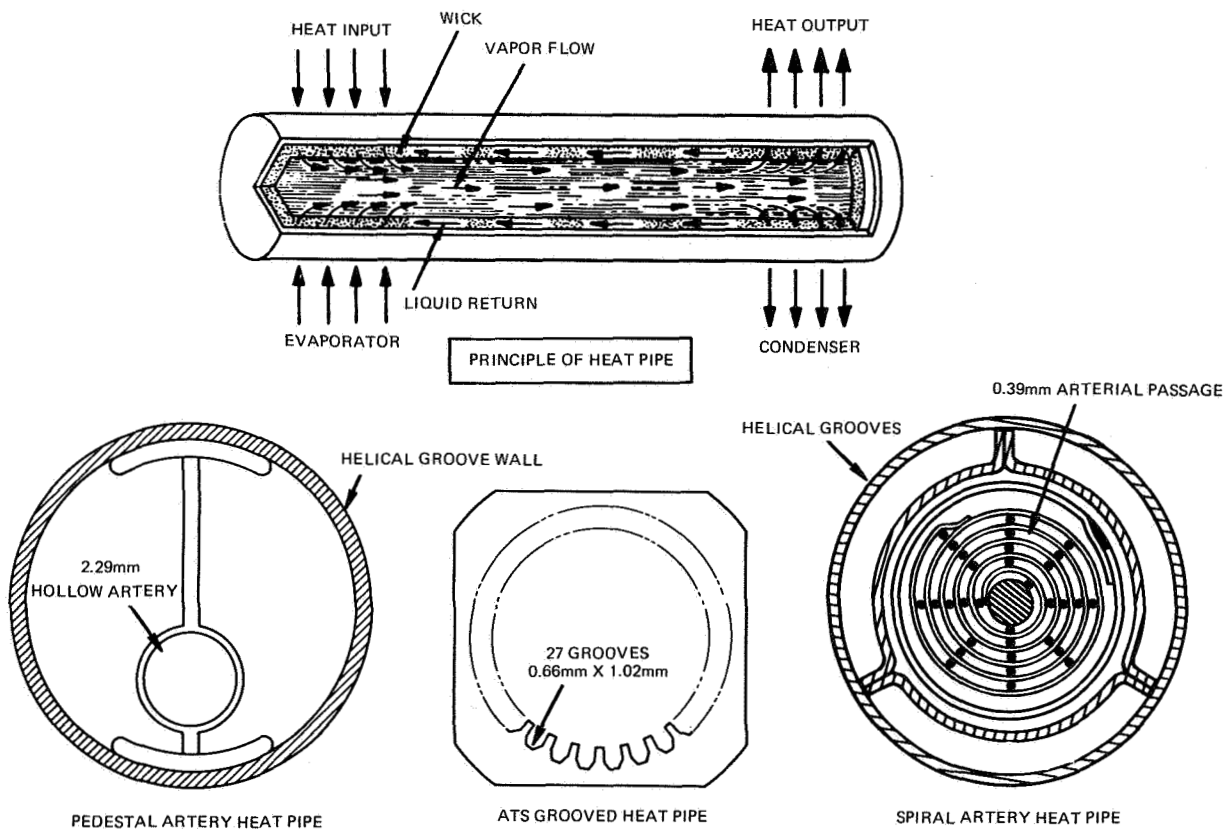


Figure 1. Typical heat pipe configurations.

Basically there are three types of pipes which we have developed over the years at Goddard. The first is the so-called pedestal artery, a hollow-channel screen system which provides a low-resistance path for fluid to return to the evaporator. It contains helical grooves on the wall for putting the fluid in good contact with the wall.

The second pipe is the grooved heat pipe which is a similar multichanneled heat pipe with a wicking system consisting of horizontal grooves.

The third pipe is a spiral artery pipe similar to the pedestal artery, except it contains many more channels for fluid to return to the evaporator.

Figure 2 shows the sounding rocket experiment which we have developed at Goddard as a quick-turnaround, low-cost item to check out heat pipes in zero-g.

In testing heat pipes on the ground, the one-g effects tend to produce incipient dryout, to cause puddling effects due to fluid falling to the bottom of the pipe, and to retard the arteries from priming. The sounding rocket provides a good vehicle for zero-g performance testing by eliminating these problems. Many parameters can be studied on the sounding rocket experiment since we have up to a kilowatt of power provided by a battery, which is not available on spacecraft. We have multiple heat pipe capability, up to 90 channels of signal conditioning, and can study many parameters such as overfill and underfill.

We have a new mission coming up that has a photographic capability: a camera and glass-heat pipes to study artery priming. We can also vary the power over the length to give us a checkout of heat transport capability.

Some of the typical data taken during a heat pipe flight experiment on a sounding rocket last October are given in Figure 3. We had five heat pipes on board, with one control heat pipe. It had the same geometry as the others, except that it contained no wicking system to bring the fluid back to the evaporator. At the point of zero-g, during free fall, the control pipe dried out as we had predicted, and the evaporator temperature rose to a high level. In the other heat pipes on-board, the evaporator and condenser maintained a constant delta T, showing that the experiment did work.

Figure 4 shows the OAO-3 with three of the heat pipes we have flown on board. They are typical of the ones flown on the sounding rocket for checkout prior to this launch, and are wrapped around the structural tube of the OAO at three levels. The Princeton Experiment Package gradients were maintained within two degrees Centigrade. Predictions without the heat pipes due to internal and external environmental changes were ten degrees Centigrade. This helped maintain the Princeton alignment in orbit.

We have one more heat pipe that is not shown here in one of the bays, mounted on the on-board processor. A variable conductance heat pipe maintained this on-board processor at between 20 and 30 degrees Centigrade during all portions of its power modes.

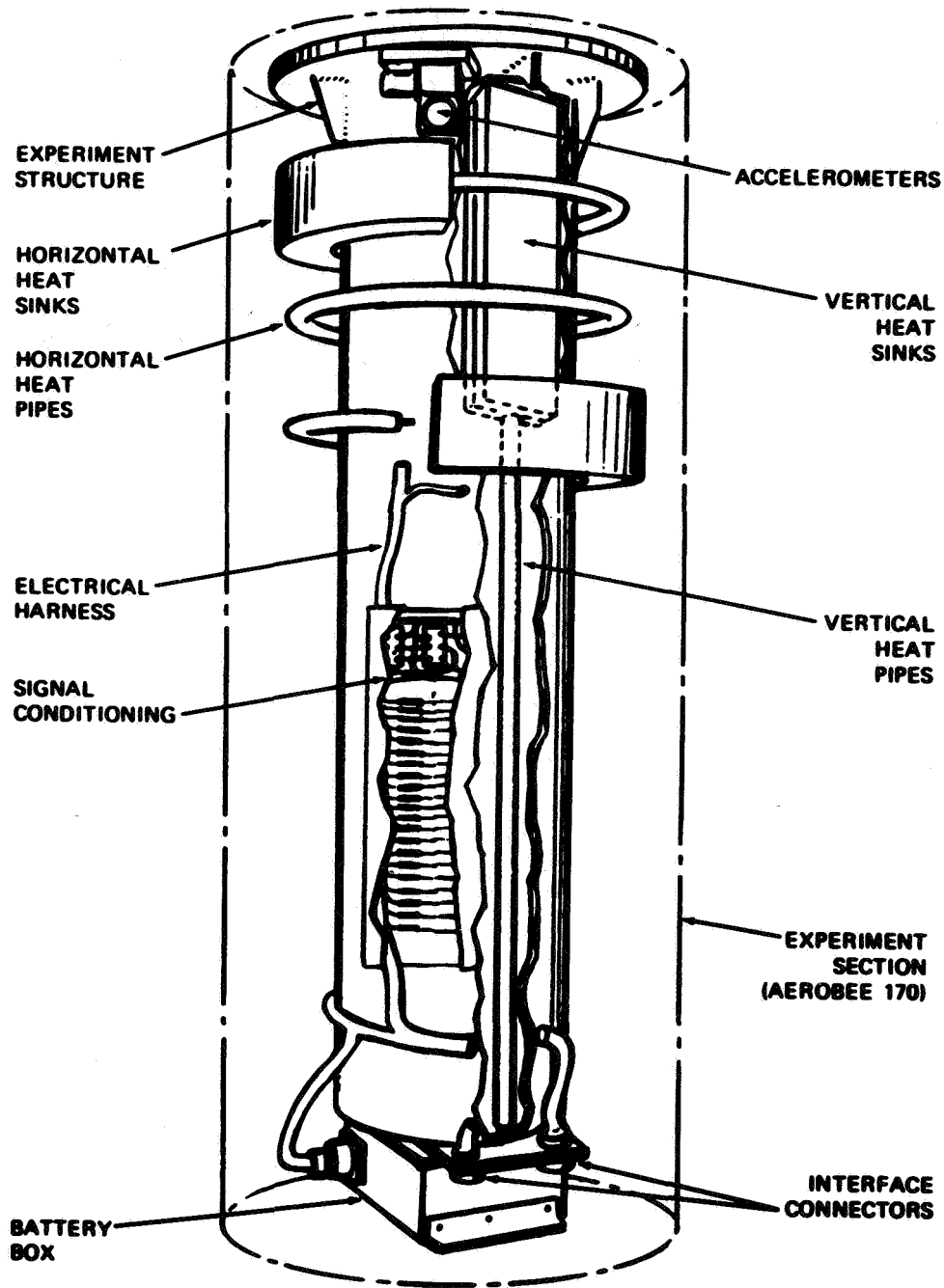


Figure 2. Experiment layout.

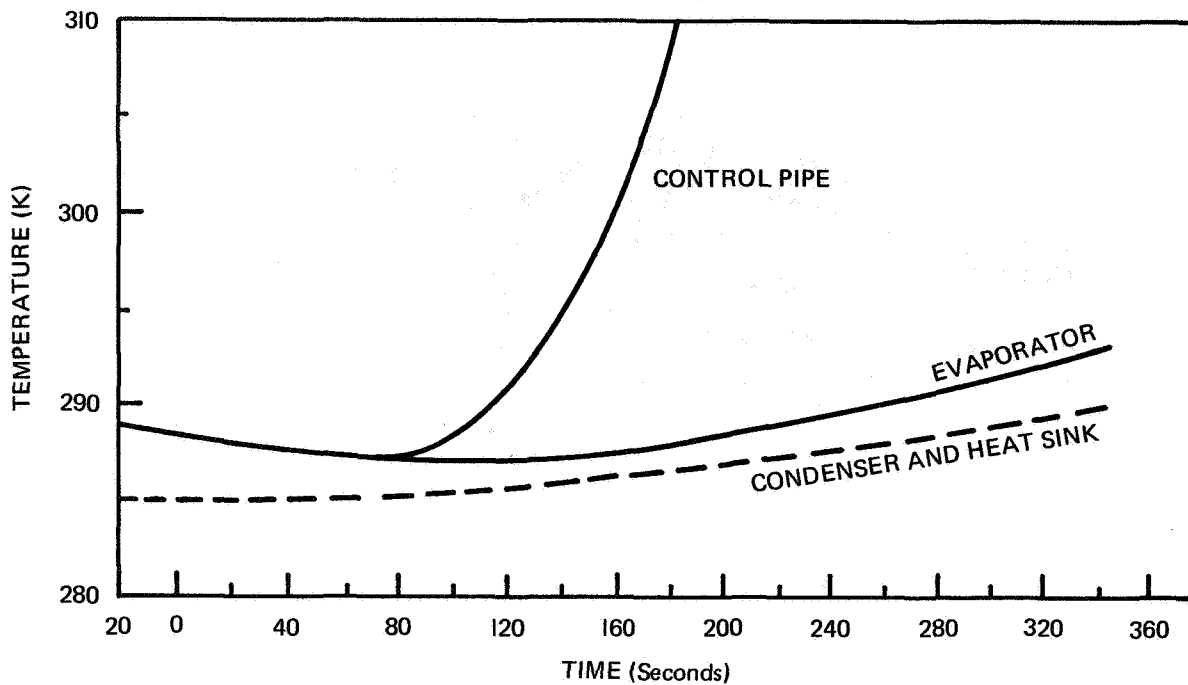


Figure 3. Thermal performance of spiral artery heat pipe.

The heat pipe worker program, a computer routine aboard the spacecraft, enabled us to activate up to 90 watts of heater power on each of these pipes, demonstrating an order of magnitude of greater capability than had ever been shown before in orbit. The heat transport capability, watts times centimeters, which is a measure of heat transport around the spacecraft, was approximately 15,240 watt-centimeters. This demonstrates that one can carry large amounts of heat over long distances and isothermalize within two degrees Centigrade.

The main function of the heat pipes on the OAO-C was to check out heat pipes over long-term life. Secondly, of course, we have maintained gradients within the Princeton Experiment. We have had up to 1000 hours in orbit, and have checked the pipes three times. No degradation from gas generation or leakage of ammonia has been evident.

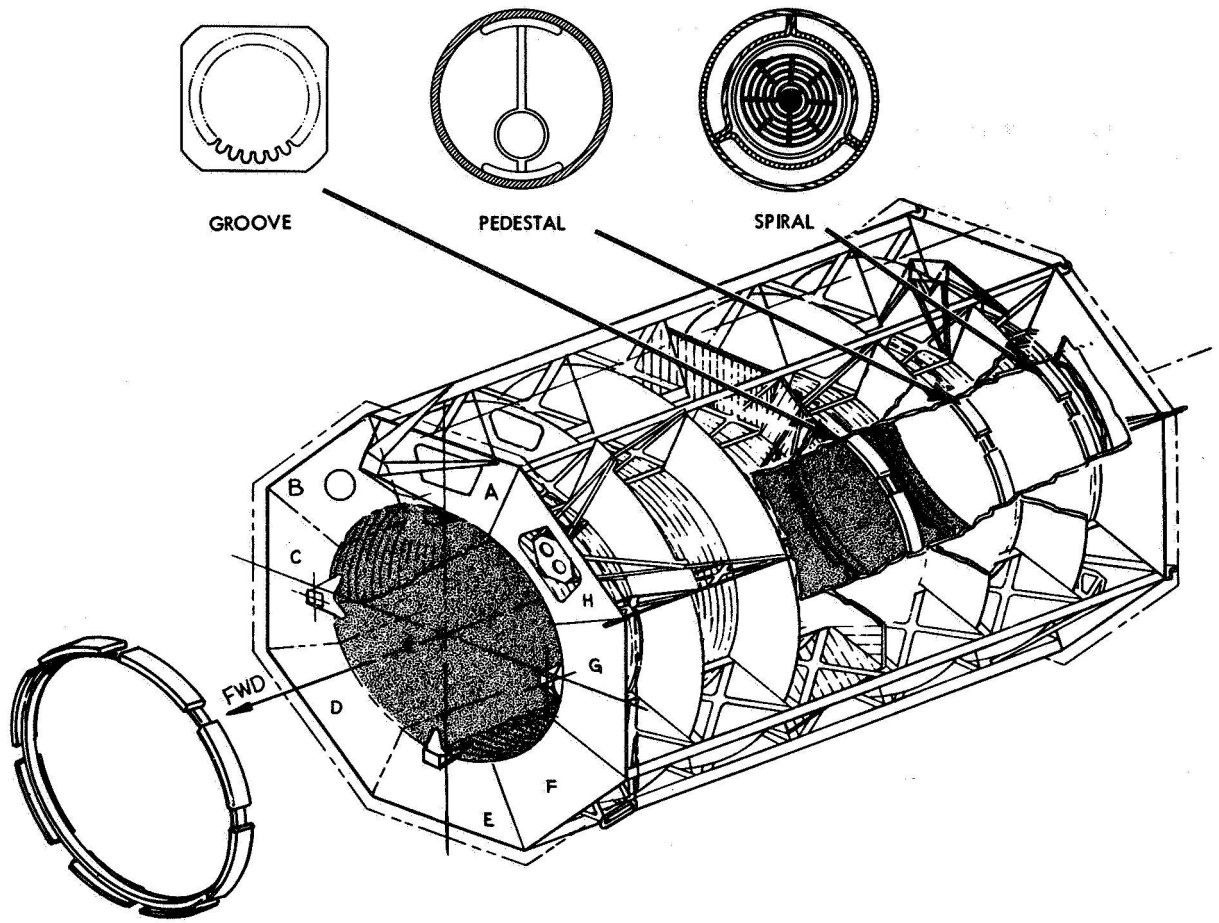


Figure 4. Positions of heat pipes in OAO-C.

TWO-DIMENSIONAL DIGITAL COMPUTERS

David H. Schaefer

This talk is a report on OAST-supported work on advanced methods of data handling. We are developing data processing systems that will extract data from optical images. These will be simple systems, orders of magnitude faster than present computers. Earth resource imagery is an example of the type of images we have in mind. Our aim is to take a job that, using conventional computers, takes, say, 20 minutes; and do the identical job in 20 milliseconds or so.

Well, how? How can we actually talk about coming up with speeds that are five orders of magnitude greater than the computers we have now? Is it by coming up with faster components? The answer is no, that is not the idea.

What we want to do is build digital computers that operate on entire binary images instead of on individual binary bits.

We are talking about computers that perform not one logical operation at a time, but many thousands of logical operations simultaneously. It is this simultaneity that provides the increase in speed. We are talking about two-dimensional extensions of standard digital computers. We are talking about computers that don't involve any scanning. We are talking about computers that don't involve any point-by-point operations.

The first thing we have to do is to build logical components that, instead of operating on a point-by-point basis, operate over entire images. For instance, if you have an image *A* and an image *B* (Figure 1), the idea is to have one component that will take these two as an input and give a logical output. Such an output can be the "AND" of the two images, the "OR" of the two images, or the negation of an image.

Say that image *A* consists of a million points. A standard computer would scan the image and take the negatives of all million points, one at a time, to produce the negative image on the right of Figure 1. You can, of course, take an image like *A* to the local drugstore and 24 hours later you have the negative of the image, and no million operations have been performed. What we want to do is to come up with very fast, real-time pieces of photographic film that will do all the operations shown in Figure 1. If we have "ANDs," "ORs," and negation elements, we have the elements to build a digital computer.

Figure 2 shows our first attempt at putting together a very primitive two-dimensional logical circuit. The input to the system is a scene that has points with neighbors and isolated points. The output will show only the isolated points. You might think of

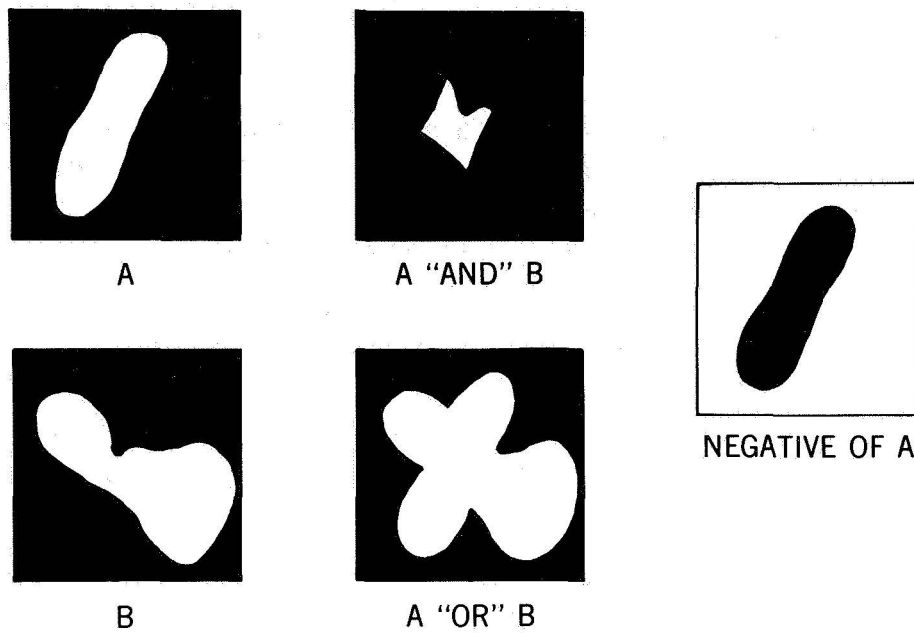


Figure 1. Two-dimensional binary logic.

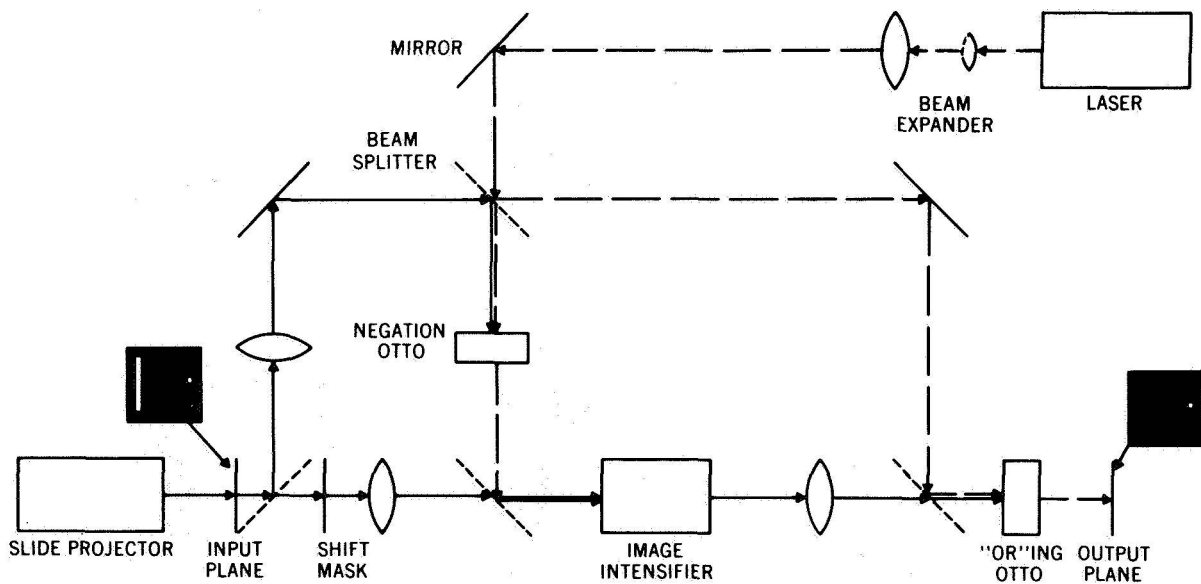


Figure 2. Isolated point detection system.

this as equivalent to an iceberg that has small pieces dropping off it. Perhaps the things you really worry about are these pieces. You would like a new picture that just shows the pieces that have dropped off, because you want to track those pieces, or you want to count them.

In Figure 2 are standard things of optics. There are lenses and there are mirrors. The unique thing is two elements: the negation element, and an "OR"ing element. These are liquid crystal devices that we have had developed for us. The negation element performs 20,000 negations simultaneously. In the area with the "OR," we do 20,000 "OR" operations simultaneously.

Figure 3 shows our very early results using the system shown in Figure 2. The upper images are inputs; the bottom images are outputs.

In summary, during the past year we have been able to build very primitive, two-dimensional, binary data processors. Using the concepts that we have demonstrated, we envision two-dimension general purpose computers. We feel that as two-dimensional computers develop, they will not only provide a method of handling images (both onboard spacecraft and on the ground); but that these computers will also have many uses not involving images. We are on the path to systems that have the potential to outclass conventional computers by four or five orders of magnitude, judged either by speed or by the complexity of the problems they can solve.

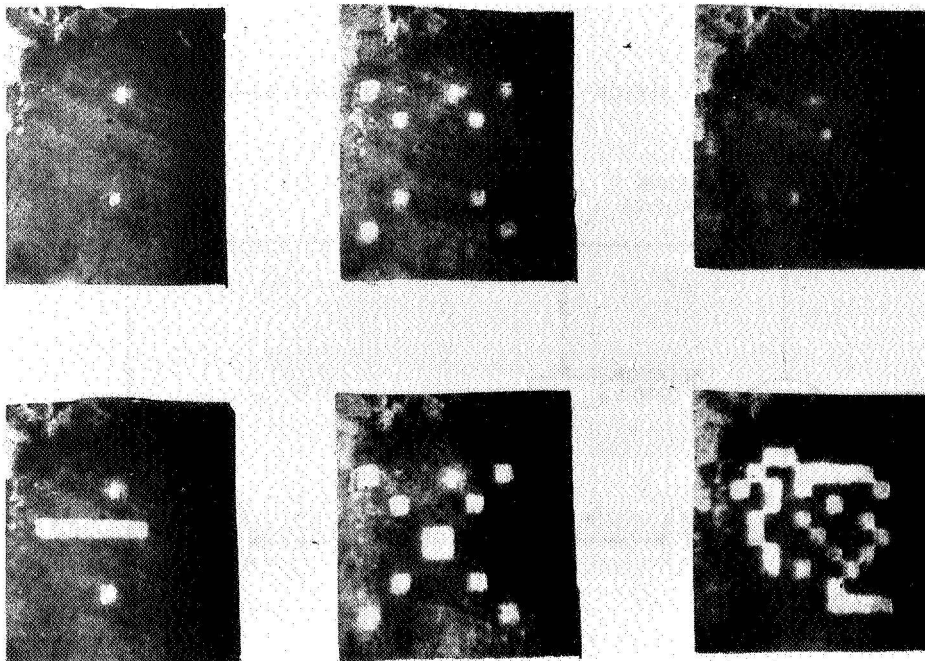


Figure 3. Experimental results using system shown in Figure 2.

SECONDARY MIRROR SUPPORT (LST)

Ewald E. Schmidt

Ever since the year 1609, when Galileo first used a telescope to study the sky, structural mirror supports have played an important role in optics. With the advent of large space telescopes, the requirement for precise pointing and alignment became more pronounced than ever.

Although mirror supports have been developed for ground-based systems, they are heavy and inefficient when used for space applications. With the help of Figure 1, let me outline the problem. Consider the Cassegrain telescope with its long secondary mirror support. For a telescope focal ratio of 12 and 3-meter diameter primary mirror, the length of the secondary mirror support is determined by the mirrors intervertex distance, about 7.3 meters (24 ft). Actually, the secondary mirror support is a metering truss: It maintains a precise position between the secondary mirror and the primary mirror. To

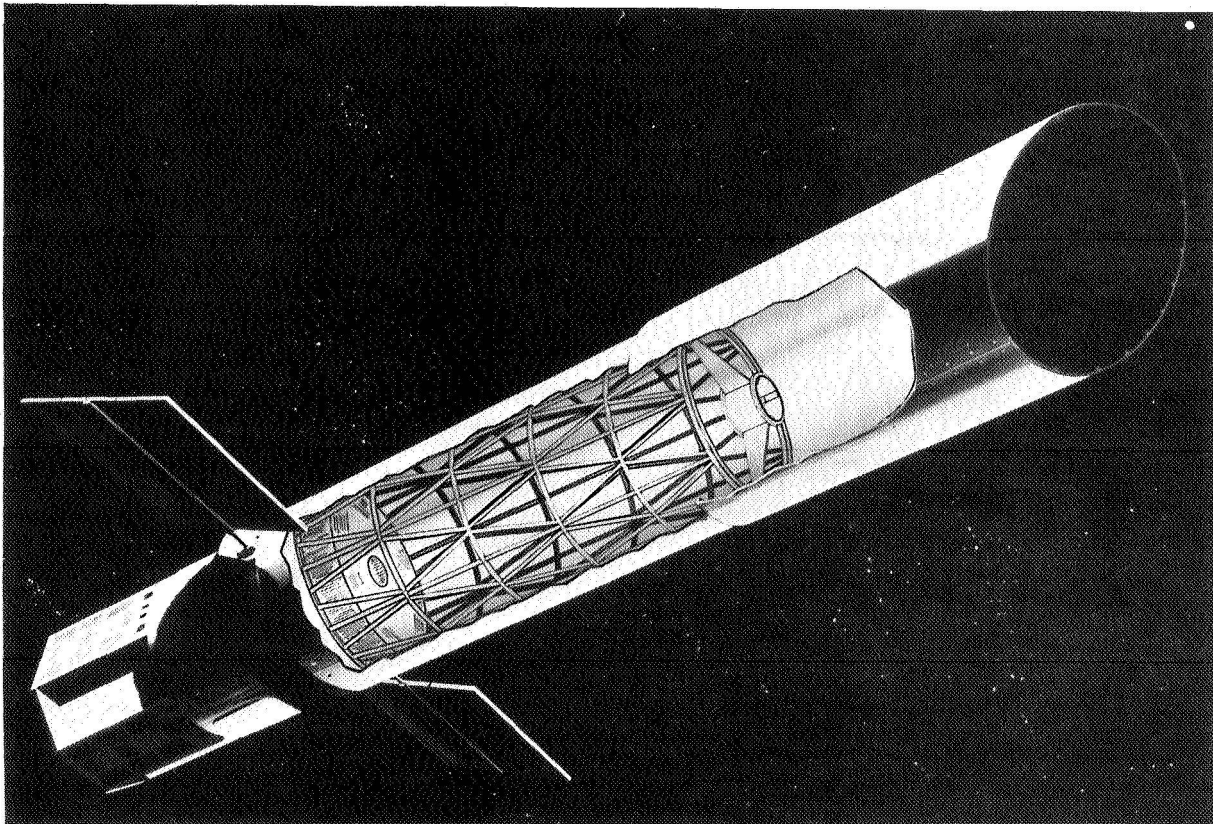


Figure 1. Large space telescope composite showing location of secondary mirror support.

achieve and to retain full optical performance, the secondary mirror support design had to meet the following requirements:

- Develop a dimensionally stable structure 7.9 meters (26 ft) tall with a natural frequency of not less than 13 Hz
- Be thermally compatible with the total telescope assembly, and able to carry the weight of mirror and support mechanism through the launch phase without damage

The most difficult requirements to meet was high dimensional stability. Unfortunately, most stable materials are either extremely brittle, expensive, and difficult to manufacture; are too heavy for flight worthiness; or simply are not available in quantities. Fortunately, a materials study made by Battelle Memorial Institute under contract to Goddard revealed that titanium alloy 6A1-4V has the highest microyield strength/density ratio of all the candidate materials. Microyield strength is defined as the stress level necessary to cause a residual strain of one-millionth of a meter per meter. For titanium 6A1-5V, this occurs at about $480 \times 10^6 \text{ N/m}^2$ ($70,000 \text{ lb/in}^2$).

With this new information on hand and after numerous trials comparing performance, dimensional stability, telescope configuration, materials, manufacturing processes, and above all, cost, the engineering model secondary mirror support looked like this (see Figure 2). By configuration, it is a cylindrical space truss having a natural frequency of

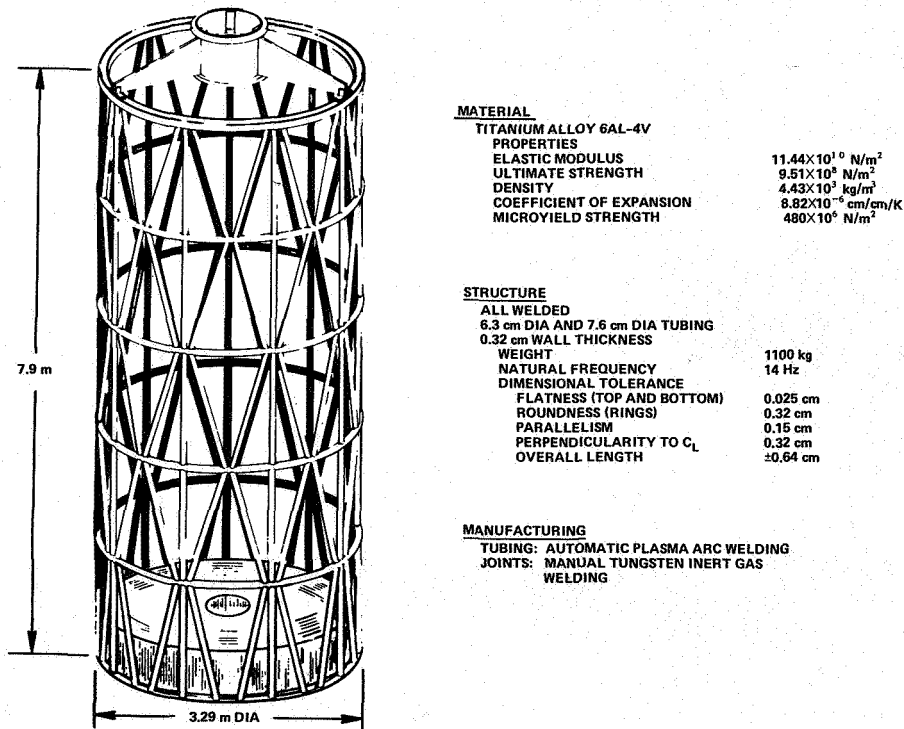


Figure 2. Secondary mirror support configuration and engineering data.

14 Hz, as determined by computer analysis and later experimentally verified through a "twang" test. It is an open structure permitting free exchange of thermal radiation across its diameter. It is capable of carrying a 230-kilogram (500 lb) secondary mirror through 15-g lateral launch acceleration without exceeding the microyield strength of the titanium alloy.

After we completed the design, manufacturing drawings, analyses, and specifications here at Goddard, Battelle Memorial Institute undertook the job of manufacturing the secondary mirror support. Figure 3 shows this structure as it appears now in Building 5, high bay area, at GSFC.

The completed structure is an all welded cylindrical truss formed from 6.3- and 7.6-centimeter (2½ and 3 in) diameter tubing made of 0.32 centimeter (1/8 in) thick titanium plate, and seam welded using automatic plasma arc welding. All other joints are hand welded using the tungsten inert gas method. Weight of this 7.9-meter (26 ft) tall and 3.4-meter (11 ft) diameter structure was kept down to 1100 kilograms (2210 lb), and the cost a mere \$90,000. It is, to the best of my knowledge, the largest all-welded titanium alloy structure.

We have shown you that large structural mirror supports which meet the stiff requirements for launch and orbit operations in particular, dimensionally stable structures made of titanium alloy, can be manufactured with present-day technology and at reasonable cost. With continuing research and development in this area, designs of astronomical telescopes and related earth observatory satellites should benefit from this knowledge.

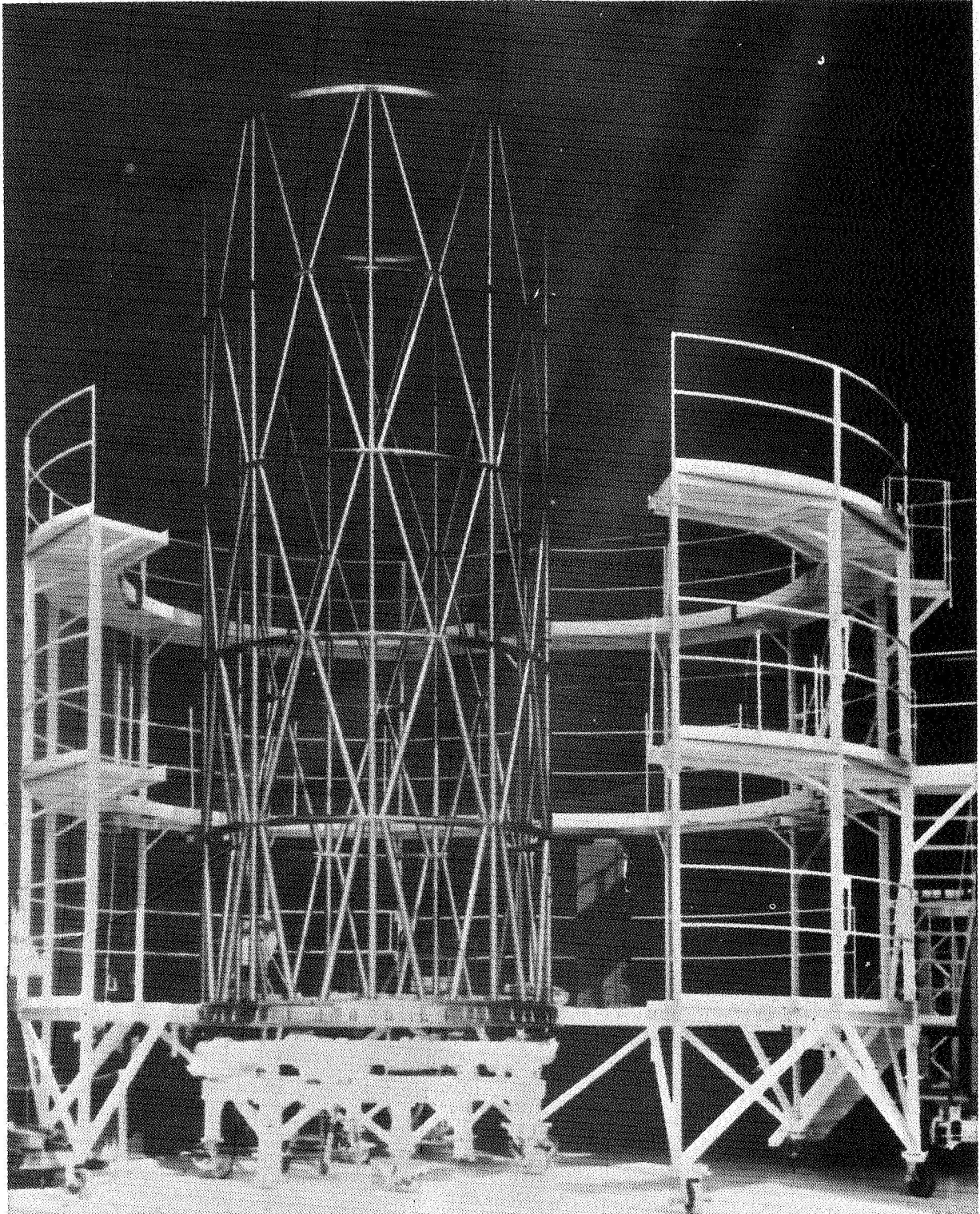


Figure 3. The secondary mirror support surrounded by work platform.

MOMENTUM WHEEL WITH MAGNETIC BEARINGS

Leo J. Veillette

In recent years, Goddard has undertaken development of practical magnetic bearings for space applications (References 1 and 2). The purpose of this talk is to present the results of one major effort of this work.

Figure 1 shows an engineering model of a momentum wheel which is suspended by magnetic bearings. It consists of a mechanical assembly on the right, and associated electronics on the left. The momentum wheel is mounted at the center of the rotor shaft and the magnetic bearings are on each end. The rotor is magnetically suspended so there is no physical contact between the rotor and the support structure. The system, therefore, can operate directly in the vacuum environment without lubrication; and it has virtually unlimited operating lifetime, independent of speed.

Figure 2 is a schematic diagram of one channel of the magnetic suspension system. It consists of a magnetic bearing at the upper right, the radial position sensor at the lower center, and suspension circuit electronics at the upper left. The magnetic bearing is con-

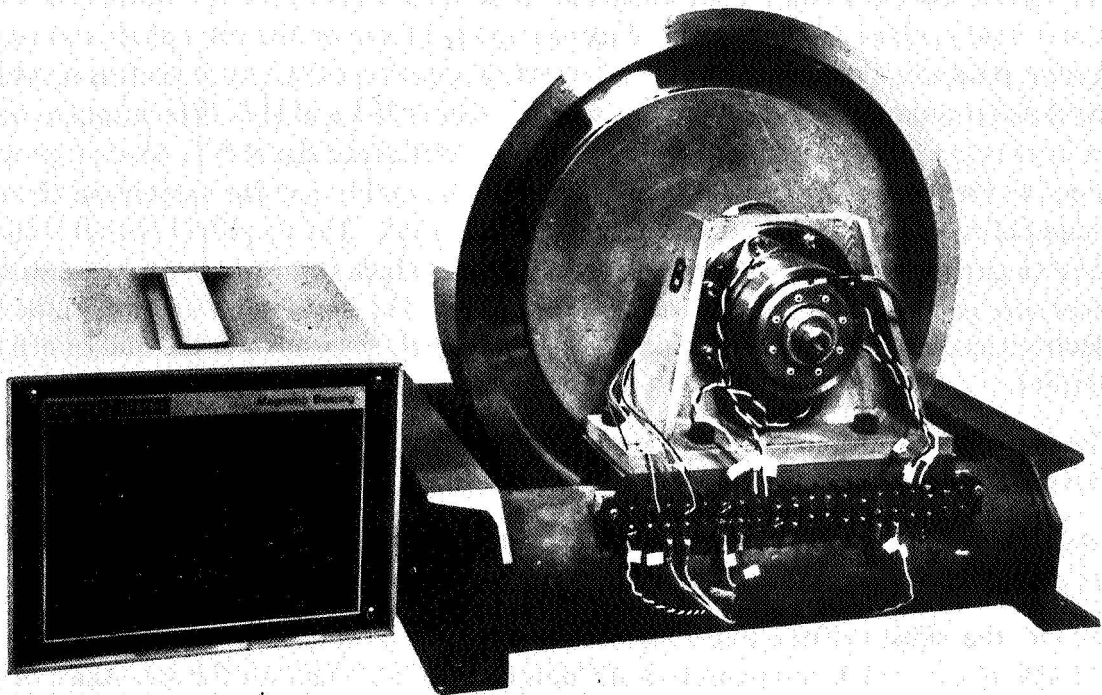


Figure 1. Engineering model of momentum wheel with magnetic bearings.

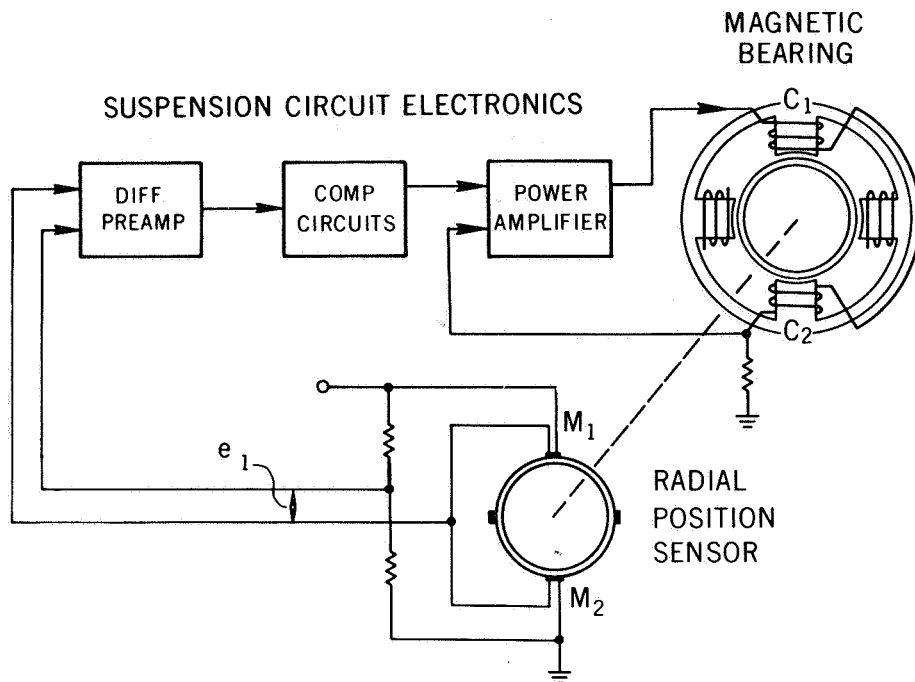


Figure 2. Schematic diagram of magnetic suspension system.

structured with four poles and associated coils, two along the vertical axis and two horizontal. The vertical coils C-1 and C-2 are connected in series as shown; and the winding direction is such that positive coil current produces an upward force on the rotor shaft and negative current produces a downward force. The vertical position of the rotor shaft is sensed in the radial position sensor, using two magneto resistors M-1 and M-2. The magneto resistors are connected in a bridge circuit which provides a difference signal E-1, which is proportional to the rotor shaft displacement. Signal E-1 is amplified in the suspension circuit preamplifier to a level of approximately one volt per mil. The amplified output is then applied to circuits which provide system damping, and which compensate for rotor structural resonance and saturation of the power output stage. The power amplifier drives the bearing electromagnet in a direction to maintain the rotor shaft suspended at the null or centered position.

The performance characteristics of the engineering model momentum wheel are listed in Figure 3, and may be summarized as follows:

First, the design value of momentum is $100 \text{ N}\cdot\text{m s}$, corresponding to 6000 rpm. So far the system has been operated to 5200 rpm.

Second, the radial stiffness under static conditions has been measured as greater than $350,000 \text{ N/cm}$, which compares to a stiffness of $110,250 \text{ N/cm}$ for the steel shaft of the rotor. This means that under load, the rotor shaft displacement in the bearing magnetic

(1) MOMENTUM	=	100 N·m s
(2) RADIAL STIFFNESS		
	STATIC >	350,000 N/cm
	DYNAMIC =	15,750 N/cm
(3) MAX. LOAD CAPACITY	=	350 N
(4) SIZE		
	ROTOR DIAMETER =	36 cm
	BEARING DIAMETER =	9 cm
(5) WEIGHT		
	ROTOR =	67 N
	BEARING =	28 N/bearing
(6) POWER		
	ELECTRONICS =	6 watts
	BEARING (FULL-POWER) =	19 watts
(7) ROTATIONAL LOSSES	⇒	0.0033 N·m/rad/s

Figure 3. Characteristics of momentum wheel with magnetic bearings.

field is less than one-third the displacement at the center of the shaft due to bending. Also, the radial stiffness under dynamic conditions is 15,750 N/cm, out to a frequency of about 80 hertz.

Third, the maximum load capacity of the system has been measured as 350 N. The design load capacity is limited by the onset of instability caused by magnetic bearing and suspension circuit nonlinearities.

Four, five and six in Figure 3 are the size, weight, and power consumption, and these are self-explanatory. Seventh, the measured rotational losses correspond to 0.0033 N·m/rad/s. This is about one-quarter the rotational loss in ball bearings which are suitable for this application.

Now, the results in this figure show that magnetic bearings are feasible for use on momentum wheels, despun antennas, scanning mirrors, and other spacecraft applications. The results also show that magnetic bearings offer entirely new suspension characteristics not previously available. Present indications are that magnetic suspension systems can be tailored to meet accurate pointing and isolation requirements for space shuttle missions.

REFERENCES

1. "Final Report, Design and Development of a Motor with a Magnetically Suspended Rotor, 5 July 1968 to 31 July 1970." NASA/GSFC Contract NAS5-11585. Cambion Thermionic Corp., Cambridge, Mass.
2. Philip A. Studer. "Magnetic Bearings for Spacecraft." NASA/GSFC X-721-72-56. January 1972.

AN IRONLESS ARMATURE BRUSHLESS TORQUE MOTOR

Phillip A. Studer

The object of this development was a high torque motor with improved servo characteristics. This included elimination of some of the nonlinearities that cause servo systems to be less than ideal, especially those that limit the ultimate system accuracy in pointing and rate control devices.

The construction technique employed dates back to the early days of electricity, before it was learned that conductors placed in slots in iron laminations behaved the same as when placed directly in the motor air gap. In the past, obtaining sufficient volume in the motor air gap for a high torque motor required a large heavy magnet structure, the rotating part of a brushless motor. The recent introduction of samarium cobalt magnets has reduced the magnet length required by a factor of five over the best Alnico available.

Figure 1 shows the motor construction in which the armature windings are cast into an

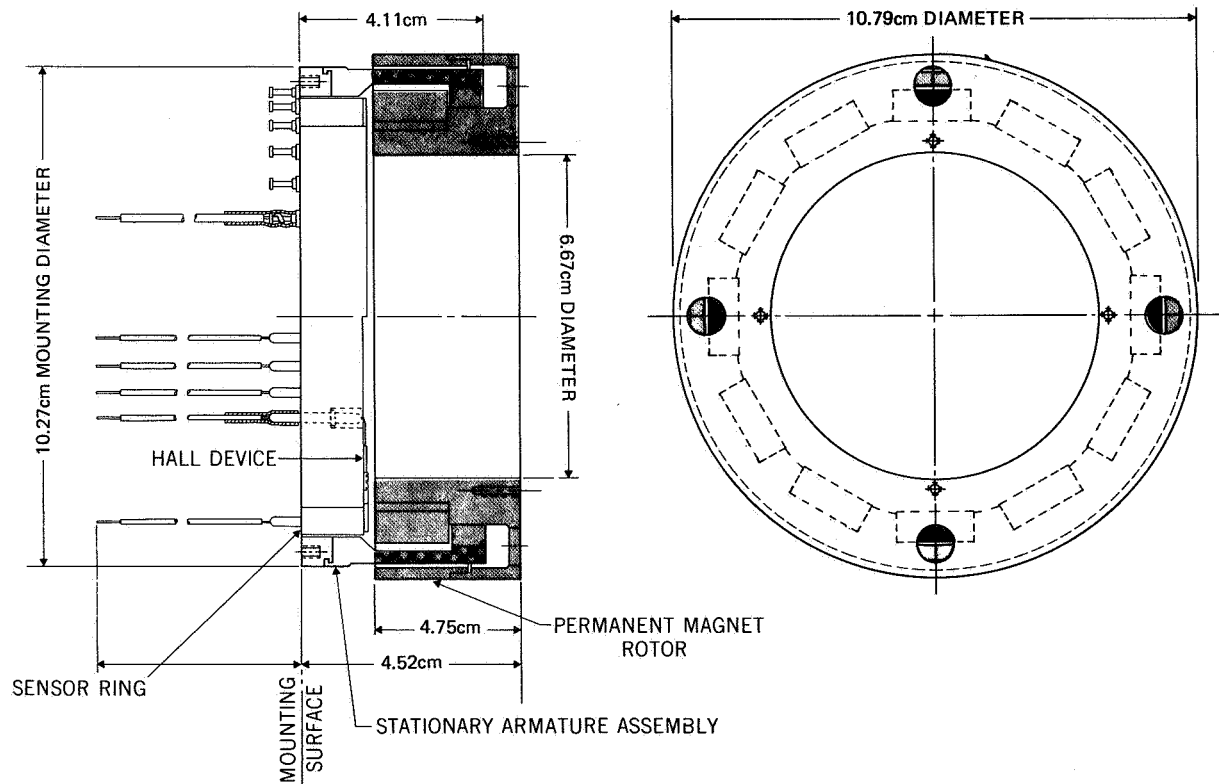


Figure 1. Ironless armature torque motor.

epoxy cylinder which is inserted into the air gap of the rotor. The armature conductors are a three-phase air core winding, integrally cast with an aluminum mounting ring which provides a good thermal path directly into the structure. The rotor is a 12-pole permanent magnet assembly with an air gap of 0.42 cm (0.165 inch) radially.

The primary reason for this type of construction is to eliminate magnetic hysteresis, which is nonexistent in this design because there is no relative motion between the rotating magnetic field and any stationary iron. The effect of hysteresis in a conventional motor is a static friction which introduces a deadband at the servo null position.

There are other benefits as well from the construction technique employed: There are no slot effects which cause "cogging" since the windings are not placed in discrete slots, and there are no static destabilizing forces between the armature and magnet assembly, which normally represent the most significant radial decentering force on the bearings at zero-g conditions. The electrical response is much faster (by an order of magnitude) since the armature is essentially an air core winding.

This motor was designed to meet the requirements of large despun systems such as flown on ITOS, INTELSAT, and others. It has a peak torque capability of 0.65 N·m (93 oz in.) in a construction with a hollow bore of 6.7 cm, and an outside diameter of 10.8 cm.

Figure 2 shows the measured performance of the engineering models compared to typical torquers of conventional construction. For a given peak torque requirement, the measured breakaway torque is substantially less than that obtainable from previously

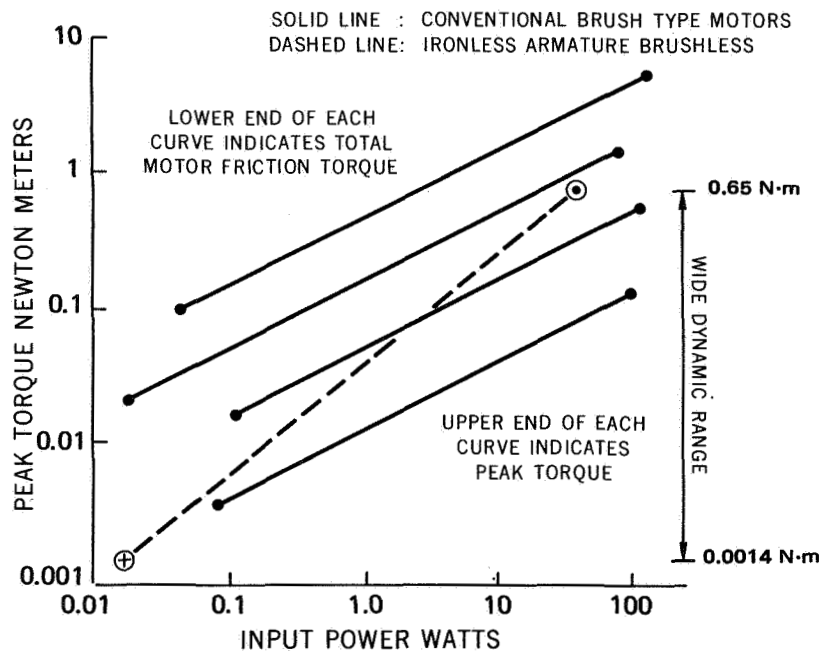


Figure 2. Working range for torque motors.

available motors. The result is not only a performance advantage but a power savings in constant speed and pointing applications, in which the motor and bearings represent the only mechanical load. These can be reduced to a fraction of a watt with a motor of this type; part of the improvement is due to the elimination of brush friction with electronic commutation and part due to a reduction of magnetic losses with the ironless armature construction. The engineering models indicate that a weight penalty of 0.23 kg is imposed by this construction for a motor of this rating.

This type of motor with its unique aspects of low losses, absence of destabilizing forces, and fast electrical response is uniquely suited to magnetically suspended systems. Combined with other developments such as magnetic bearings and rotary transformers, the motor provides a completely noncontacting system with no lubrication requirements and essentially unlimited life. Such a system will be able to attain and maintain higher accuracy at high levels of efficiency.

Four engineering models of this motor have been built and are currently under evaluation in the Mechanical Division labs. Smaller motors of this type could be built which would be ideal for scanning mirror devices such as radiometers. It is believed that a torque motor of this size and type would be ideal for laser communication applications which have beamwidths so narrow as to push the state-of-the-art in servo pointing systems.

SECTION II
SENSOR TECHNOLOGY

OVERVIEW

Henry W. Price

A proper title for this section would be Sensor and Sensor Related Technology—the first six speeches are in the applications area, the last four are in space sciences. Of the first six, three of the sensors are in orbit: the MSS, the RBV, and the VHRR. The speakers will discuss sensor construction and operation. The data will be presented in the Earth Observations Sections of *Significant Accomplishments in Sciences, Goddard Space Flight Center, 1972*.

MULTISPECTRAL SCANNER (MSS), ERTS-1

Joseph Arlauskas

The multispectral scanner is presently in orbit on the ERTS-1 spacecraft. The MSS permits simultaneous imaging in three visible bands and one near-infrared. The images from these bands provide much of the data necessary for management of the earth's environmental resources. This data is being presented in the form of a 185-kilometer swath on the earth with a resolution of approximately 80 meters. The isometric cutaway view in Figure 1 illustrates the configuration of the MSS.

The optical image of the earth is reflected by the scanning mirror into the double-reflector telescope type optics. The scanning mirror is oscillating at a 13.6 Hz rate and provides the crosstrack scan along the orbital path.

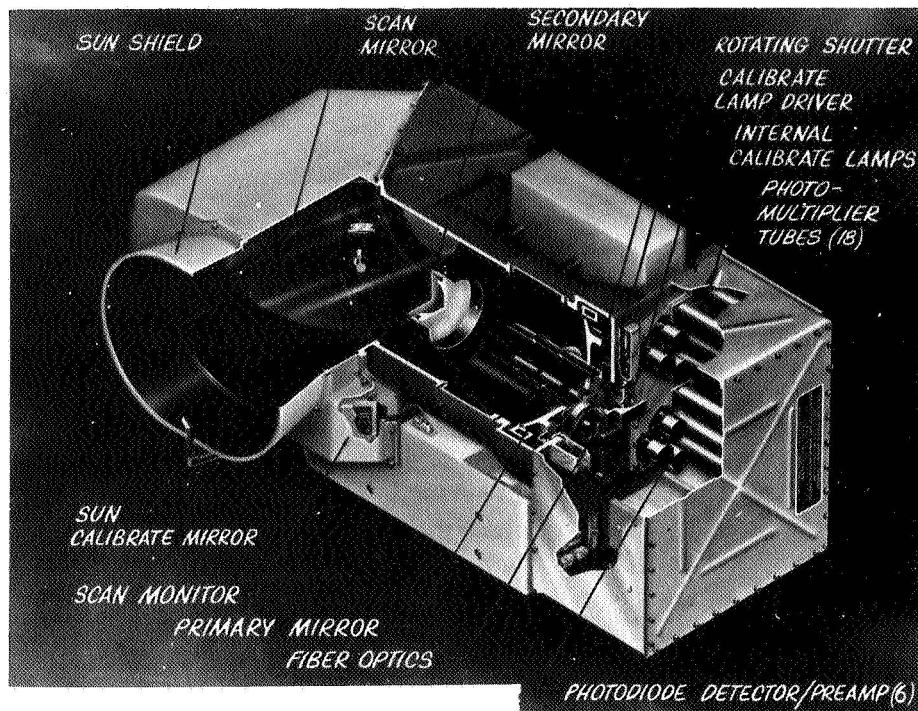


Figure 1. The four-band multispectral scanner (MSS).

There is a four-by-six fiber optics array positioned at the focused area of the telescope. This array transfers the optical image to the 24 detectors, six photomultiplier tubes (PMT) per visible band, and six silicon photodiodes (SPD) for the near-IR band.

Figure 2 summarizes the optical image transfer from the earth to an electrical signal from the detectors. The image of the earth in the 185-kilometer swath is swept across the fiber array and appears in the form of six lines/band/scan. As the spacecraft advances at orbital velocity and the scanning mirror oscillates, the next scan is swept across the swath at precisely the correct instant and provides continuous coverage along the orbital track.

The twenty-four analog detector outputs are digitized and multiplexed into a 15 Mbps stream and transmitted from the spacecraft.

During alternate retrace cycles of the scanning mirror, an internal calibration signal provides a method of equalizing gain changes that may have occurred in the six channels of one spectral band. A sun calibrate signal is also provided once each orbit as an alternate means of calibration.

The complete subsystem dissipates approximately 65 watts and weighs 54.4 kilograms.

The results of the multispectral scanner are shown in Figure 3, a color composite image of the Baltimore-Washington area taken on September 23, 1972. Three bands were combined to construct this composite. Healthy plants and trees which are very bright in the infrared are shown as bright red. Suburban areas with sparse vegetation appear as light

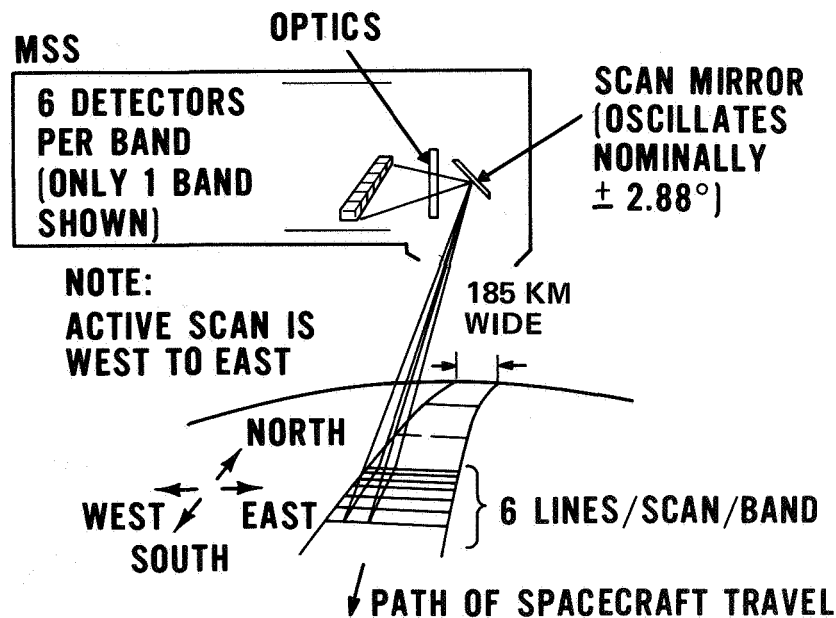


Figure 2. MSS ground scan pattern.

pink, and barren land as light gray. Cities and industrial areas show as green or dark gray and clear water is black/dark blue. Some of the geographical landmarks are:

- Washington, D.C.
- Baltimore
- Chesapeake Bay
- Jet contrail
- Patuxent Naval Station
- Dulles Airport
- I-95, 70-N, Baltimore-Washington Parkway

Analyses of typical scenes indicate that resolution is on the order of 80 to 90 meters for small targets and 50 meters for extended targets such as roads, rivers, and bridges.

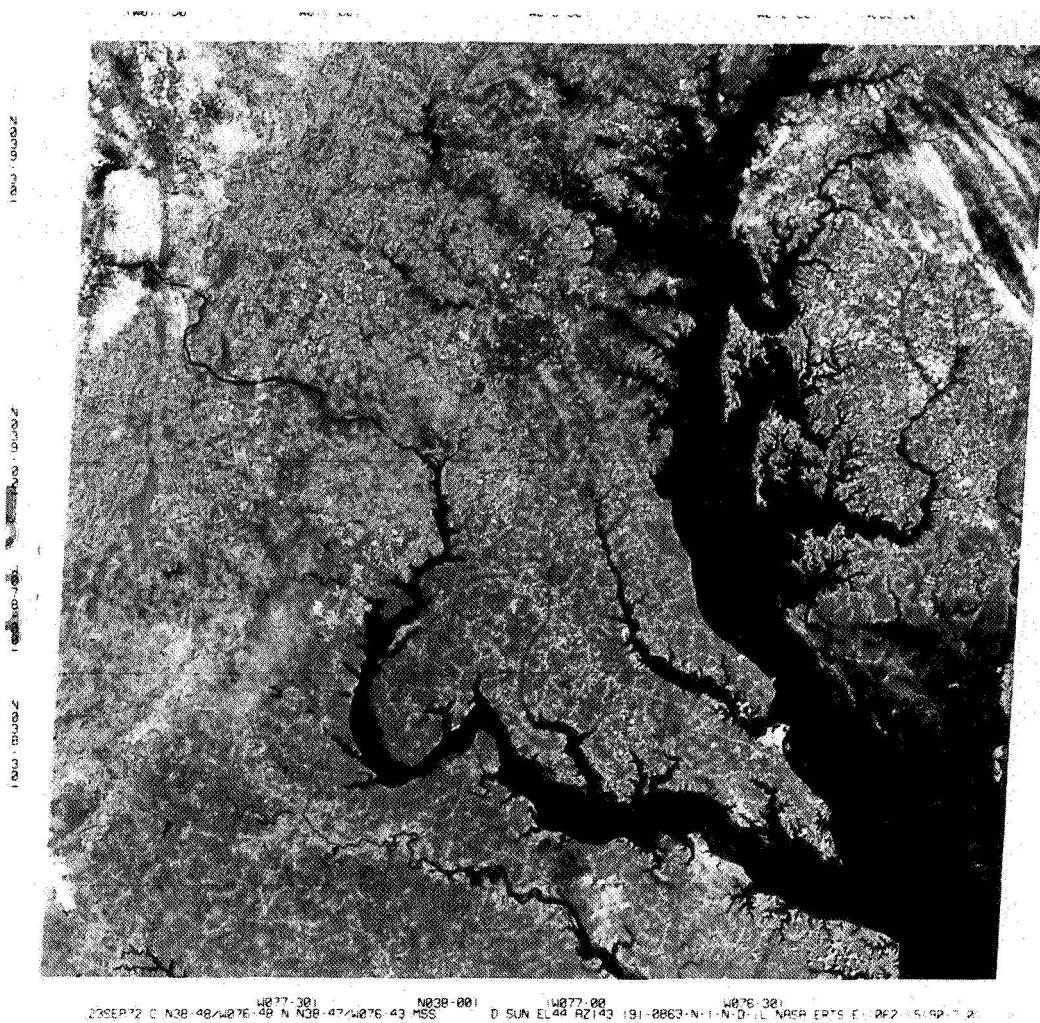


Figure 3. Baltimore-Washington scene. Source: NASA ERTS E-1062-15190 color composite. Original in color: can be ordered from EROS Data Center, Sioux Falls, S.D. 57198.

TWO-INCH RETURN BEAM VIDICON (RBV) MULTISPECTRAL THREE-CAMERA SUBSYSTEM

Oscar Weinstein

The two-inch Return Beam Vidicon (RBV) multispectral three-camera subsystem (Figure 1) was developed and built as one of the two principal sensor payloads for the ERTS-A and -B missions. The performance of the cameras on ERTS-1 has been excellent, meeting or exceeding all expectations, especially in the area of geometric fidelity and stability.

The three cameras are coaligned in the spacecraft to view the same nominal 190 kilometer square ground scene but in different spectral bands. When the separate images are processed and superimposed in their respective colors, they provide a single false-color image containing the radiometric and cartographic information required for the ERTS system. The three spectral regions covered by the RBV subsystem are the blue-green (475 to 575 nanometers), red (580 to 680), and the near infrared (690 to 830). The three cameras are exposed simultaneously to facilitate registration of the three separate images into the final color composite.

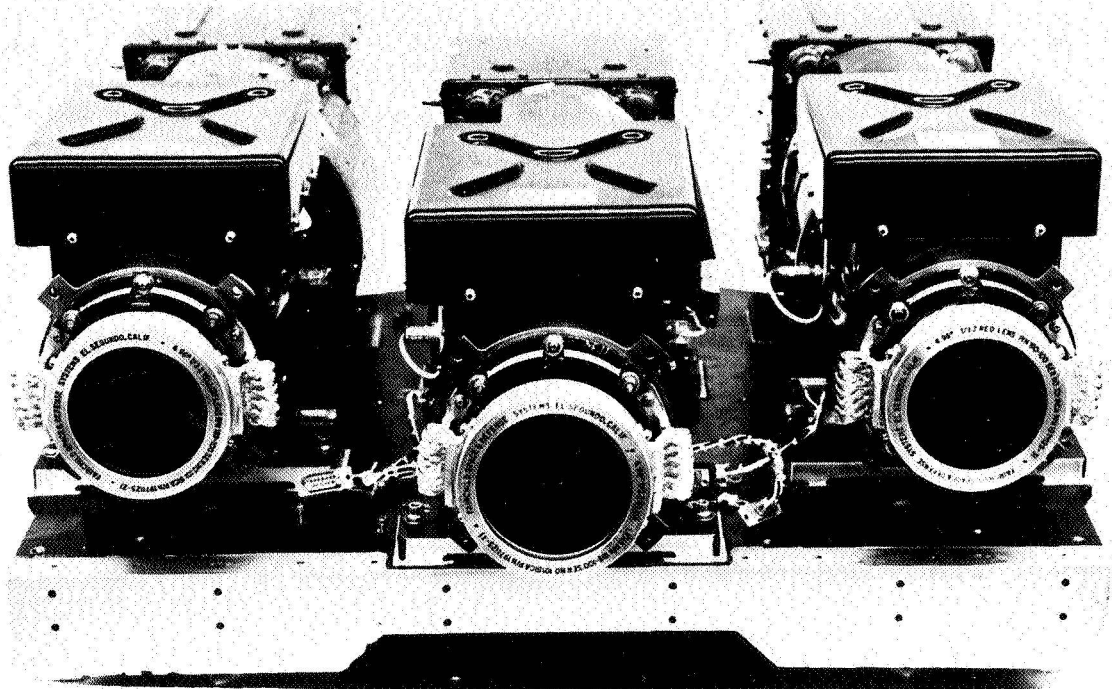


Figure 1. ERTS camera system.

available. This data can then be used to facilitate accurate global mapping with any other imaging system.

Translated in terms of laboratory performance, the RBV camera subsystem, with 4500 TV lines resolution and 33 dB signal-to-noise at $0.8 \mu\delta/cm^2$, represents a factor of five improvement over any previously flown television camera subsystem. Its geometric stability, better than 0.1 percent, represents an order of magnitude improvement.

As shown in block diagram form (Figure 3), the subsystem consists of three RBV cameras, and a camera controller combiner (CCC). Each camera includes a sensor unit and an electronics package. The three cameras are basically identical except for the spectral transmission of the lens and the readout interval delay. The three sensors are mounted on a base-plate which serves both as a precise alignment reference and as a thermal control element. Each sensor contains a Return Beam Vidicon and its associated electronics plus some of the most critical circuitry. The rest of the circuits for each camera are contained in the electronics package.

The CCC performs two basic functions: First, it develops all the subsystem timing signals, and second, it accepts the three parallel video outputs and combines them into a serial stream, injecting at the same time the required horizontal and vertical composite sync and the spacecraft time code to generate the final composite video signal. The complete subsystem dissipates 172 watts average and weighs 88.5 kilograms (195 lb) including the base-plate.

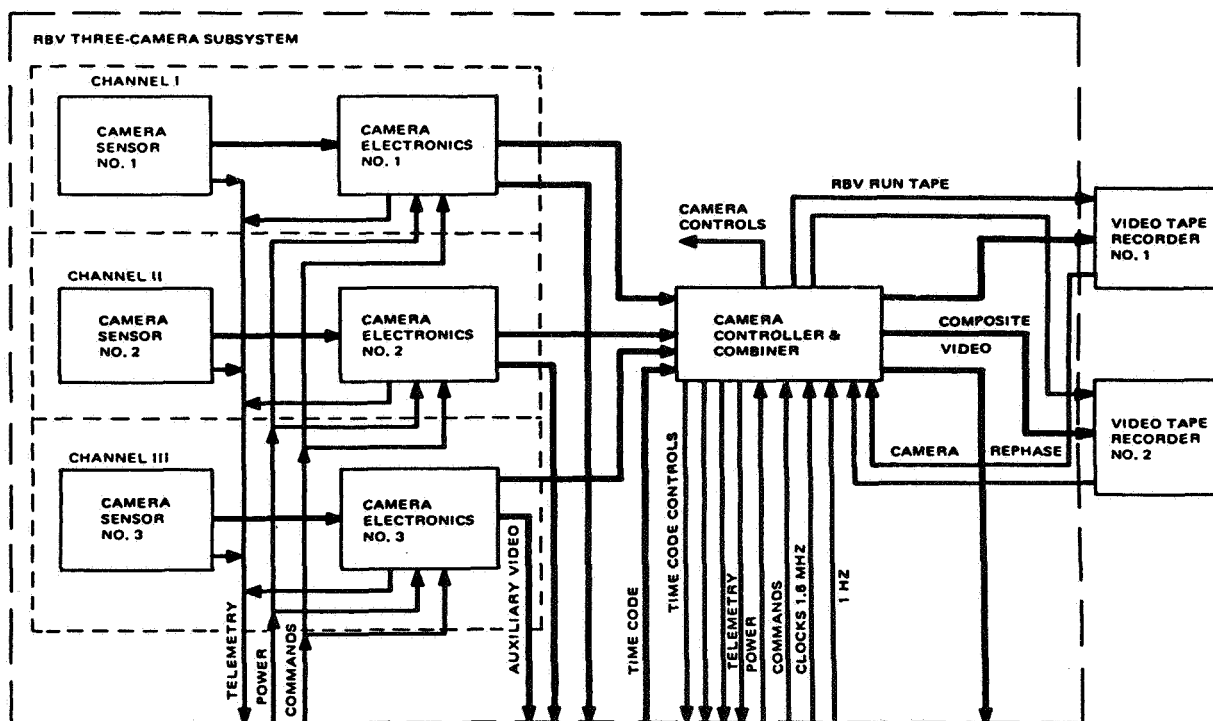


Figure 3. Three-camera subsystem, block diagram.

The heart of the camera is the Return Beam Vidicon. This tube employs an ASOS (anti-monium sulfide oxysulfide) long storage photoconductive surface, and a unique electro-optical configuration to achieve high resolution and signal-to-noise performance. The high resolution is achieved by using a four-node nonuniform focus field; high signal-to-noise is obtained by amplifying the modulated return beam with a five-stage electron multiplier. A nine-by-nine reseau pattern deposited on the tube faceplate serves as a very accurate geometric reference for the correction and registration of the three separate images.

Two other significant improvements contributing to the camera's high quality performance are a thermally compensated lens system with extremely low distortion and high MTF; and a versatile two-bladed focal plane shutter system capable of being commanded to five different exposure times to accommodate variations in scene radiance.

Two RBV camera subsystems have been built to date: one is presently operating in the ERTS-1, and the second one is scheduled to be used aboard ERTS-B late next year.

ERTS WIDEBAND TAPE RECORDER

John M. Hayes

The ERTS Wideband Video Tape Recorder can store, in one pass, an amount of data equivalent to that contained in 300 copies of *Webster's Collegiate Dictionary*. It is the highest-rate and largest-capacity digital tape recorder ever launched.

In 1967 it became apparent that NASA would need a video bandwidth tape recorder, and in 1968 we commenced a program that resulted in the development of the ERTS tape recorder. This is a four megahertz base band.

High data rate implies high tape speed, in that the number of flux reversals per centimeter is limited. It is nearly impossible to run tape longitudinally at the velocities necessary, so a rotary head is used in the transverse mode. In Figure 1 the head wheel can be seen. It has four magnetic heads mounted on the periphery, and is about five centimeters (2 in) in diameter. The head wheel rotates at 18,750 rpm and gives us a head-to-tape surface speed of nearly 5080 centimeters (2000 in) per second. In the meantime, the tape runs longitudinally at a reasonable speed of 30.5 centimeters (12 in) per second.

The transport unit is shown in Figure 2. There is also an electronics unit of about the same

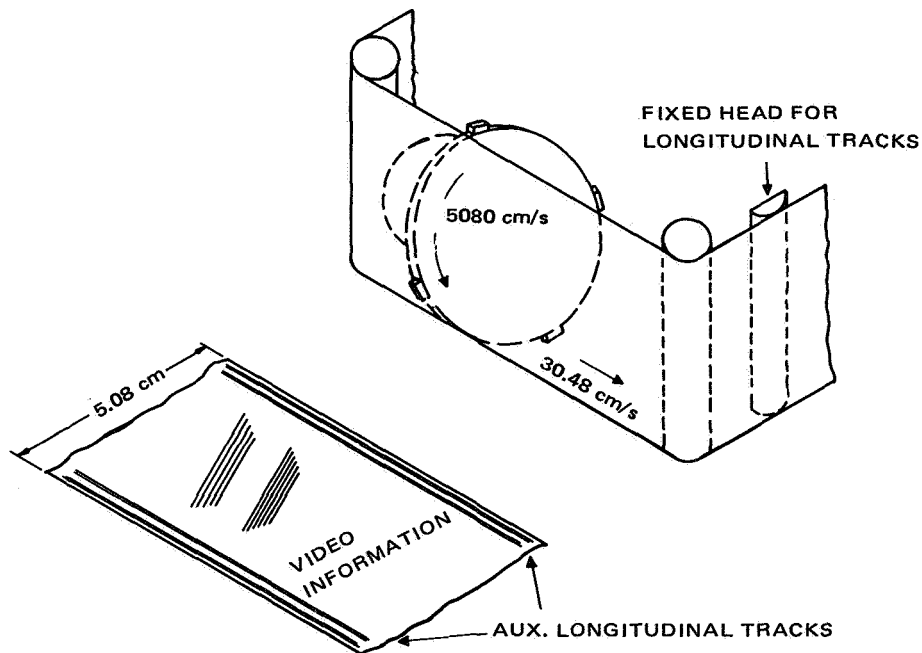


Figure 1. Head/tape interface.

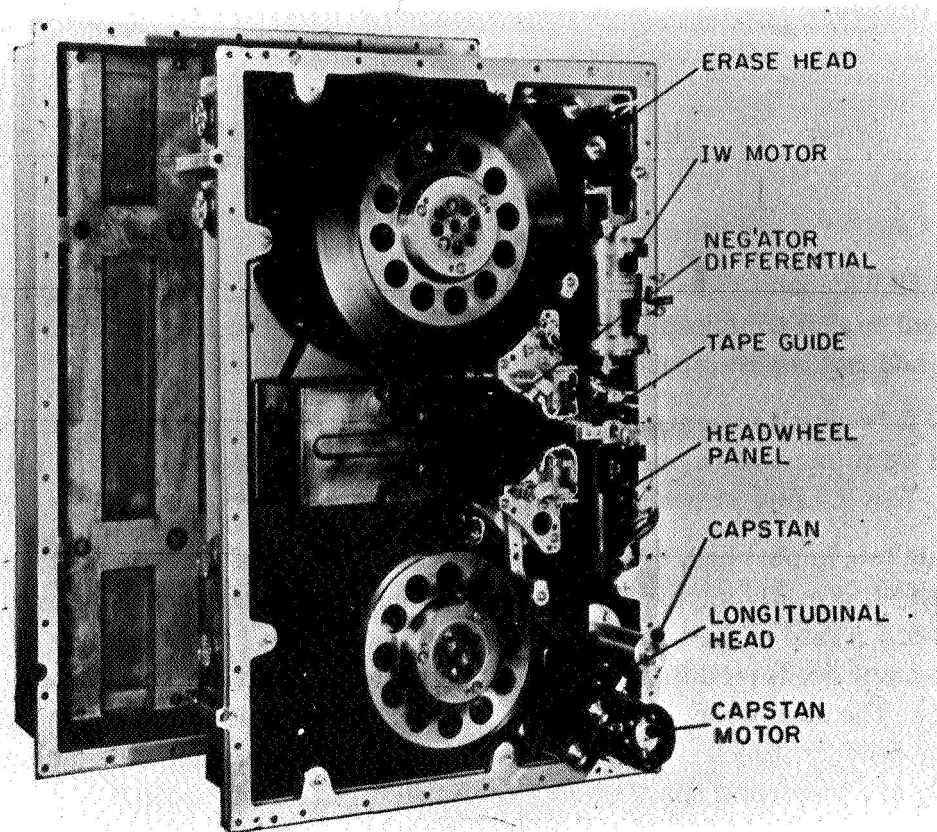


Figure 2. ERTS VTR transport.

size, 50.8 centimeters (20 in) tall. The head wheel panel is a removable panel that holds the head wheel, the head wheel motor, and the drive shoe. The rest of the components are pretty much as in any other tape recorder. This device has 610 meters (2000 ft) of five-centimeter-wide (2 in) tape. It records for 30 minutes and its four-megahertz bandwidth, with a signal-to-noise ratio of better than 39 dB, would be sufficient for color television. This device could be used for a normal half-hour color television show.

Partway through the development, when it was decided to put the MSS on the spacecraft, we were asked to handle its 15 megabits per second. This is where we spent most of the development time and money. We handle the 15 megabits per second rate with a typical bit-error rate of 10^{-5} . Time-base error of the instrument is on the order of one-half TV element per line, or one part in 10^4 . But since you don't get something for nothing, the device weighs 34.5 kilograms (76 lb).

The most obvious technological advancements are in the digital area (Figure 3); the digital rate of this device is approximately 15 times that of any recorder flown previously. Its digital capacity is on the order of 300 times that of any recorder launched before. There was a previous Air Force recorder at six megahertz with a life of something less than 100

BEFORE ERTS	ERTS NEED	CAPABILITY
<ul style="list-style-type: none"> ● DIGITAL DATA: <ul style="list-style-type: none"> RATE: NASA = 16 kbs AF = 1 Mbs CAPACITY: $\sim 10^8$ bits 	<ul style="list-style-type: none"> 15 Mbs (BER = 10^{-4}) 10^{10} bits (10 min) 	<ul style="list-style-type: none"> 15 Mbs (BER $\approx 10^{-5}$) 3×10^{10} bits (30 min)
<ul style="list-style-type: none"> ● ANALOG DATA: <ul style="list-style-type: none"> NASA: 60 kHz AF: 6 MHz 	<ul style="list-style-type: none"> 4 MHz (39 dB) 	<ul style="list-style-type: none"> 4 MHz (~ 43 dB)
<ul style="list-style-type: none"> ● LIFE: <ul style="list-style-type: none"> AF: 6 MHz ≈ 100 hrs Grd Rec's ≈ 100 hrs 	<ul style="list-style-type: none"> 500 hrs 	<ul style="list-style-type: none"> 5 Grd Life Tests >1000 hrs

Figure 3. Technology advancement.

hours. ERTS requires on the order of 500 hours and we plan on getting there, so that's an advancement of five to ten times in life on the analog.

Concerning performance in orbit, we have two units on board ERTS-1, and either unit will store the output of either the MSS or the RBV. One unit has been secured due to a short in the power supply transformer. The other device is operating excellently, returning images from the 85 or 90 percent of the earth that is not available in real-time. Figure 4 relates to that – it's a rather psychedelic slide of the Amazon River.

We also provided the ground station recorders that will store data from either of these sensors. For the future, aside from ERTS-B, this device will fly on Skylab in April 1973, and we are looking forward to EOS in a two-speed mode – a slow-speed record, and high-speed playback. This would be about a 1.2 megabit record and 30 megabit per second playback. We have a mechanical test running that is up around 2500 hours, so we think we can achieve life from that mode. We feel the device is usable at up to 30 megabits per second.

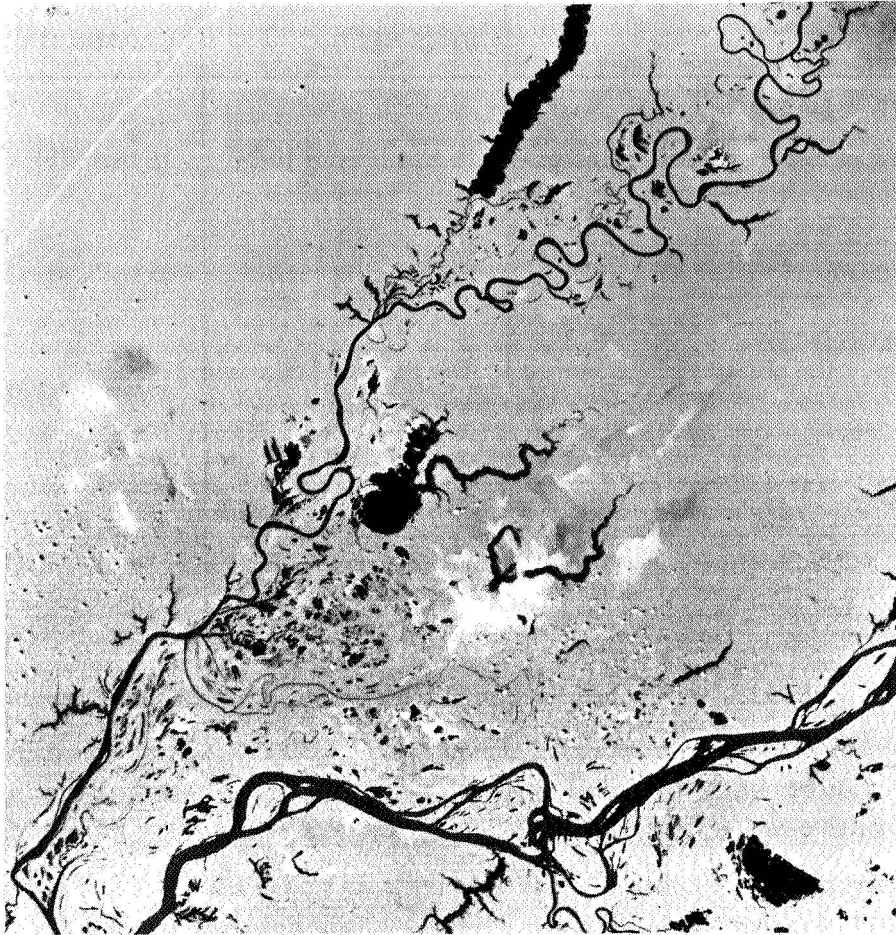


Figure 4. Composite image of the Amazon River. Source: NASA ERTS E-1008-13481-(5,7)01. Original in color; can be ordered from EROS Data Center, Sioux Falls, S. D. 57198.

VISIBLE INFRARED SPIN-SCAN RADIOMETER

James E. Phenix

The visible infrared spin-scan radiometer (VISSR) may be considered as a camera system capable of simultaneously providing both visible and infrared earth and cloud-cover pictures every 20 minutes from the geostationary synchronous meteorological satellite (SMS). With a 0.9-kilometer resolution in the visible spectrum and a 9-kilometer resolution in the IR spectrum, the VISSR/SMS system will, for the first time, enable investigators to study atmospheric dynamics through 24-hour continuous observation of cloud altitudes, patterns, motion, and temperature distributions.

A cross section of the 62-kilogram VISSR scanner, which has a length of 1.5 meter and diameter of 0.45 meter, is shown in Figure 1. The scanner may be conveniently divided into six basic elements as follows:

- A 2.9-meter focal length, 0.41-meter diameter optical system consisting of three solid beryllium mirrors with focus adjustment capability in both IR and visible channels
- A primary and redundant torque motor/encoder servo-scan drive system which, in 18.2 minutes, steps the dynamically balanced 18-kilogram scan mirror assembly a total of 1820 times to a precision of 1 arc second. It is through the combined spacecraft spin and mirror stepping that the raster scan composite earth picture is developed
- Eight photomultiplier tubes, each of which views, through separate fiber optics strands, a 0.9-kilometer square scene
- A primary and redundant HgCdTe detector combination which is passively cooled to 95 K and is capable of providing radiance temperature measurements between 180 K and 315 K to a sensitivity of approximately 0.5 K
- Two IR and eight visible channel preamplifiers
- A beryllium housing for lightweight thermal and structural stability

Not shown is a 6-kilogram, 20-watt electronics module which contains circuitry for interfacing the scanner electronics with the spacecraft, provides the logic circuitry for scan drive and focus operations, and conditions the scanner signal channels.

As of November 2, 1972, Santa Barbara Research Center, the VISSR prime contractor, has successfully assembled, tested, and delivered an engineering model VISSR. In addition, SBRC is currently subjecting the first in a series of three flight models to environmental tests at Hughes Aircraft Company, El Segundo, California. These tests are expected to be completed by November 15. Some of the significant measured performance parameters are in Figure 2.

In summary, it is appropriate to mention that the 0.9 kilometer resolution solid beryllium optics, the 81 K passive radiation cooler, the beryllium structure, and the precision scan drive system are, as a result of the VISSR program, now state-of-the-art achievements. As an integrated operational system, VISSR will be the most sophisticated radiometer in NASA's history.

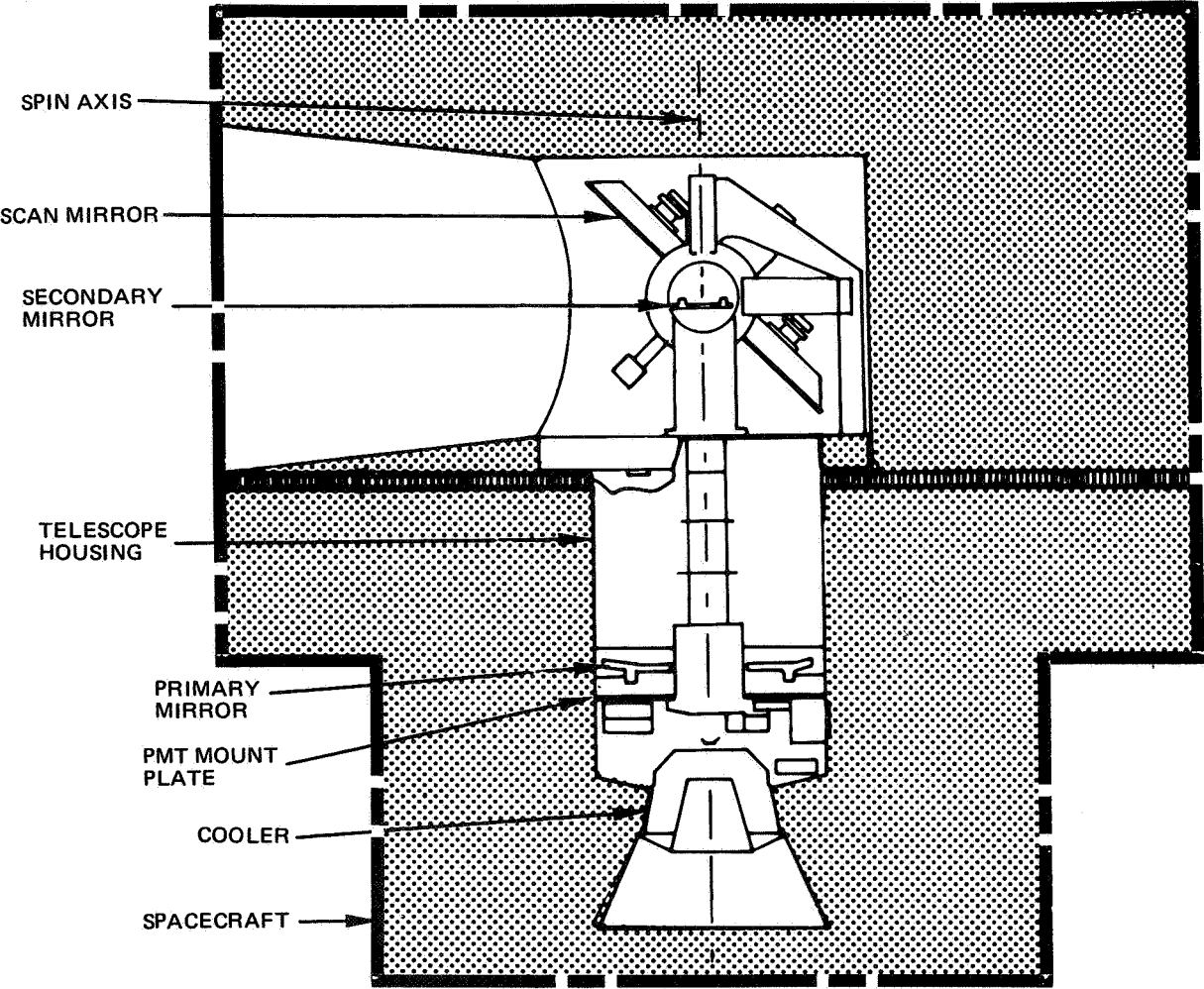


Figure 1. VISSR/SMS.

- **VISIBLE CHANNELS (0.55 TO 0.75 MICRONS)**
 - S/N = 37 AT 50 PERCENT ALBEDO
 - MTF = 0.40 AT ½ NM
- **IR CHANNEL (10.5 TO 12.5 MICRONS)**
 - S/N = 565 AT 315 K
 - NEDT = 0.15 AT 300 K
 - 0.60 AT 200 K
 - MTF = 60 AT 5 NM
- **PASSIVE RADIATION COOLER TEMPERATURE 81 K**
- **STRUCTURAL INTEGRITY QUALIFIED TO PROTOTYPE LEVELS**
- **SCAN DRIVE QUALIFIED**

Figure 2. Verified VISSR performance characteristics.

MULTISPECTRAL IMAGE DISSECTOR CAMERA FLIGHT TEST

Bernard L. Johnson

Two years ago I gave a report on the image dissector camera (IDC) operation and lab testing. Now I would like to extend that report to discuss results of a flight test program aboard a high altitude aircraft. But first I would like to briefly review the IDC operation.

Figure 1 shows how the IDC operates. Three earth scenes, each 185 kilometers by 60.96 meters are imaged through a single lens onto a photocathode surface containing three spectral filterstrips, thereby producing three separate spectral signatures on the photocathode surface. An electron image is formed, accelerated, focused, and electromagnetically deflected across an image plane which contains three sampling apertures, behind which are located three electron multipliers for signal pick-off.

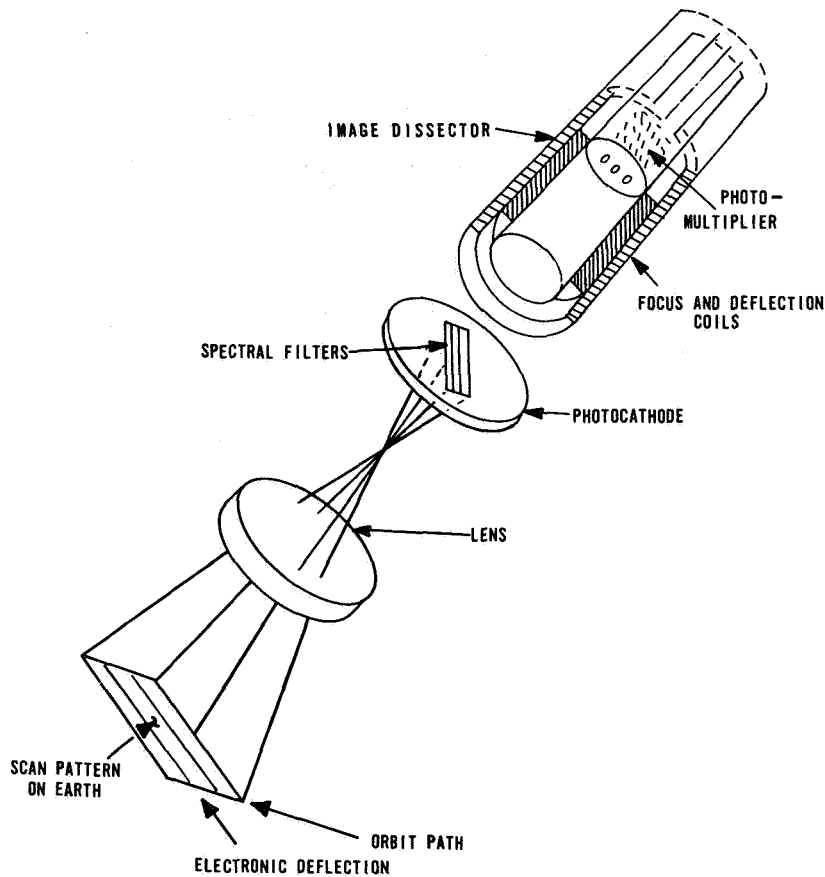


Figure 1. Schematic diagram of the IDC system.

In the two years since the first report, two significant tests have been performed. A transparency from Apollo 9's SO65 experiment was obtained and reproduced through the IDC with such good results that it was decided to extend testing to actual earth scenes. At this time Rome Air Development Center became interested in the cameras and a mutually agreeable program was worked out. They supplied the aircraft and recording instruments, NASA supplied the camera and film processing.

Figure 2 is a composite picture taken from 9.2 kilometers over Annapolis, Maryland. Like all experiments, the results were extremely good in some areas and somewhat discouraging in others.

On the plus side, we note in the fairly uniform radiance areas over water that there are no microphonics. This is not surprising since there are no mechanical moving parts to generate them. In the same area we note also that there is no striping. This too is not surprising as there is just one channel per band.

We observe overall high resolution. At this altitude and lens system we were expecting 1.2 meter ground resolution. This does not allow us to identify cars but does allow us to see trucks and buses, and we have been able to single them out in several of the photos. We observe overall good registration. This is a direct result of the single lens and camera concept.

You might wonder how we handled roll motions of the aircraft. Did we use a stable platform? No, the electronic deflection feature allows us to use a gyro error signal injected into the camera itself to correct for aircraft motion. We estimate that a reduction of 40 milliradians to less than 150 microradians, a single resolution element, was accomplished using this technique.

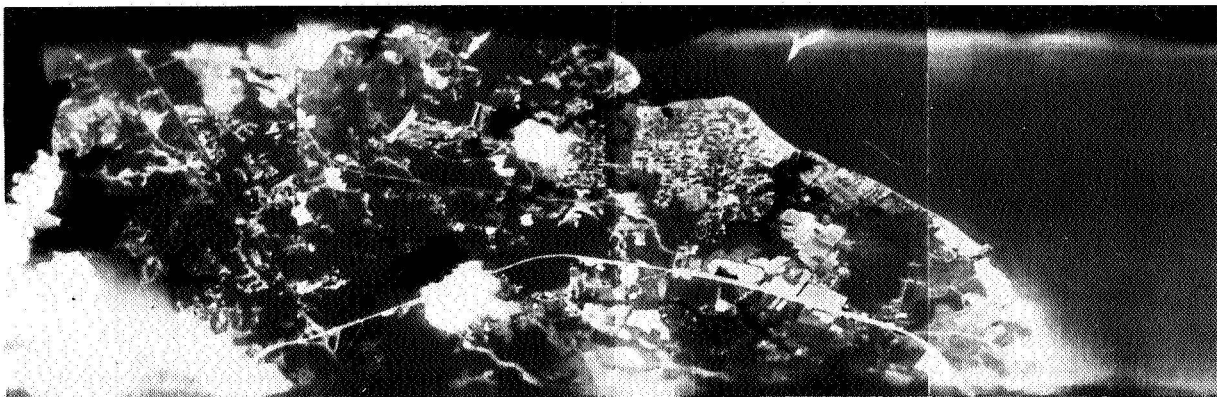


Figure 2. IDC image of Annapolis, Maryland. Original in color.

On the negative side we note a poor signal-to-noise ratio. This is attributed to an off-the-shelf lens, degraded photocathode, tape recorder noise, and the fact that the IDC is a non-integrating sensor.

In conclusion, we have demonstrated that it is possible to build a simple, lightweight, and potentially low cost system that can furnish high quality, registered multispectral images. As such, the MSIDCS should be seriously considered for future applications where such characteristics are important.

VERY HIGH RESOLUTION RADIOMETER

Joseph R. Schulman

The VHRR or very high resolution radiometer was specifically designed to work on an operational, meteorological satellite, and as such is flying now, successfully producing high-quality visible and infrared images from ITOS-D.

It is a two-channel instrument. The visible channel operates in the 0.6 to 0.7 micron region, the IR in the 10.5 to 12.5 micron band. The device has a resolution in both spectral bands of 0.9260 kilometers from a 1460-kilometer polar orbit, and scans from horizon to horizon. The visible channel operates with scene brightness up to $342,626 \text{ cd/m}^2$ (10,000 fL) and uses a silicon photodiode as the detector.

The infrared channel operates from a scene radiance equivalent to temperatures in the range of about 185 to about 315 degrees kelvin, and has a temperature discrimination (NE Δ T) of approximately three degrees at 185 kelvin and one degree at 315 kelvin. These numbers have been demonstrated in tests. We have not yet made measurements from orbit. The infrared channel uses a mercury-cadmium telluride detector, operating at 107 degrees kelvin.

Figure 1 shows an optical schematic diagram of the device. The scanning mirror is canted at 45 degrees, and rotates at 400 rpm. The optics is a Dahl-Kirkham mirror, Cassegrain system. A dichroic beamsplitter directs the visible and IR energy into the respective detectors.

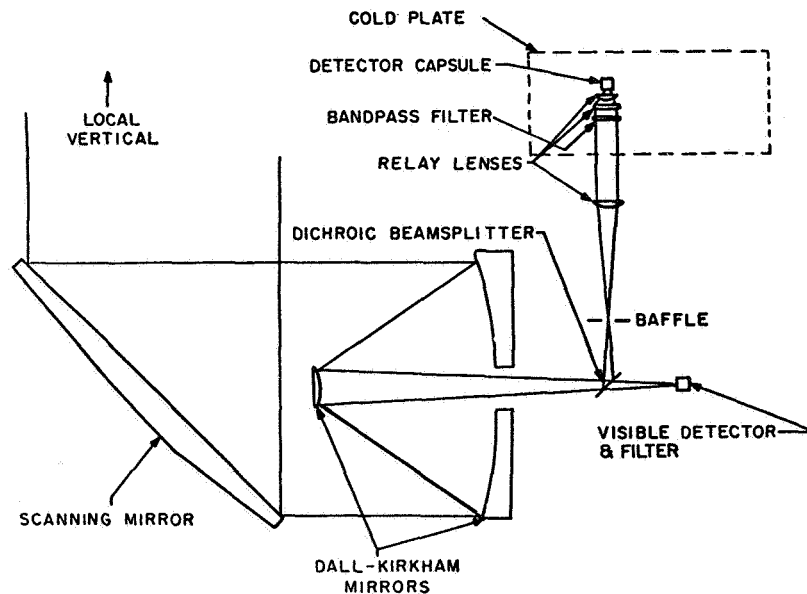


Figure 1. VHRR optical schematic diagram.

The visible energy goes through the beamsplitter to the visible filter and the silicon photodiode detector. The infrared energy is reflected from the dichroic beamsplitter through a series of relay lenses and a bandpass filter into the IR detector capsule. This is located on the passive radiative cooler, which we will discuss later.

A unique feature of the cooler design is the coupling between the instrument and the cooler; the cooler, represented by the dotted configuration, is through a collimated beam. It gives us leeway in the alignment of the various portions of the instrument.

Figure 2 is a photograph of the instrument. The rotating mirror is here. The optics is hidden. The mirror drive motor is a brushless drive motor servoed to operate at 400 rpm. The electronics is distributed, naturally, in the rear of the cooler so you can't see it. However, it is of standard plug-in board construction. The cooler consists of an outer frame, an inner frame, and a cold patch.

The outer frame has second-surface mirrors for cooling. These second-surface mirrors have low absorptivity and high emissivity. The inner frame cooling uses second-surface mirrors; perpendicular to the outer frame is a low emissivity gold.

The white surface is the cold patch, and the string-looking thing is a thermocouple wire. The detector is also shown.

Perhaps the most important technological advance is that the VHRR is the first NASA cooler in orbit operating on an instrument in the 100 degrees kelvin range. It is a two-

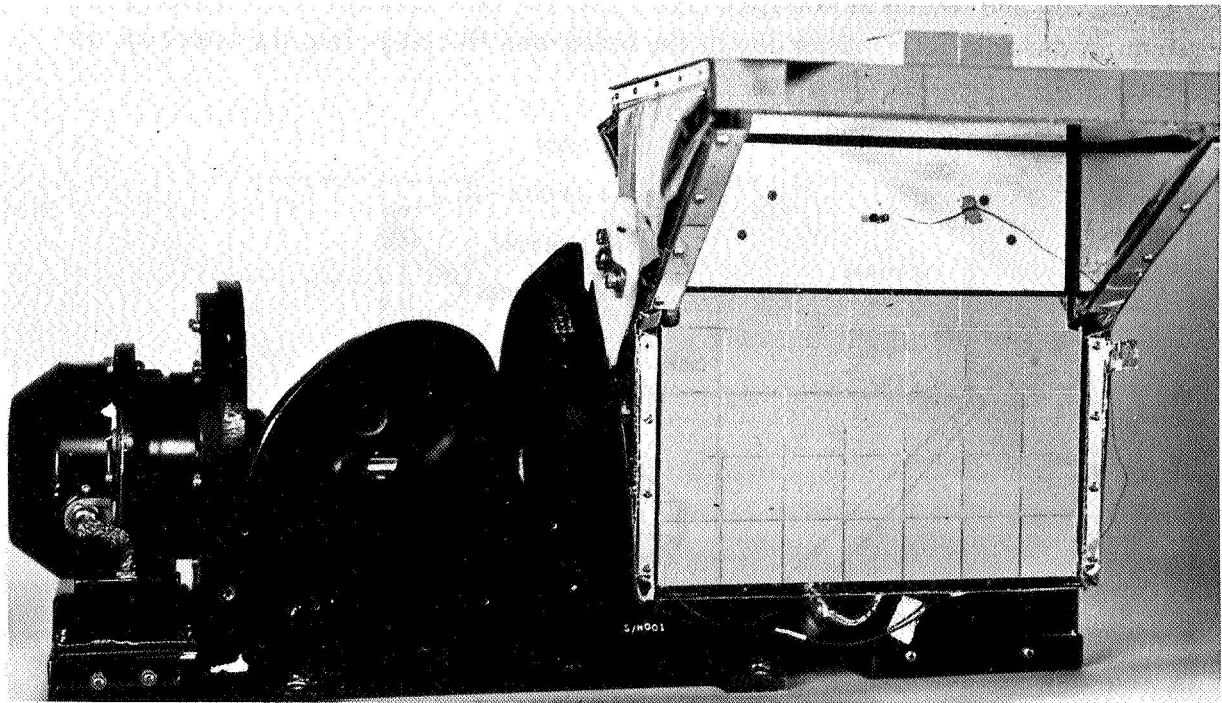


Figure 2. VHRR instrument.

stage, radiant cooler, with a cooled outer housing, and has a field of view as shown in Figure 3. During the first ten days of operation, we had some anomalous behavior for which we don't yet have the answers.

The design of the cooler is such that the outer frame is supposed to operate in orbit at 214 K, the inner housing at 150 K, and the coldplate, without thermal control, should go down to 95 K.

We use a thermal control servo to obtain the control point of the coldplate to 107 degrees — we servo-heat it up, in effect.

In flight, we have obtained the temperatures shown. The main anomaly is the 239 versus 214 degrees difference between the flight and design data. However, the cooler has been designed with sufficient margin to permit within-spec operation of the detector even though we have had higher temperatures on the outer house frame, and slightly higher temperatures on the inner housing.

The coldpatch would operate at 97 degrees kelvin on Serial No. 102 and 101 degrees kelvin on Serial No. 104, if we did not servo the control to 107 kelvin. This gives us an idea of the margin we have; we would like to have more, and we could perhaps obtain an additional few degrees if we could resolve the outer frame anomaly.

Figure 4 would be useful in showing the construction, a cross section of the VHRR cooler.

The inner frame is shown here with a honeycomb panel, second-surface mirrors, the gold that I mentioned, the cold patch, the detector, the filters, and the outer housing. The inner frame and the outer frame are insulated with blankets and with low-conductive standoffs. And, as shown in the far corner, the coldplate is tied to the frame with Kapton bands.

TWO-STAGE RADIANT COOLER WITH COOLED OUTER HOUSING
 90°X188° FIELD OF VIEW ON ANTI-SUN SIDE OF SPACE-CRAFT — 1460-km

STAGE	DESIGN		FLIGHT	
	No. 102 and 104	No. 102	No. 102	No. 104
OUTER HOUSING	214 K	238 K	237 K	
INNER HOUSING	150 K	160 K	165 K	
COLD PLATE	95 K	97 K	101 K	

[WITH 107 K CONTROL POINTS]

Figure 3. ITOS-D VHRR radiant cooler, the first NASA 100 K cooler in orbit.

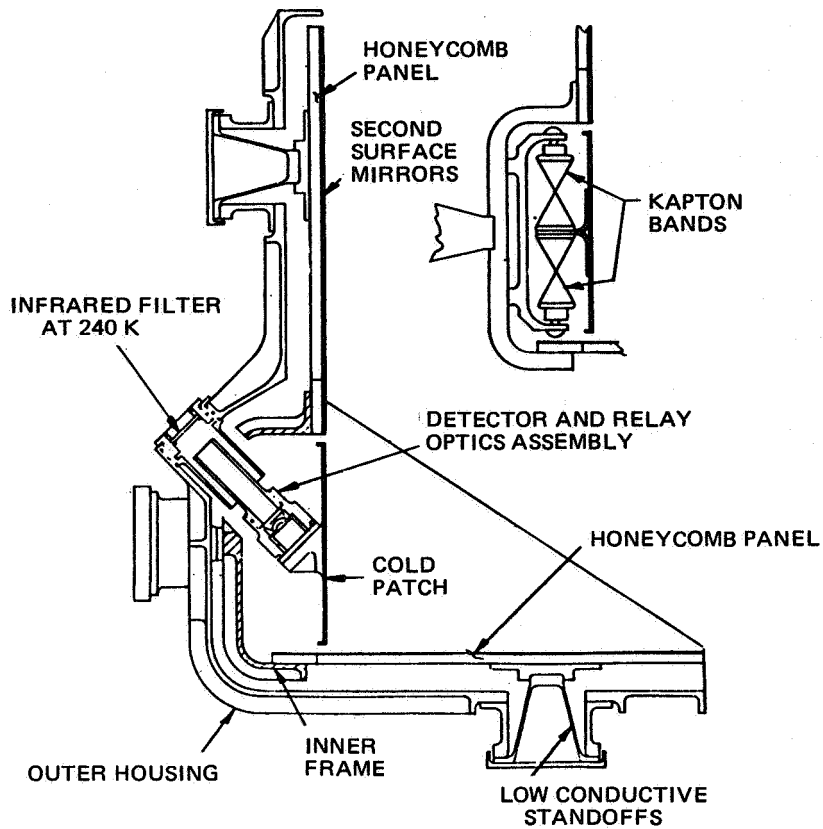


Figure 4. Cross section of VHR cooler.

I think the visible and IR cloud cover pictures that have been taken, once the ground station was set up properly, were quite startling, really.

MEMBER OF THE AUDIENCE:

I have seen the picture data, it looks just great. But there was this other question, that I haven't really gotten the answer to. You know there was gain variation, and it wasn't well understood, and you sort of partially explained it, and the instruments we had on board did not exhibit this spacecraft-on, spacecraft-off kind of situation. Have you done enough calibrations in orbit to know that the system is operating stably?

MR. SCHULMAN:

I really can't answer that right now. Perhaps NOAA might be able to answer it a little better, but they seemed to be quite satisfied with the performance of the instrument. That is all – I can't give you any numbers.

MEMBER OF THE AUDIENCE:

What is the weight of the cooler? And how thick are the walls?

MR. DONAHOE:

I think it runs about 2 kilograms (4 or 5 lb). The outer housing is a magnesium casting — so it is on the order of 1/16 to 1/8. The passive outer housing attaches the cooler to the scanner.

MEMBER OF THE AUDIENCE:

The overall weight?

MR. SCHULMAN:

It is 10 kilograms (22 lb).

THE GSFC COSMIC RADIATION EXPERIMENT FOR THE PIONEER F/G JUPITER MISSION

James H. Trainor

This experimental hardware is probably the Center's best example of an extremely light-weight, low-power design for severe environmental conditions. In fact, comparing other experiments of our own and others on IMP-I and H, we have succeeded in more than a factor of three reduction in weight and power. Flight performance is excellent, and costs were not really affected.

The first figure shows an external view of the experiment. The red-tag items and carry-handles are still on in this photograph. As discussed in an earlier paper, this experiment has three sensor telescopes for the detection of nuclear particles. The lowest energy sensor is contained within the Pb-Al shield, obvious in the center of the figure. A higher energy sensor is shown protruding through the side wall. The highest energy sensor system can't be seen; it is mounted internal to the package at 45° across the front corner at the top. The individual elements within a sensor are silicon discs (actually reverse-biased, totally depleted diodes) with areas from 50 mm² to 10 cm² and thicknesses from 50 microns to 2.5 mm. Our lowest energy thresholds are at 50 keV and range to 5 MeV for electrons, 800 MeV for protons, 600 MeV/nuc for helium and to 200 MeV/nuc for ions through neon. We are able to identify particles and often distinguish isotopes. We monitor a great many logical count rates with respect to time and sector of spacecraft spin.

Weight was the major problem. With just over one kilogram in the lowest energy system with the Pb shield and a total weight of approximately 3.2 kilograms, that leaves just over two kilograms for all else. All else includes more than 8000 discrete electronic components per system; more than 50,000 transistors — largely in medium and large scale integrated circuits; the other sensors; low and high voltage power supplies; the data system; and the mechanical system. This was all to be subjected to a hard ride, since our qualification vibration was to 40 g's.

We were able to accomplish this successfully using less than 10 percent of the total weight for the mechanical system. Both the baseplate and the top plate you see are aluminum honeycomb with 0.3 mm (0.012 in) skins. The top is only 3.2 mm (1/8 in) thick. The side panels are magnesium trusswork with 5-mil aluminized mylar bonded as the skin. The circuitry inside was stacked like a sandwich, cross-tied to the side trusses and to each other. Each electronics layer was interleaved with a sheet of flexible, compressible polyester-urethane foam for vibration damping.

Figure 2 shows a top view of one of the circuit boards for the linear electronics systems. Note the technique used here — daughter boards (15 mm by 30 mm) mounted on-edge on

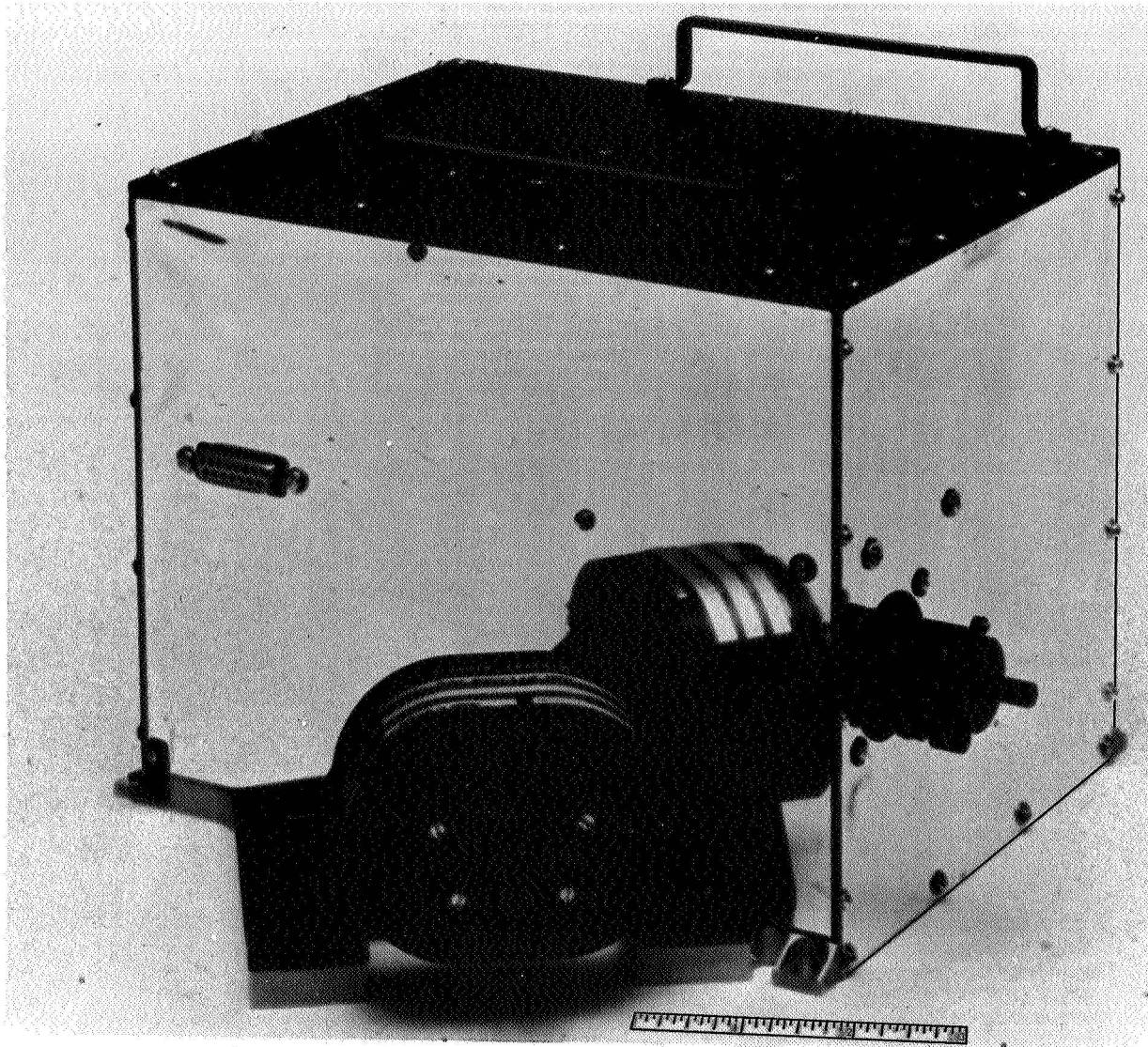


Figure 1. GSFC cosmic radiation experiment for the Pioneer F/G Jupiter mission.

the mother board or interconnect board. Again the polyester-urethane foam for damping is visible. There would also be a large sheet above and below this board in the stack-up.

You can see another lightweight technique at work here also. Many of the daughter boards are hybrid, thick-film circuits on ceramic substrates. Note the chip capacitors, discrete diodes in the glass dot packages with ribbon leads, and dual transistors in ceramic pacs (TO-80). You can't see special tantalum capacitors in rectangular plastic packages with alloy 180 leads. The overall construction also leads to a very low magnetic signature as required for the Pioneer mission – in our case approximately 1γ at 45 cm and is mostly due to integrated circuit packages.

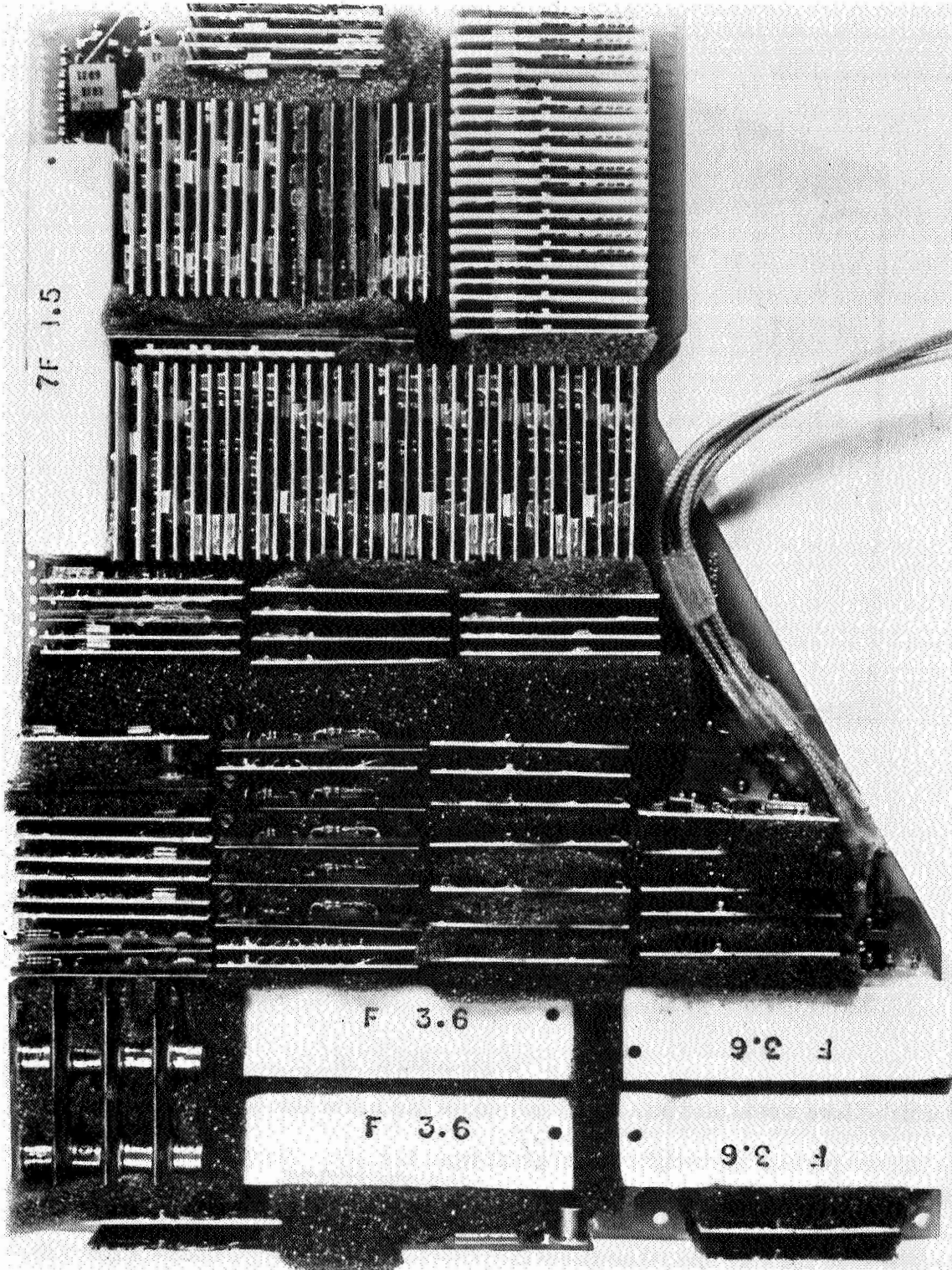


Figure 2. Circuit board for a linear electronic system.

The third figure shows front and back views of a daughter board from the P-channel MOSFET data system. These are the GSFC family of custom MOSFET bugs made by American Micro Systems Incorporated and used in Imp, Pioneer, and Helios to date. The welded interconnect uses gold-plated alloy 180 ribbon wire and nail-head terminals of the same materials. The relative simplicity of the interconnect is obvious. It's really great when you can have a powerful data system of greater than 50,000 transistors, which weighs less than one-half kilogram and uses less than 0.75 watt.

The total power for the experiment is 2.3 watts and this is very low considering all the electronics. At the beginning I mentioned that we were at a factor of more than three below previous competitive designs. This was accomplished by using low power design techniques everywhere: 100 microamp collector currents in bipolar transistors, for instance, and power strobing those circuits was not needed 100 percent of the time.

Time doesn't allow, but further severe constraints were imposed by the temperature range and the radiation environment including the spacecraft RTGs and the Jovian radiation belts. The experiment is functioning well and the date of closest approach at Jupiter will be December 4, 1973.

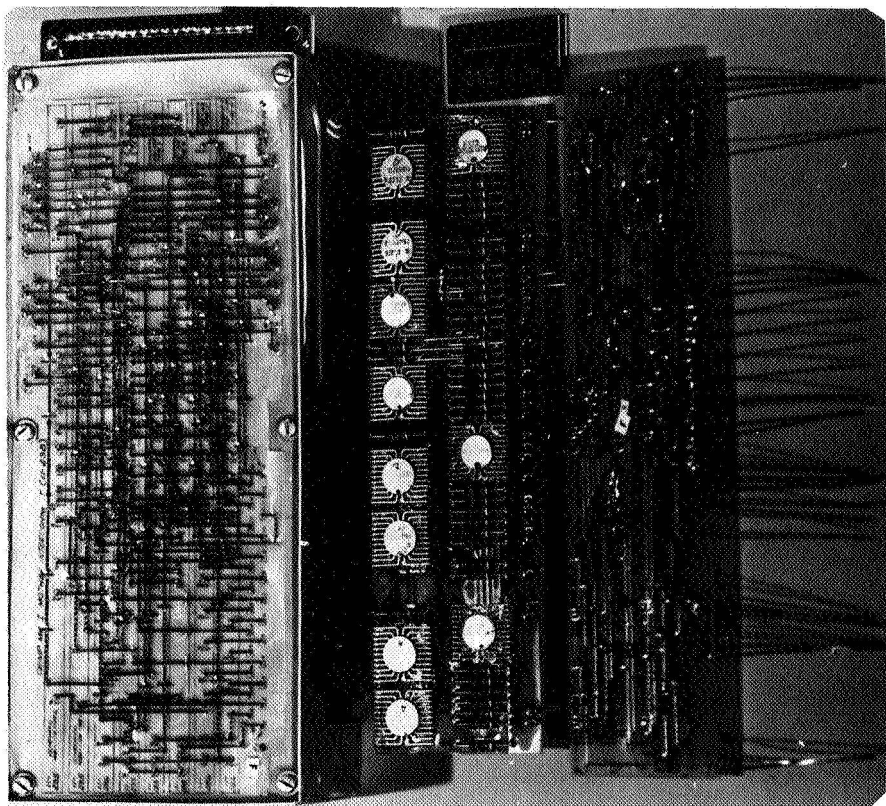


Figure 3. Front and back views of a daughter board from the P-channel MOSFET data system.

THE INTERNATIONAL ULTRAVIOLET EXPLORER

Albert Boggess

The International Ultraviolet Explorer is a new astronomical satellite still in the design stage. It is a Delta-launched satellite, weighing approximately 365 kilograms (800 lb), with an intended lifetime of three to five years, and it will serve as a precursor to the Large Space Telescope. The essential features of the satellite are its geosynchronous orbit, a 45-centimeter aperture telescope, and a high performance UV spectrograph using television tubes as detectors. It will be used as an international research facility, with NASA, ESRO, and the British Science Research Council each contributing to the hardware and participating in operation. Figure 1 shows an artist's concept of the satellite in orbit.

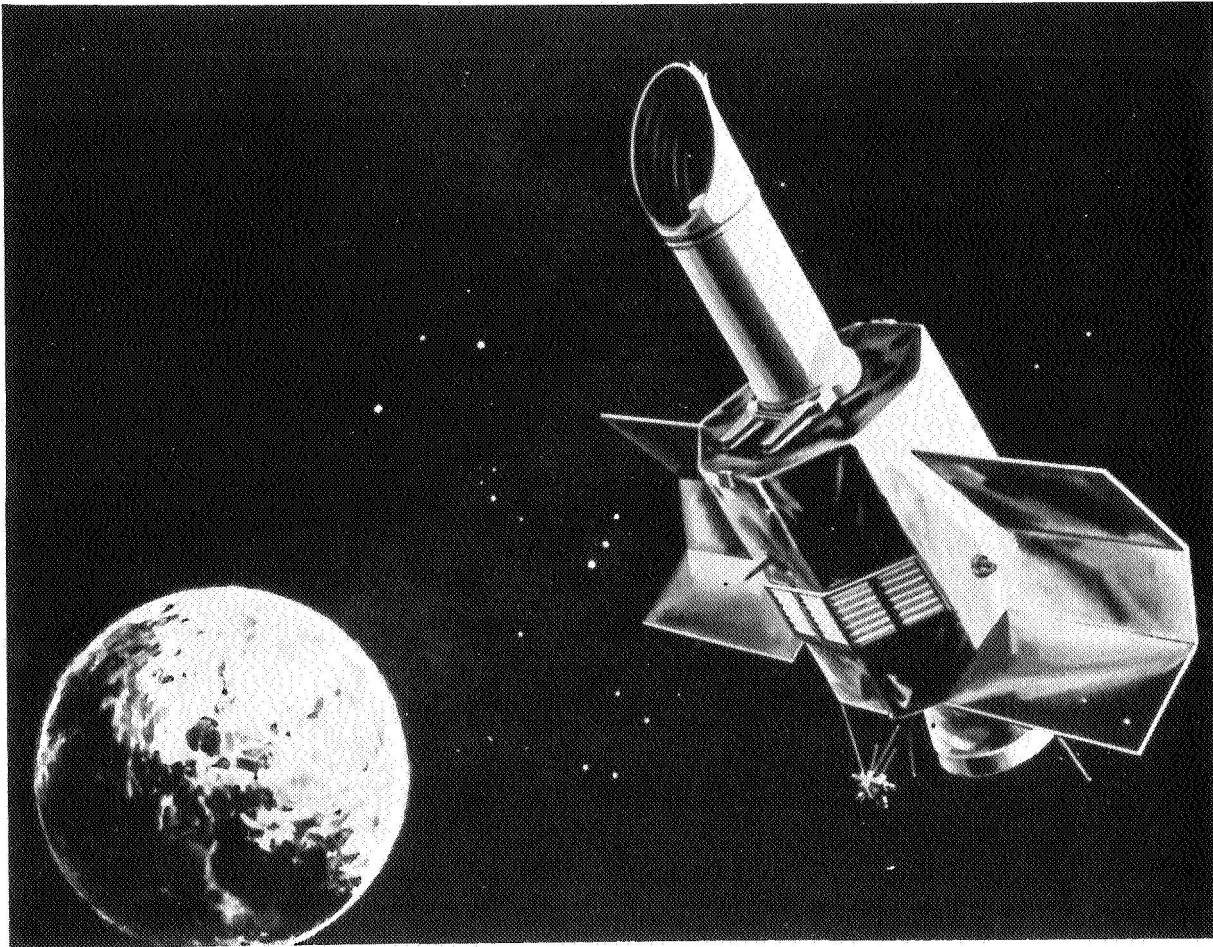


Figure 1. The IUE spacecraft.

One can see the telescope tube sticking out of the satellite proper, with a cylindrical baffle on top. The primary mirror is located near the base of the tube. The solar arrays, which are to be provided by ESRO, are shown extended, and one sees at the back end the station-keeping thrusters, antennae, and the apogee kick motor. Control is provided by a gyro package which, with periodic stellar updates, will be able to maintain inertial pointing to one second of arc for arbitrarily long periods of time. The satellite is to be stationed over the Atlantic, where it can be operated from ground stations either in the U.S. or in Europe. The anticipated usage is 16 hours per day from the U.S. and 8 hours per day controlled from Europe.

The optical system shown in Figure 2 includes a conventional Ritchey Chretien f/15 telescope, 45 centimeters in diameter. In the rear compartment are the spectrographs. I won't try to go through the complicated optical system in detail. There are two echelle spectrographs packaged side-by-side which provide a total wavelength coverage from 1150 to 3200 Angstroms at either high dispersion (0.1 Angstrom resolution) or low dispersion (6 Angstrom resolution). The large masses in the spectrograph cavity are the television cameras. A total of three tubes is required to record the spectra plus various auxiliary data. Each of these tubes has a spare, so that there is a total of six TV systems on board the spacecraft.

The spectrum detectors must record an image like that shown in Figure 3. Here we see a spectrum broken into short segments, starting at 1150 Angstroms down at the bottom and increasing from left to right at a dispersion of about one Angstrom per millimeter. The bottom order is only about a millimeter long, but the spectrum then picks up on the next line on the left and continues on, order by order, all the way to the long wavelength limit. The variations in density are due to spectral lines, and the job of the TV

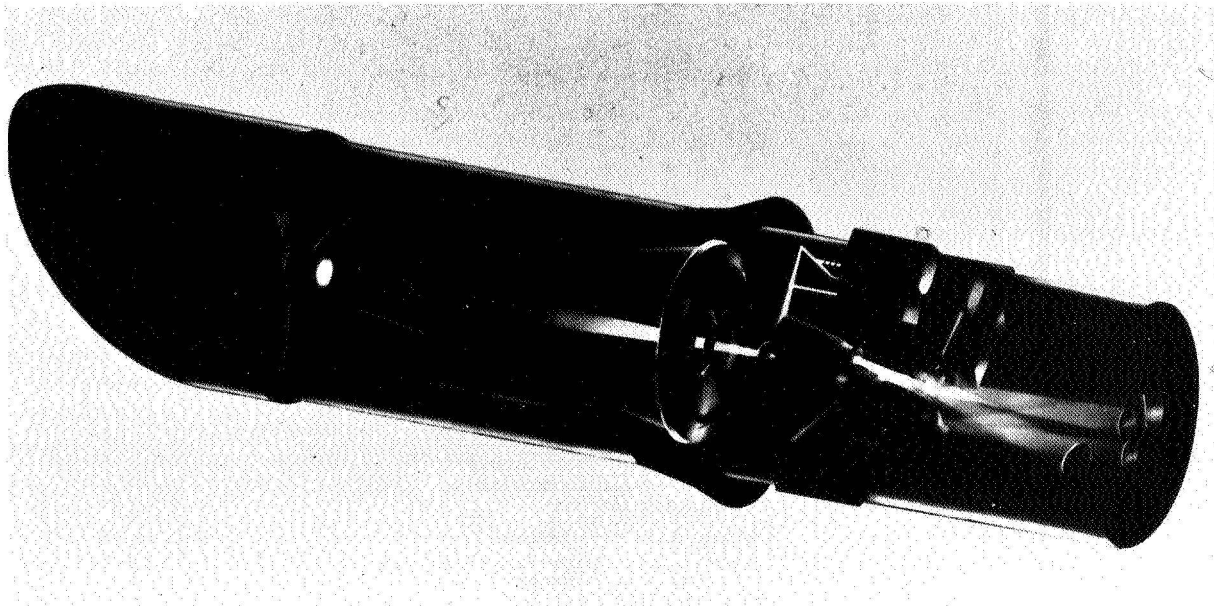


Figure 2. IUE scientific instrument.

tube is to record the positions, e.g. the wavelengths, and the photometric profiles of these various features.

At the bottom of the picture, where the information density is greatest, the format corresponds to a bar chart with a spacing of 5 line pairs per millimeter, but the resolution of the tube must be greater than this implies. It should be greater because accurate photometric measurements must be obtained both in the spectrum and in the background between orders in order to make stray light corrections to the data.

The detector system that we have developed for this purpose includes the Westinghouse WL 30893 electrostatically focused SEC Vidicon, operated digitally. This tube meets the rather severe weight and volume requirements imposed on the system, but has a fiber optic faceplate which is able to transmit only visible light. In order to make this tube UV-sensitive, it is coupled with a proximity focused photon converter with a cesium telluride photocathode.

The combination, then, the photon converter plus the SEC Vidicon, gives us an ultraviolet detector system which is capable of recording spectra such as these with a photometric statistical accuracy of some 2 percent.

The schedule requires that this system be flown about four years from now. At that time, it will present the highest capability astronomical research facility in orbit; and that will continue to be the case until the launch of the LST itself.

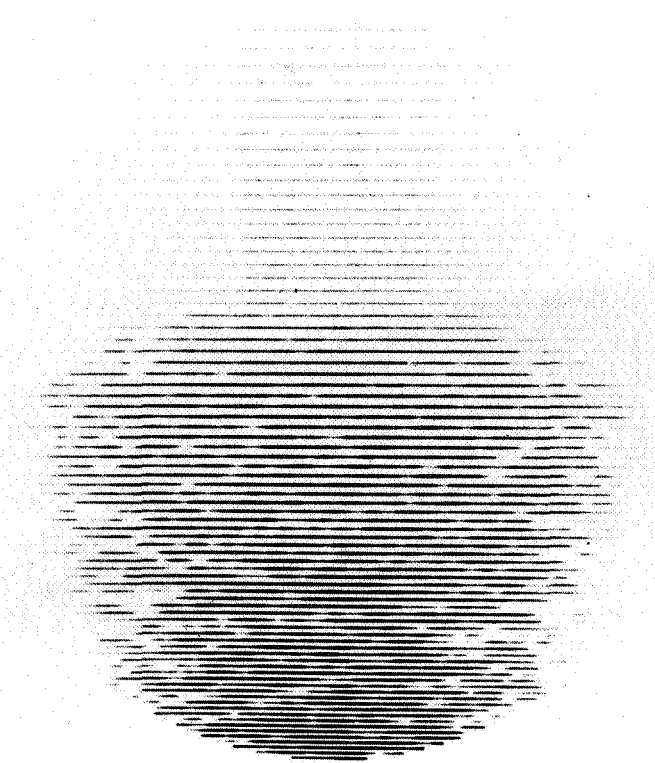


Figure 3. An Echelle spectrogram.

SCIENCE INSTRUMENTATION PACKAGE, LST

George Levin

At Goddard we have three LST-related RTOPs and I have selected one for discussion today; namely, the Optical Instrument System for the Large Space Telescope (LST).

I chose this particular RTOP for two reasons. First of all, it is the one that is the furthest along technically, and therefore, we can present more results than on any of the others.

Secondly, I want to speak on this RTOP because it represents the heart of our participation in the LST program with Marshall Space Flight Center. As you are undoubtedly aware, Marshall has project responsibility for the LST and will be supplying the spacecraft and the telescope. Goddard is responsible for providing the science instrumentation package, as well as mission and data operations.

To begin with, about a year ago the LST Science Steering Committee issued a series of recommendations. These recommendations were combined with certain mission constraints to produce a set of scientific objectives. We took these scientific objectives and integrated them with a Goddard pre-Phase-A Instrument Design Study, added certain spacecraft constraints which we got from Marshall Space Flight Center, and produced a series of parametric science instrumentation package designs.

These parametric science package designs were gradually reduced to a reference science instrumentation package design for the Phase-A study. That reference design is the one that I will be discussing.

Overlaying this entire process was a directive from the program scientist and the Science Steering Committee that we produce a dynamic, flexible science instrument package design for use in a national astronomical space observatory during the entire decade of the 1980s.

Let's begin with Figure 1 and take a look at the recommended instruments from the Science Steering Committee.

As you can see, the instruments are broken into two categories. First of all, let's examine the primary category, which consists of the three instruments shown. The primary category is defined as instruments which must be in any LST.

The secondary category which was designated by the Steering Committee is defined as instruments which should be put on the LST on an "as available" basis. I use the term "as available" to mean if we have the weight, power, money, and space to put them in.

PRIMARY	I	DIFFRACTION LIMITED CAMERA
	II	LOW DISPERSION SPECTROGRAPH
	III	HIGH DISPERSION SPECTROGRAPH
SECONDARY		ASTROMETRIC MACHINES
		PHOTOMETERS
		HIGH TIME RESOLUTION
		HIGH INTRINSIC ACCURACY
		POLARIMETERS
		F/12 CAMERA
		FOURIER INTERFEROMETER
		INFRARED INSTRUMENTATION
	VERY HIGH DISPERSION SPECTROGRAPH	

Figure 1. LST steering committee instrument recommendations.

Figure 2 is a pictorial version of the Phase-A design of the science instrumentation package.

First of all, the telescope is located to the left, with light travelling from left to right. The instruments are shown in their respective locations within the science instrumentation package design. This particular design was set up so that the instruments are located for independent removal or refurbishment during the life of the mission.

Instruments between the first and second structural rings are removed radially, and instruments between the second and third structural rings are removed axially.

The structure between the first and the second rings is generally referred to as the focal plane structure, and the structure between the second and third rings is called the science instrumentation package (SIP) aft structure.

Figure 3 is a functional block diagram of the science instrumentation package. The area between the first and second structural rings, or the focal-plane structure, is shown in this block; and located there we also find three of the four instruments which make up the faint object spectrograph; the fourth instrument is located in the aft SIP structure.

At this point it is important to note that it was impossible to design a single instrument that would operate over the entire wavelength that was recommended by the Science Steering Committee. For this reason we actually have four separate instruments making up the faint object spectrograph.

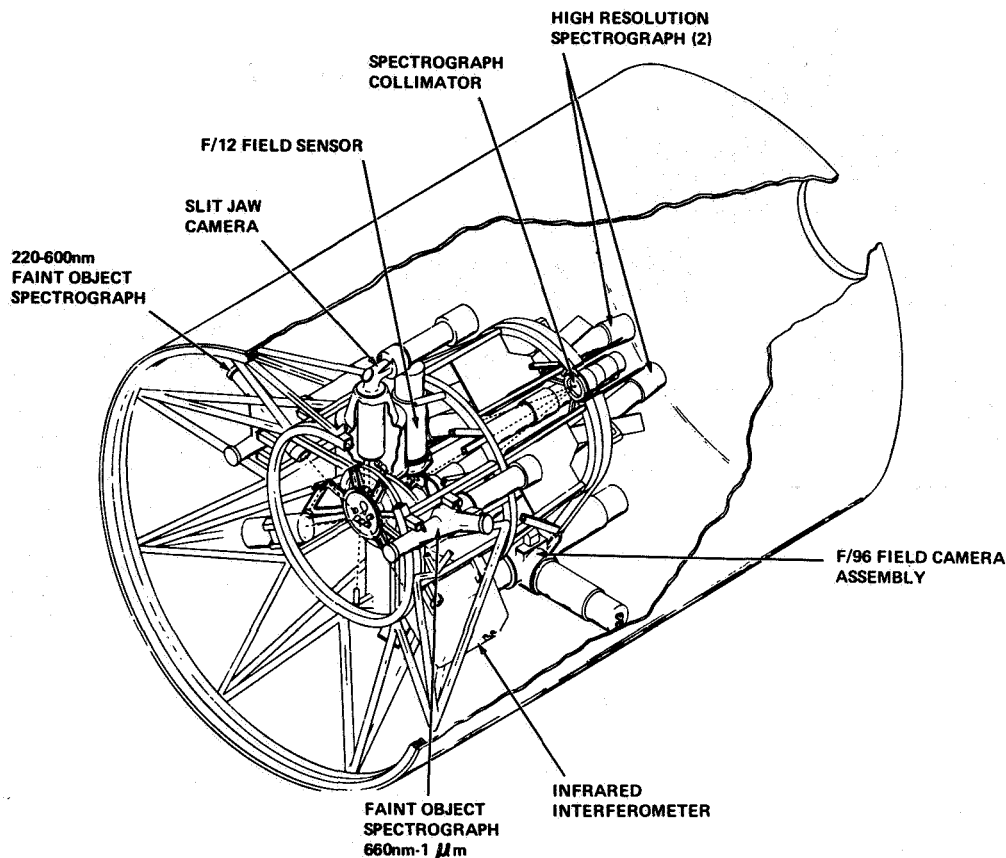


Figure 2. Scientific instrument package.

In the focal plane structure, you find the F-12 camera. This is the only secondary instrument which we are packaging from the list of secondary instruments provided by the Science Steering Committee.

In the aft SIP structure, we have the high-resolution spectrograph, as well as an unassigned bay, that is to say, room for an as yet undesignated or unassigned instrument.

In addition, in the area of the science instrumentation package you see the third or final of the primary instruments recommended by the Science Steering Committee, the diffraction limited camera. The diffraction limited camera consists of a single set of optics, but again requires three sensors to operate over the entire range that was recommended by the Science Steering Committee.

In conclusion, I would like to say that the results of our study showed that we could produce a dynamic, flexible package for use in a national astronomical space observatory during the 1980s. Such a design would incorporate all of the primary instruments that were recommended by the Science Steering Committee, as well as at least two of the secondary instruments.

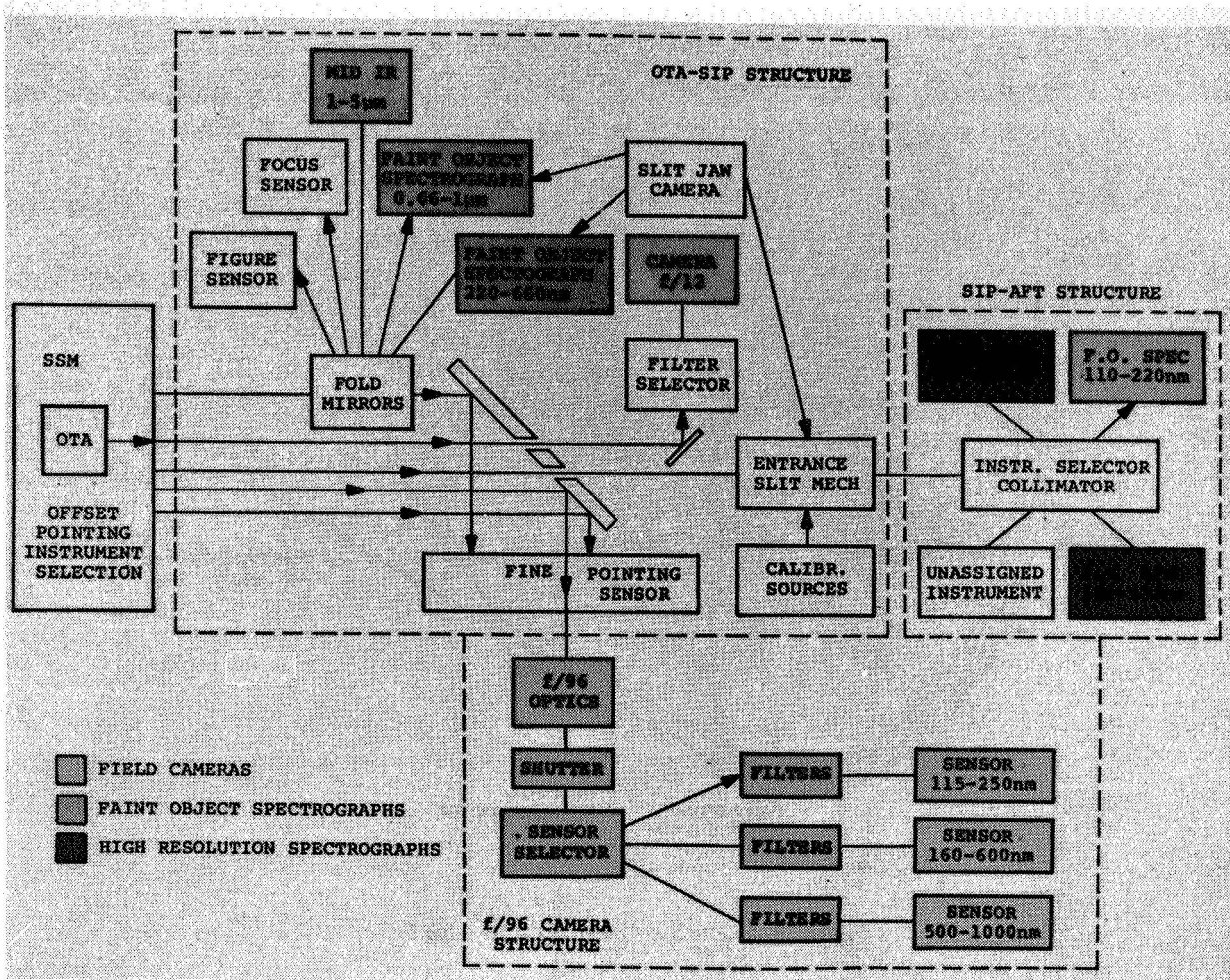


Figure 3. Scientific instrument package functional block diagram.

GLANCING INCIDENCE TELESCOPES FOR SPACE ASTRONOMY

Jose Alonso, Jr.

In the past several years we've reported on our efforts to develop glancing incidence telescopes for Space Astronomy Applications. By glancing telescopes I'm referring to the Wolter Type I and II, and the Cassegrain systems. Figure 1 shows a Wolter type II designed for use in the extreme ultraviolet region. The incoming rays first are incident on a concave parabola and reflect to a convex confocal hyperbola. The rays reflected by the hyperbola are then directed to the other hyperbolic foci which is the system focus. The Wolter type I and the Cassegrains operate similarly.

The subject of this report deals with a technique that we've found for determining the state of polarization of a light source by evaluating its image at the focus of a glancing telescope. This is a significant discovery in that we've extended the information gathering capabilities of the glancing telescopes, from solely collecting spatial and spectral information to include polarization information. An analysis of the central disc of the diffraction image will reveal

- If the light source is polarized
- The plane of polarization
- The degree of polarization

When polarized light is incident at the aperture of a diffraction limited glancing telescope, the central disc of the diffraction pattern takes on an elliptical configuration. This ellipticity

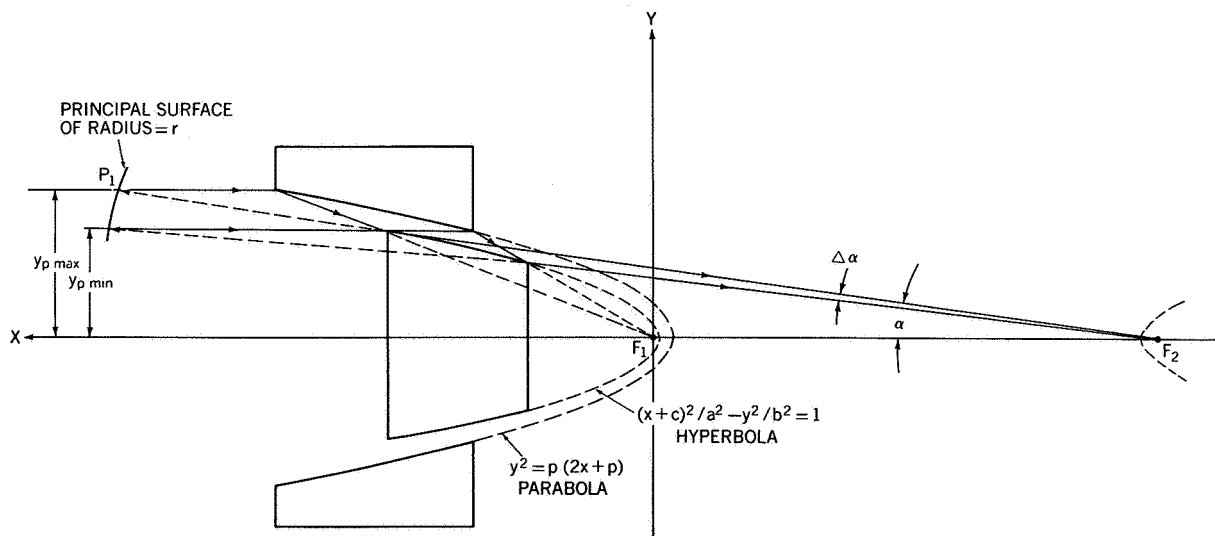


Figure 1. Wolter type II glancing telescope.

is caused by the tendency of the electric vector component in the plane of incidence to be absorbed by the reflecting material.

Figure 2 shows the image of a Type II telescope illuminated with plane polarized laser light of 6328\AA wavelength. Note that the major axis of the ellipse is along the plane of polarization, and the ratio of the ellipse axes is about 1.33. This same result was obtained by program "Daphne" (a computer program designed to evaluate the electric field at the image of an optical system). We reported on the development of this program in 1970. In Figure 3, using the program to further the investigation of this ellipticity phenomena, the following is shown: As the state of polarization goes from plane polarized to decreasing degrees of elliptically polarized light, the ellipticity of the central disc goes from a maximum at plane polarization to zero at circular polarization. These curves give us a direct relationship between the degree of polarization of a light source and the ellipticity of the central disc for this particular telescope, independent of the light source wavelength.

Therefore, ellipticity of the central disc indicates that the light source is polarized. The major axis of the ellipse indicates the direction of polarization for the plane polarized case; it also indicates the direction of the largest electric vector for the elliptically polarized case. And finally, with the use of Figure 3, the degree of polarization can be obtained with the ratio of the major axis to minor axis of the ellipse.

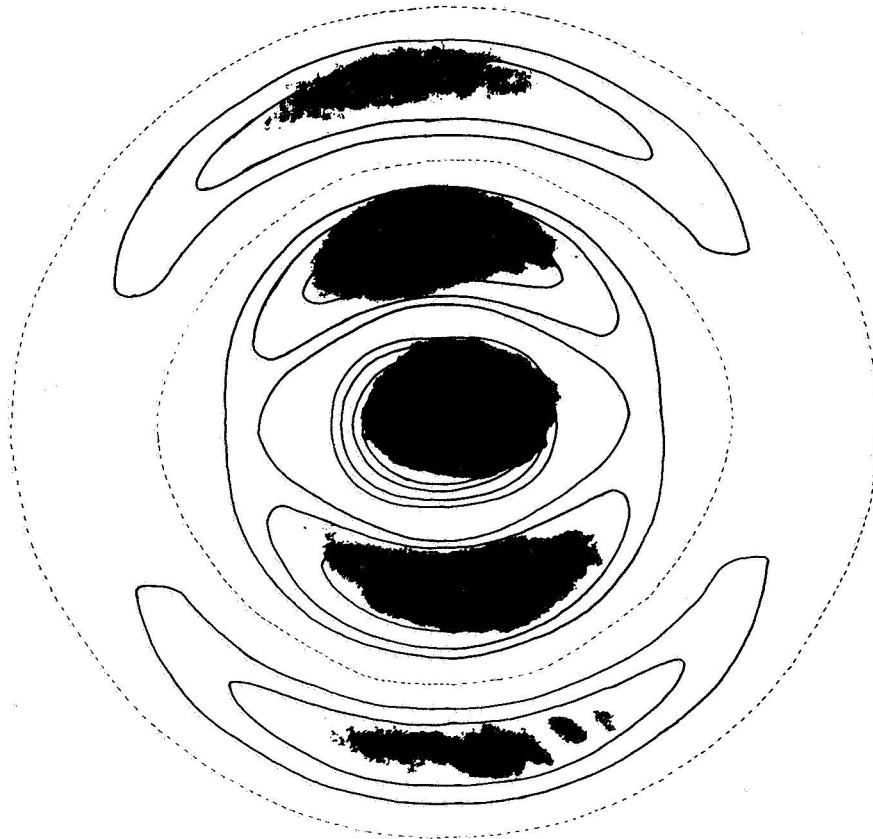


Figure 2. Results of wave analysis and actual photograph.

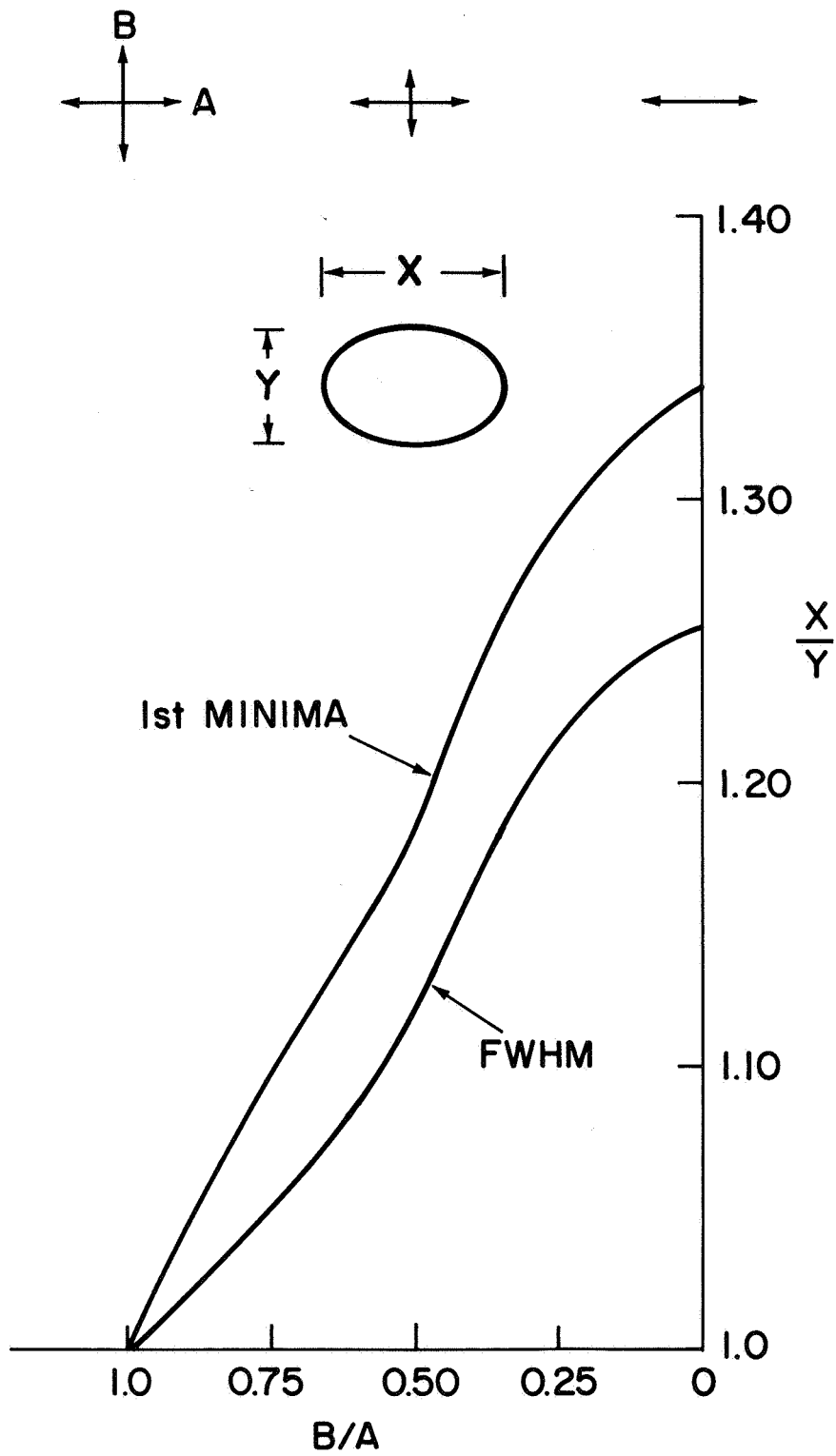


Figure 3. Degree of polarization versus image center ellipticity.

SECTION III
GROUND OPERATIONS

OVERVIEW

Albert G. Ferris

My job is to try and change your direction a little, to come down to the ground and talk about operations. As John Clark remarked yesterday, the title of these sessions, Science and Technology Presentation, is really wrong; it should be Science, Technology, Ground Operations, and Applications Presentation. The reason for including ground operations is that a significant amount of Goddard's efforts, resources, and accomplishments are in that area.

Ground operations as depicted in Figure 1 are a set of installed capabilities and functions that are accomplished on the ground. Ground operations bring the wishes, the desires, and the needs of flight direction (data management in a broader sense) to execution, so as to cause the satellite to acquire data for scientists and engineers. Obviously, there's a high degree of interaction between the elements of the principal sessions of these presentations — the onboard processing influences ground operations, and so forth. In a sense, the ground operations are the hands and arms of flight direction/data management in dealing with the satellite. Not only is there a multiple path through the ground operations, but varying relationships and interfaces are always present. This is true for a single mission, and we are actually operating in an environment of many simultaneous missions. In addition, there is a wide range of mission complexity. Ground operations is a blend of both unique and general solutions; some missions and their requirements demand very explicit, detailed, specific solutions. Others use generalized capability.

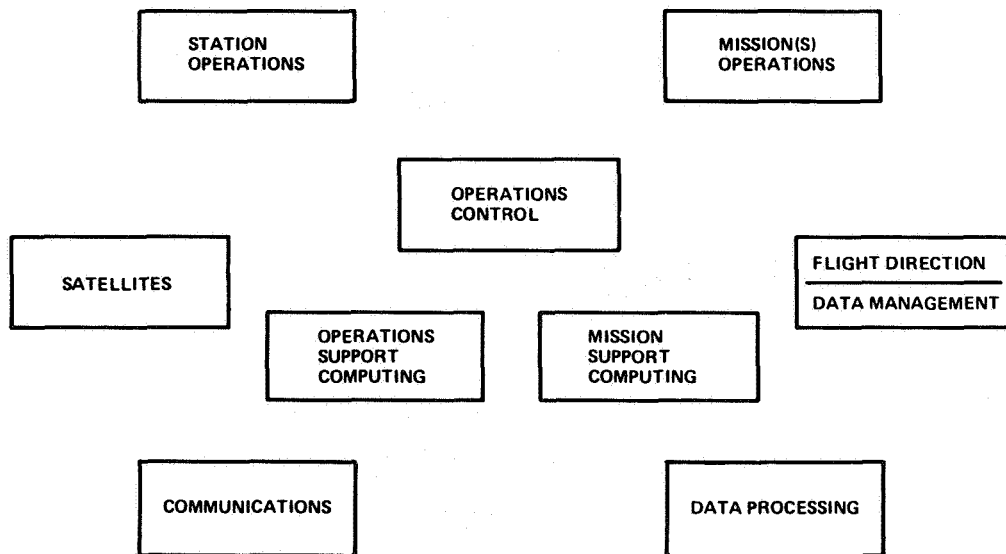


Figure 1. Ground operations.

At Goddard, there are some 35 to 40 missions operating at any given time. Some of the most recent examples are the ERTS-1, OAO-C (Copernicus), IMP-H, and SSS. To do this job, continuing development is required. When we talk about developments, we are more accustomed to talking about the ground systems, that is, the hardware and the components. There is another dimension which I would like to briefly put in perspective for you. Some of the papers you will hear will attempt to show how the not-so-hardware is involved and its development in its own right.

The systems for ground operations are outlined in Figure 2. These systems include both hardware and software. When we think of software, we usually think of computer programs. To ground operations, software is much more than that: it is procedures (independent from those embodied in software), knowledge, ability to accomplish, and, of course, the people who have that knowledge and capability. So the concept of software is somewhat broadened from the usual meaning and sense.

Automatic data processing equipment plays a big role in ground operations. However, in the context of development, it is not an area of technology where great developments are presently required. We are able to use existing technology to solve our problems. Development will be required in the future to help accomplish the ground operations in an effective manner.

HARDWARE

- **TRACKING**
- **TELEMETRY**
- **COMMAND**
- **COMMUNICATIONS**
- **DISPLAY**

SOFTWARE

- **PROGRAMS**
- **PROCEDURES**
- **KNOWLEDGE**
- **PEOPLE**

Figure 2. Ground operations systems.

Developments in ground operations come about basically in the four ways shown in Figure 3:

First, new capability to meet new requirements. Things we have to do that we haven't done before: new hardware, new ways, new means, new speeds, new responses.

Second, improved systems and techniques to meet the variation in requirements. Do things differently in order to accommodate the adjusting requirements of missions as their health and welfare change, as their demands change, as new objectives come up.

Third, exploit our capability to find ways in which they can be applied to new problems, new requirements, in order to make the ground operations more effective for the users to accomplish their ends.

And fourth, expand a unique solution into a general application.

- **CREATE CAPABILITY TO MEET REQUIREMENTS.**
- **IMPROVE SYSTEMS & TECHNIQUES TO MEET INCREASED REQUIREMENTS.**
- **EXPLOITATION OF CAPABILITIES & SYSTEMS IMPROVE TECHNIQUES.**
- **EXPANSION OF UNIQUE SOLUTION TO GENERAL APPLICATION.**

Figure 3. Ground operations development.

I hope that you will be able to identify some of these aspects in the papers that will follow. We have assembled a selection papers across the spectrum of systems, operations, and generalization of specific solutions.

Figure 4 shows the agenda for the ground operations session. The things I would like you to note are:

- In the area of antennas, the specific technology being developed for the precise tracking requirement
- In the tracking area we have exploited our capability in order to meet a new type of requirement
- The papers in the area of orbit determination and control will try to depict some flavor of the control dimension which is not always obvious and apparent
- In the case of attitude determination and control, we are trying to typify the generalization of unique solutions; a system has grown from the need to do single and simple attitude determination into a multicustomer environment for determination, prediction, and control

- In mission operations we are dealing with how to interface with flight direction. The flight director would like the "system" to be transparent to him. He would like to talk about and to his satellite in its language and terms
- In image data processing, we've taken the time to prepare a couple of papers on specific selected subjects. We have been working diligently to bring the ERTS-1 image processing facility into operation. There's more to be said, and I think that in the future you will hear a lot about image data processing.

ANTENNAS

- **ADAPTIVE GROUND-IMPLEMENTED PHASED ARRAY FOR TORS.**
- **COMBINATION OPEN-LOOP, CLOSED-LOOP, AND ADAPTIVE COMPENSATION; THEIR APPLICATION TO AN OPTICAL TRACKING TELESCOPE.**

COMMUNICATIONS

- **HIGH-EFFICIENCY GROUND DATA TRANSMISSION.**

TRACKING

- **VERY LONG BASELINE INTERFEROMETRY.**
- **RESULTS OF MARINER MARS TRACKING AND CALIBRATION EXPERIMENT.**

ORBIT DETERMINATION AND CONTROL

- **THE CALCULATION OF EFFICIENT, HIGH-PRECISION ORBITS BY OPTIMUM MATCHING OF FORMULATION AND NUMERICAL INTEGRATOR.**
- **ERTS ORBIT MAINTENANCE.**

ATTITUDE DETERMINATION AND CONTROL

- **ATTITUDE COMPUTATION SYSTEM.**
- **MISALIGNMENT ESTIMATION SOFTWARE SYSTEM.**
- **SPACECRAFT REORIENTATION VIA SLEWING ABOUT NONORTHOGONAL AXES.**

MISSION OPERATIONS

- **COMPUTER ASSISTED INTERACTIVE RESOURCE SCHEDULING SYSTEM.**
- **INTERACTIVE EXPERIMENTERS (AND MISSION CONTROL) PLANNING PROCEDURES.**

IMAGE DATA PROCESSING

- **ELECTRON BEAM IMAGE CORRECTION FOR ERTS.**
- **A PHOTOGRAPHIC PROCESSING CONTROL METHOD FOR ERTS IMAGERY.**

Figure 4. Ground operations session agenda.

ADAPTIVE GROUND IMPLEMENTED PHASED ARRAY

Robert E. Spearing

One of the more significant problems facing the designers of the tracking data relay satellite (TDRS) is that of establishing a VHF system design. The design must be tolerant of the high level radio frequency interference (RFI) environment which may be encountered by the TDRS and its low data rate users. An adaptive ground implemented phased array (AGIPA) can provide significant improvements in signal-to-RFI ratio.

Studies conducted for and by Goddard Space Flight Center have shown that the RFI levels received by a synchronous altitude satellite would range considerably above the channel thermal noise for a fixed field of view antenna coverage as depicted in Figure 1. The TDRS

FIXED FIELD OF VIEW

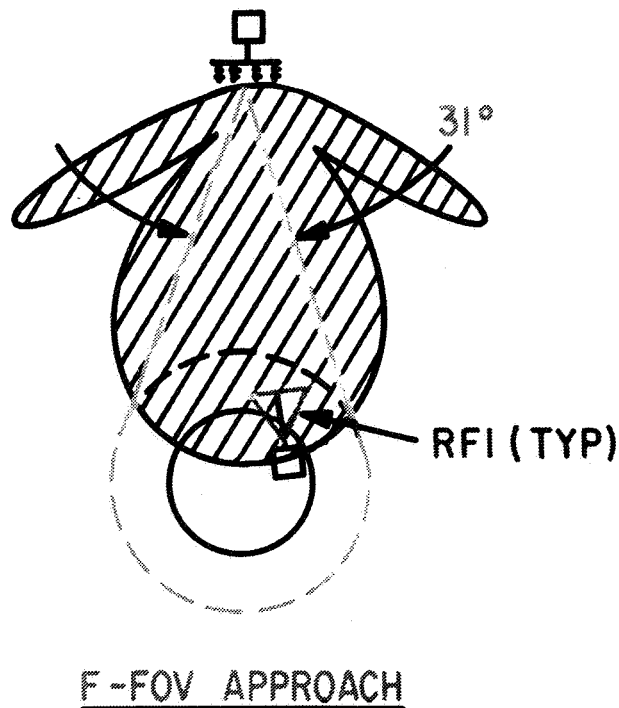


Figure 1. Antenna coverage, fixed field of view.

requirements for the low data rate channel are to provide a means for up to twenty satellites to simultaneously use the TDRS. The fixed field of view antenna would not afford reliable service for these users even in the absence of RFI.

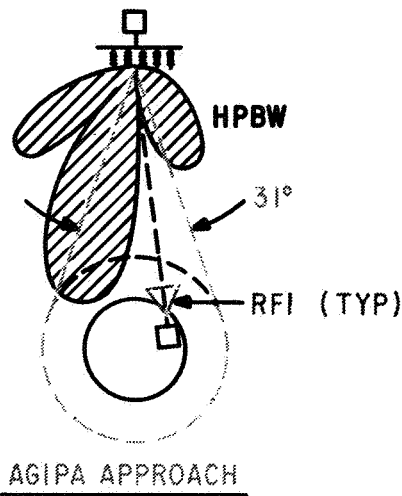
A study conducted by Magnavox for GSFC concluded that the most efficient method of operation for the LDR link is to make use of wideband spread spectrum PSK modulation techniques which would provide:

- Multiple Access
- Multipath Rejection
- Processing Gain Against RFI

Further analysis of the link requirements indicated that even more processing gain than that afforded by utilization of the entire 2 MHz VHF bandwidth is required.

The only other potential area of improvement is to increase the directivity of the antenna beam, which would result in rejection of RFI outside the antenna field of view and increase the signal gain as in Figure 2. Consequently, an approach was devised using a phased array

AGIPA



- ADAPTIVE GROUND IMPLEMENTED PHASED ARRAY
 - ADAPTIVE SPATIAL FILTERING OF RFI
 - ADAPTIVE POLARIZATION FILTERING OF RFI
 - HPW- 8° SR AGIPA (5λ)
(VARIABLE 4°-13°)
- } FOR MAXIMUM SIR

Figure 2. Adaptive ground implemented phased array.

which could form an independent narrow beam for each user satellite without requiring complex system implementation in the TDRS.

The technique which was evolved utilized the TDRS as a platform for five VHF antenna array elements. It relayed the signals from each antenna element to the ground station (GS) where all of the adaptive beam forming, beam steering, and signal processing could be performed, thus alleviating the normal complexities and physical constraints involved in spaceborne signal processing of multiple signals.

An adaptive ground implemented phased array (AGIPA) retains the advantages of a high gain array with only a small amount of additional on-board equipment, while providing as many independent narrow tracking beams as there are user satellites. The overall TDRS system using AGIPA is shown in Figure 3.

Signals originating from low altitude user satellites are received at the TDRS by the five element VHF ring array. Both horizontal and vertical polarizations from each of the five antenna array elements are multiplexed and transmitted down to the ground station (GS). Therefore, ten individual channels, one for the vertical and horizontal output of each antenna element are relayed to the GS via the Ku-band TDRS-GS transmission link.

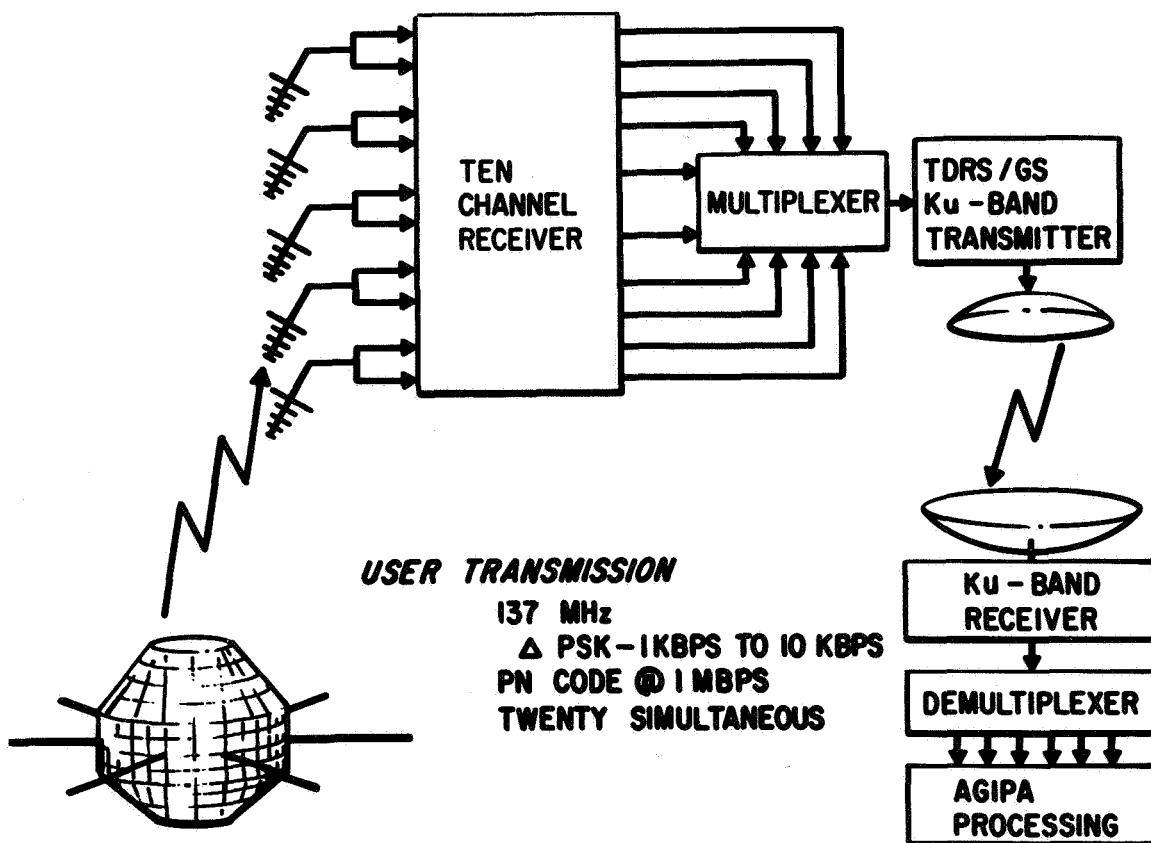


Figure 3. AGIPA implementation for TDRS.

On the ground the unique pseudo-random code transmitted by each LDR satellite is utilized to separate the different received signals into forty channels, one for each user. Thus, the contribution from each array element is made available for each user, enabling the computer controlled adaptive signal processing receiver to individually synthesize a tracking beam which maximizes the signal-to-interference ratio.

The method devised to evaluate the performance of the AGIPA system was to simulate the user to TDRS to ground station portion of the return link. The VHF array was scaled to S-band so that the demonstration tests could be performed inside of an anechoic chamber with a range of between 9 and 15 m (30 and 50 ft). To simulate the actual environment which the TDRS will encounter, there are up to ten S-band RFI sources at 2298 MHz \pm 1 MHz located on a panel at the transmitting end of the chamber; along with the desired signal, which is mounted on a pulley system to simulate the dynamic relationship between user and TDRS. Figure 4 illustrates this arrangement.

The multiplexer-demultiplexer and Ku-band TDRS-GS link, although important parts of the overall system, are not required in evaluating AGIPA performance and will therefore not be implemented during this development program. The five S-band array elements are

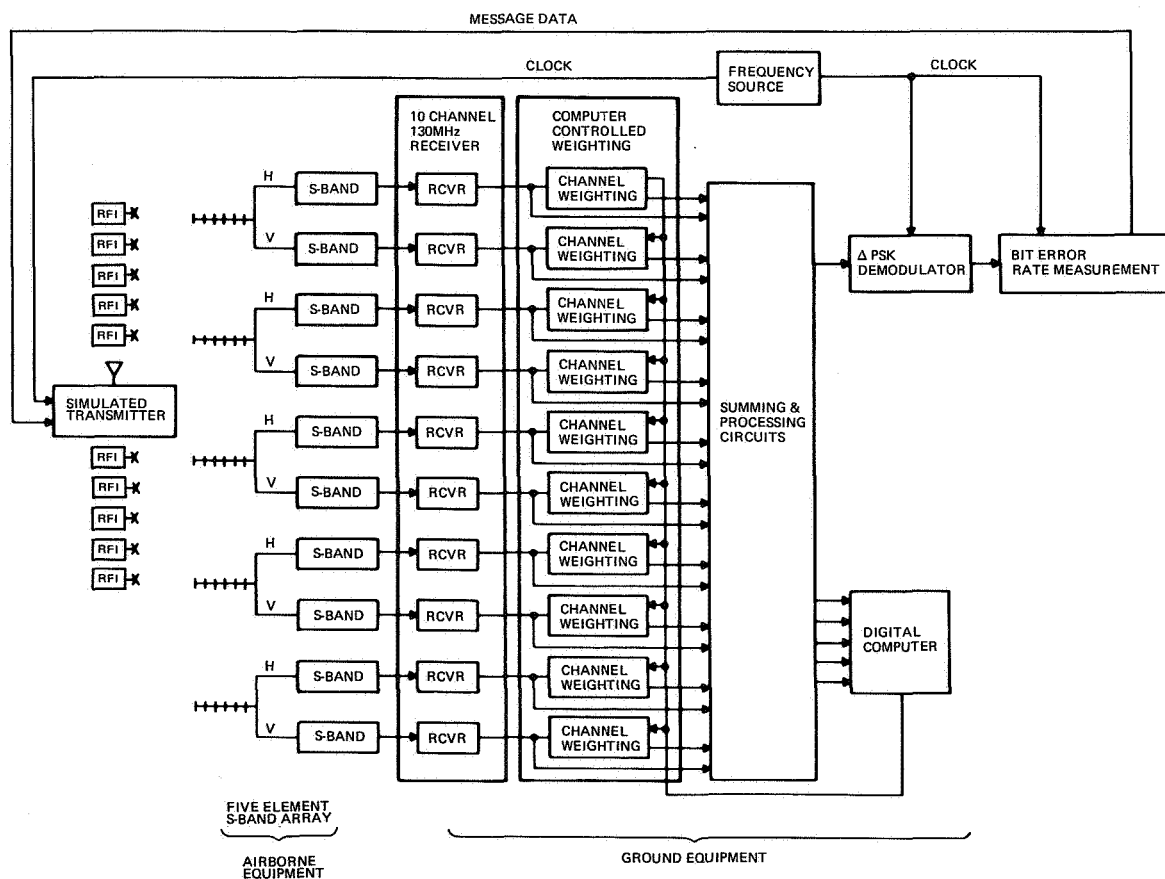


Figure 4. Simulated AGIPA system.

thus connected directly to an S-band front end which translates the received spectrum to the 137 MHz VHF operating frequency. Thus, all the RF processing circuits are implemented at the TDRS design frequency so that the circuit parameters are directly transferable to actual TDRS requirements.

The GS processing consists of weighting the amplitude and phase of each of the ten array channels, so that the beam formed adaptively places the RFI signals in nulls, and the desired signal near or on the peak of the beam depending on the condition which optimizes S/RFI. The 10 input channels are summed and the desired sum signal and the interference sum signals are separated. In parallel with the summing process, the desired signal and interference signals from the individual input channels are also identified and separated. The resultant desired and interference signals from the sum and individual channels are correlated, and the correlator outputs are used to compute the proper amplitude weighting and phase adjustments for the beam steering and shaping network. The proper values and direction of correction to be applied to the amplitude weighting and phase adjustment network are made in a computer. This is programmed to make iterative changes until the resultant sum signal-to-interference ratio has been maximized. The adaptive signal processor utilizes amplitude and phase, as well as polarization information from the desired and interference signals, to effectively point the major lobe of the array pattern to the desired signal; it is simultaneously putting a null on the interference signals. To accomplish this, however, the desired signal need not always be on the peak or near the peak of the major lobe in order to maximize the signal-to-interference ratio, but may frequently be well off the peak.

Testing performed using the simulation equipment has demonstrated that a good correlation exists between predicted and actual results. Figure 5 illustrates the optimization achieved for a typical scenario of the Atlantic region. The peak of the antenna beam can be seen pointing near the spacecraft position, with the majority of interfering sources located at or near nulls in the antenna beam. Improvements in low data rate performance using this technique have ranged up to approximately 15 dB. As a result of this demonstrated performance, the AGIPA concept has been incorporated as part of the design baseline for TDRS Phase B study program which is presently in progress.



$\Delta\text{SIR} = +11.7 \text{ dB}$

Figure 5. Optimization, typical scenario, Atlantic region.

percent of the drive signal to the telescope instantaneously, thus aiding in the high frequency response of the telescope and minimizing the effects of static friction in the bearings.

The second type of compensation is the conventional type, termed closed-loop compensation. Its primary function is to minimize the effects of disturbances such as wind gusts.

The third type of compensation, termed adaptive compensation, differs from conventional closed-loop compensation in that it incorporates self-learning or self-adjusting features; namely, self-adjusting parameters which track out unwanted parameter variations in the telescope. Adaptive compensation provides the precise input – the adaptive input – to compensate for these variations.

The goal of adaptive compensation is to force the adaptive error to zero, thus forcing the axis velocity to follow or track the ideal velocity. The ideal velocity is generated as the output of the model reference system, embodying the ideal or nominal characteristics of the telescope dynamics. Adaptive compensation is based on advanced control-theory techniques, namely, Liapunov stability theory. As far as we know, adaptive compensation has previously received application only in autopilots.

The next two figures summarize the field tests which were conducted on a tracking telescope made available at the Goddard optical site.

The command velocity for this test run (Figure 2) embodies the characteristics of a satellite in a 1000-kilometer orbit with a command rate varying from zero degrees per second on the horizon to 1.5 degrees per second directly overhead. The conventional system position error – the difference between the command velocity and the command

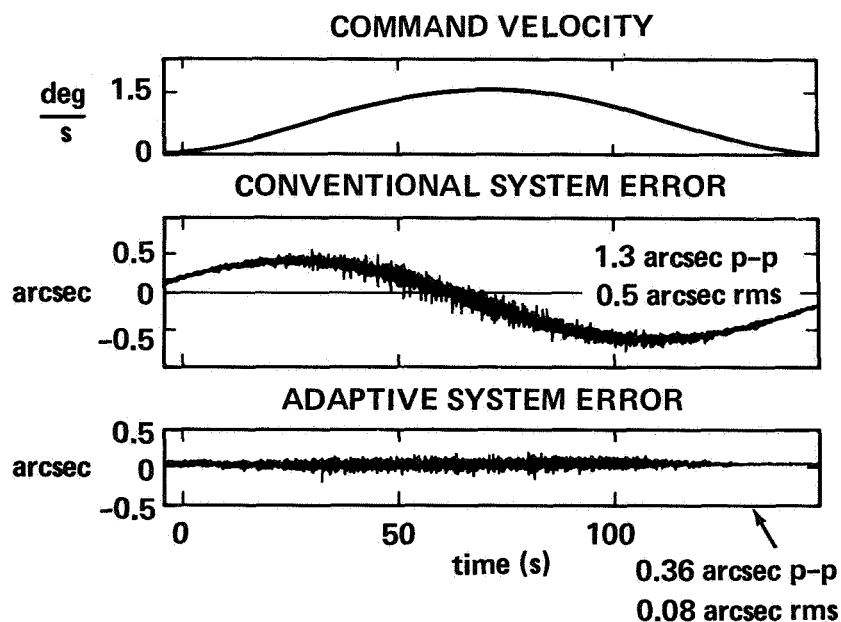


Figure 2. Tracking a satellite in a 1000-km orbit.

position — resulted from utilization of the control system presently in use, and yields a peak-to-peak error of 1.3 second of arc or an rms error of 0.5 second of arc. The peaks in error occur at the points of maximum acceleration of the command velocity.

The adaptive system error, on the other hand, utilized in conjunction with the other forms of compensation, yields a peak-to-peak error of 0.36 second of arc, and an rms error of 0.08 of a second of arc, which represents more than a factor of six reduction in rms pointing error.

Furthermore, one can easily see that the low-frequency components of the error which were present in the conventional system design have been completely eliminated. The blurred signal which remains if spread out in time would indicate a nine- to ten-cycle resonance, which is precisely the structural resonance of the Y-axis, which has to be considered a fundamental limit in any control system design.

The same kinds of data are shown in Figure 3 for a command velocity which embodied the characteristics of what would be considered a worst-case satellite for an X-Y configuration. This is a satellite in an 80-kilometer orbit passing directly overhead. The entire pass is completed in a time period of less than two minutes; the command rate varies from zero degrees per second on the horizon to three degrees per second directly overhead.

In this example, the conventional system yields a larger peak-to-peak error, namely 3.6 seconds of arc; and an rms error of 1.3 second of arc. The combined compensation approach, utilizing the adaptive system, on the other hand, again completely tracks out the low-frequency error and yields a peak-to-peak error of 0.7 of a second of arc; and an rms error of 0.2 second of arc. This is again a reduction by more than a factor of six.

In summary, then, a model-referenced parameter adaptive control system, as it is correctly termed, has been utilized in conjunction with more traditional forms of compensation, in order to achieve a reduction of rms pointing error by more than a factor of six.

MEMBER OF THE AUDIENCE:

It appears that the adaptive errors are entirely very low frequency compared with any system resonance. Is that a fundamental limitation?

DR. GILBART:

Well, are you referring to the resonance which existed on the adaptive system, the high-frequency signal?

MEMBER OF THE AUDIENCE:

No, I'm referring to the fact that in all cases it was the low-frequency components that you are removing by the use of the adaptive procedure.

DR. GILBART:

Yes, it will actually compensate for higher frequency errors. In this case, the only contribution to the error in the conventional system design was a low frequency error signal, plus a very high frequency error signal, namely, the nine- to ten-cycle per second resonance.

If the mount was an Az-El configuration and the satellite was overhead, there would be higher frequency components, and these components would be tracked out as well. But the nine- to ten-cycle oscillation represents a limit that cannot be corrected – to compensate for that resonance, higher frequency signals would have to be provided, but those signals would only drive the mount into further resonance.

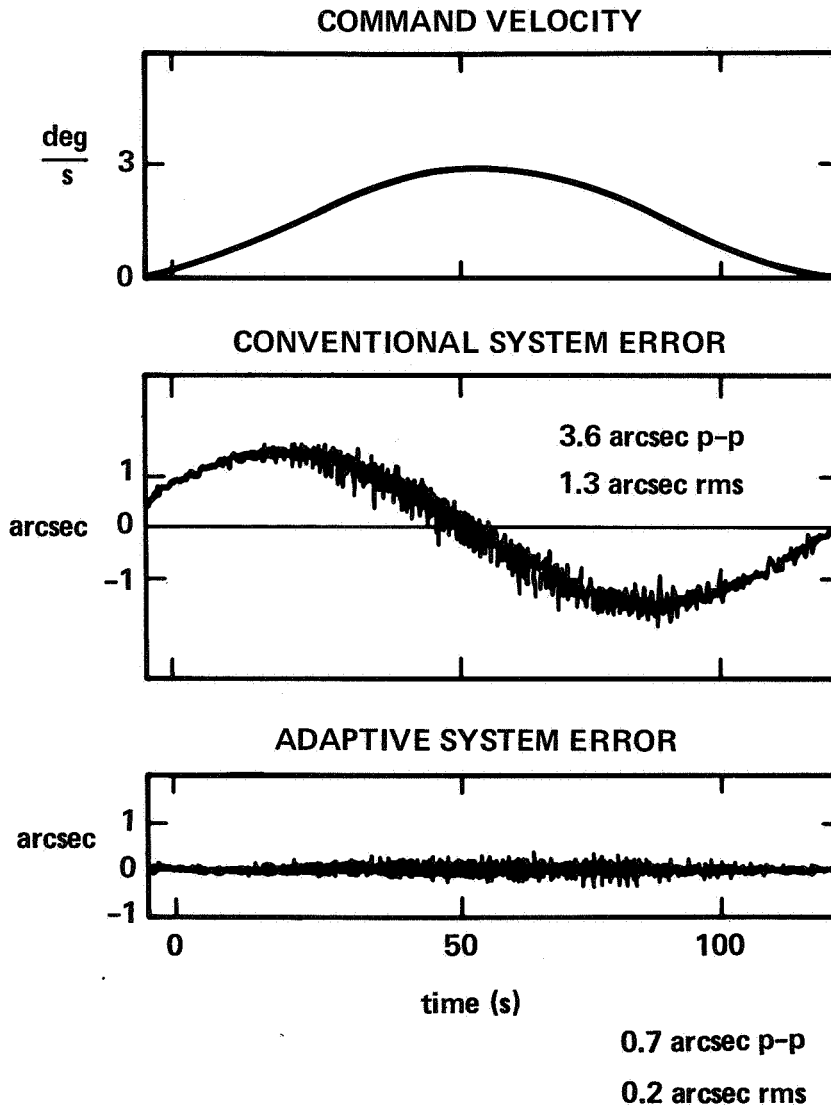


Figure 3. Tracking worst-case satellite.

HIGH EFFICIENCY GROUND DATA TRANSMISSION

William B. Dickinson

In the past, data transmission throughout the NASCOM Network (Figure 1) had been limited to 2400 bits per second per voice bandwidth channel.

This limitation was due to, first, incomplete understanding of the transmission characteristics of the international leased voiceband circuit, and second, overly conservative communication technology in the design of data modulators/demodulators (or modems).

Given that the bandwidth of these voiceband channels is about 2700 Hz, the bandwidth efficiency was only one bit per second per Hz bandwidth. There were two things that motivated us to achieve a higher efficiency, namely: cost effectiveness on expensive international circuits and a real need for higher data rates for support of GSFC spacecraft and the Skylab.

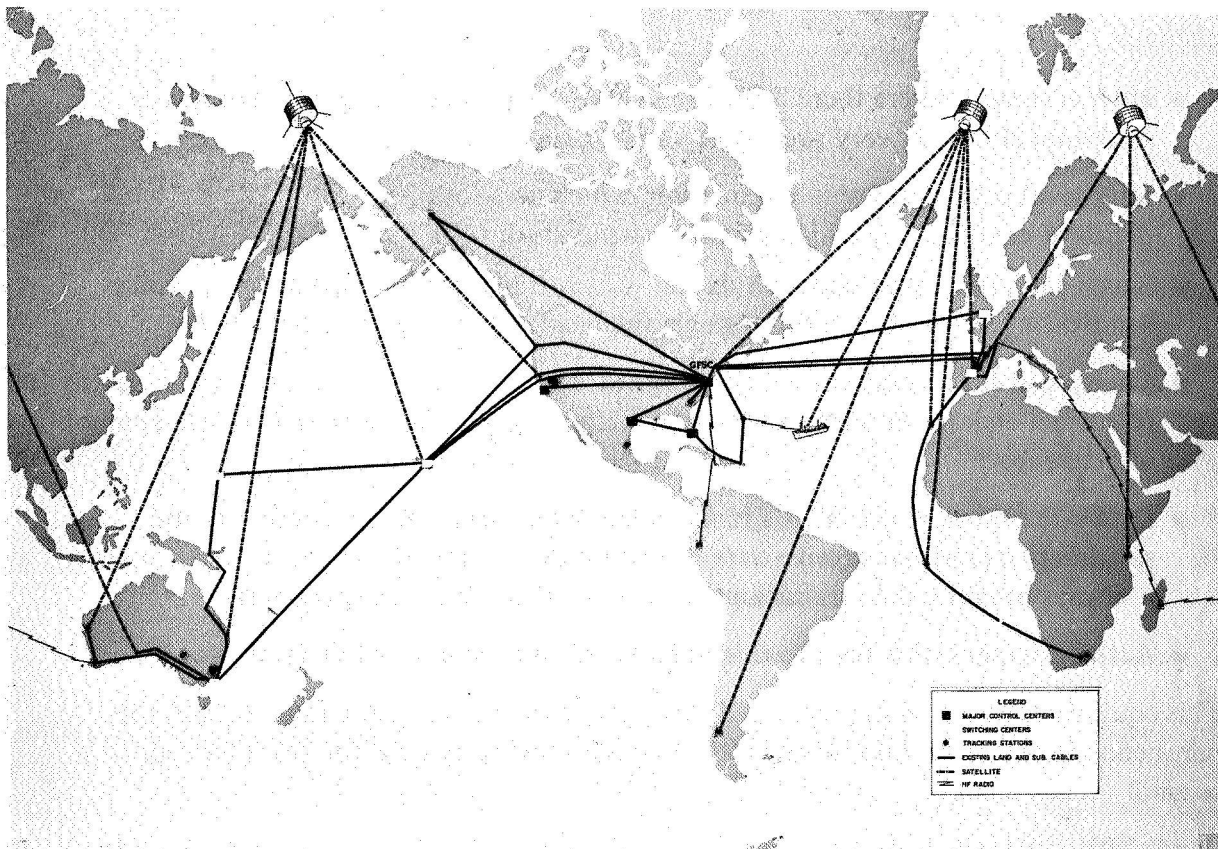


Figure 1. NASCOM network trunking plan.

Recognizing the problem of increasing the voiceband data efficiency, the following approach was taken (Figure 2):

- Initially a program of channel measurement and characterization was instituted
 - Width – Amplitude versus frequency response and delay versus frequency response
 - Depth – Random noise, impulse noise, and amplitude linearity
 - Stability – Incidental modulation (amplitude and angle) signals levels
- Established limits for new parameters and reconfirmed certain existing limits which could be realistically maintained
- Tested various modulation techniques – amplitude, angle (phase modulation, PM mostly)
- Selected the optimum equipment technology
- Implemented and verified performance

Data modem characteristics (Figure 3) determined to be either essential or optimum that is, the best compromise of efficiency and performance for international voice bandwidth channels are:

- High accuracy, where there is precise knowledge of rate in receiver, and where optimum clock recovery procedure can be used
- Multilevel pulse amplitude modulation, which uses four levels, two bits per level, depth of channel, and which conserves bandwidth
- Single-sideband amplitude modulation, which translates data spectrum to voice bandwidth, efficient because of single sideband, and not double sideband
- Transversal filter equalizer, which is an automatic and continuously adaptive device to correct channel amplitude and delay distortion, thereby eliminating intersymbol interference
- Data scrambling, which adds a random-like bit sequence to the send data and subtracts it from the receive data to restore the original data stream. In between it always provides data transitions for the equalizer and timing recovery
- Active compensation for phase instability, transmission of a low level pilot tone

This equipment has been implemented throughout the network at a rate of 7200 bits per second in the same voice bandwidth channels previously used for 2400 bits per second.

Bandwidth efficiency is about 3:1 versus the previous 1:1; the level of performance is fully acceptable for all network operations.

It has been demonstrated that state-of-the-art communications technology can be implemented and reliably operated on a global basis and NASCOM is currently the only network now doing this. We are currently pursuing the same line of investigation to increase the transmission rates and efficiencies on circuits with bandwidths greater than the typical speech channel.

- CHARACTERIZE INTERNATIONAL CHANNEL
WIDTH
DEPTH
TIME STABILITY
- ESTABLISH MAINTENANCE LIMITS
- TEST AND EVALUATE MODULATION/DEMODULATION
AND CODING TECHNIQUES
- SELECT OPTIMUM EQUIPMENT TECHNOLOGY
- IMPLEMENT AND VERIFY PERFORMANCE

Figure 2. Increase voiceband data efficiency.

- HIGHLY ACCURATE/STABLE DATA RATES ($\pm 1 \times 10^{-5}$)
- MULTI-LEVEL PAM (4-LEVELS)
- SINGLE-SIDEBAND AM
- TRANSVERSAL FILTER (TIME DOMAIN) EQUALIZER
- DATA SCRAMBLING FOR TRANSPARENCY AND
CLOCK RECOVERY
- ACTIVE COMPENSATION FOR CHANNEL PHASE
INSTABILITY

Figure 3. Data modem features.

VERY LONG BASELINE INTERFEROMETRY

Irving M. Salzberg

The area of technology involved in this presentation is the metric tracking of remotely located vehicles with earthbound tracking devices. In particular this discussion will present the new technology of determining the distance between two vehicles located on the surface of the moon, while one vehicle is in motion with respect to the other.

Figure 1 defines the problem more precisely and shows both the geometric situation and the hardware used to gather and reduce the data. The tracking objective is to determine the distance "D" between the Lunar Rover Vehicle (LRV) (depicted as radio frequency source 1) and the stationary Lunar Module (LM) (radio source 2) as the Rover moves about on the lunar surface.

This is accomplished by simultaneously receiving both monochromatic radio signal emissions at each of two separated earth receiving stations. These stations collect N-count Doppler data on each source and then transmit this data to a central processing facility. At the central processing facility, the Doppler data from both sites on source 1 is used in an algorithm which essentially differences the Doppler to compute $\dot{\theta}_1$; $\dot{\theta}_2$ is similarly determined. The difference between these angular rates is then computed and geometry provides \dot{D} in the plane of the presentation screen. If a third site is used, \dot{D} in two dimensions can be calculated. Thus it is possible to determine the motion of the lunar rover vehicle with respect to the LM in two selenographic directions. If we have an initial position or epic location for the LRV, it is possible to integrate the rate data and determine distance. Goddard Unified S-band stations with dual tracking capability have been used to gather double differential very long baseline interferometry (DDVLBI) data on Apollo-16 and Apollo-17.

This technique has some delightful properties which enhance its accuracy beyond that expected when computing the normal VLBI or single difference $\dot{\theta}$ measurement. Since a double differencing of the Doppler raw observable occurs in the algorithm to obtain \dot{D} , systematic or environmental errors common to both sources or both sites cancel at least to the first order. Thus effects that we have difficulty in accurately modeling, such as ionospherics, motion of the moon, distance between tracking sites, and differences in frequency standards all tend to cancel, yielding surprisingly accurate results. Therefore precise VLBI angular rate measurements to determine the rate of change in distance between two remote monochromatic sources is theoretically attractive and, from a hardware point of view, completely practical.

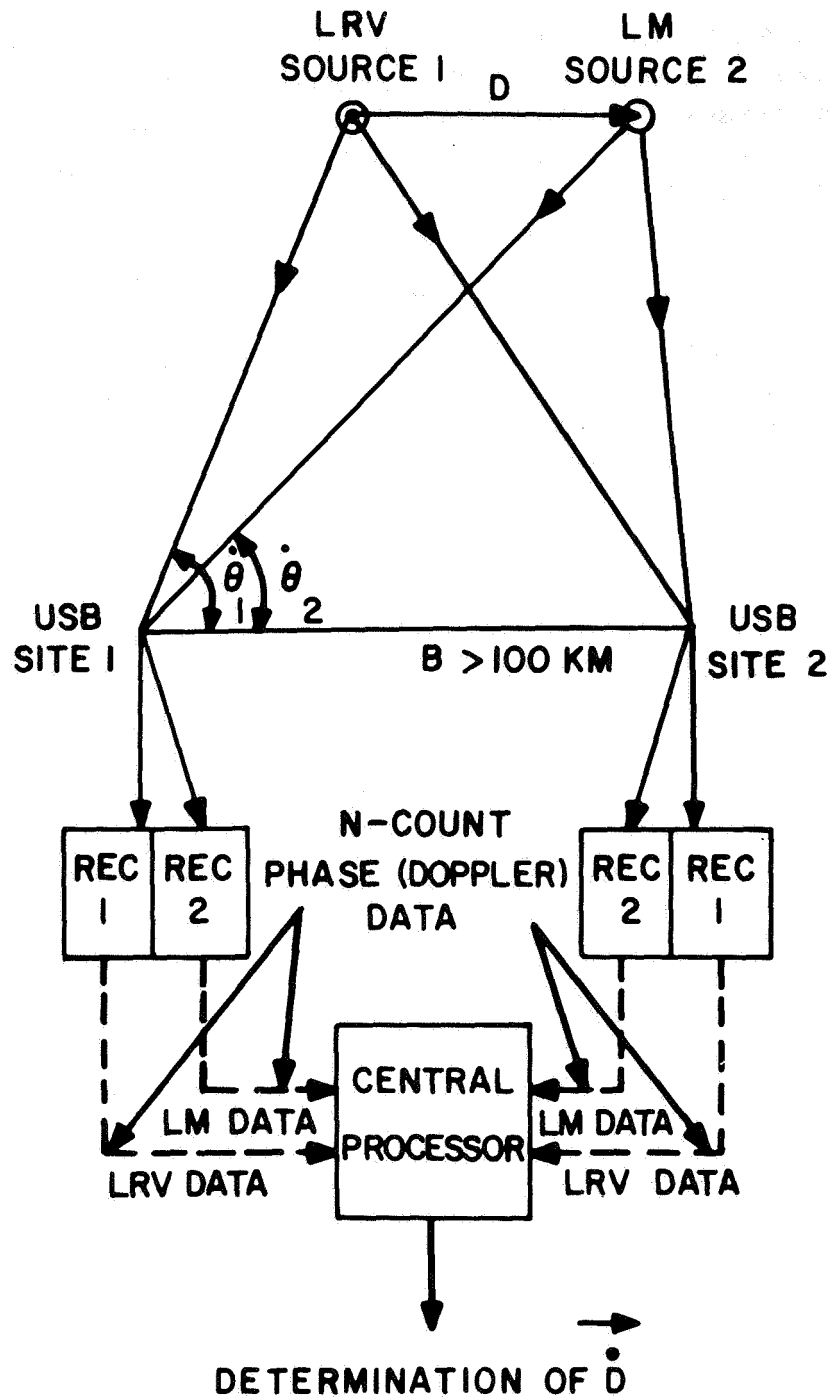


Figure 1. Double difference monochromatic VLBI.

We have now defined the tracking objective and outlined the software and hardware technology required for its solution. Let's go on to the results obtained when DDVLBI tracking was actually accomplished during the Apollo-16 mission.

Figure 2 depicts, as a function of time, the pertinent events of the LRV traverse for Apollo-16 EVA 1. The traverse commenced at 20 hours, 50 minutes, 40 seconds on April 21, 1972. The epic selenographic location of the LRV was approximately 84 meters south and 54 meters west of the LM. Madrid, Ascension, and Merritt Island dual USB stations were tracking the LRV and LM at this time when the LRV transmitter was switched to the monochromatic transmission mode. Within seconds the LRV departed from the LM, heading towards Plum Crater. Arriving at Plum Crater, the LRV transmitter was switched from the monochromatic transmission mode and was not reconfigured until seconds prior to the LRV's departure from Plum Crater heading towards Spook Crater. After a 25-minute stay at Spook Crater the LRV returned to the LM and parked approximately three meters from it. Redundant Goldstone data was available for the second and third portions of the traverse. The darkened boxes shown in the first and third traverse portions are of particular significance. During these periods the LRV was stationary and DDVLBI data was available.

Summarizing the statistics of these two periods, we find that noise on the determined North-South, East-West lunar separation distance never exceeded one meter (Figure 3). DDVLBI data did indicate, however, that the LRV was moving at about 15 mm/sec when in actuality it was motionless with respect to the LM. This difficulty is attributed to systematic drifts in the hardware between receivers at one site. Hardware improvements were implemented for Apollo-17 to reduce this drift.

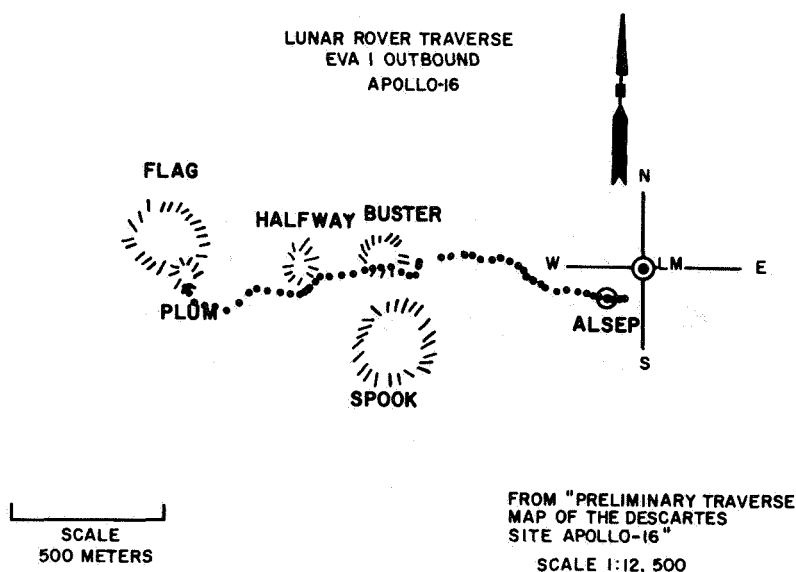


Figure 2. EVA 1, Apollo-16

Integrating angular data every 20 seconds starting from the provided epic position yields the results shown in Figure 4 for portion one of the traverse. Similar results are available for the return trip which place the computed parked position of the LRV approximately ten meters from the position indicated by the astronauts.

	<u>BIAS (DRIFT) (MM/S)</u>	<u>NOISE (METERS)</u>
21:06:40 TO 21:12:40		
N-S	-8	0.98
E-W	-12	0.42
22:55:00 TO 23:01:40		
N-S	-9	0.67
E-W	-2	0.58

Figure 3. Noise and bias of DDVLBI data.

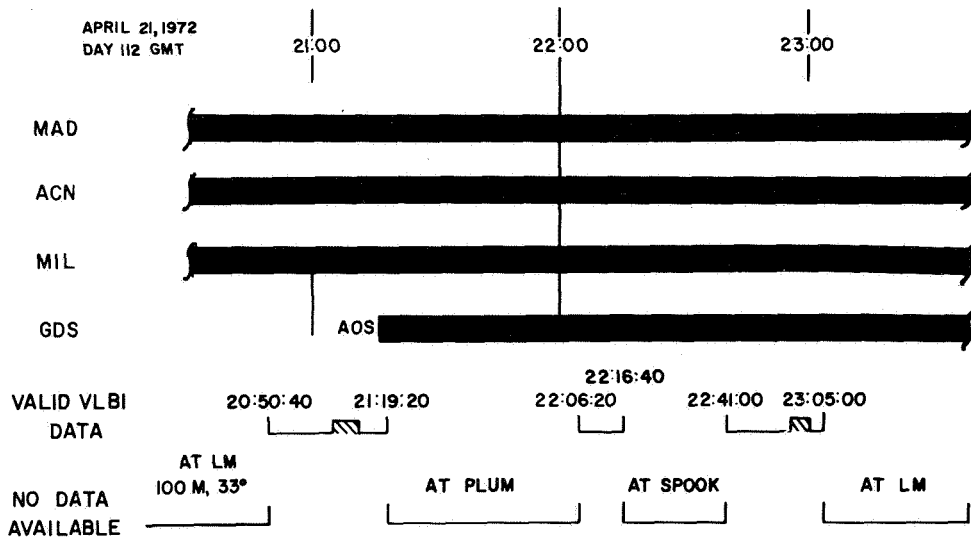


Figure 4. Events and time line for traverse of EVA 1, Apollo-16.

Based upon the nature and size of the drift rates, noise, and closure figures, a conservative estimate of the LRV position error when using DDVLBI computation techniques is 25 meters with noise of less than one meter (Figure 5). This technology was used on Apollo-17 to aid lunar scientists in reconstructing the path taken by the astronauts in the LRV for all three EVA's. It is felt that with minor hardware modifications DDVLBI tracking has direct application in more precisely defining lunar librations and may also have direct application in determining precise distances between mother-daughter class satellites.

TECHNOLOGY AREA: EARTH-BASED TRACKING AND POSITION DETERMINATION OF SPACE VEHICLES

PROBLEM: ACCURATELY DETERMINE THE DISTANCE BETWEEN THE LUNAR ROVER VEHICLE (LRV) AND THE LUNAR MODULE (LM) WHILE THE LRV IS IN MOTION FOR SUPPORT OF APOLLO LUNAR RESEARCH.

NEW TECHNOLOGY: DEVELOPMENT OF DOUBLE DIFFERENCED VLBI.

RESULTS: APOLLO-16 LRV TRACKED ON THE MOON TO AN ACCURACY OF 25 METERS WITH NOISE OF LESS THAN 1 METER, DRIFT BIASES OF 15 mm/S.

POTENTIAL UTILIZATION OF NEW TECHNOLOGY: LUNAR LIBRATION STUDIES, PRECISE MOTHER-DAUGHTER SATELLITE TRACKING.

Figure 5. Summary.

RESULTS OF MARINER MARS TRACKING CALIBRATION EXPERIMENT

James W. Ryan

I would like to describe the Mariner-Mars 1971/USB Tracking Calibration Experiment – an experiment in which the Networks Directorate succeeded in using the Apollo Unified S-Band Tracking Network as a tool for determining very high accuracy geodetic parameters.

Early in 1970 the Networks Directorate was faced with the problem of determining center-of-mass station coordinates for the Apollo tracking sites which would be accurate to the ten-meter level. The site coordinate set in use at that time both at Goddard and at the Manned Spacecraft Center was derived from in-depth analysis of the S-Band Doppler data from the early Apollo missions. These coordinates had an associated uncertainty of 50 meters. At that time in 1970 we realized that the further analysis of Apollo data would not lead to ten-meter accuracy coordinates; different, more powerful techniques were required.

The Jet Propulsion Laboratory had used planetary transfer and encounter Doppler tracking data to determine ten-meter accuracy coordinates for the sites of the Deep Space Network. This fact, plus the realization that there was to be a mission to Mars in 1971 with a USB compatible transponder, led us to plan and carry out what came to be known as the MM71/USB Tracking and Calibration Experiment.

The experiment consisted of five tracking periods in which all USB sites tracked Mariner-9 in the three-way Doppler mode: These sites did not radiate the spacecraft, but only tracked the returning signal. The first tracking period began at launch and lasted ten days. The remaining four periods lasted five days each; one in July, two in October, and one in November after the spacecraft had achieved orbit about Mars. In total, well over 2000 hours of station contact time was logged.

In the experiment design phase we carried out error analysis which simulated accurately the type and amount of tracking data which we expected to receive. It also simulated the characteristics of the unmodeled systematic and environmental effects, and the statistical scheme to be used to reduce the data. This error analysis predicted that the resulting geodetic parameters should be in error by no more than five meters.

The reduction of the actual experiment data has proceeded in two phases. The first phase was, so to speak, “quick and dirty,” and was completed last December – less than one month after the end of the final tracking period. The geodetic parameters which resulted from this preliminary data reduction were used at MSC to support Apollo-16 and Apollo-17.

This first-cut reduction, because of the speed with which it had to be completed, was not as thoroughgoing as the reduction which was simulated in the prelaunch error analysis. As a result, we could expect up to 15-meters error in the recovered station coordinates. This increased error budget was almost entirely caused by our lack of an ionospheric correction scheme. The final processing is now in progress and is being carried out in accordance with the prelaunch error analysis; in particular it involves sophisticated ionospheric modeling scheme.

I would like to describe some of the characteristics of the set of geodetic coordinates which we recovered in the preliminary data reduction.

We recovered longitude and distance of the earth's spin axis. We did not recover z-height, that is, distance north or south of the earth's equatorial plane. Deep space Doppler data is nearly insensitive to errors in z-height.

Using no a priori constants, we determined the geodetic parameters for all USB sites, both 9- and 28-meter (30 and 85 ft) sites. However, the coordinates of the 28-meter sites were known a priori with an accuracy of five-meters based on the coordinates of the colocated Deep Space Network sites. Figure 1 shows the differences between the Mariner recovered values in the 28-meter site parameters and the values of those parameters based on the DSN positions. The longitude agreement is outstanding. The spin axis discrepancies are within our predicted 15-meter error bound, and moreover they are in the direction indicated by the lack of an ionospheric model. These results suggest strongly that the 15-meter error bound is realistic.

Figure 2 shows the differences between the Mariner recovered parameters for the USB nine-meter sites and the values of those parameters used to support Apollo-14. One overriding conclusion can be drawn: The results of this preliminary data reduction have provided significant improvements to the USB geodetic parameters.

We have been able to compare the Mariner values of longitude and distance of spin axis for the nine-meter sites, with the same parameters derived from the GSFC 71 Geodetic Set. This coordinate set is a worldwide, center-of-mass network of geodetic positions determined at Goddard by Marsh, Douglas, and Klasko. The parameters are based on optical and laser observations of the GEOS satellites. The Mariner results and the GSFC 71 Set agree to

SITE	LONGITUDE DIFFERENCE (METERS)	SPIN AXIS DISTANCE DIFFERENCE (METERS)
GOLDSTONE, CALIF.	0	-12
MADRID, SPAIN	0	- 6
HONEYSUCKLE CREEK, AUSTRALIA	-3	+ 2

Figure 1. USB 28-meter prime sites geodetic differences (MM71 T and CE preliminary set less JPL location set 25).

SITE	LONGITUDE DIFFERENCE (METERS)	SPIN AXIS DISTANCE DIFFERENCE (METERS)
MERRITT ISLAND, FLA.	+33	-32
GREENBELT, MD.	+22	-60
BERMUDA	+64	-35
GRAND CANARY ISLAND	-6	+5
ASCENSION ISLAND	+27	+5
CARNARVON, AUST.	-22	+18
GUAM	+50	-29
KAUAI ISLAND, HAWAII	+4	0
CORPUS CHRISTI, TEXAS	+24	+17

Figure 2. USB 9-meter site geodetic differences (T and CE values less Apollo-14 values).

within ten meters rms. This is important, since the Mariner and GEOS results are based on very different techniques. The first is based on Doppler tracking of a spacecraft in deep space and is totally uncorrelated with the earth's gravity; the second is based on angle and ranging data of spacecraft in earth orbit and is closely tied to the earth's gravity. The two techniques now appear to be converging on the same world.

To sum up – what we have achieved so far?

One, our preliminary results have provided geodetic parameters with an accuracy of 15 meters for use in Apollo-16 and -17. Two, these preliminary results are in rather good agreement with the GSFC 71 Set. And three, we are on schedule with the final data reduction and expect to have five-meter-accuracy site coordinates by next spring.

I think we have established, as Figure 3 indicates, that USB Doppler data can provide geodetic information with accuracies comparable to those produced by laser ranging.

**PROBLEM: DETERMINE GEODETIC PARAMETERS OF STDN USB SITES
TO FIVE-METER ACCURACY FOR APOLLO AND SKYLAB PROGRAMS**

**SOLUTION: ALL STDN USB STATIONS TRACK MARINER-9 IN DEEP SPACE
IN THREE-WAY DOPPLER MODE; USE THIS DOPPLER DATA TO
DETERMINE GEODETIC PARAMETERS**

**RESULTS: PRELIMINARY RESULTS PROVIDE GEODETIC PARAMETERS WITH
AN UNCERTAINTY OF 15 METERS FOR USE IN APOLLO-16**

**PRELIMINARY RESULTS AGREE TO WITHIN TEN-METERS OF THE GSFC
1971 GEODETIC SET**

FIVE-METER ACCURACY ANTICIPATED BY SPRING 1973

NEW TECHNOLOGY:

**ESTABLISH THAT USB DOPPLER DATA PROVIDES GEODETIC RESULTS
WITH ACCURACIES COMPARABLE TO LASER RANGING DATA**

Figure 3. Mariner-Mars 1971, unified S-band tracking and calibration experiment.

**THE CALCULATION OF EFFICIENT HIGH PRECISION ORBITS
BY OPTIMUM MATCHING OF THE FORMULATION
AND NUMERICAL INTEGRATOR**

Carmelo E. Velez

The objective of this research was to find improved computer algorithms to compute orbits, i.e., orbital trajectories, and the improvements we were seeking were in the areas of either efficiency or accuracy. The goals of this work, as well as some applications, are outlined in Figure 1.

For example, we'd like to increase the speed at which we can compute an orbital path, at a given accuracy level, or we'd like to increase the maximum accuracy levels we can currently achieve with our present technology. We'd expect this type of research to have direct applications in the areas of operational orbit determination in an environment where we routinely compute the trajectories of 30 or 40 satellites for the purposes of maintaining tracking or reducing experimental data. A more efficient algorithm could lead to significant reductions in the amount of computer time used for this operation. As to applications in the area of satellite geodesy, as you know we are in the process of trying to reduce very high precision tracking data such as laser data or very long baseline interferometry. Therefore, we'd like to improve the maximum accuracy level that we can achieve from the algorithms we now have. And finally, in the mission planning area, typical computer programs which perform mission planning operations (such as lifetime studies or maneuver analysis) go through the process of computing orbits over many resolutions; and as a result take up a considerable amount of computer time. We would expect a more efficient algorithm to improve this operation also.

- **RESEARCH GOAL**

- TO DEVELOP EFFICIENT, HIGH ACCURACY ORBIT COMPUTATION PROCESSES FOR EARTH SATELLITES BY OPTIMUM SELECTION OF THE ANALYTICAL FORMULATION AND INTEGRATION METHOD
- AN OPTIMUM METHOD MINIMIZES THE NUMBER OF PERTURBATIVE ACCELERATION COMPUTATIONS FOR A GIVEN ACCURACY

- **APPLICATIONS**

- OPERATIONAL ORBIT DETERMINATION
- SATELLITE GEODESY
- MISSION PLANNING

Figure 1. Calculation of precision satellite orbits with nonsingular elements.

The approach we are taking is trying to find an optimum matching of formulation, that is, equations which describe the motion of an artificial satellite, and the numerical process by which we solve these equations.

Figure 2 shows an example of what we are talking about. The top equation is the equation of motion of a satellite in the classical form. This is the typical form that you find in most computer programs existing today.

The second equation is a new equation that we're trying to calibrate against the first one. This particular equation is consistent with the first in that they both describe the motion of the satellite. The second equation, though, is especially "tuned" for specific types of satellites. In particular, it is suited for satellite of the geosynchronous type; or satellites which have a low eccentricity inclination, such as many of the geodetic satellites.

During the course of our research, we coupled these two formulations with optimum numerical methods, and performed experiments to see what happened in terms of overall accuracy and efficiency.

Figure 3 indicates some of the results of the experiments we performed. First of all, note that we're plotting error against cost. The number of function evaluations is directly proportional to computer time. So you can see that as more computer time is used the errors decrease. And you can also see that the curves level off, which means that we do achieve a maximum accuracy boundary at a certain point.

The dotted lines represent the results of the computation of an orbit of the synchronous type, for 28 revolutions over all cost and accuracy ranges. And we can see that over the total accuracy spectrum — from a kilometer accuracy down to a centimeter accuracy — the curve representing the new method (the dots) performed significantly better than the classical method.

$$\text{I COWELL: } \ddot{\vec{x}} = \frac{-\mu\vec{x}}{|\vec{x}|^3} + \vec{P}(t, \vec{x})$$

II VARIATION OF PARAMETER (GAUSSIAN FORM):

$$\dot{\vec{\alpha}} = \frac{\partial \vec{\alpha}}{\partial t} + \frac{\partial \vec{\alpha}}{\partial \vec{x}} \cdot \vec{P}(t, \vec{x})$$

WHERE $\vec{\alpha}$ IS A NON-SINGULAR SET OF ORBITAL ELEMENTS, e.g. EQUINOCTIAL

$$a \qquad p = \tan \frac{i}{2} \sin \Omega$$

$$h = e \sin (\omega + \Omega) \qquad q = \tan \frac{i}{2} \cos \Omega$$

$$k = e \cos (\omega + \Omega) \qquad \lambda = M + \omega + \Omega$$

(BROUCKE AND CEFOLA, 1972)

Figure 2. Formulations.

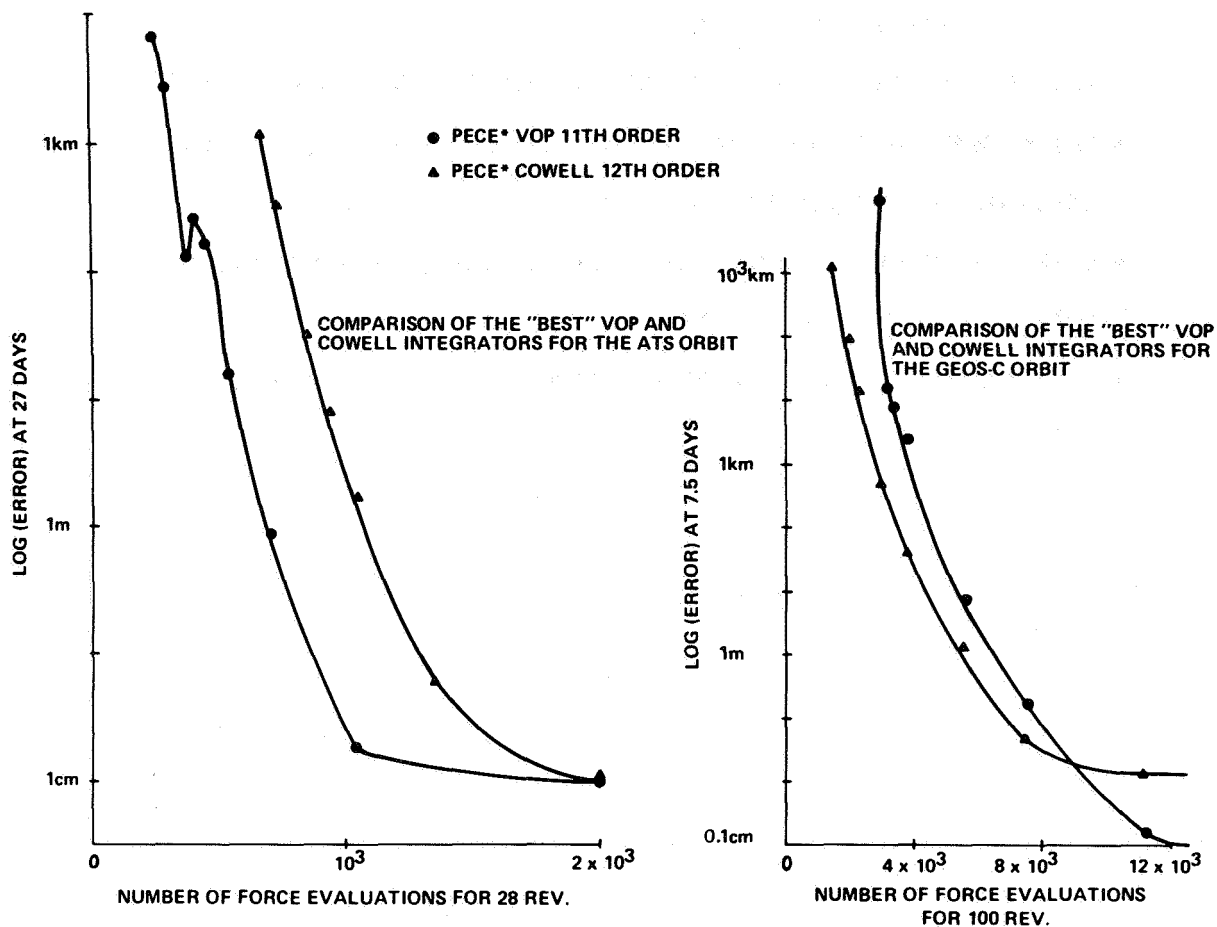


Figure 3. Comparison of the VOP and Cowell integrators.

This means that if you ask for a given accuracy anywhere between a kilometer and a centimeter, you are going to do better efficiency-wise with the new method.

On the other hand, we tried the same processes on a geodetic type orbit (a two-hour satellite, which is much closer). In this case we did not find any improvement using the "variation of parameter" (VOP) approach, as we are calling these new algorithms. But we did find this: that when you ask for very high accuracy down in the submeter region, the new method is able to achieve it, and the classical method is not.

And this was the significant result. We are saying that we can achieve accuracies that were not obtainable before by classical techniques.

Figure 4 shows some of the conclusions that we drew from this particular set of experiments: First, that there is no "best" method available for all accuracies for all orbits. And so we are developing a system to be responsive to that type of requirement. We are making them flexible so that we can use either a new orbit theory or a new numerical process to meet the particular problem at hand.

- NO "BEST METHOD" FOR ALL ORBITS AND ACCURACIES IS AVAILABLE
- PECE* VOP IS SUPERIOR (50%) OVER COWELL FOR GEOSYNCHRONOUS ORBITS
- PECE* COWELL IS SUPERIOR (10-20%) FOR CLOSE EARTH SATELLITES WITH LARGE GEOPOTENTIAL PERTURBATIONS
- STABILITY ANALYSIS INDICATES THE POSSIBILITY OF EXPLORING HIGHER ORDER INTEGRATION METHODS WITH VOP
- POSSIBILITY OF USING AVERAGED EQUATIONS FOR DEFINITIVE ORBIT DETERMINATION

Figure 4. Conclusions.

The new VOP method was superior to the classical method for the geosynchronous orbit. However, it wasn't so for the geodetic satellite, the two-hour satellite. However, again, it was able to achieve accuracies well below the classical boundary.

I also want to point out two byproducts. We discovered that from the stability analysis we performed, our warehouse of numerical methods didn't contain methods that would probably be optimum for this new formulation. So we are looking for new numerical methods that we feel will make the VOP formulation even more efficient.

And finally, this particular new formulation is amenable to numerical averaging, and we feel this can also lead to significant efficiency improvements.

ERTS ORBIT MAINTENANCE

Arthur J. Fuchs

The ERTS orbit maintenance problem arises from the requirements on the ERTS spacecraft to repeat its orbit every 18 days to within a tolerance of ± 18.5 kilometers for a one-year period, and to maintain the orbit in a sun-synchronous mode. In Figure 1 are the error sources that might cause the ground trace to drift outside of the tolerance bounds.

The ERTS requirements, particularly the ground trace requirement, are very sensitive to small errors in the orbit and the dynamic model. The first three items, uncertainty in orbit determination, orbit adjust performance errors, and dynamic model uncertainties, are very common. They give rise to errors in both knowing what the orbit is and in predicting the orbit drifts.

Let me dwell for a moment on the fourth item – the unmodeled errors. In designing an orbit maintenance procedure, we were concerned about a number of possible unmodeled errors, such as fuel leaks in the orbit adjust system, fuel leaks in the attitude control system, and uncoupled thrusts in the attitude control system. This last item turned out to be extremely important. One approach that we could have taken in maintaining the orbit was to choose the best dynamic model possible in the design of an orbit, that would satisfy the requirements for a one-year period, and to continually correct to this orbit if we drift outside our tolerances.

In light of the sensitivity of the requirements to small errors, we felt this procedure would require frequent corrections and we looked for another approach. In doing this we asked: Is there other information available that we may utilize? Another requirement that we have for the ERTS project is to determine the position of the spacecraft in its orbit very accurately for the ground data handling system, or specifically for the data processing facility. We made use of this information.

In Figure 2, the solid line on the lower portion of the curve represents the actual ground trace errors that the spacecraft experienced over the first $3\frac{1}{2}$ repeat cycles. We've modeled

- **UNCERTAINTY IN ORBIT DETERMINATION**
- **ORBIT-ADJUST SYSTEM PERFORMANCE ERRORS**
- **DYNAMIC MODEL UNCERTAINTIES**
- **UNMODELED ERRORS**

Figure 1. ERTS requirements error sources.

these ground trace errors in terms of some key parameters, namely the mean semi-major axis and inclination and their rates of change. We fit the actual data to our model in a least squares sense, and deduce from the data the initial offsets to these key parameters as well as their rates of change. We can then extrapolate forward analytically what the drift in the ground trace is going to be in the future.

As you can see from Figure 2, the ground trace error rapidly exceeded the 18.5 kilometer tolerance. The value of $da/dt = 2.79$ (times the nominal semi-major axis decay) is interesting. The nominal decay is based upon our model of atmospheric drag, solar pressure, and so on. The actual data tell us that the spacecraft is experiencing a decay almost three times this value. Although in implementing this procedure it is not necessary to know the cause of the increased rate of change, this can be examined a posteriori. We now know that this dynamic behavior is due to the spacecraft attitude control system thrusting on a regular basis. How can we use this information?

In Figure 3, the solid line on the left is the same ground trace error of Figure 2 drawn to a different scale. Recall that the tolerance on this error is ± 18.5 kilometers. We hypothesize that our best estimate of what the orbit is going to do in the future can be based on what

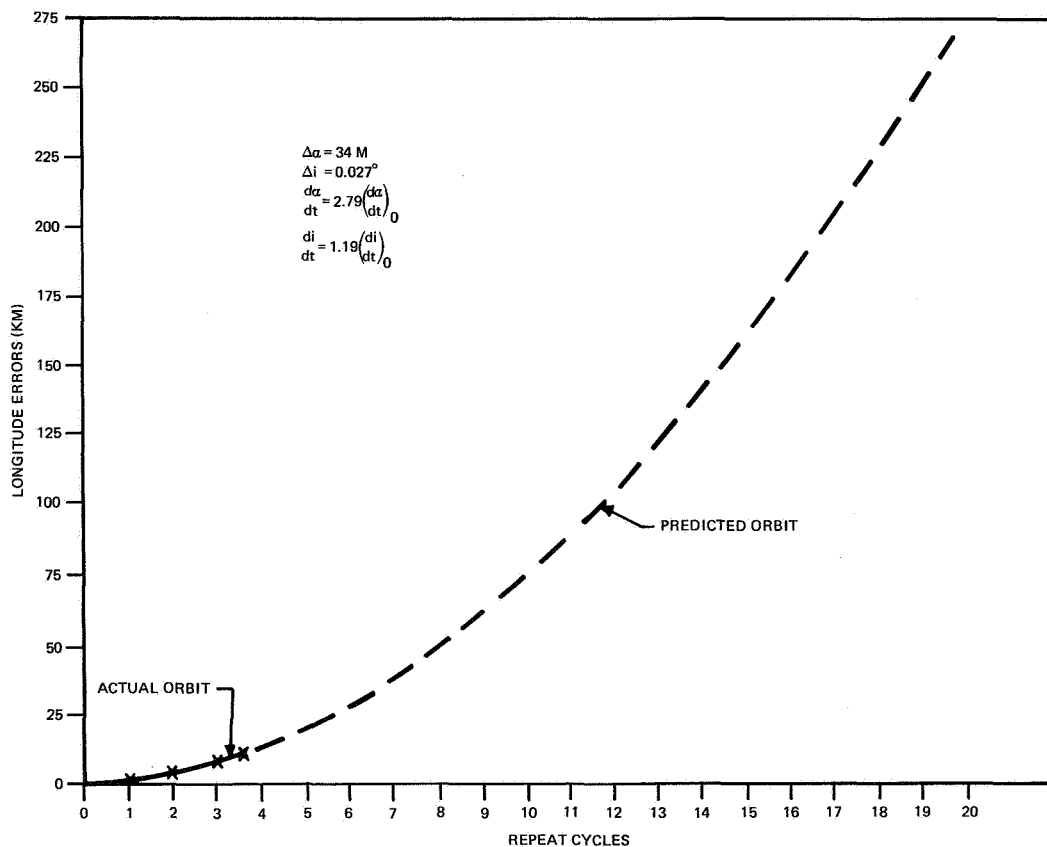


Figure 2. Orbit maintenance, least squares solution.

it has done in the past. By using the dynamic behavior determined over the actual part of the orbit, we can easily compute a correction to the orbit. This correction will reverse the error drift to keep our requirements within the ± 18.5 kilometer bounds. Approximately one month prior to the time when the ground trace would have exceeded the bounds, we notified the ERTS Project of the drift and decided on a time to make a maneuver.

The curve which is labeled “best-estimate orbit” is an extrapolation of this correction, using the dynamic behavior deduced from the actual data in our analytic model. The curved solid line represents actual data points that have been determined since the correction was made. As you can see, we’re tracking this curve very well. By implementing this procedure we feel that we can limit the frequency of corrections and the amount of fuel that we’ll have to use in maintaining the ERTS orbit.

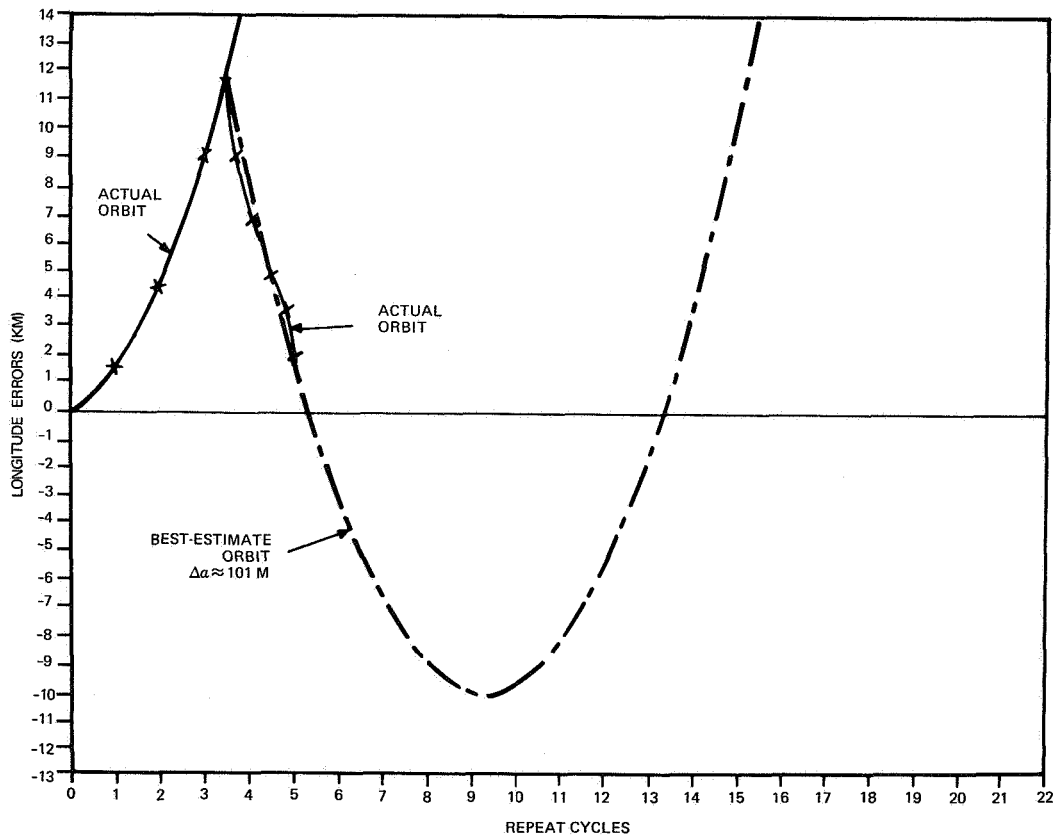


Figure 3. Actual and predicted ground trace history.

ATTITUDE COMPUTATION SYSTEM

Roger D. Werking

Over the past ten years, spacecraft mission requirements for attitude determination and attitude control have been increasing.

The types of attitude sensors from mission to mission are varied but may be broken into classes such as horizon detectors, sun sensors, magnetic field detectors, and star sensors. Likewise, the control systems vary from mission to mission but in general use gas thrusters or magnetics to perform spin axis precession. Because of the commonality of the basic attitude determination and control concepts, a broad base of experience can be carried from mission to mission.

The Attitude Determination Office was charged with the responsibility of attitude determination and control for a number of unmanned satellite mission. To meet these commitments, the use of large scale computers became a necessity.

However, the use of large scale, general purpose computers presents problems when used for attitude support activities.

Figure 1 presents the three major obstacles which had to be overcome:

1. NEED TO GET PERTINENT ATTITUDE DATA TO ATTITUDE COMPUTER.
2. NEED TO OPERATE WITH PROGRAMS IN AN INTERACTIVE ENVIRONMENT.
3. NEED FOR CENTRAL ATTITUDE SUPPORT AREA.

Figure 1. Problems faced using large scale computers for attitude support.

- Because the attitude determination functions require the processing of spacecraft telemetry data, it is necessary to get this data to the attitude computer in a timely manner. The use of printout is undesirable due to data volume: the use of magnetic tape requires the completion of an event (pass) before data can be transferred, thus limiting response time.

- In a batch processing environment, it is very difficult to satisfy a rapid response requirement for job submission via card decks, and for reviewing results via hard copy printout. This is even further complicated by the decision making processes which must be included in the various attitude programs which could be better handled by other techniques.
- Because of the general support nature of the computer environment, it is difficult to maintain a central point of contact between the various attitude related functions. The attitude activities for any mission are dynamic by nature and require the continuous updating of attitude results and attitude commands. The contact necessary to accomplish this type of support requires a central area of activity.

With the launch of SAS-1, an attitude computation system became a reality. Figure 2 depicts the important items which make up the attitude computation system.

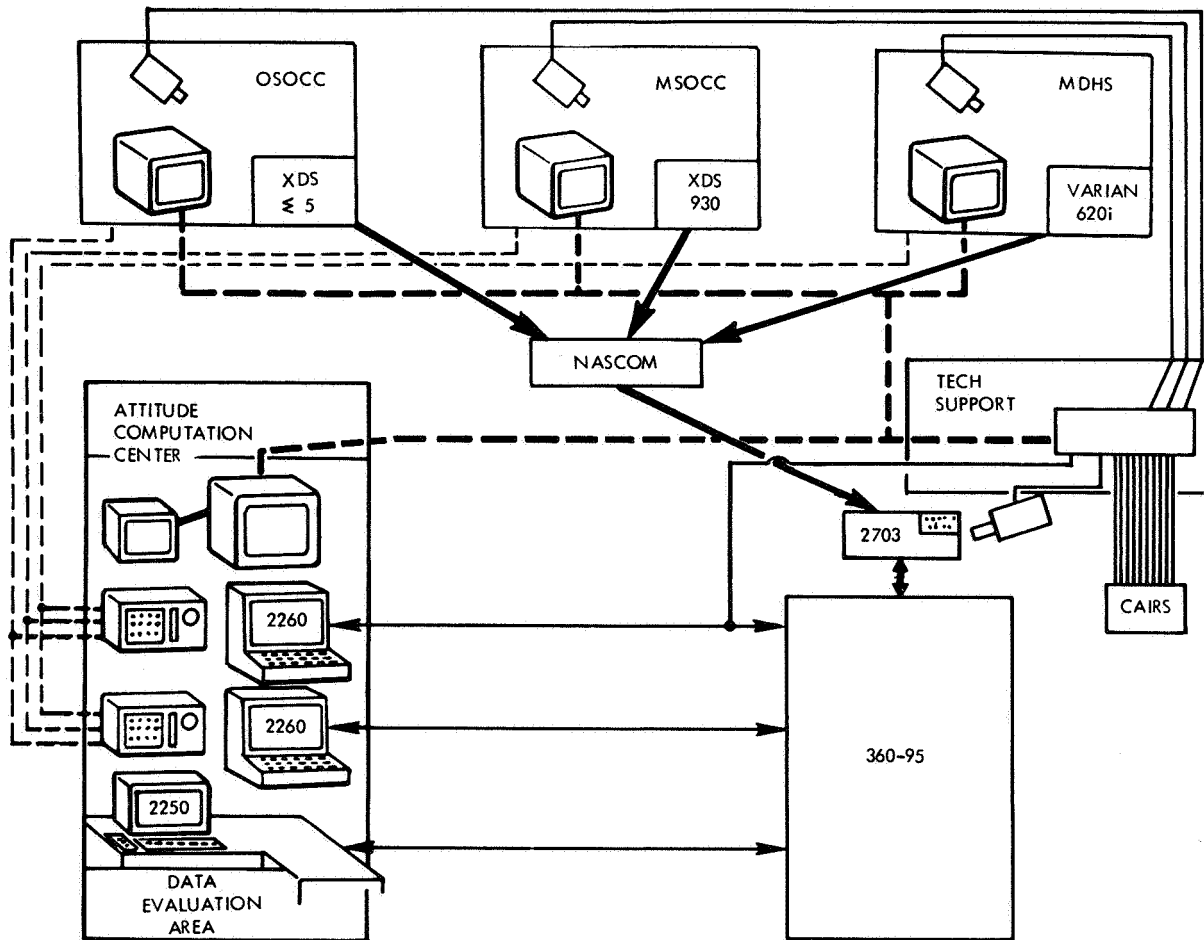


Figure 2. Attitude computation facilities.

The system's major components include: the ability to transfer the attitude data from the control center to the attitude computer at a rate of 2400 bps; an attitude computation center which houses communications, closed circuit TV, graphics devices, and a data evaluation area; and the use of interactive graphics devices to schedule jobs and to control program flow.

The attitude computation system has been able to take advantage of computational power which exists at GSFC in a rapid response environment to support the requirements of a number of spacecraft missions. This system is located near the control centers and we believe it is utilizing the existing facilities in a highly efficient and effective manner.

A most recent example of the need for this type of support was demonstrated at the launch of SSS-1 when the spacecraft experienced nutation build-up at the rate of about three degrees per day, and could have resulted in mission failure. Figure 3 depicts the functions which were performed to implement an active nutation damping operation.

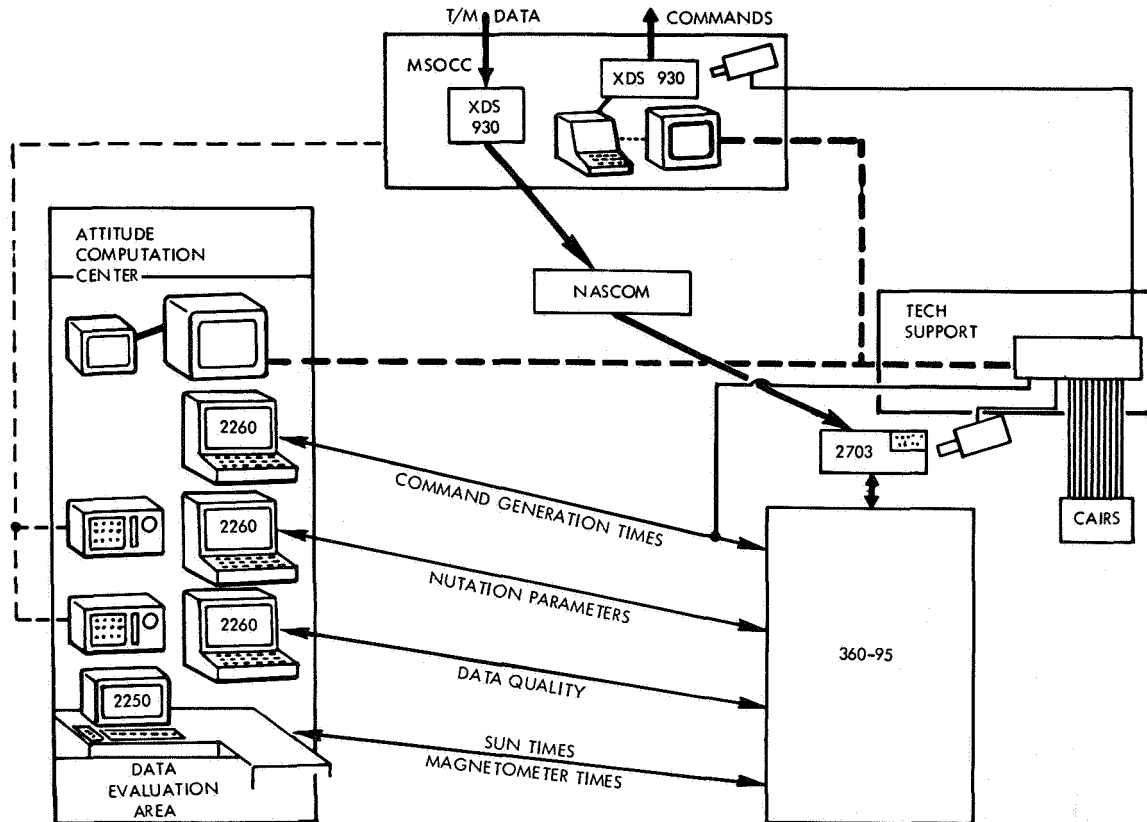


Figure 3. SSS-1 nutation control.

The SSS Attitude System was designed to determine attitude, using optical aspect and SCADS data. This system was modified to display magnetometer and sun times as seen from spacecraft telemetry. Nutation phase and amplitude parameters were computed by the system and displayed on a second device. A third was used to evaluate the quality of the telemetry data. And a fourth was used to combine the results of the other processing functions to generate the command times, which were necessary to activate a magnetic coil at a precise time within the 16-second spin period and were returned to the control center via CCTV. The attitude computation center was temporarily expanded to meet the graphics requirements.

The resources available to the attitude computation system provided a base from which the contingency support could be readily developed within 24 hours and was instrumental in mission success.

MISALIGNMENT ESTIMATION SOFTWARE SYSTEM

Richard L. desJardins

I want to describe a system of computer software and spacecraft and ground system activity called the Misalignment Estimation Software System (MESS). This enables spacecraft precision attitude sensors such as startrackers and inertial reference assemblies to be aligned and calibrated from the ground after the spacecraft has achieved orbit.

Advantages of this approach will be pointed out and actual results of application of MESS to OAO-C will be given.

Spacecraft with very high precision three-axis attitude slewing and maintenance requirements typically combine a number of external reference sensors, such as startrackers and sun sensors, with one or more internal reference sensors or inertial reference assemblies. These units are bolted to the spacecraft structure and carefully aligned to the coordinate axes. But the sensors have such high precision that even residual misalignments are detectable. Therefore these residual misalignments are measured during test and integration and modeled in the computer so that account may be taken of them when the spacecraft is being controlled.

When the spacecraft is launched, however, extreme mechanical vibration causes changes to these misalignments, and once in orbit, the solar duty cycle and resulting variations in thermal load on the structure again cause changes to the misalignments. Finally, the slew angle scale factors of the gyros must be calibrated against the weightless conditions in orbit. Therefore, to achieve the high precision of which these units are capable, it is necessary to redetermine the misalignments after the spacecraft has achieved orbit and again from time to time throughout the mission.

Before describing the technique used in MESS, let it be clear that this is mathematically a nontrivial problem. The difficulty is that parameters are not directly observable in general, but only the attitude sensor errors resulting from them. Any particular observed error—for instance, if it is observed that the spacecraft is pitch-slewing off to one side—is attributable in general to a combination of several misalignment parameters.

Therefore, the analyst must first of all define the type and number of exercises which will render specific misalignment parameters visible, and secondly, he must process the observed errors to determine statistically the best estimate of misalignments which caused those errors.

From an information flow point of view, all MESS exercises are conceptually identical. In the uplink flow, given a nominal spacecraft model, MESS generates an exercise designed to

render visible a particular set of misalignments (Figure 1). The exercise is sent to the spacecraft, and in performing it, the spacecraft inserts the misalignments of interest into the information in the form of attitude sensor errors. The information is downlinked to MESS, which processes it to arrive at estimates of the misalignments. These estimates are then used to correct the spacecraft model in the data base.

As MESS was developed, its architecture and analysis were kept general where possible, so that a version could be implemented to support other spacecraft and attitude sensors aboard those spacecraft. In this connection, we are currently investigating the application of MESS to ATS-F and G.

However, the version currently implemented is for OAO (Figure 2). Included in this implementation are five gimballed startrackers, for each of which both an arbitrary rotational misalignment as well as a shift in the inner gimbal null position are modeled; a boresighted

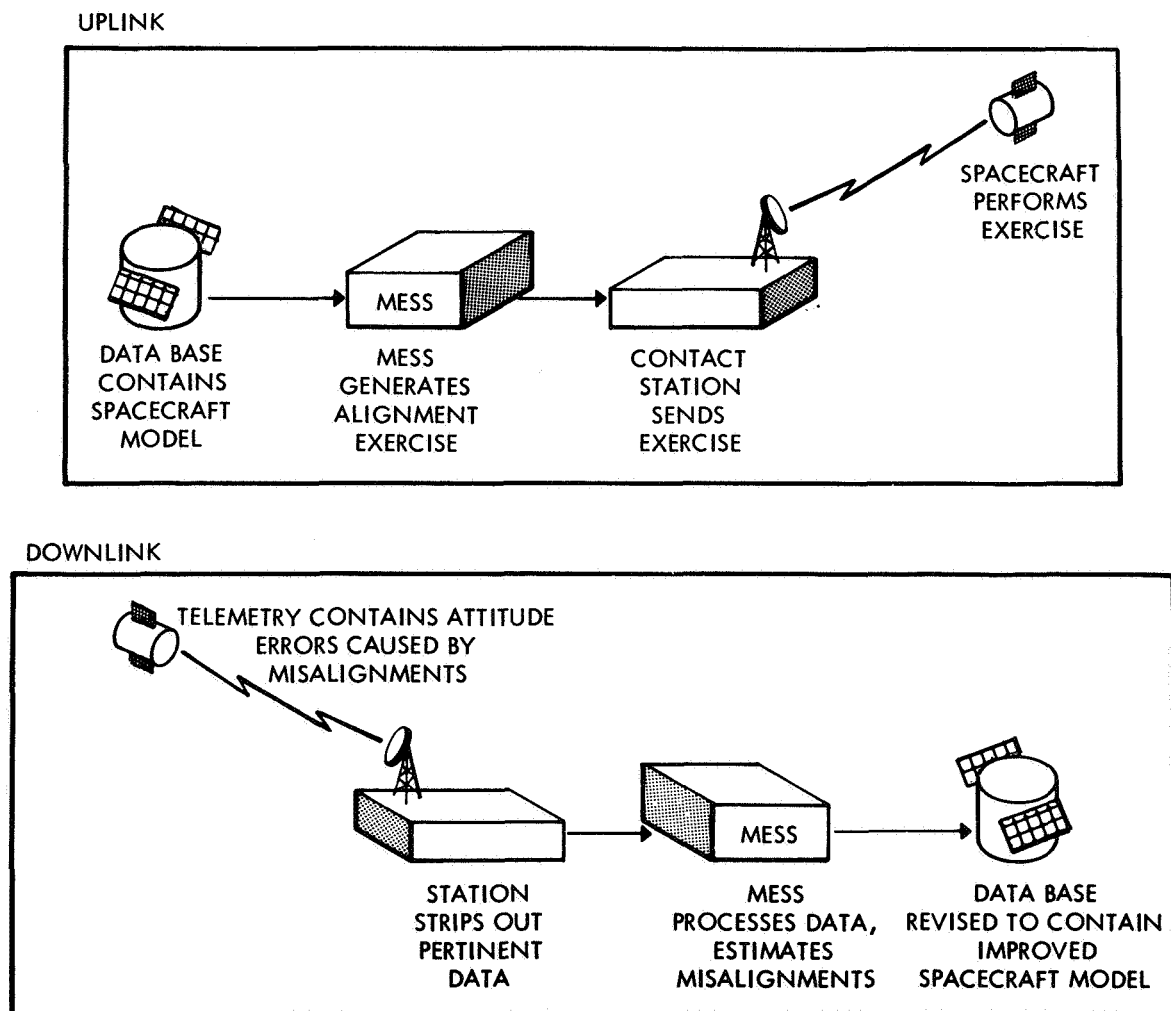


Figure 1. MESS information flow.

	TOTAL
EACH GST: THREE ROTATIONS OF GIMBAL PLATFORM	15
INNER GIMBAL NULL SHIFT	5
BST: PITCH AND YAW OFFSET FROM FES	2
IRU: FOR EACH AXIS, TWO OFFSET MISALIGNMENTS	6
FOR EACH AXIS, TWO SLEW ANGLE SCALE FACTORS	6
	34

Figure 2. Misalignments modeled in MESS/OAO.

startracker, for which an arbitrary offset from the experimenter's fine error sensor is modeled; and three independent inertial reference assembly slew axes, for each of which an offset misalignment and separate positive and negative slew angle scale factors are modeled.

Figure 3 is a summary of the results of the initial in-orbit alignment of OAO-C. "Before" means after launch but prior to in-orbit alignment. You can see that the maximum sensor errors have been reduced fivefold on the gimballed startrackers. After aligning the gimballed startrackers, we were then able to align the experimenter's fine error sensors to the same reference, which resulted in a threefold improvement in overall open loop pointing. We were able to improve slew accuracy by a factor of better than two, and we helped determine compensation terms to dramatically decrease the drift rates of the gyros as shown.

It is important to note here that careful analysis and design of necessary exercises and development of supporting software can minimize interference of in-orbit alignment operations with productive spacecraft operations. For example, the initial in-orbit alignment and calibration of all the sensors shown here consumed only about 10 percent of the first eight days in orbit. (The other 90 percent of course was occupied with initial stabilization and spacecraft and experiment checkout.) As another example, all of the startrackers on OAO-C can be realigned at any time desired in about one hour of orbital operations.

In summary, the MESS system and underlying concepts

- have been developed
- have been used successfully on OAO-C to improve precision by better than twofold
- and are available for use on other spacecraft which have precision attitude-sensing requirements

.SENSOR	MAXIMUM ERROR	
	BEFORE	AFTER
GIMBALLED STAR TRACKERS	2.5 ARCMIN	0.5 ARCMIN
FINE ERROR SENSOR (RELATIVE)	1.5 ARCMIN	0.5 ARCMIN
INERTIAL REFERENCE UNIT (20° SLEW)	1.4 ARCMIN	0.6 ARCMIN
IRU DRIFT RATES	50 ARCSEC/HR	3 ARCSEC/HR

Figure 3. Misalignments modeled in MESS/OAO.

SPACECRAFT REORIENTATION VIA SLEWING ABOUT NONORTHOGONAL AXES

Paul B. Davenport

I will be presenting a synopsis of a mathematical technique which was developed to meet the demanding requirements for precise spacecraft reorientations. By a reorientation I mean either a change in pointing which requires slews about two axes, or a total change in attitude which requires motion about three axes.

Normally it is assumed that these slews take place about orthogonal axes. Thus a yaw of 90° followed by a pitch of 90° , followed in turn by a roll of 90° , will reorient the spacecraft so that it is pointing vertically and the sunshade is parallel to the desk.

In reality, however, the motion is controlled via devices mounted on the spacecraft; and these devices may be slightly skewed, due to mounting imperfections, launch stress, thermal bending. Thus, a misalignment of the first axis actually causes the spacecraft to move like this, a misalignment of the second axis adds to the error like so, and finally the third axis may also be skewed so that the final attitude looks like this.

I think you can see by this simple demonstration that for precise reorientations we can no longer afford the computation luxury of orthogonal axes. Even if the misalignments are small, they can accumulate and even grow. In the example just shown, a one-minute error in each axis would have caused a pointing error of over $3\frac{1}{2}$ minutes, and unless the errors at this attitude are nulled out the next reorientation will be even worse. The elimination of the errors, however, will require additional commands and loss of valuable time; and if the errors are large an attitude determination may be required.

To solve this problem of skewed axes, a mathematical procedure was developed which determines the exact slews relative to any known axes. The axes may be completely arbitrary; their coordinates merely reside on a data base which can be changed at any time without affecting the software.

Given the desired reorientation, the procedure then determines all of the two-legged or three-legged slews which will accomplish the reorientation. For example, there are 12 possible permutations of three axes, and if they are orthogonal each always has two solutions. The nonorthogonal case, on the other hand, gives some surprising results, including the nonexistence of a solution: Consider a large reorientation where the three axes are nearly collinear. In this connection, it can be shown that every three-axis reorientation can be accomplished by three successive slews, if and only if the middle axis is perpendicular to the other two.

The development of this procedure was initiated to meet the precise requirements of the OAO Copernicus spacecraft, and it is performing this function quite adequately even though two of the axes lack orthogonality by $2\frac{1}{2}$ minutes.

Even though it was small misalignments which motivated the investigation, the resulting procedure is quite general and may have many other applications. For example, in some cases it may be possible to relax the alignment requirements during installation. In fact, since the procedure is completely general it may be useful when the axes are skewed on purpose.

Many control systems are presently being designed around a skewed concept – one such system mounts the sensors on the six nonparallel sides of a dodecahedron; as in Figure 1. The advantages of such a design are threefold: It is redundant – any three can fail; failures or false signals can be detected by majority logic; and it is more precise.

In Figure 2 we have a few examples of the various control configurations and their applications, and although there are many variations, each is based on a geometric figure having symmetry. However, the procedure I have been describing is flexible enough so that even symmetry is not required. The most sophisticated control system ever launched into space is based on such a principle. This system uses a triad of semicircular canals which for some reason or another are nonorthogonal (see Figure 3).

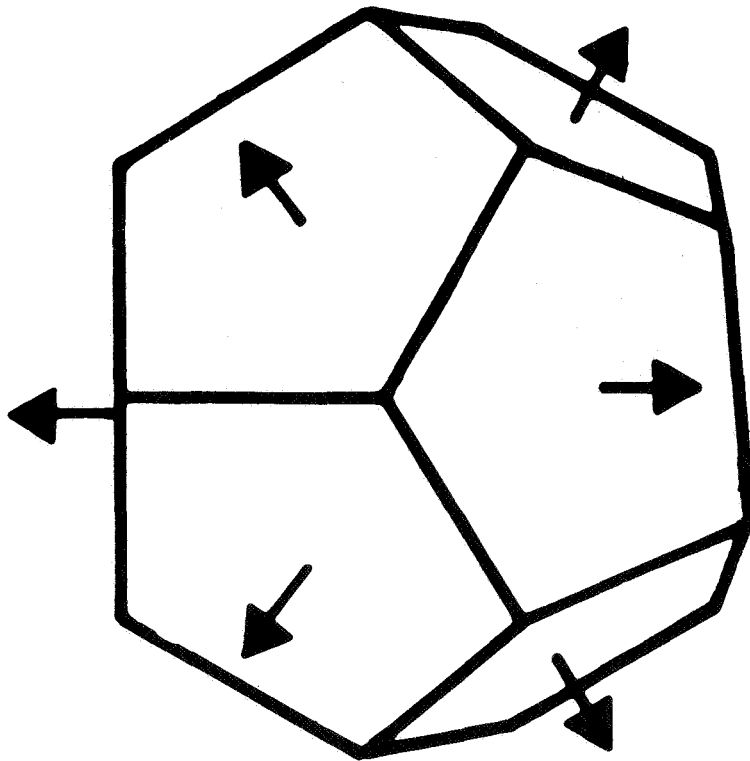


Figure 1. Dodecahedron mounting.

AXES	DESIGN GEOMETRY	APPLICATION
3	CUBE (orthogonal)	OAO – GYROS
4	PYRAMID (nonorthogonal)	HEAO – REACTION WHEELS
4	OCTAHEDRON (nonorthogonal)	
6	DODECAHEDRON (nonorthogonal)	HEAO – GYROS
6	CONE (nonorthogonal)	IUE – GYROS

Figure 2. Control configurations.

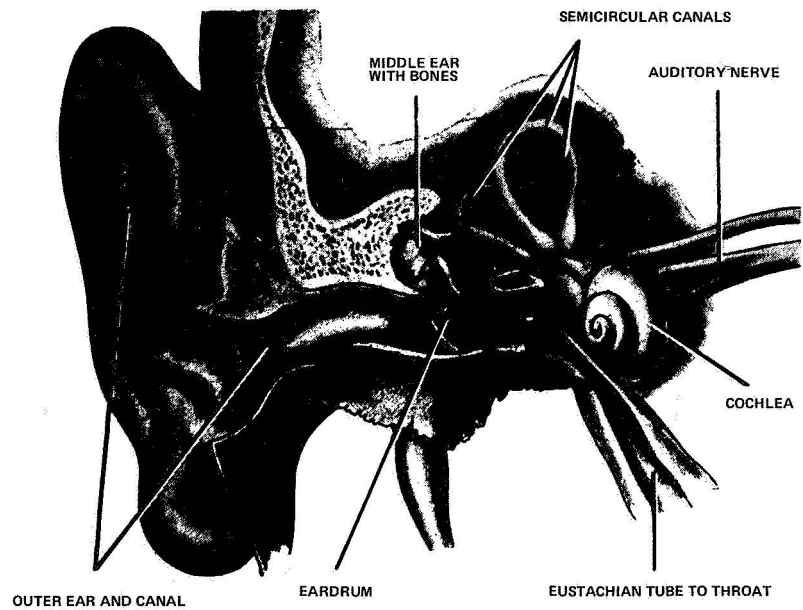


Figure 3. The human ear.

COMPUTER ASSISTED INTERACTIVE RESOURCE SCHEDULING SYSTEM

Carl E. Gustafson

Several years ago it became apparent that the task of scheduling mission support for spacecraft was becoming more difficult with the increasing complexity of spacecraft and of on-board experiments. It was clear that manual methods then in use would not be suitable for coping with the expected increase in the scheduling workload. Therefore (refer to Figure 1), the development of the Computer Assisted Interactive Resource Scheduling (CAIRS) System was undertaken to assist in the preparation of the necessary mission support schedules.

Schedulers were working with 45 spacecraft across 20 network stations (Figure 2). Individual schedules were required for telemetry data and associated commands, communications circuits, and four types of tracking capabilities.

Approximately 20,000 individual spacecraft station contact points were available in each scheduling week. Of these possibilities about 3000 were being scheduled for telemetry data, 2500 for tracking data, and about 1500 for spacecraft commanding purposes.

Complexity in the scheduling process resulted not only from the scheduling types required and quantities involved, but from the nature of the mission themselves (Figure 3). Scheduling considerations were based on the type of spacecraft and capabilities available for ground support. The variety of tracking capabilities and the multiple nature of the ground support capability complicated the scheduling of resources.

COMPUTER ASSISTED INTERACTIVE RESOURCE SCHEDULING SYSTEM

Figure 1. CAIRS.

NUMBER OF SPACECRAFT SUPPORTED	45
NUMBER OF NETWORK STATIONS	20
NUMBER OF SPACECRAFT-STATION CONTACTS	20,000 WEEKLY
NUMBER OF SCHEDULED TASKS:	
TELEMETRY	3000 WEEKLY
TRACKING	2500 WEEKLY
COMMANDS	1500 WEEKLY

Figure 2. Quantities.

- 1. FIVE SUPPORT TYPES**
- 2. VARIABILITY IN SCHEDULING REQUIREMENTS**
 - SPACECRAFT FREQUENCIES
 - ANTENNA TYPES
 - COMMANDING REQUIRED
 - VOICE OR DATA LINES NEEDED
 - Q/L OPERATIONS REQUIRED
- 3. MULTIPLE NETWORK CAPABILITY**
- 4. THREE ORBITAL CATEGORIES**
- 5. REAL-TIME RESCHEDULING**

Figure 3. Scheduling complexity.

A further consideration in the scheduling process was the type of orbit presented by the spacecraft. Three orbital categories were represented: namely, near earth, elliptical, and synchronous. Changes to the weekly schedule were necessary after transmission of the original schedule. These changes occurred because of updates to the ephemeris data, changes in mission support requirements, spacecraft anomalies or emergencies, loss of station resources, and rescheduling due to new launches.

Prior to CAIRS, schedules were built on charts using colored pencils and symbols to keep track of spacecraft differences and support types. Ephemeris data, station capabilities, and spacecraft requirements were obtainable only from hard copy sources which required considerable lookup time.

The theory behind the development of the CAIRS System was to provide the scheduler with a tool he could use to more efficiently produce the mission schedules. Conflicts in mission support were to be resolved by the scheduler, utilizing the CAIRS System to point out the conflicts and the nature of the resource deficiency. Concurrent with the improvement in scheduling capability would be a quick turnaround capability for real-time re-scheduling, as well as quick access to information for improvement in mission control.

The mission scheduling process begins with the ephemeris data being input to the CAIRS System (Figure 4). Requests for support are defined in three ways:

- The Project Operations Control Centers inputs are entered from punched cards. Approximately 3500 of 5000 requests are input in this manner.
- Additional support requirements are input interactively through the CRT.
- The computer automatically requests support where mission requirements have been specified. This capability is used sparingly at this time.

After all the mission requests for support have been entered, the CAIRS System begins the scheduling process utilizing a previously entered priority table. When a request for support cannot be satisfied because of insufficient resources, that request is output to a printer listing along with a notation as to the nature of the deficiency.

When the system processor has completed all priority levels, a "no conflict" schedule has been created. At this point roughly 90 percent of the requests for support have been satisfied. The power of the CAIRS System is exemplified in that 1600 M/T events are

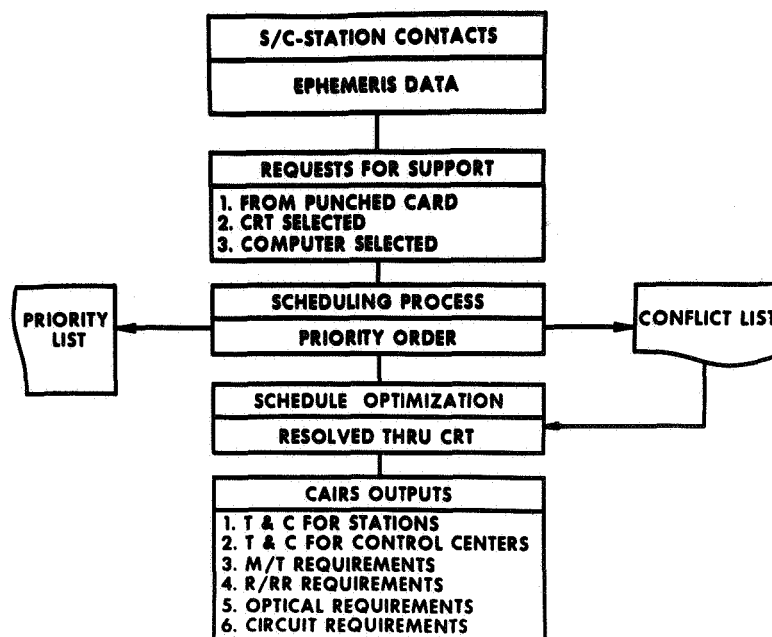


Figure 4. Scheduling process.

scheduled by this processor in 14 minutes. The operator now takes the conflict listing and refits those events lacking support, using the interactive CRT capability for resolution.

After optimization, the CAIRS System outputs the mission requirements schedules in teletype format, ready for transmission.

The net result of the CAIRS development has been a system which more effectively schedules complex mission support requirements faster, and with less error than was possible with manual methods, thereby improving the overall mission support (Figure 5). Spacecraft requirements, station capabilities, and ephemeris data are all contained in the CAIRS data base, thereby negating the need for stacks of paper, colored pencils, symbolic representations, and good memories.

The CAIRS System saves time by reducing the scheduling operation from hours to minutes. Also, since the system outputs the mission schedule requirements ready for transmission, the hours previously required for teletype tape generation – the operation most prone to error – has been eliminated.

The time needed for rescheduling has been greatly reduced, due to the interactive and schedule creation capabilities of the CAIRS System, and the display of current schedules and resource availability on demand readily accomodates the dynamic nature of the real-time scheduling problem.

The CAIRS System has been in operational use since October 1971.

1. MORE EFFECTIVE SCHEDULING

- **IMPROVED MISSION SUPPORT**
- **SAVINGS IN TIME**
- **REDUCTION IN ERRORS**

2. REAL-TIME RESCHEDULING

Figure 5. CAIRS results.

INTERACTIVE EXPERIMENTERS' PLANNING PROCEDURES AND MISSION CONTROL

Richard L. desJardins

I want to describe a very promising approach to spacecraft and experiment operation planning, based on an interactive CRT system.

Planning for space astronomy operations begins in the space dimension (Figure 1). In this dimension we can identify spatial interrelationships among prospective targets and also prohibit constraint regions such as effective body sizes. This planning approach is satisfactory for static, long-term targeting. However, there are many more constraints besides occulting bodies, and most of these constraints are extremely dynamic, such as the motion of the earth, which may sweep through this picture many times a day. Therefore most constraints cannot be effectively represented in the space dimension.

The complexity of planning in the time dimension, however, becomes apparent when even a few constraints are included, as in Figure 2. The planner may have to take account of ground contacts, target occultation by the effective earth, and spacecraft night periods; also variations in background count due to trapped particle radiation. He must especially consider all the hardware interrelationships and restrictions internal to the experiment, or between experiments, or among all the experiments, the spacecraft, and the external constraints.

Previous approaches to planning were to provide the planner with computer-produced aids, then when he had devised an entire plan, to run it through the computer and check its validity against all the constraints and restrictions. Frequently this approach necessitated a number of reruns until these iterations converged to a valid plan. It should be stressed that these reruns were not always due to human error, but were frequently forced by the dynamic interrelatedness of many of the restrictions (i.e., the precise restrictions depend on the activity itself, and hence cannot be fully known until the plan is generated).

It was a strain with the previous planning procedures to run two times real-time on the OAO, due to the reruns, the time getting on and off the computer, and so on.

The planning system I want to describe today, called PROFILE, allows the planner to validate his plan interactively as it is being generated segment by segment, and thus eliminate those reruns. This system is in daily operational use by the University College of London experimenter on OAO-C. Using this system, he is routinely generating a 24-hour schedule in one hour of operator time, and less than four hours total elapsed staff time. This is six times real-time, which is a threefold improvement over forerunner systems.

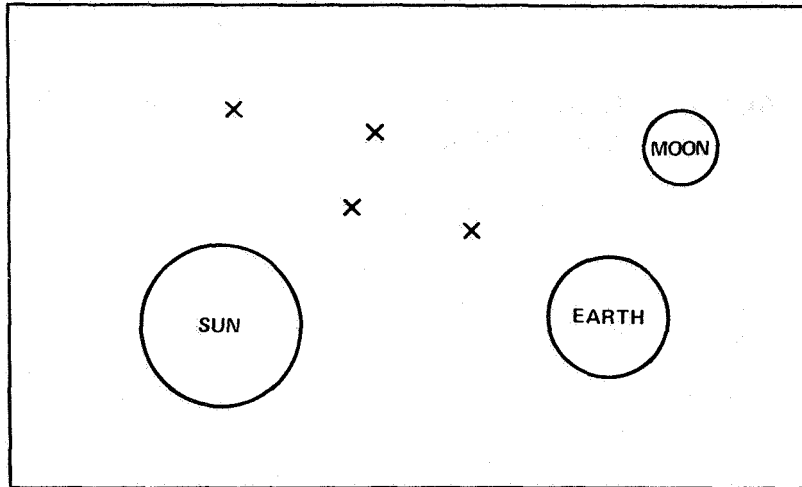


Figure 1. Experiment planning: the space dimension.

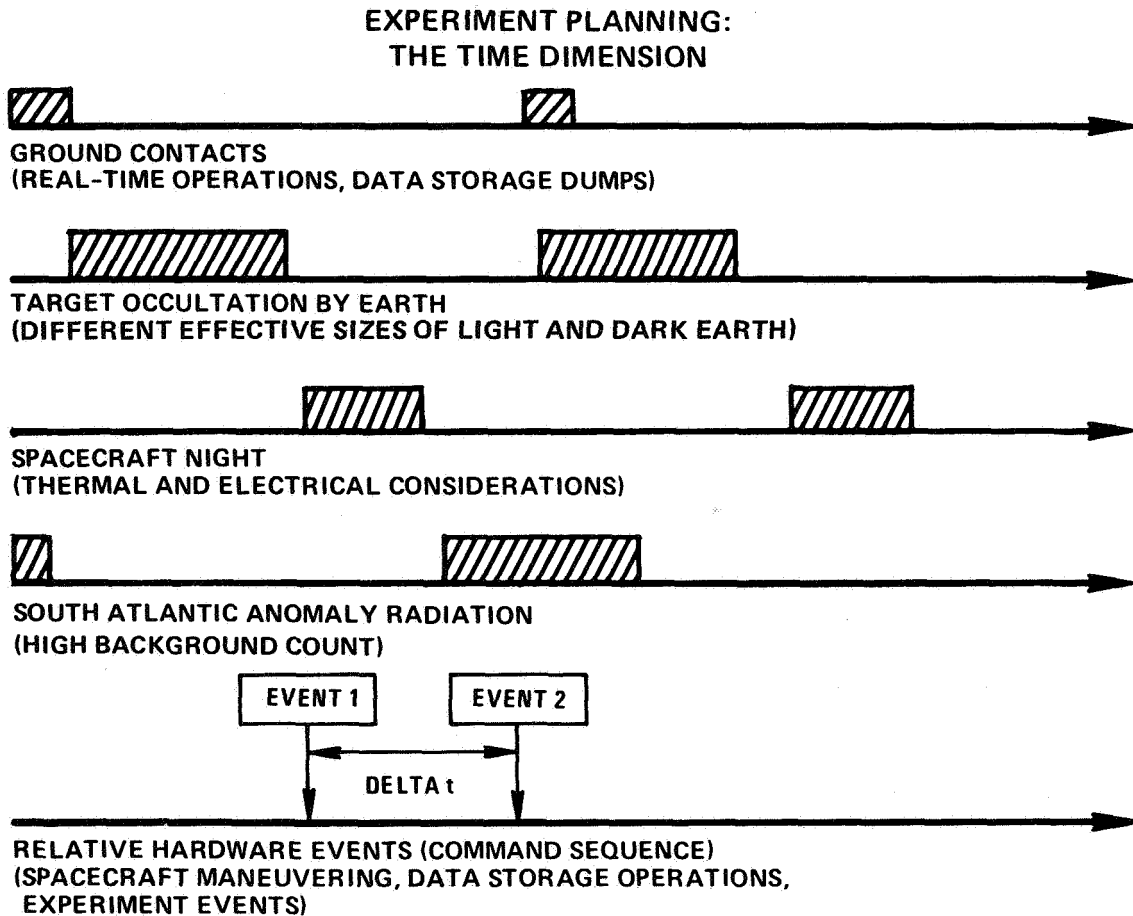


Figure 2. Experiment planning: the time dimension.

The planner at the CRT terminal brings up an initial display containing a blank time line initialized to the time interval of interest. Figure 3 is an actual photograph of the display to emphasize that this is a real system that is in use today. Unfortunately it is hard to read, so I have taken the liberty of having it transcribed to print. The time line shown in Figure 4 is GMT; the experimenter may work with a spacecraft clock time scale if he chooses. The Attitude Control Display area allows the planner to input times, spacecraft attitudes, and specific slew maneuvers if desired, as well as verbs to control the software system itself. The operator has all sorts of capability for shifting things up and down, left and right, for expanding and contracting the time scale, for manipulating things, copying things, and logging things to the printer.

In Figure 5 the experimenter has displayed some of his constraints on the time line. The ground contact shown is Rosman 982, and spacecraft sunrise occurs at approximately 7:17. The target at right ascension 4:39, declination 22:51, is unocculted by the earth until approximately 7:37.

Let us suppose that after examining these constraints, the planner decides that immediately after the contact he will perform a segment of activity involving the fine error sensor, then slew to a new target pointing.

First, he calls out the commands which perform his activity segment with the fine error sensor. You can see in Figure 6 the English language schedule being built up to describe the command sequence he is generating; on the time line, a representation (the interval of E's) that the fine error sensor is enabled, and the specific times (the T's) that events are called out in the command sequence. Let me point out that specific event times such as those shown may be entered into the schedule as needed, simply by pointing the light pen at the time mark of interest on the time line — a push of the light pen causes the appropriate time field to be entered into the schedule by the computer.

In Figure 7 the experimenter has entered a new desired target pointing into attitude 2, and the computer in turn has first computed the optimum roll angle to maximize solar paddle power, then has calculated the shortest slew maneuver which will take the spacecraft from attitude 1 to attitude 2. On the time line, the computer has displayed the slew and settle interval for the maneuver. The experimenter sees that following the maneuver he has only a minute or so before the target becomes occulted by the earth. Since this is not enough time to do anything useful, he shifts to the other end of the occultation interval to begin experimenting.

The Experiment Control Display is shown in Figure 8. The configuration or state of the UCL experiment is completely defined by the settings or values of 18 parameters, e.g., 3 sensitivity parameters, 2 pulse shape discriminator parameters, and so on. Configuration 1, the current configuration, is always given in the top row. Configuration 2, the desired configuration, is input by the experimenter to the second row; actually he need enter only parameter change values (“*” means “stays the same”). The operator has a super-convenient way to enter change parameters to configuration 2; all he need do is point the light

pen at the parameter field he wants changed and the next parameter value in cyclic order will be entered by the computer. Thus a push of the pen at the first sensitivity parameter will set the configuration 2 value to "L" for "low"; the next push will set it back to "H". At "iris," consecutive pushes will set the change value to 3, then 4, then 1, then back to 2, and so on. In this way, a few quick strokes of the pen to set up the desired configuration 2, one stroke of the pen on the time line to enter into the specific time field the time at which he wants the indicated configuration change to occur. Three things happen: The command sequence which effects the configuration change is computed and entered on the schedule (Figure 9). The current configuration is automatically updated on the display to the new configuration and a T is marked on the time line, indicating the time of the change to the current configuration. The system is now ready to respond to the next configuration change desired.

Figure 10 shows the last display in the original form to highlight the fact that the planning system shown here is not only a design, but is in daily operational use. It represents a significant technological advance over its predecessors. It is very responsive, very flexible, easy to add new capability to; in a quick-turnaround situation, it is unexcelled. I feel confident in predicting that many of the features which exist on this system today will find their way into spacecraft and mission control systems of the future.

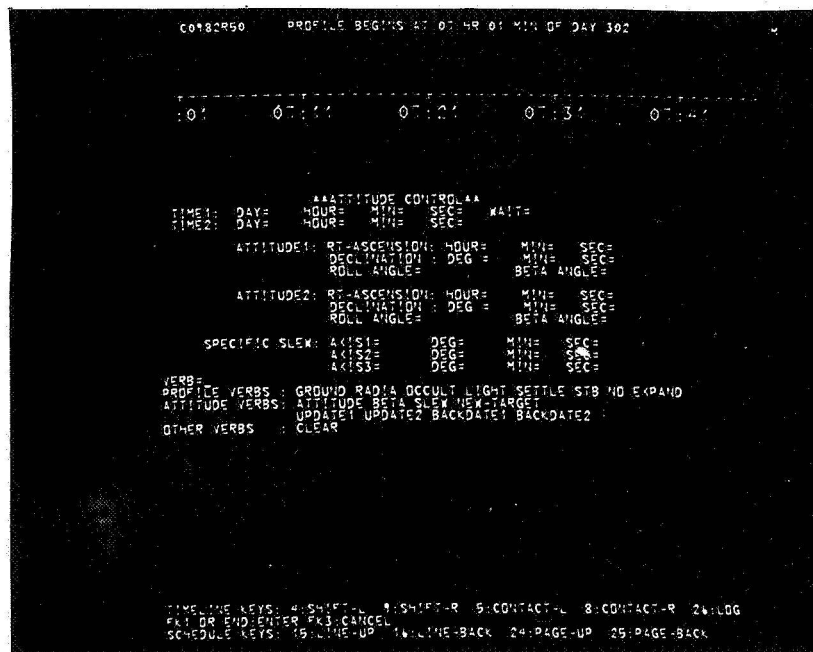


Figure 3. Actual photograph of CRT Display 1.

```

C0982R50      PROFILE BEGINS AT 07 HR 01 MIN OF DAY 302      M
+-----+-----+-----+-----+
:01          07:11          07:21          07:31          07:41

**ATTITUDE CONTROL**
TIME 1: DAY = HOUR = MIN = SEC = WAIT =
TIME 2: DAY = HOUR = MIN = SEC =

ATTITUDE 1: RT-ASCENSION: HOUR = MIN = SEC =
             DECLINATION: DEG = MIN = SEC =
             ROLL ANGLE = BETA ANGLE =

ATTITUDE 2: RT-ASCENSION: HOUR = MIN = SEC =
             DECLINATION: DEG = MIN = SEC =
             ROLL ANGLE = BETA ANGLE =

SPECIFIC SLEW: AXIS 1 = DEG = MIN = SEC =
                AXIS 2 = DEG = MIN = SEC =
                AXIS 3 = DEG = MIN = SEC =

VERB =
PROFILE VERBS : GROUND RADIA OCCULT LIGHT SETTLE STB NO EXPAND
ATTITUDE VERBS: ATTITUDE BETA SLEW NEW-TARGET
                UPDATE 1 UPDATE 2 BACKDATE 1 BACKDATE 2
OTHER VERBS:   CLEAR

TIMELINE KEYS: 4: SHIFT-L 9: SHIFT-R 5: CONTACT-L 8: CONTACT-R 26: LOG
FK1 OR END: ENTER FK3: CANCEL
SCHEDULE KEYS: 15: LINE-UP 16: LINE-BACK 24: PAGE-UP 25: PAGE-BACK

```

Figure 4. Artist's description of CRT Display 1.

```

C0982R50      PROFILE BEGINS AT 07 HR 01 MIN OF DAY 302      M
GR R R R R R R R 0 9 8 2      G
O                               O O O O O O O O O O
+-----+-----+-----+-----+
:01          07:11          07:21          07:31          07:41
N N N N N N N N N N N N N N N N      P
RIGHT ASC = 4 39 14.44, DEC = 22 51 46.0

**ATTITUDE CONTROL**
TIME 1: DAY = 302 HOUR = 7 MIN = 0 SEC = 52 WAIT =
TIME 2: DAY = HOUR = MIN = SEC =

ATTITUDE 1: RT-ASCENSION: HOUR = 4 MIN = 39 SEC = 14.44
             DECLINATION: DEG = 22 MIN = 51 SEC = 46.0
             ROLL ANGLE = BETA ANGLE =

ATTITUDE 2: RT-ASCENSION: HOUR = MIN = SEC =
             DECLINATION: DEG = MIN = SEC =
             ROLL ANGLE = BETA ANGLE =

SPECIFIC SLEW: AXIS 1 = DEG = MIN = SEC =
                AXIS 2 = DEG = MIN = SEC =
                AXIS 3 = DEG = MIN = SEC =

VERB =
PROFILE VERBS : GROUND RADIA OCCULT LIGHT SETTLE STB NO EXPAND
ATTITUDE VERBS: ATTITUDE BETA SLEW NEW-TARGET
                UPDATE 1 UPDATE 2 BACKDATE 1 BACKDATE 2
OTHER VERBS:   CLEAR

TIMELINE KEYS: 4: SHIFT-L 9: SHIFT-R 5: CONTACT-L 8: CONTACT-R 26: LOG
FK 1 OR END: ENTER FK 3: CANCEL
SCHEDULE KEYS: 15: LINE-UP 16: LINE-BACK 24: PAGE-UP 25: PAGE-BACK

```

Figure 5. CRT Display 2.

```

C0982R50      PROFILE BEGINS AT 07 HR 01 MIN OF DAY 302      M
GRRRRRRRRR0982      G
O      EEEEEEEEEEE      OOOOOOOOOOO
+-----+-----+-----+-----+-----+-----+-----+-----+
:01      07:11      07:21      07:31      07:41
NNNNNNNNNNNNNNNNNNNN      N
RIGHT ASC = 4 39 14.44, DEC = 22 51 46.0

ENTER ONE OF THE FOLLOWING:
RECORD GENERATION VERBS: N D H F V C T E S M *
RECORD MODIFICATION VERBS: INSERT REPLACE DELETE
OTHER VERBS: CONTROL UCL COPY ENDCOPY

```

```

-----
00010 N 00982 R 302 07 01 28
00020 HOLD ATTITUDE 9
00030 E 302 07 14 302 07 24
00040 C PEP, 1HLA, 2SLA, 2SPA, SRRA, ENDC
00050 T 302 07 14
00060 HOLD ATTITUDE E
00070 T 302 07 19
00080 C PEP, 1SLA, 1HLA, 2HLA, ENDC
00090 T 302 07 24

```

TIMELINE KEYS: 4: SHIFT-L 9: SHIFT-R 5: CONTACT-L 8: CONTACT-R 26: LOG
END OR 1: ENTER 6: RE-INIT 31: RETURN 22: CANCEL-ALL 3: CANCEL VERB
SCHEDULE KEYS: 15: LINE-UP 16: LINE-BACK 24: PAGE-UP 25: PAGE-BACK

Figure 6. CRT Display 3.

```

C0982R50      PROFILE BEGINS AT 07 HR 01 MIN OF DAY 302      M
GRRRRRRRRR0982      G
O      EEEEEEEEEEE      OOOOOOOOOOO
+-----+-----+-----+-----+-----+-----+-----+-----+
:01      07:11      07:21      07:31      07:41
NNNNNNNNNNNNNNNNNNNN      N
*
RIGHT ASC = 4 39 14.44, DEC = 22 51 46.0

**ATTITUDE CONTROL**
TIME 1: DAY = 302 HOUR = 7 MIN = 24 SEC = 59 WAIT =
TIME 2: DAY = 302 HOUR = 7 MIN = 36 SEC = 15

ATTITUDE 1: RT-ASCENSION: HOUR = 4 MIN = 40 SEC = 38.46
DECLINATION: DEG = 22 MIN = 54 SEC = 29.4
ROLL ANGLE = 143.85231 BETA ANGLE = 36.486958

ATTITUDE 2: RT-ASCENSION: HOUR = 5 MIN = 32 SEC = 54.92
DECLINATION: DEG = 22 MIN = 0 SEC = 6.6
ROLL ANGLE = 136.67832 BETA ANGLE = 48.436237

SPECIFIC SLEW: AXIS 1 = ROLL DEG = -2 MIN = 47 SEC = 00.0
AXIS 2 = YAW DEG = -9 MIN = 41 SEC = 31.0
AXIS 3 = PITCH DEG = 7 MIN = 17 SEC = 3.1

VERB =
PROFILE VERBS: GROUND RADIA OCCULT LIGHT SETTLE STB NO EXPAND
ATTITUDE VERBS: ATTITUDE BETA SLEW NEW-TARGET
UPDATE 1 UPDATE 2 BACKDATE 1 BACKDATE 2
OTHER VERBS: CLEAR
TIMELINE KEYS: 4: SHIFT-L 9: SHIFT-R 5: CONTACT-L 8: CONTACT-R 26: LOG
FK 1 OR END: ENTER FK 3: CANCEL
SCHEDULE KEYS: 15: LINE-UP 16: LINE-BACK 24: PAGE-UP 25: PAGE-BACK

```

Figure 7. CRT Display 4.

ELECTRON BEAM RECORDER IMAGE CORRECTION FOR ERTS

Paul Heffner

Video data from the Earth Resources Technology Satellite (ERTS) are entered into the initial image generation system at the Goddard Space Flight Center. The data are placed on film using an electron beam recorder (EBR). If the video data were applied directly to the EBR, both radiometric and geometric errors would result in the output film imagery.

To correct for these errors, a hardware unit called EBRIC was designed, fabricated, and incorporated in the image processing system. EBRIC is an acronym for Electron Beam Recorder Image Corrector. It operates under the control of a process control computer, as it varies the video signal and the x and y deflection signals of the EBR.

EBRIC corrects errors that basically fall into three categories: static, slow varying, and dynamic. Figure 1 gives examples of error conditions for each of the categories. An example of a static error condition is the multispectral scanner mirror velocity profile. Slow varying conditions are those that are nearly systematic, but tend to drift over a period of several weeks. An example here is the boresighting of the sensors with respect to each other, and with respect to the spacecraft attitude measurement system. Dynamic conditions are those that vary from frame to frame or within a frame, such as multispectral scanner attitude variations that are caused, for example, by spacecraft roll.

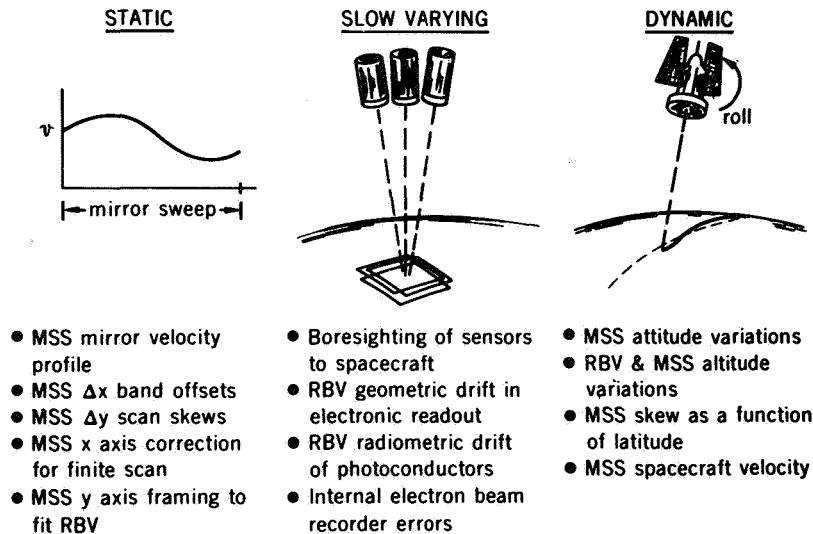


Figure 1. Error categories.

Resident in the core of the process control must be all information necessary to perform correction at the time video data are being processed. The manner in which this information is entered depends on the category. Referring to Figure 2, the static information is entered before launch by parameter card. For the slow varying conditions, the information is brought in from a computer tape (called an EBRIC tape) prior to video processing. For the dynamic conditions, another computer tape is used concurrent with processing. This tape has been named the image annotation tape. It is generated in another segment of the NASA data processing facility where both orbit data and spacecraft attitude data are merged.

The process control computer absorbs this information as needed and sums it in appropriate order. Then, in proper sequence and time, the computer delivers correction coefficients to EBRIC. This function is performed as the video data are being processed through the controller to EBRIC, where the EBR video and deflection signals are being altered to permit generation of a corrected film image. Except for Canadian data, the system shown in Figure 2 processes 100 percent of all received ERTS video data.

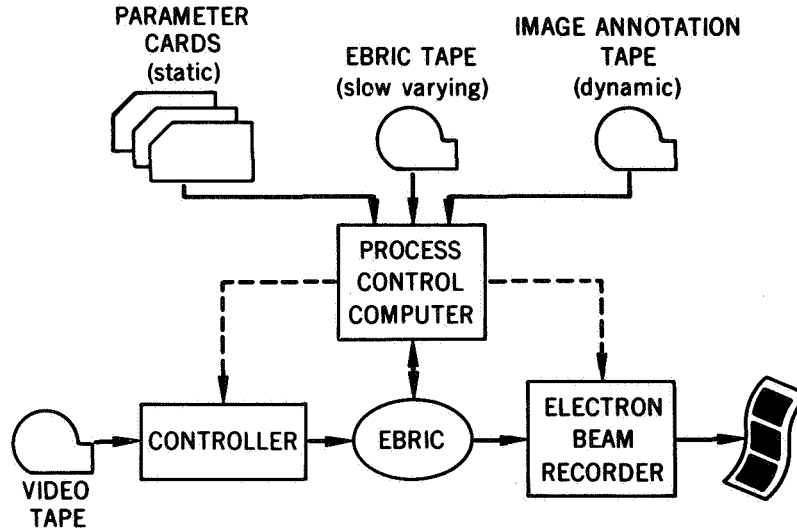


Figure 2. Initial image generation subsystem.

The EBRIC tape is generated using the EBRIC loop as shown in Figure 3. Here, another subsystem is used to calibrate the entire system. By processing video tapes through EBRIC in a nearly normal fashion (using a current EBRIC tape), a film copy is generated. After photo processing, the image is entered into viewer-scanner equipment within the scene correcting subsystem. The viewer-scanner equipment operates with its own dedicated process control computer as it measures the radiometry and geometry of the image. Automatically, a new EBRIC tape is generated which reflects changes which have occurred over the past several weeks. This new EBRIC tape is then brought into the initial image generation system where it becomes a current work tape for one or two weeks.

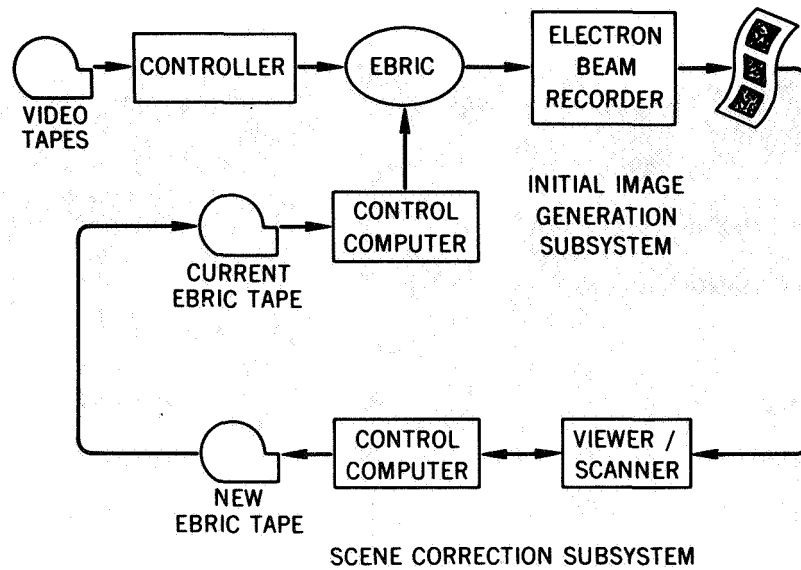


Figure 3. EBRIC loop.

In Figure 4 is shown an example of EBRIC correction. On the left is an uncorrected multi-spectral scanner image of southern California. On the right is a corrected image. There are many corrections in the picture on the right. The only one immediately obvious is that of skew; and this is put in by EBRIC to compensate for earth rotation as a function of latitude. As a measure of performance, USGS measured an ERTS image and found that the geometric correction given by EBRIC was within 70 meters rms.

In summary, an on-line correction capability has been satisfied by the design and implementation of EBRIC; and by the way in which EBRIC is configured with the total ERTS system at the Goddard Space Flight Center.

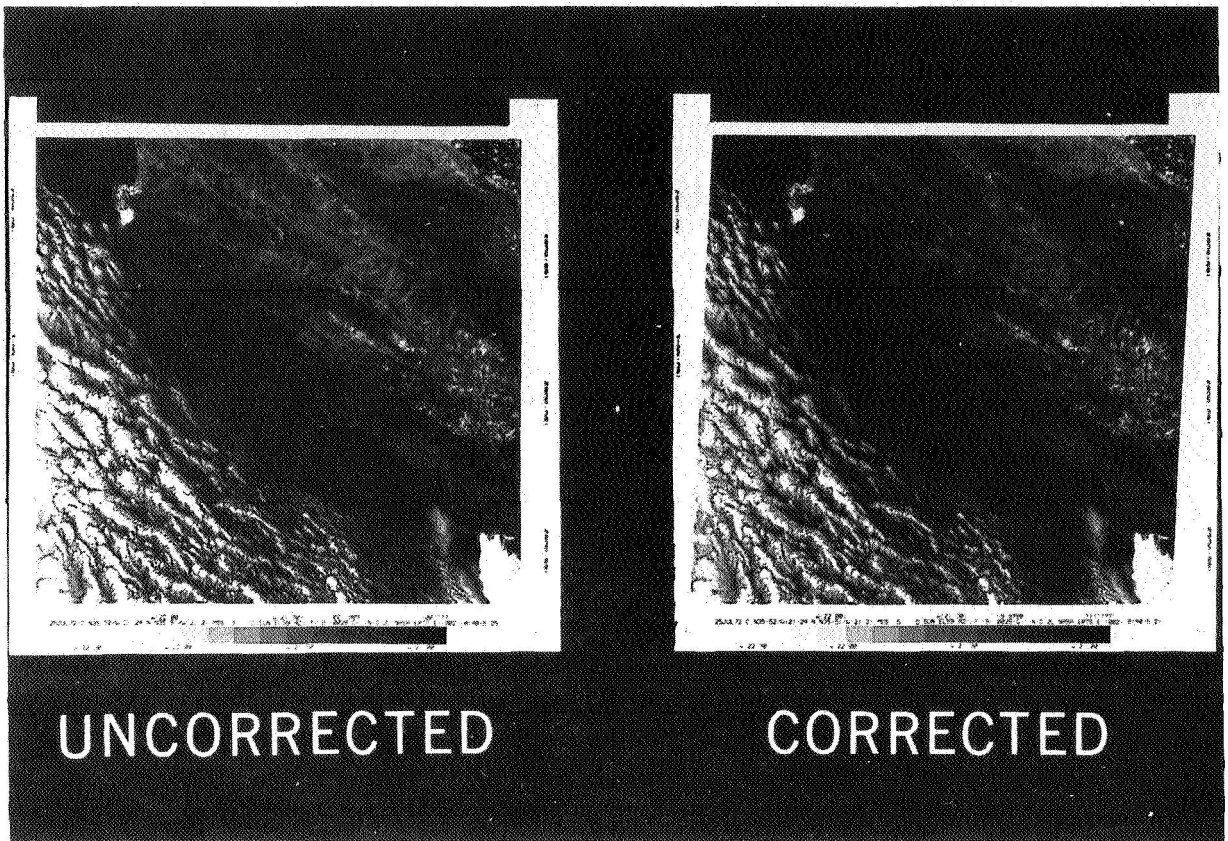


Figure 4. Example of EBRIC correction.

A PHOTOGRAPHIC PROCESSING CONTROL METHOD FOR ERTS IMAGERY

Bernard Peavey

The ERTS NASA Data Processing Facility (NDPF) is required to produce large quantities of film products (transparencies) with extremely high radiometric quality. This required quality (or accuracy) is not only unique to NDPF's Photographic Laboratory, it is also unprecedented in the history of photographic processing. The variation in density range must be limited, and tone reproduction must be uniform and consistent all the time. The stringent radiometric accuracy is necessitated by the fact that significant scientific information is presented in very small changes in radiance, and hence density. Such changes can be as small as 0.03 density units, and must be preserved by the photographic process. In addition, this degree of accuracy must be maintained consistently in order to permit comparison of temporal changes in the observed (imaged) scenes. Production of large quantities of transparencies (approximately 10,000 per day) having the required radiometric accuracy is made possible by the unique processing techniques, and by this processing control method developed and implemented in NDPF's Photographic Laboratory.

The photographic processing control method, hereafter called "the method," was developed to provide the capability of assuring production of high quality film products, detecting processing problems which adversely affect the required quality, and accomplishing these functions very accurately and rapidly to maintain production throughout. Because the information exposed on the actual film is not known in advance, an indirect approach is used to establish system performance and acceptance tolerances. This is based on exhaustive tests and analyses, which were conducted as part of the method development to confirm that the required accuracy would be achieved and maintained for all film products. Thus, special control targets were designed to encompass the required range of performance parameters (also called response variables), measurement and curve fitting techniques were implemented to collect performance data rapidly and accurately, and a feedback procedure was established to indicate what malfunctioned or was set erroneously. Basically, as shown in Figure 1, the method involves two operations: equipment certification, and process verification. Equipment certification exercises the equipment in a standard manner to assure that it is operational over the entire range of required capability before it is used for actual production. This is analogous to the calibration of a telemetry system, where the system is tested at given bit rate and SNR, and its performance is measured in terms of bit error rate. Process verification, on the other hand, is employed with every roll of film (which may be 30 to 45 meters long) to assure that the processing was in control for each particular product. It is noted that production of different products requires the equipment (photographic printers and processors) to be set up differently, thus providing opportunity for error.

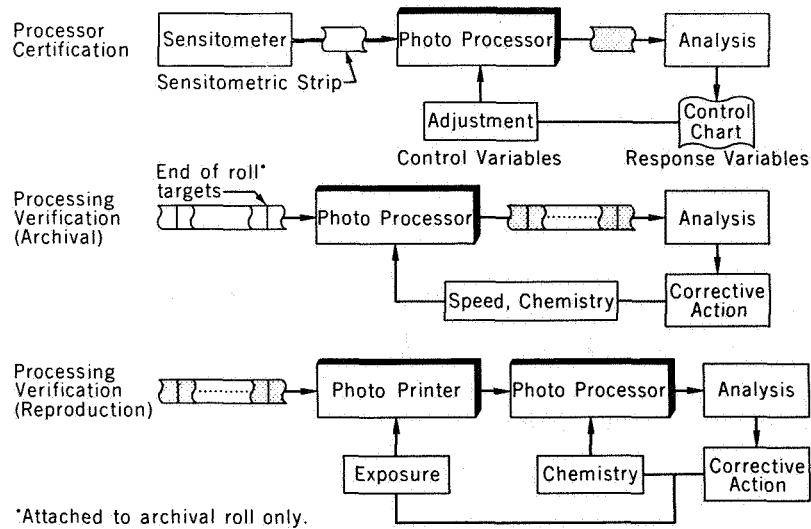


Figure 1. Photo processing control elements.

Both operations make use of control targets, i.e., sensitometric strips for equipment certification and end-of-roll targets (ERT) for process verification. These targets are depicted in Figure 2. They are produced by the sensitometer, which is a precisely calibrated exposing device, in a manner providing discrete levels of exposure, and hence density, to cover the range shown on the characteristic curve. The sensitometric strip is a standard 21-step gray wedge or tablet, whereas the ERTs are made of the same film as that used for archival products. The 22-step ERT is used to provide data on the average gradient, relative exposure, and base plus fog; whereas the five-step ERT is used to provide data on the density range variation and resolution. They are attached to the archival rolls only, and are carried with each subsequent generation to monitor reproduction fidelity. These characteristics or response variables represent and are a measure of the product quality. Therefore, by accurately determining these variables and applying the predetermined tolerances to them, the required quality of the output products can be and is maintained.

The particular target format and shape (circles) were chosen to allow rapid measurements with a standard densitometer. The five-step target contains five equal exposure levels (densities) distributed over the entire 70mm area in order to determine the processing uniformity, so that the measured density range is actually the variation of density over the target surface. The sixth spot is a standard Air Force tri-bar resolution target which is used to determine the processing effects on resolution aspects.

The a priori known target exposure values are stored in a computer. In analyzing the processed targets, the corresponding density values are fed to the computer for curve fitting. This procedure minimizes measurement error. After having correlated the density values with the computer stored exposure values, the actual response variables are determined and displayed in real time. These response variables are then checked against their control limits

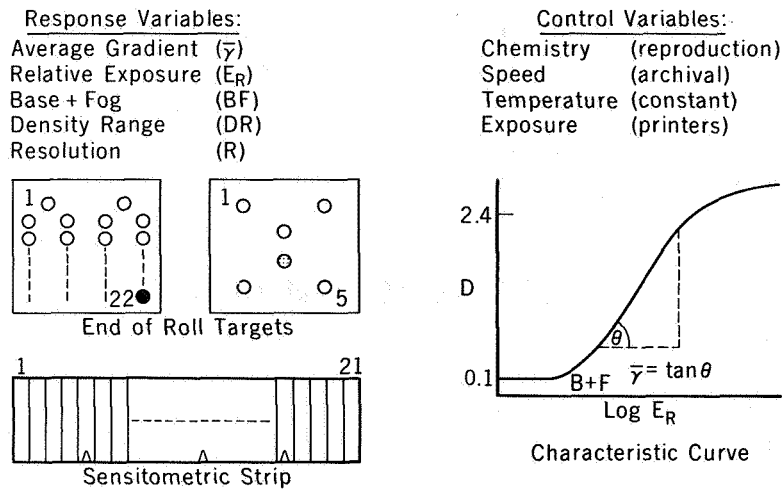


Figure 2. Response and control variables.

shown in Figure 3. It is seen that each response variable corresponds to a control variable (processing parameter) such as chemistry flow rate, processor speed m/s, exposure time, and temperature. Most of the time (90 percent) the response versus control variable relationship holds, and is used in taking corrective action when the control limits have been exceeded. In order to maintain the required accuracy, extremely tight control limits are imposed. This dictates the accuracy with which the response variables must be determined, since erroneous determination thereof will result in adverse reaction. The target analysis is performed in less than five minutes, and the course of action to be taken is determined almost immediately thereafter.

The method described herein proved to be an effective means by which high quality photographic processing could be maintained. The established control limits assure rendition of the required radiometric accuracy so as to preserve the dynamic range of the sensors in the produced transparencies. This method has been in use since launch of ERTS-1, and has been applied thus far to the production of more than 900,000 images. It is interesting to note that virtually no problem affecting the quality of images produced by the NDPF has gone undetected.

CONTROL LIMITS AND CORRECTIVE ACTION

$\bar{y} < \pm 6\%$ \longrightarrow Processor Chemistry
 $E_R < \pm 2.5\%$ \longrightarrow Printer Exposure
 $DR < 5\% (0.1)$ \longrightarrow Processor Chemistry
 $BF < 5\% (0.1)$ \longrightarrow Film, Printer, Processor

ATTRIBUTES OF METHOD

- Unique targets to match film and density range.
- Rapid measurement of targets and accurate determination of Response Variables.
- Minimum Control and Response Variables.
- Effective Control Limits to maintain required quality.
- Near real-time operation to optimize equipment utilization.

Figure 3. Method characteristics.

SECTION IV
COMMUNICATIONS AND NAVIGATION

OVERVIEW

James L. Baker

In the following presentations we will attempt to give a few samples of our work in communications theory and practice. Goddard is performing research and development throughout the entire communications spectrum; the results you will hear today encompass work from VHF through laser frequencies.

The objectives of our work in communications are:

- To make maximum use of the existing frequency bands
- To learn how to use higher frequencies
- To obtain knowledge on how to cope with interference phenomena
- To characterize and optimize the different communications and ranging channels
- To apply all these to the benefit of mankind

Using VHF for many years we've been accumulating data, and allocating assignments into an almost unbelievably crowded band. We've been trying to find ways to get around the problems of this crowding, and the effects of absorption, scintillation, and fading. We've also studied the effects of increasing power in the link, narrowing beamwidths, and using space and polarization diversity combining.

At millimeter wavelengths (MMW), we've been studying the effect of the troposphere by using the limited capability of ATS-5 at 15.3 and 31 GHz. The results of this work have played an extremely important role in the deliberations of the CCIR and its recommendations. A recent direct benefit is the help toward the design of the DOMSAT links, of which five of the eight proposals to the FCC utilized frequencies above 15 GHz.

The information was also instrumental in planning the Canadian technology satellite to be launched in 1975. A significant improvement in this data base of propagation information at different MMW frequencies will be provided by the ATS-F.

The work on the laser is still in the advanced research and development state when compared to the millimeter wave systems, and work on lasers is urgently needed, not only for future communications, but for its utility in accurately tracking the satellite to determine its position. The application of lasers to tracking of the spacecraft and determination within meters, is a sure way to obtain the high accuracy needed in the position fixing of ships and aircraft for surveillance, using a realtime computation of satellite position. This could be accomplished with a laser reflector on the spacecraft. Our plan is to continue to examine and

analyze the communication links of the spectrum from VHF through laser frequencies; but we need good and steady spacecraft transponders.

The status of our work over this communication frequency spectrum is that at VHF and microwave frequencies we have the tools, techniques, and years of data to better understand the severe ionospheric and exospheric perturbations in the equatorial region and the auroral regions caused by magnetic storms, sun spot activity, and other effects not yet completely understood. At MMW we have the tools and techniques, but not much data. Here the problem is rainfall and how to overcome its effects, which will be explored in great detail by the ATS-F experiments. At laser frequencies we are now developing the tools and techniques and have precious little data from spacecraft.

The problems we expect to be encountering in laser earth/space propagation are different, and can be more severe than at microwave and millimeter wave frequencies. The signal perturbations are due both to random changes in the atmospheric index of refraction, causing focusing and beam steering effects; and a reduction of total transmissibility due to clouds and fog.

The speakers who follow have done an outstanding job and are very motivated in the pursuit of their tasks, not only because their work is interesting but also because each can see a direct impact and benefit of his work in the design of communication and tracking links in satellite applications of space.

IONOSPHERIC FADING EFFECTS ON THE EQUATORIAL ZONE

Thomas S. Golden

Through the Goddard program of ionospheric scintillation investigation, we made a discovery of major significance to microwave communications from space. We have found that in the equatorial region, unlike the auroral region, there appears to be significant fading of microwave signals due to the effects of the ionosphere. Our observations at microwave frequencies have been from 1550 to 2300 megahertz. Channels in these bands have been allocated for manned and unmanned spacecraft, and for traffic management satellite applications. By equatorial region I mean that region of the earth between plus and minus 25 degrees geomagnetic latitude. By auroral region I mean that region of the world between 60 degrees geomagnetic latitude and the magnetic poles. When I speak of scintillation fading, I mean that fluctuation of the received signal power caused by effects of a disturbed ionosphere.

In Figure 1 we see plots of received signal power as a function of time. The upper traces

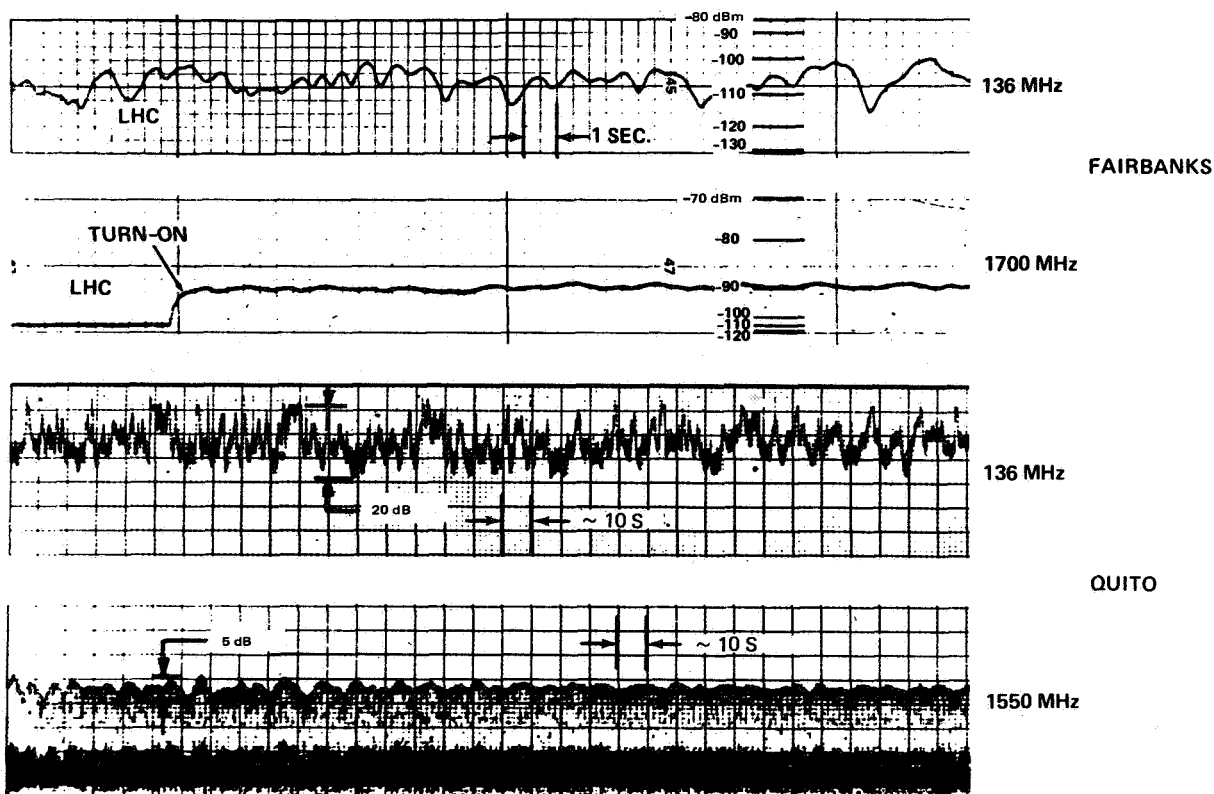


Figure 1. Comparison of VHF and microwave fading in the auroral zone (microwave 1700 MHz) and the equatorial zone (microwave 1550 MHz).

are from the auroral zone at Fairbanks, and were recorded simultaneously from a weather satellite at 136 megahertz and 1700 megahertz. The important thing here is that while the intensity of the 136 megahertz fading amounts to about 14 dB, the fading at 1700 megahertz is essentially negligible, about 0.6 dB. This behavior follows a theoretical inverse frequency dependence, which is as predicted for these fading effects. On the geographic equator at Quito, Ecuador, however, this inverse frequency dependence law is violated. The simultaneous records from ATS-5 show that at VHF, we saw 20 dB of fluctuation of the signal, and at the same time, we saw a surprising 5 dB at 1550 megahertz, or L-band. The bottom record appears the way it does because of the spinning of ATS-5 and it corroborates Jim Baker's statement that we are unable to extend beyond simple amplitude analysis because of the lack of a good satellite transponder at L-band.

Figure 2 shows us when fading is likely to occur in the equatorial region. Here we see a plot of the 136 megahertz fading events that were reported over an entire year of Mini-track operations at Quito, Ecuador. These operations were distributed more or less uniformly throughout all the hours of the year. Data are presented by the week along the longer axis, and by hour of the day along the shorter axis. The third, or vertical dimension is the percentage of the scheduled passes for which scintillation effects were reported.

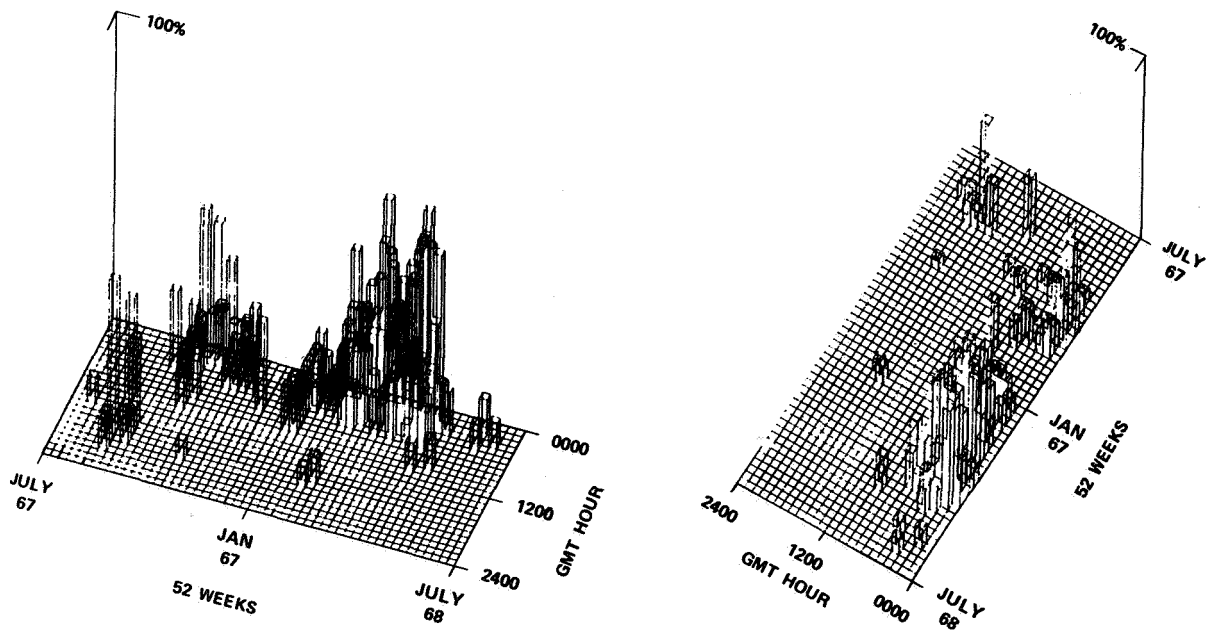


Figure 2. Three-dimensional plot of percentage occurrence of VHF scintillation effects shown as a function of time of the day and week of the year. Equatorial and nighttime predominance are illustrated.

While this represents VHF behavior, it's the kind of behavior our observations have led us to expect at microwave frequencies as well.

You can see in the right-hand picture now, that most of the events occur between 0000 and 1000 hours, Greenwich mean time. This happens to be during nighttime at Quito, since midnight there is 0500 hours.

The left-hand view of this same data shows another trend, namely, the increased percentage of occurrences around the weeks of the equinox. There is hardly any scintillation at all during the weeks around June and December. However, during the times of March and April and September and October, you can see definite behavior characteristics that have been identified as ionospheric scintillation. The important thing here is that the greatest probability of occurrence of fading in the equatorial region seems to be at night at the time of the equinoxes.

In Figure 3 we can see what the impact of this fading is on a communication link. This is a

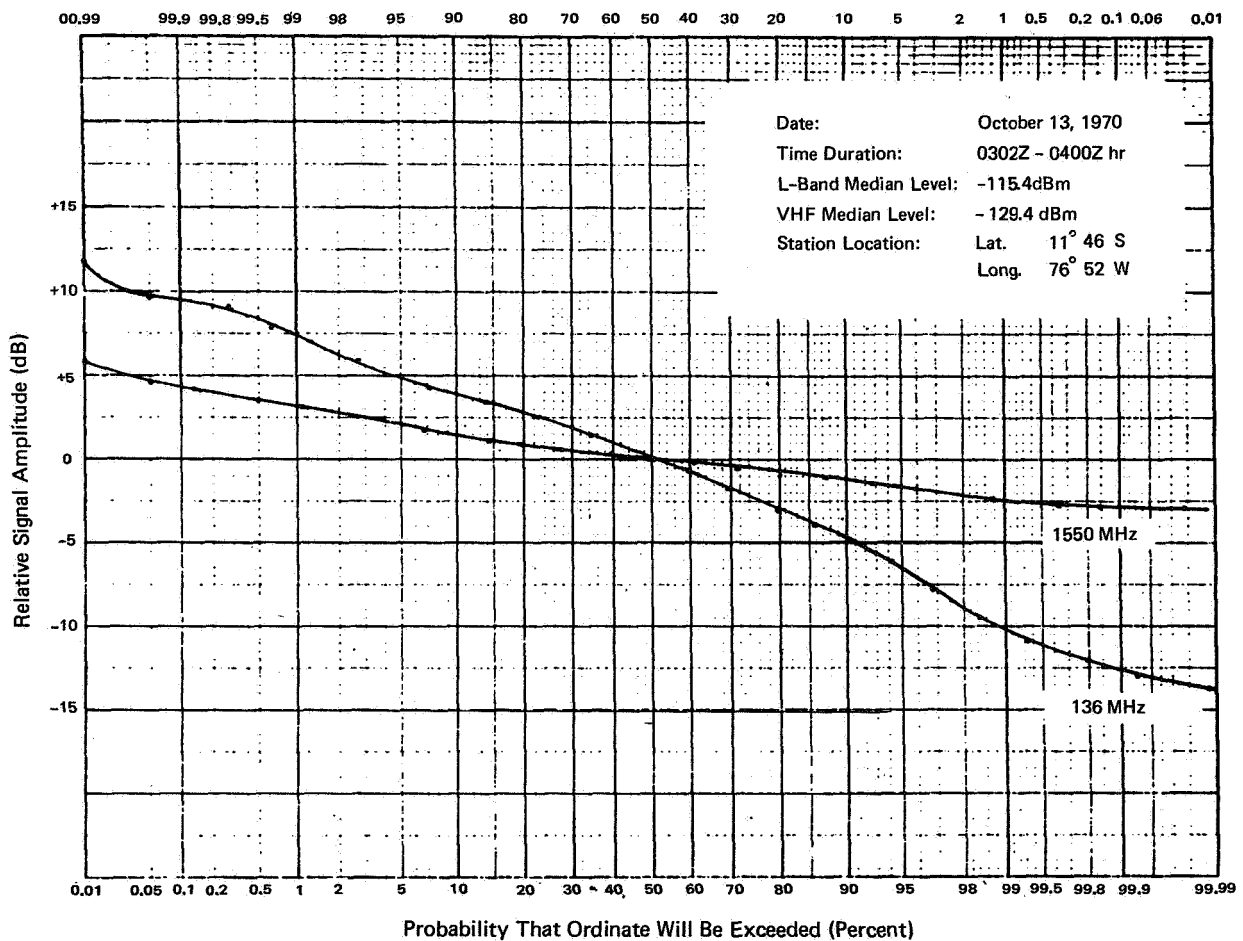


Figure 3. Typical fading in dB below the median signal value versus percent of time. Illustrates margin requirements for reliability of communication.

cumulative probability distribution of fading over a two hour period taken at Lima, Peru, on the geomagnetic equator. This curve means that for one percent of the time, read across the top, during this two hour period, the signal level for 1550 megahertz was 2 dB below the median level. Incidentally, the departure from median signal level is plotted in dB above and below zero. For 136 megahertz, this was 10 dB for one percent of the time. And for 0.1 percent of the time, at 1500, the fading is 3 dB below the median. This constitutes a serious problem to communication links if you have to communicate during periods of scintillation, since 3 dB essentially means two to one in transmitter power or channel capacity from your satellite.

The conclusion is that while fading occurs at night, around the times of the equinoxes, the fading depth is large enough that it must be considered in designing a space communications system. The magnitude of fading we've discovered at the equator violates existing theories for scattering, and constitutes a problem that must be reckoned with in system design.

ATS-5 MILLIMETER WAVE PROPAGATION MEASUREMENTS

Louis J. Ippolito

I'd like to describe the problems that would occur as we move up into the frequency bands where the wavelength is on the order of magnitude of raindrop diameter, and the rain therefore becomes a problem. The communication designer has to go to these higher frequency bands as more and more users require more and more bandwidth. Virtually all of our present communication links are at frequencies below 10 gigahertz, but systems are being designed to go to the bands above 10 GHz; it is necessary to define these bands, to determine the propagation problems, and to look at ways to overcome them.

The first flight experiment available to evaluate frequencies above 10 gigahertz was the ATS-5 propagation experiment, launched in August 1969. Figure 1 shows the basic configuration of the ATS-5 experiment. A downlink was available at 15.3 gigahertz with a full earth coverage horn to provide participants throughout the U.S. and Canada the opportunity to observe the signal over long periods of time. They had a chance to determine attenuation and fading characteristics as a function of rainfall rate and other meteorological parameters.

OBJECTIVES: TO DETERMINE THE PROPAGATION CHARACTERISTICS OF 15 AND 32 GHz EARTH-SPACE LINKS AND TO EVALUATE PERFORMANCE CHARACTERISTICS OF OPERATIONAL MILLIMETER WAVE SYSTEMS.

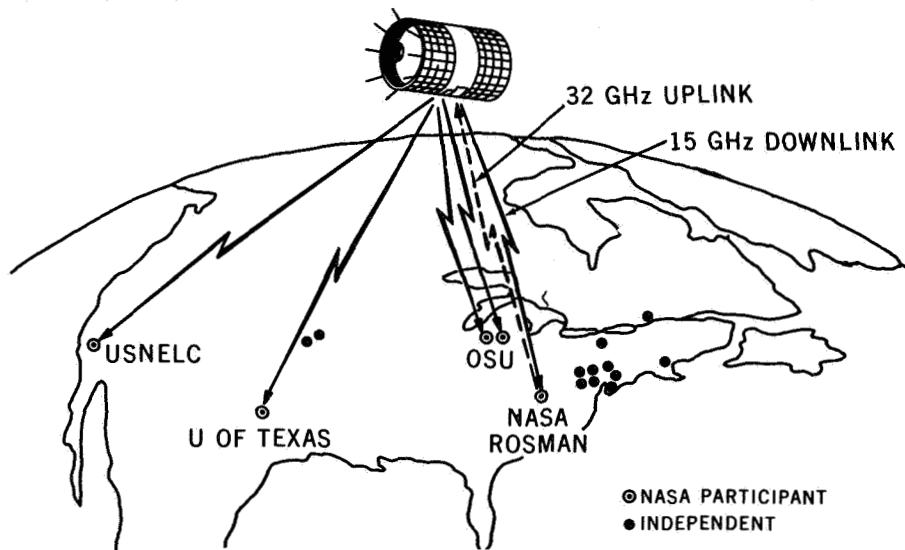


Figure 1. The ATS-5 Millimeter Wave Experiment, launched in August, 1969, provided the first operational earth-space link at frequencies above 10 GHz. Fourteen ground stations participated, with nearly two years of experimental measurements.

In addition, an uplink at 32 gigahertz was implemented at Rosman, North Carolina, to evaluate similar characteristics at the higher frequency band. Fourteen stations participated in the experiment during two years of satellite operations. Besides measuring the basic parameters, we studied the correlation of the attenuation with radiometric data, radar data, rain gauge data, and standard meteorological data.

I'd now like to discuss two of the major results of the ATS-5 experiment. First, the level of the attenuation that was experienced throughout the U.S. will be summarized; and second, a method to overcome the attenuation problem will be described.

Figure 2 gives an indication of the magnitude of the attenuation problem at 15.3 gigahertz. Here we see five locations where sufficient data were available to give a yearly statistic and the values in dB are the values required at those sites to maintain a 99.99 percent reliability. That is roughly a one hour a year outage time.

MEASURED POWER MARGINS FOR 99.99% RELIABILITY (ANNUAL BASE)

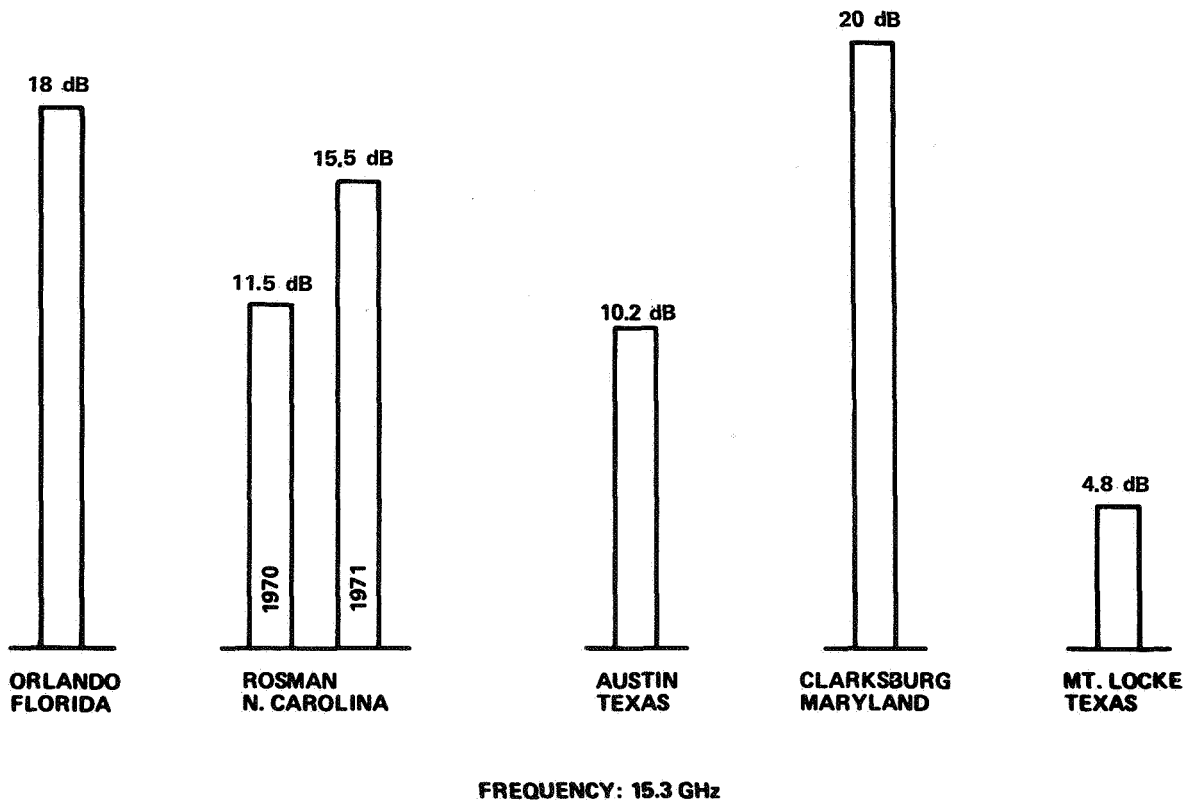


Figure 2. Measured attenuation at five locations showed large variations which did not coincide with the general weather profiles of each location. Also, annual measurements taken at one location (Rosman) for two consecutive years showed a 4-dB difference in maximum levels.

You can see, for example, at Orlando, Florida, which has a fairly high rainfall, an 18 dB margin was required to maintain a 99.99 percent reliability. The values range as high as 20 dB at Clarksburg, Maryland, down to fairly low margins in the desert area at Mt. Locke, Texas.

I'd like to make two points about this type of result. First, you can see that at Rosman, where we had two years of data available, the yearly margins differed by 4 dB. Therefore, looking at only one year of data can be sometimes misleading in determining site margins. The second point is that the sites are listed in order of decreasing rainfall towards the right; however, the attenuation statistics did not generally follow that trend. Note that Clarksburg, Maryland has lower average rainfall than three other sites, yet is showed the highest attenuation.

So, in summary we see that the margins can vary quite a bit, they can be quite severe, and they don't necessarily follow the expected results from rain gauge data.

There are ways to overcome attenuations of this type. We investigated the most promising technique—site diversity. In this technique, two ground stations separated by a few kilometers are utilized. Intense rain cells are usually quite small in size, and if the stations are separated by an adequate distance, there will be a high probability that only one site will be undergoing attenuation from the rain cell at a given time.

Figure 3 summarizes the measurements at Columbus, Ohio, where two sites were located, roughly four kilometers apart. The dashed arrows show the direction toward the satellite. Here we see the enhancement that diversity can produce. On the left are time plots of received signal power for a storm which passed over the two sites. The upper graph shows the attenuation experienced at site 1. A fade of about 10 dB occurred at site 1, but very little attenuation was noted at the second site. The attenuation moved to site 2 about ten minutes later.

We can look at this type of measurement over a long period of time, look at the enhancement we get, and the result is summarized in the plots on the right of Figure 3. The two upper curves show the attenuation characteristics of each site individually, for example, the attenuation exceeded 12 dB about 2 percent of the time at either site.

However, if we go to diversity switching, and select the site with the lowest attenuation, we get a tremendous improvement, e.g. for a 9 dB fade, we have about a 100 to 1 improvement or reduction in time outage. For a given percentage, we can reduce our margin by as much as 4 to 5 dB. We see here a very powerful technique to overcome the heavy attenuation problem when percent reliabilities of 99.9 percent or better are required. In applications where reliabilities of this level are required, but you can't place the site in a low rain area, site diversity is a very powerful technique to overcome the attenuation.

SITE DIVERSITY MEASUREMENTS AT COLUMBUS, OHIO UTILIZING THE ATS-5 SATELLITE

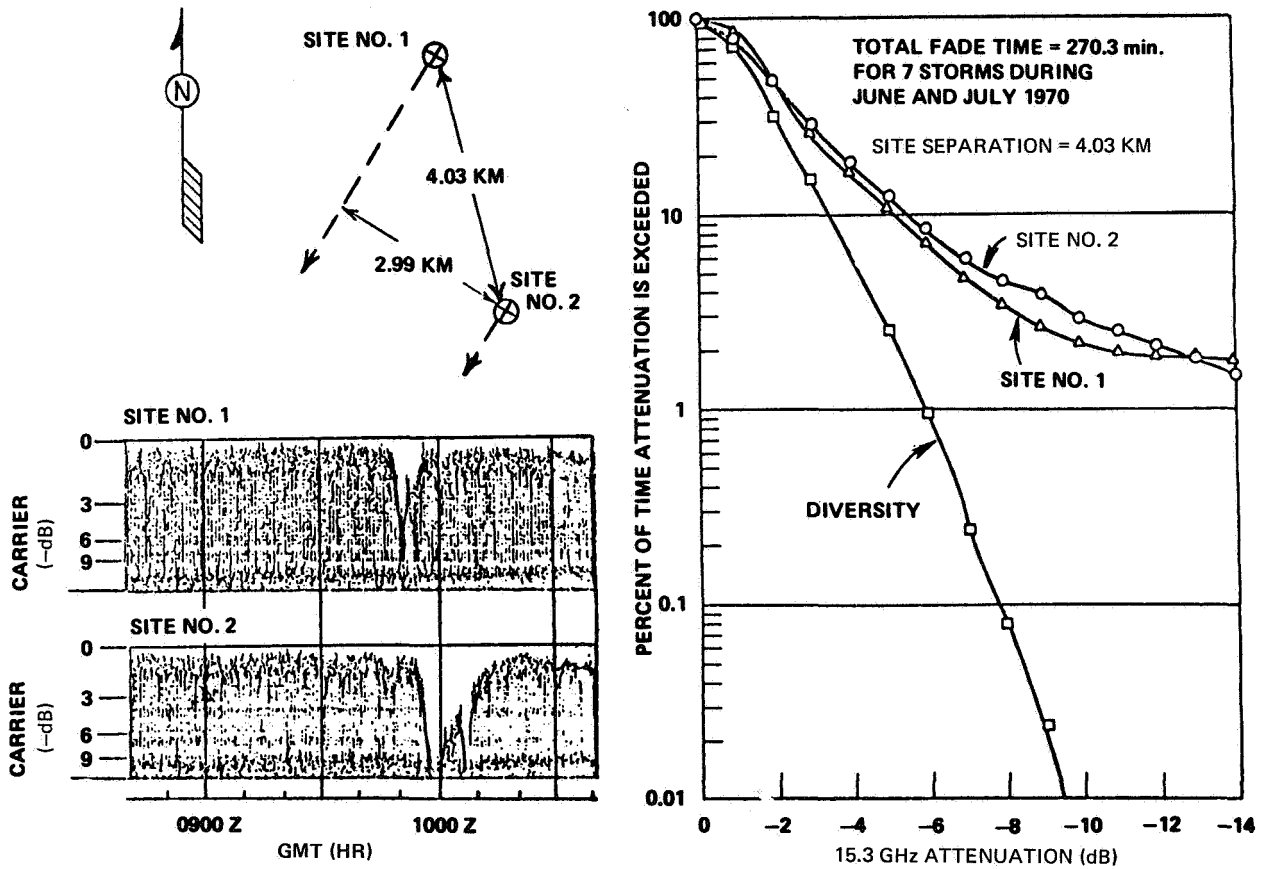


Figure 3. Dual site diversity with a 4-km separation showed improvements of 100-to-1 in outage time and 6-dB improvements in margin requirements over a single station.

COORDINATION PROCEDURE FOR RADIO RELAY AND COMMUNICATION SATELLITE SERVICES

Jerome Eckerman

When the communication satellite service was established in the early 1960s, the frequency bands allocated were shared in common with the microwave relay service, which is the widespread network of terrestrial microwave line-of-site links. The problem of interference between receivers and transmitters of the microwave relay service on the ground and the communication satellite service was anticipated; and rules, called siting criteria, were established for siting ground stations.

In 1963 at the International Telecommunications Union Extraordinary Administrative Radio Conference, the sharing criteria for these services was based on the then available propagation data, which considered only troposcatter and ducting type mechanisms. The very important mechanism of rain scatter was not well enough in hand, and because of this technology gap the drafters of the regulations omitted precipitation-scattered interference from inclusion in the regulations.

It was anticipated that at the next World Administrative Radio Conference in 1971 the procedures would be updated. The Office of Telecommunications Policy in 1968 requested that NASA establish a large program to develop the models and perform the experimental verification to demonstrate that the models were correct, so that there could be such a modification of the siting criteria.

Figure 1 shows how this is handled. The siting criteria, which includes rain, is quantitatively described by a coordination distance. This is a contour around a ground station, such that relay links outside this contour are unlikely to provide interference signals above some desired level for a given percent of the time.

The ingredients in this "rain" coordination procedure which was established required a rain storm cell size, a statistical description of the rainfall rate within the cell valid for most of the earth's surfaces. Also required was the use of certain approximations, for instance, Rayleigh scatter, constancy of the precipitation with altitude, and an analytic relation between radar reflectivity and rain rate.

One of the very important parts of the coordination procedure model was the global rain rate statistic model. This was the key to linking the propagation statistics to measurable meteorological statistics. Data from ten years and 67 National Weather Service rain gauge network stations were statistically analyzed. We found that we could divide the United States into five climate regions, based on total yearly rainfall, number of thunderstorm hours per year, and so on.

When we extended this model globally, we divided the world, as seen in Figure 2, into the five types of climate regions where the parameters were the same as in the U.S. Finally, in each climate region, numbered 1, 2, 3, 4, 5, you see the surface rainfall for clock-minute surface rainfall rates in millimeters per hour, versus percent of the time in which that rainfall rate is exceeded.

In Figure 3 I've shown a typical plot from the coordination procedure as it was adopted at the World Administrative Radio Conference last year; this is for Rain Climate Region 2, which is the one we live in. Frequency is along the abscissa. The parameter shown on the curves is the transmission loss; and the coordination distance required for this frequency is shown on the ordinate.

Hearings are being held by the FCC for the procedure's adoption into the domestic satellite regulations; Office of Telecommunications Policy is considering adopting this for the Department of Defense Systems.

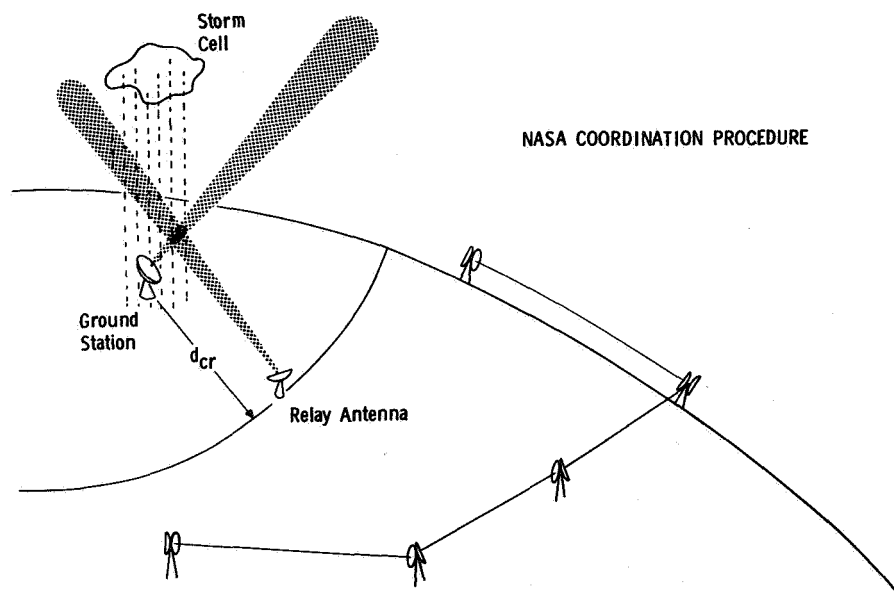
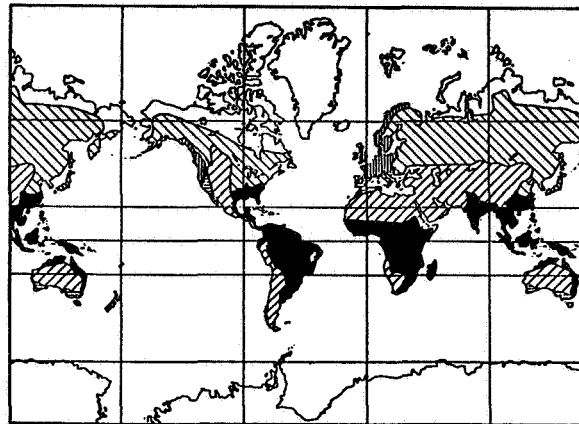


Figure 1. A coordination procedure which includes the effect of precipitation was developed in an extensive program by NASA at the request of OTP. This procedure has been adopted by the WARC.




 1
 2
 3
 4
 5

Regions corresponding to rainfall rate distributions of Fig. 3

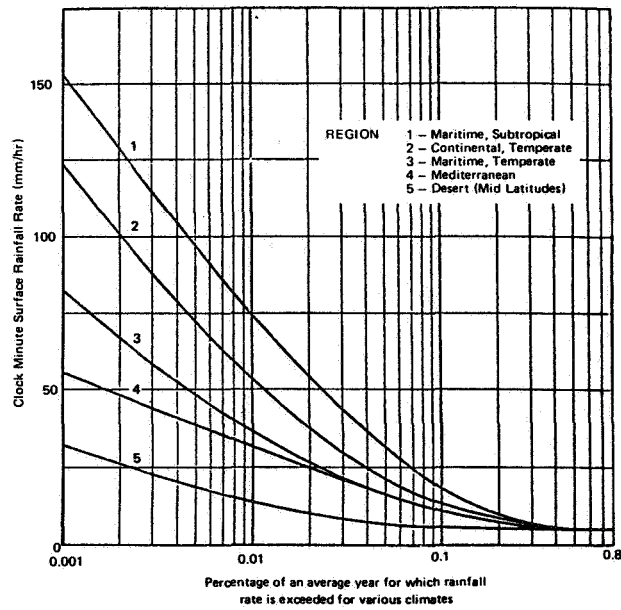


Figure 2. This global rainfall statistics model is an important element of the model on which the coordination procedure was based.

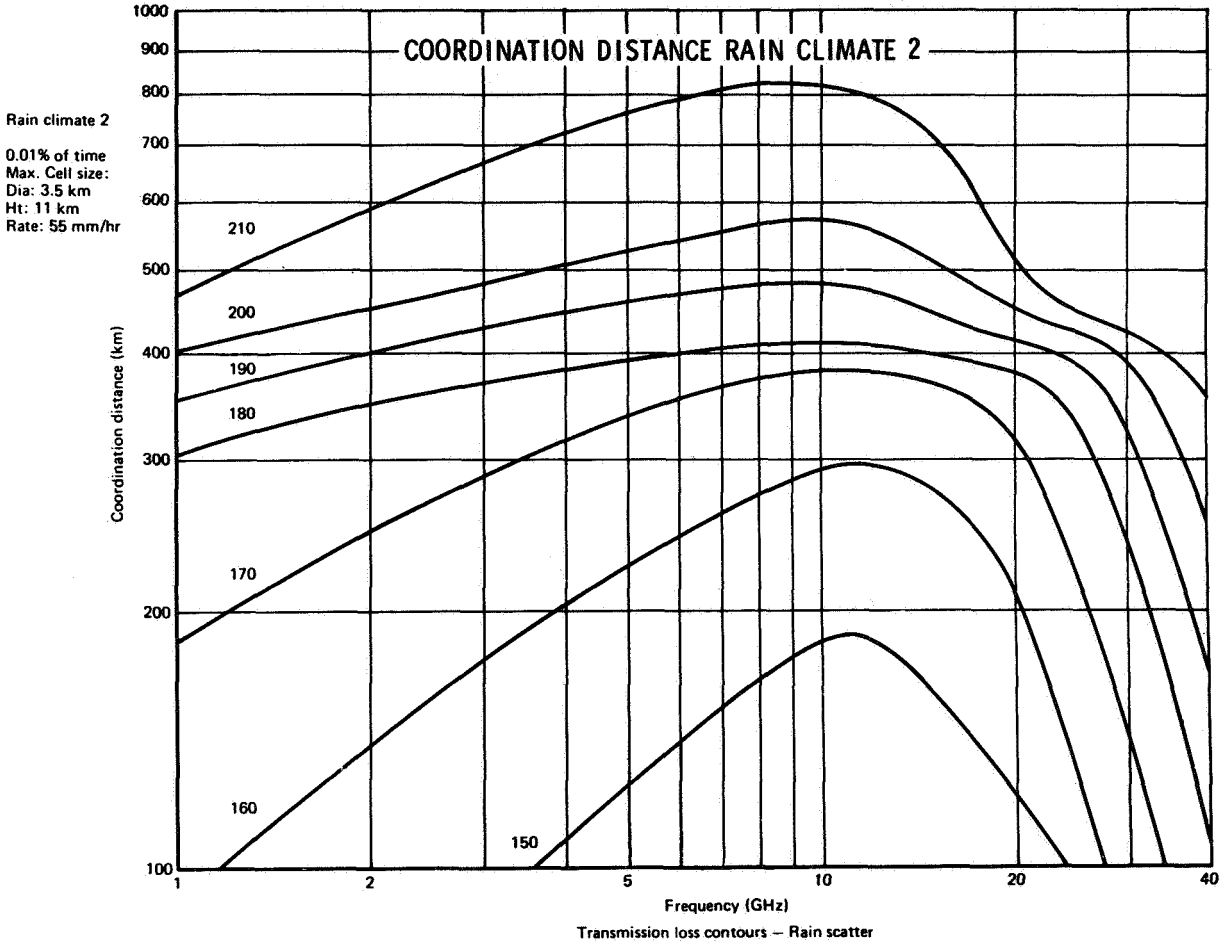


Figure 3. The analytical procedure upon which the coordination procedure was based is conservative, resulting in reduced chances for interference between services.

BALLOON ATMOSPHERIC PROPAGATION EXPERIMENT MEASUREMENTS

Peter O. Minott

The use of visible and infrared lasers for communication between ground and spacecraft has advantages over present radio frequency methods of higher bandwidths obtainable and smaller satellite transponders. The Laser Data Systems Branch has been actively developing both the visible Neodymium-Yag laser and the infrared carbon dioxide laser as communication devices.

Figure 1 illustrates the type of systems we have under consideration. The figure shows

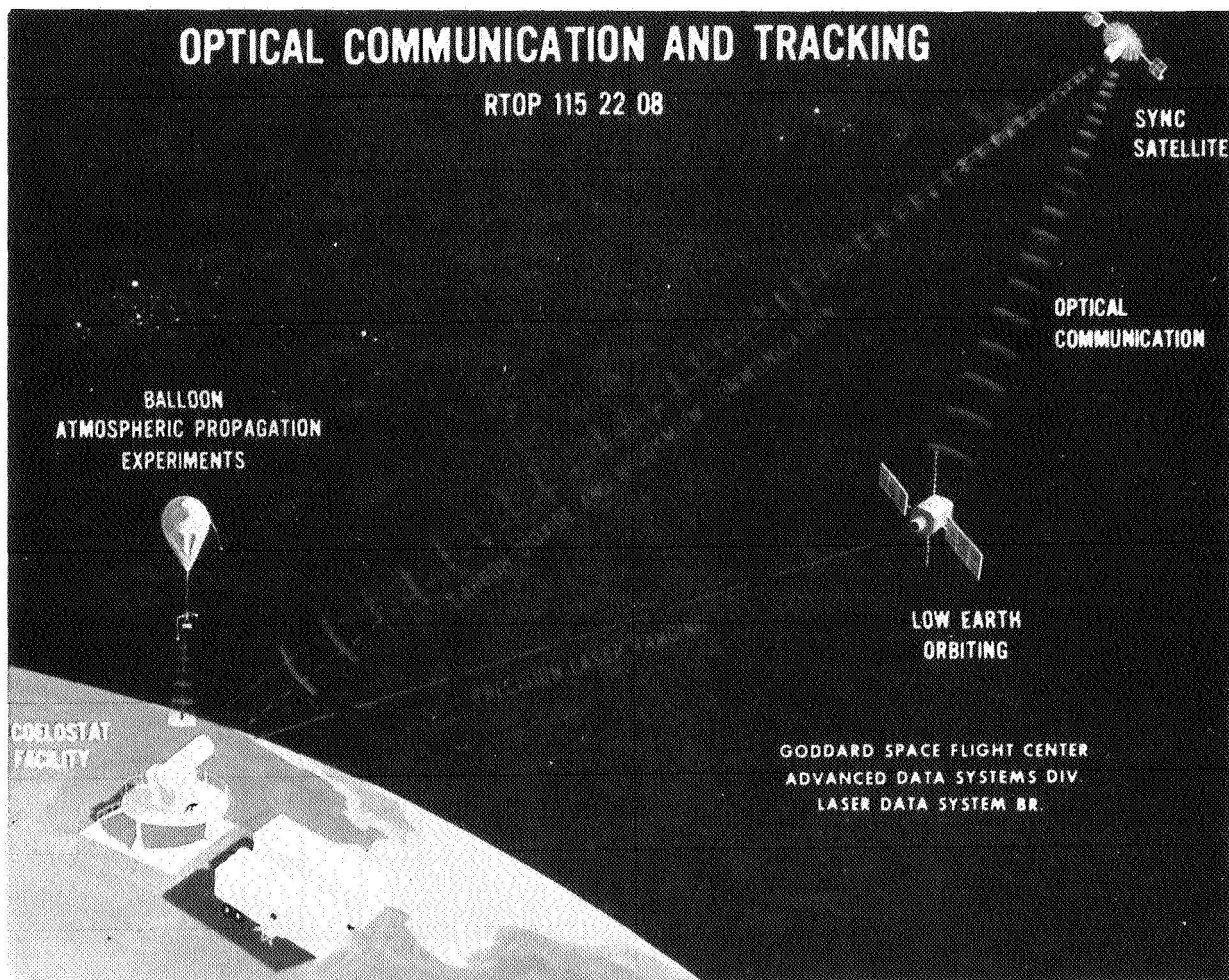


Figure 1. Fading caused by atmospheric turbulence on a space-to-ground laser propagation path seriously degrades pulsed binary laser communications, by a degree which may be much greater than predicted from stellar scintillation studies.

that our interest is in high data rate, in two-way communications between a synchronous spacecraft and the ground; as well as between low earth-orbiting spacecraft and synchronous spacecraft, for data relay purposes.

One of the key problems in using lasers for duplex earth-to-space communications is the fading and distortion of the transmitted signal caused by turbulence in the atmosphere. In order to measure these atmospheric effects, the Laser Data Systems Branch has performed a series of laser propagation experiments, using instrumented payloads on high altitude research balloons. The balloons were well above the altitude at which atmospheric turbulence occurs.

The high altitude balloon is used to simulate the spacecraft end of the propagation link. My discussion today is on the results of these experiments, which are applicable to the visible Neodymium-Yag laser communications systems.

A typical picture of the fading of a light beam propagating through the atmosphere is shown in Figure 2. The data, which was taken by observing a star with a 15-centimeter aperture, demonstrates that the fading is a completely random function of time, and can be quite severe.

Most of the available data comes from observations of stellar fading, or scintillation. But this data is not necessarily the same as would be observed from a laser, because starlight

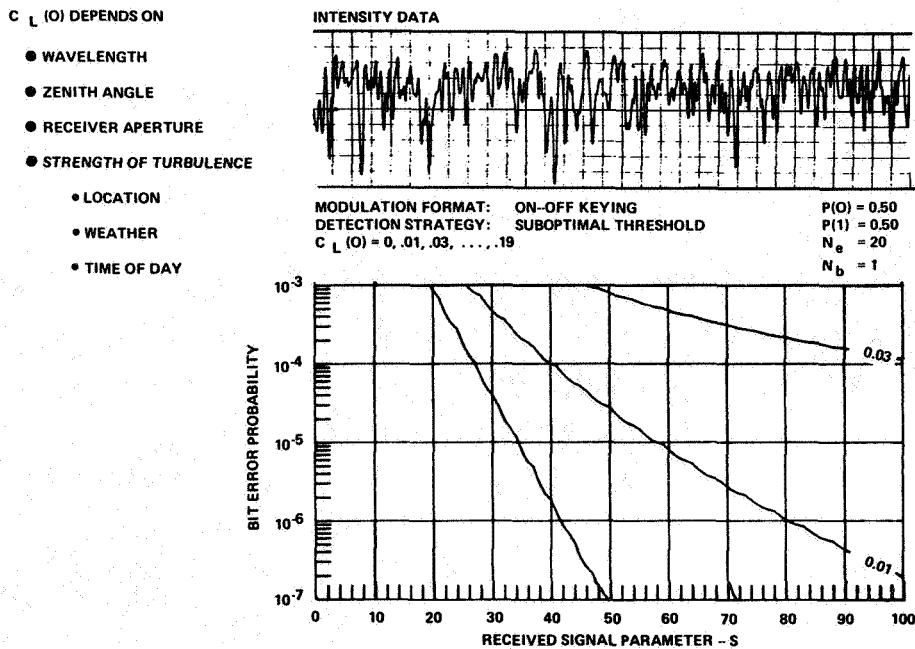


Figure 2. Fading can be predicted based on a knowledge of the strength of fading and the correlation of fading between two points derived from measurements made with a ground-to-balloon propagation experiment.

is not as monochromatic or coherent as a laser.

One of our objectives was to compare stellar fading with laser fading. We know that the strength of fading, which is measured in terms of the mean square deviation of the logarithm of wave amplitude (called "log amplitude variance") is a function of the parameters shown in the list on the left-hand side of the figure.

The graph on the lower right of the figure shows a relationship between system bit error rate and signal photoelectrons per bit for a pulsed Neodymium-Yag communications system operating in a typical modulation mode.

The graph shows the bit error rate in the presence of various degrees of atmospheric fading. Clearly, even a small amount of fading, as shown by the $C_{\ell}(0)$, equals 0.03 line. This requires a substantial increase in system margin to maintain a fixed bit error rate in the presence of fading.

In order to characterize the strength of fading, we have obtained the data shown in Figure 3 from our balloon experiment. The first chart shows the cumulative probability of log amplitude variance, and it is plotted in such a manner that a straight line indicates a log-normal distribution of fading.

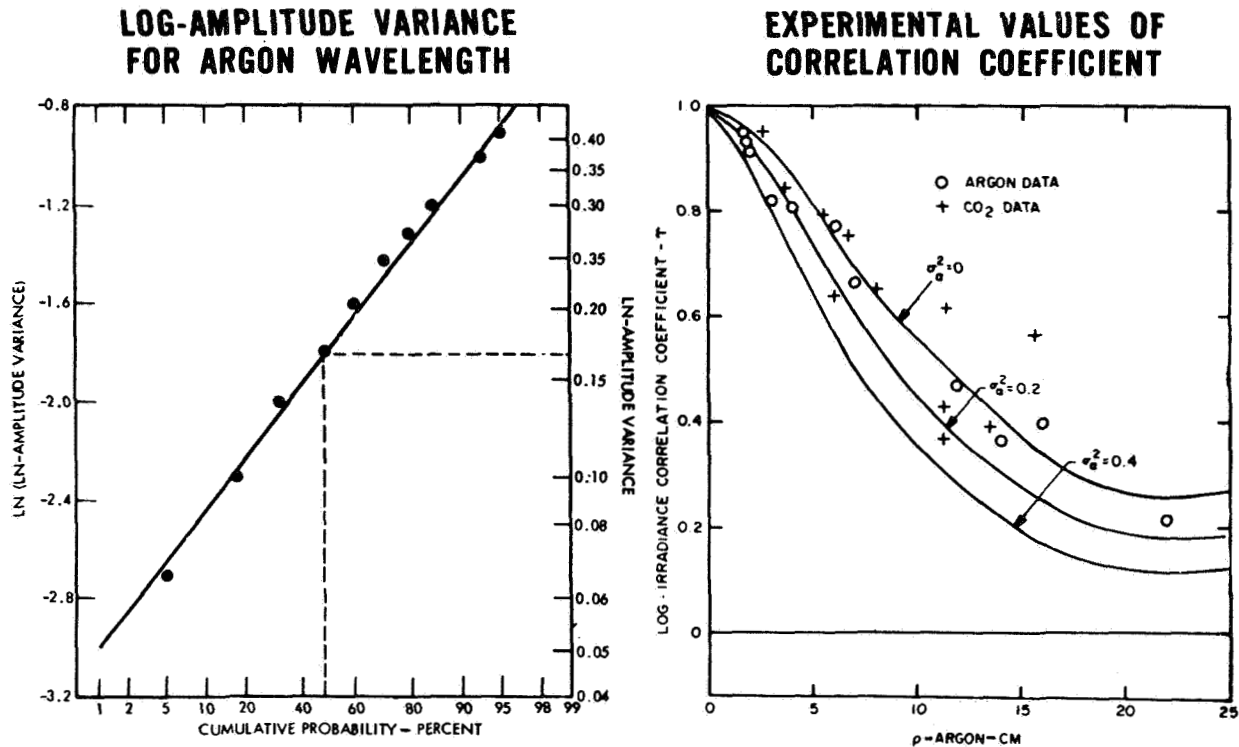


Figure 3. From the results of our experiment, fading caused by turbulence can be predicted for any aperture receiver and is well correlated to stellar scintillation magnitudes.

The second curve shows the correlation between fading at two points in the receiver plane separated by a distance ρ , in centimeters.

The data were taken for both the Argon wavelength, which is 5145 Angstroms, and the CO₂ wavelength of 10.6 microns. Using these data, we can predict the variance of the signal in a large aperture telescope.

Figure 3 shows the result of our study. Strength of fading is predicted for lasers on the basis of the balloon measurements by the three lines shown in the figure.

This upper line is the maximum we expect (a plus 3 sigma value); the solid line is a mean value; and the minimum is a minus 3 sigma value. On the vertical axis, we have the rms signal variation divided by the mean signal level in logarithmic coordinates; and on the horizontal axis, we have the receiver aperture in meters.

The values for stellar scintillation from a number of different authors are plotted in Figure 4 and indicate a good correspondence between stellar and laser scintillation. Beyond an aperture of about ten centimeters, the standard deviation of the signal decreases as approximately the reciprocal of the diameter.

This graph also gives an indication of the magnitude of the strength of scintillation. Using this data, we feel we will be able to predict the bit error rates for Neodymium-Yag laser communications systems.

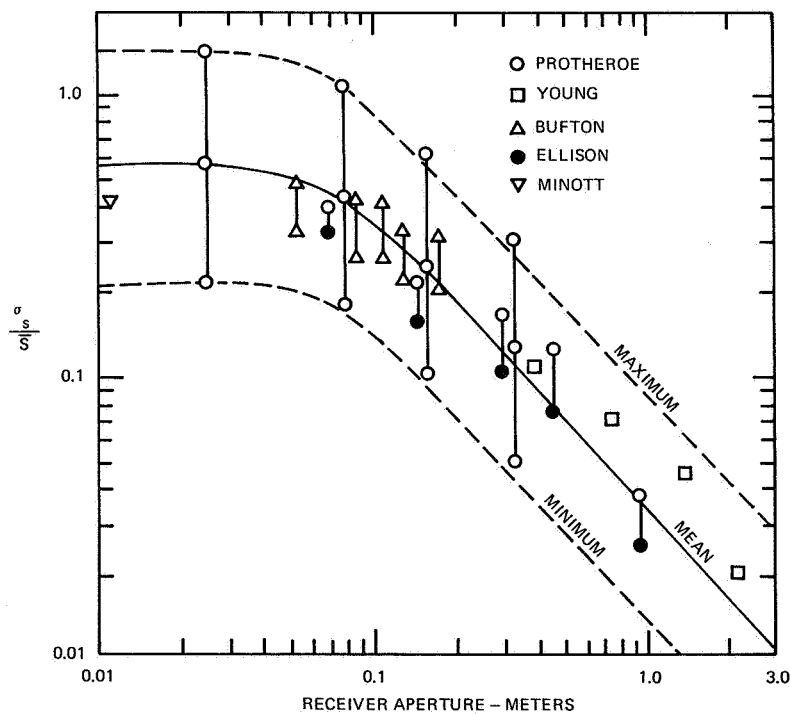


Figure 4. Scintillation as a function of receiver aperture (nighttime - 45° zenith angle).

THEORETICAL AND EXPERIMENTAL COMPARISON OF AN ULTRA-HIGH-SPEED LASER DATA TRANSMISSION SYSTEM

Mona Tycz

The performance of a digital optical data transmission system is specified by the probability that the system erroneously decides a signal has or has not been transmitted. Two factors which induce signal fading and thereby decrease system performance are atmospheric scintillation and transmitter pointing inaccuracy.

We can see in the first figure that a known signal, having been transmitted through the atmosphere, becomes a random signal at the receiver. Depending upon the physical model chosen to represent the atmosphere, it can be shown that the received signal intensity obeys log-normal, or the square of Ricean or Rayleigh, statistics.

We likewise see that if we couple transmitter pointing jitter with the far-field Gaussian intensity profile of a laser beam, then the received signal intensity will vary randomly, as the beam randomly jitters about the receiver. If we assume that the tracking-error signals at the transmitter are random, zero mean, Gaussian, and of equal variance on two orthogonal axes, then the received signal intensity will obey beta statistics. This received signal intensity can be completely described by the beta distribution, the ratio of the Gaussian intensity half-power, half-beam width, and the rms tracking error.

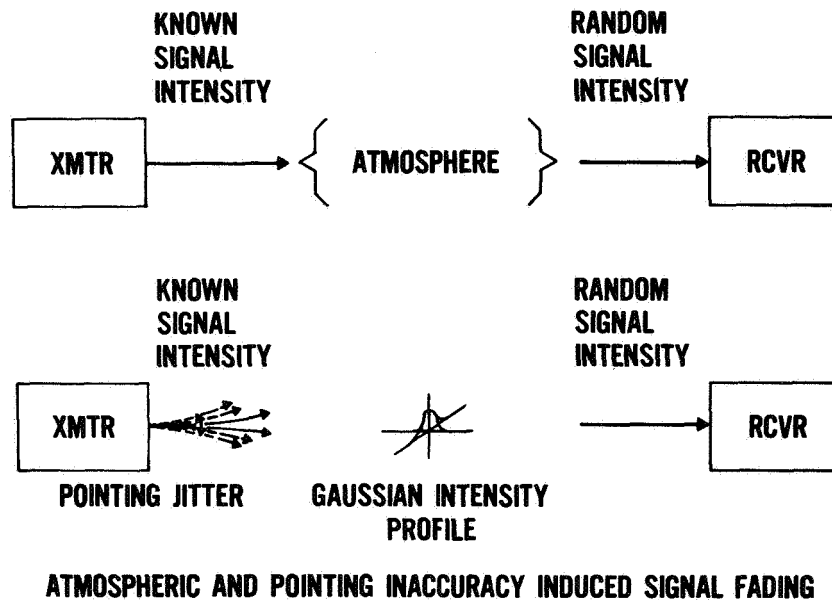


Figure 1. Optical communication system channels.

We currently have operating in-house a 400 megabit per second Neodymium-Yag Optical Data Transmission System. Since this system obeys or is governed by Poisson statistics, its performance cannot be specified by the well known signal-to-noise ratio. We have therefore conducted a theoretical analysis, in-house, of the system performance when subject to these types of perturbations. As to be expected, large families of performance curves are generated by varying such things as modulation format, receiver design, background noise levels and modulation extinction ratio. Therefore, we shall present only some typical results.

We have plotted in the second figure, for both curves, the system performance, or bit error probability, versus the average received signal when a binary 1 is transmitted for zero background and infinite modulation extinction ratio. The on-off key modulated signal in the figure to the right has been subjected to varying degrees of atmospheric scintillation; in the figure to the left, to varying degrees of relative tracking error. In both cases, the receiver incorporates adaptive thresholding techniques. That is, as the average received signal varies, the decision level which determines if a binary 1 or 0 has been transmitted will also vary.

Again, in both cases, the left most curve represents the system performance in free-space channel and is therefore a theoretical limit for the chosen parameters.

If we desire to maintain a system performance or probability of error of 10^{-6} , and assume that the system is subject to atmospheric scintillation of log-amplitude variance 0.01, or a

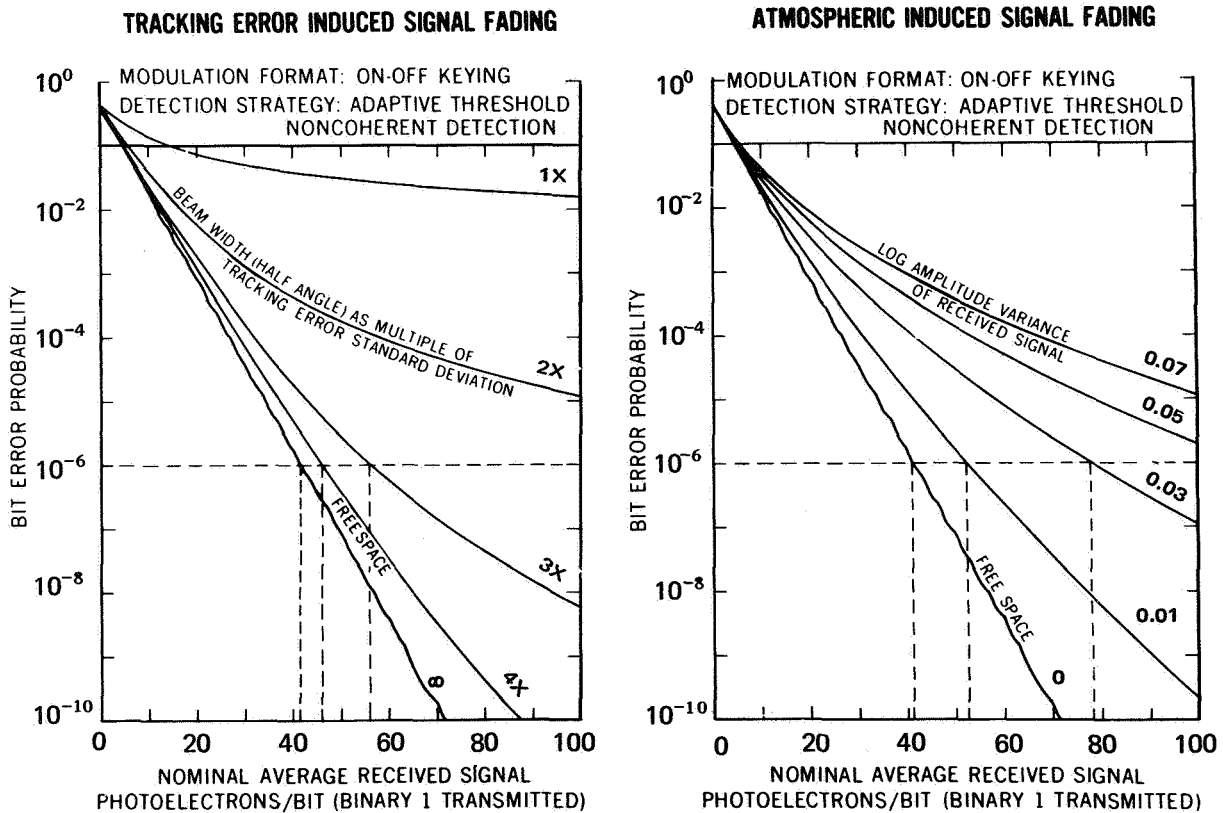


Figure 2. Binary optical communication system performance.

transmitter beam width to rms tracking error ratio of 3, then we must increase the received power by approximately one dB. This can be achieved in various ways; for example, by increasing the transmitter power or the receiver aperture diameter. This is obviously a trade-off between such things as system complexity and transmitter power requirements, or receiver weight.

In the development of any data transmission system, one needs not only an in-depth theoretical understanding of the system performance, but also a firm experimental basis upon which to proceed. We have therefore developed in-house a channel simulator, capable of producing the effects of both atmospheric scintillation and the transmitter pointing problem. Figure 3 demonstrates to us the functions of the channel simulator we currently have operating. It consists of a Gaussian noise source which is fed into analog processing electronics, which in turn drive a linearized acousto-optic modulator. The intensity transmitted through the modulator obeys the same statistics as the applied voltage. The processing electronics are capable of providing log-normal, Ricean, Rayleigh, or chi-squared random voltages for simulating atmospheric scintillation. The beta random voltages are for simulating the pointing inaccuracy induced signal fading.

The electronics consist simply of analog modules, multipliers, and the like, which perform the appropriate mathematical operations to generate the desired random voltages. The performance of the channel simulator is measured in terms of its ability to accurately simulate the desired channel. In Figure 4 we will look at the performance of the log-normal channel. We see there a comparison of data taken from the modulated intensity of a beam having been transmitted through the channel simulator, as compared to actual experimental data taken from the GEOS-B experiment.

The GEOS-B experiment consisted of an argon laser beam that was transmitted through the

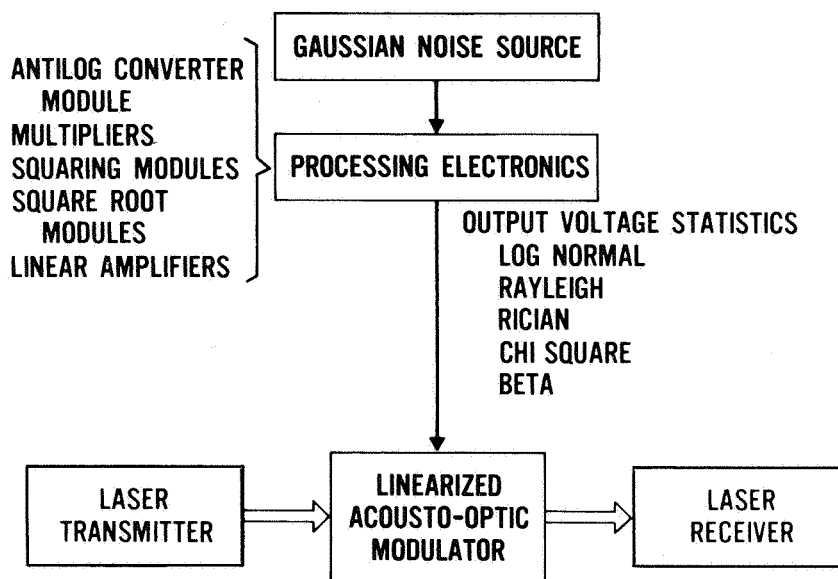


Figure 3. Channel simulator system.

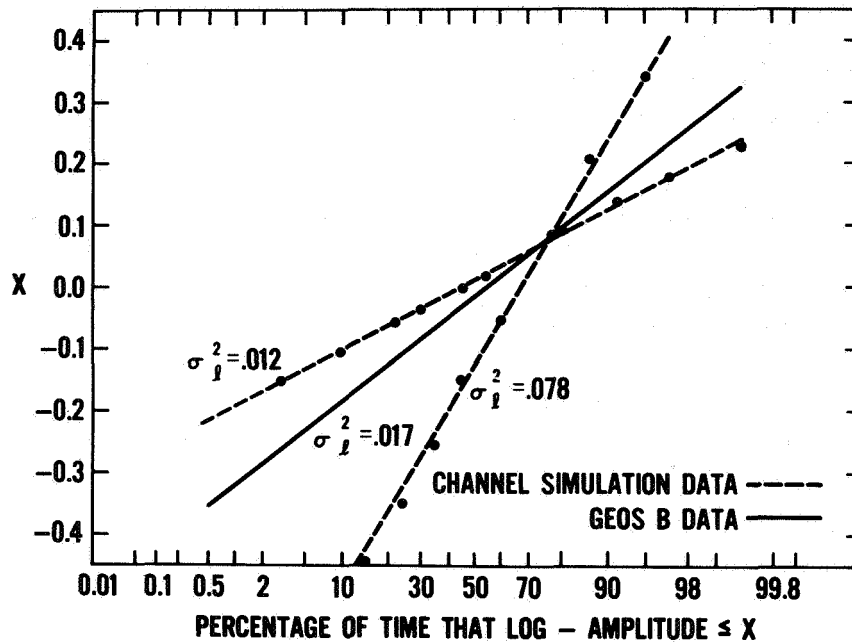


Figure 4. Comparison of channel simulator log-normal statistics with GEOS-B data.

atmosphere to a low earth-orbiting satellite. The received analog signal was then telemetered to ground. On ground, a statistical analysis was performed on the atmospheric scintillated intensity, and we see the resulting data plotted as the bold line.

We have plotted the range of values that the log-amplitude can take on versus the percentage of time that it is actually less than or equal to those values. The dotted or dashed lines represent data taken from the channel simulator. The linearity of the data indicates that the modulated signal intensity is indeed log-normal. The slope of the lines is indicative of the degree of atmospheric scintillation, which we can vary here from a log-amplitude variance of 0.01 to 0.08.

Similar tests, as well as the chi-square distribution test, will be performed for all channels of the channel simulator. Having completed this analysis, the channel simulator is to be incorporated into our 400 megabit per second Neodymium-Yag Data Transmission System. The performance of the composite system will then be evaluated and compared with the theoretical predictions.

THE WAVEGUIDE CO₂ LASER

John J. Degnan, III

A heterodyne laser communication system between a low earth orbiting satellite and a satellite in synchronous orbit is subject to a time-varying Doppler shift, due to the relative motion between the two satellites.

If we consider ERTS (Figure 1) as a typical low earth orbiting satellite, we obtain a peak shift of approximately plus or minus 700 megahertz at the 10.6 micrometer CO₂ wavelength. This peak shift occurs when the orbital plane of the low earth orbiting satellite contains both the synchronous satellite and the earth's polar axis.

At Goddard, we are presently building a double conversion receiver to track this Doppler shift. The transmitter signal is mixed with the laser local oscillator signal in an infrared mixer. The resulting signal is then passed through a wideband IF amplifier into an RF mixer, whose second input is provided by a VCO controlled by a phase-locked Doppler tracking loop.

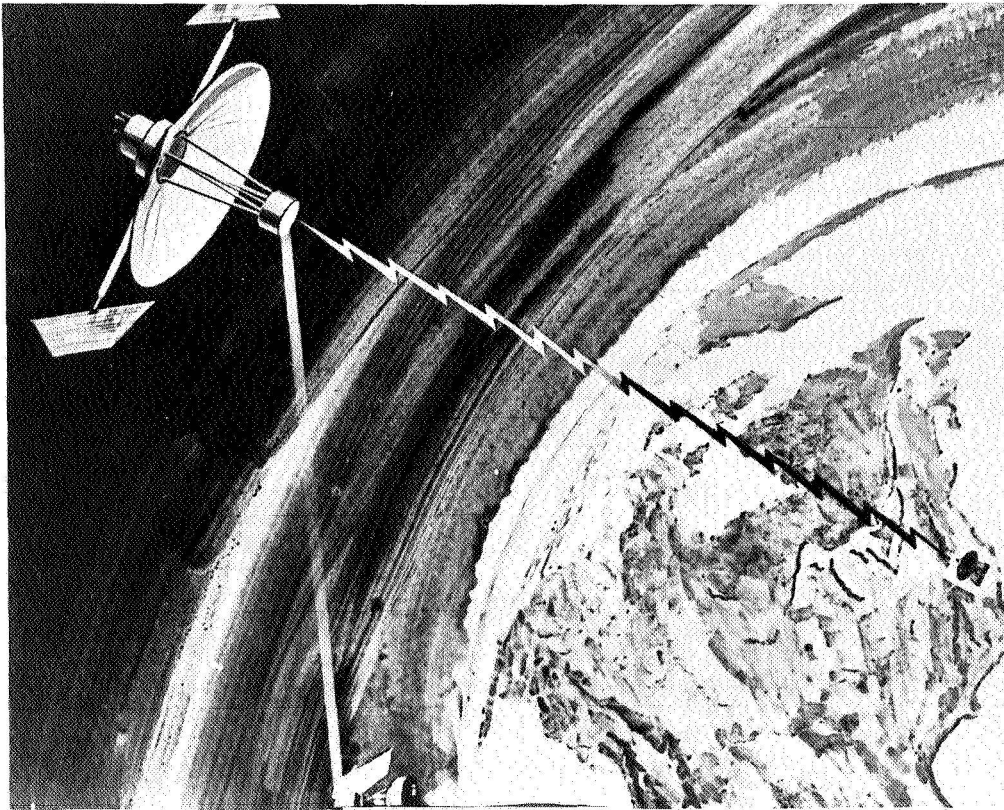


Figure 1. Low earth-orbiting to synchronous satellite laser data transfer line.

The effect of the motion on the frequency spectrum is shown at the top of Figure 2, where we've chosen the origin of the frequency spectrum to coincide with the center of the molecular line on which both the laser transmitter and laser local oscillator are operating.

At the peak Doppler point, the transmitter frequency is shifted by 700 megahertz with respect to line center due to the motion. We have assumed here a 300 megahertz information bandwidth superimposed on the center frequency.

As the satellite progresses in its orbit, this Doppler shift decreases until at the equator, where there is no longitudinal relative motion between the two satellites, the Doppler shift is zero. At this point, the laser local oscillator, which has been offset from line center by 200 megahertz, shifts operation to the opposite side of the molecular line. This avoids spectral fold-over as the satellite proceeds to negative Doppler values.

The difficulty with this scheme is the fact that we must be able to offset the laser local oscillator by an amount greater than one-half the information bandwidth that we're trying to send.

In this case, we've assumed a 200 megahertz offset, which is 50 megahertz more than the 150 we would need. The difficulty with this is that conventional CO₂ lasers have a tuning range of only plus or minus 50 megahertz. This imposes severe restrictions on the information bandwidth that we can send.

This problem has been relieved by the invention of the waveguide CO₂ laser, which is presently being developed at Goddard.

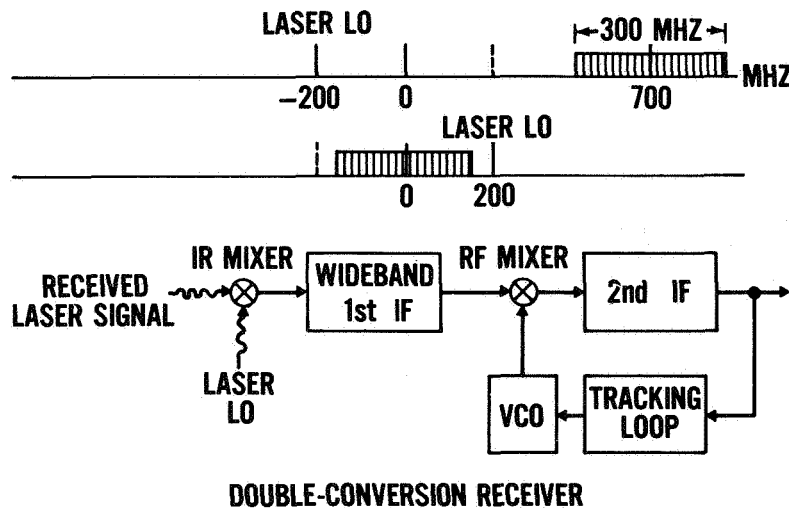


Figure 2. CO₂ laser oscillator tunability requirements and double-conversion receiver.

Briefly, the waveguide laser (Figure 3) is characterized by a very narrow capillary, typically 1 or 2 millimeters in diameter, which contains the laser gas mix. The smaller capillary results in a larger gain per unit length, which allows the device to be operated at pressures as high as 500 torr, compared to about 20 torr for a conventional CO₂ laser.

Pressure broadening of the molecular line accounts for the increased tunability of the laser.

In a waveguide laser, the capillary is placed between two reflectors which provide feedback to support the laser oscillation. Because loss is an important factor in determining the tunability of the laser, we have recently conducted at Goddard an extensive theoretical and experimental program to determine the effect of the various mirror parameters shown here on the coupling efficiency between the waveguide and the resonator.

This has resulted in a series of design guidelines for low-loss waveguide laser resonators. In addition, we've computed the near and far field intensity patterns for this new type of laser, and compared them to experimentally measured intensity cross-sections in the laboratory.

A third contribution that Goddard has made is the development of a new technique to determine two important laser parameters, G_0 , the small signal gain, and I_s , the saturation intensity.

These two parameters (plotted in Figure 4) are important in choosing the optimum operating pressure, the optimum discharge current, and also the optimum mirror reflectivity for the laser. Briefly, the method consists of placing a small coupling plate inside the laser resonator, and measuring the power reflected off the plate as a function of the plate angle.

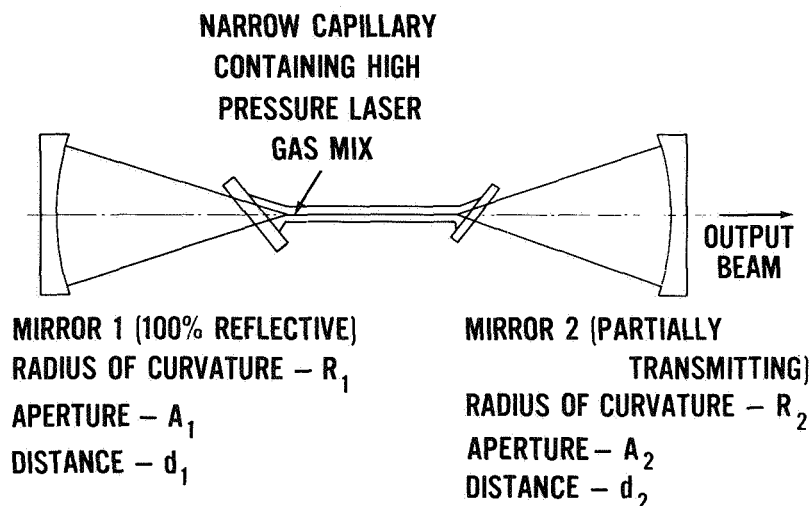


Figure 3. Schematic of a waveguide laser.

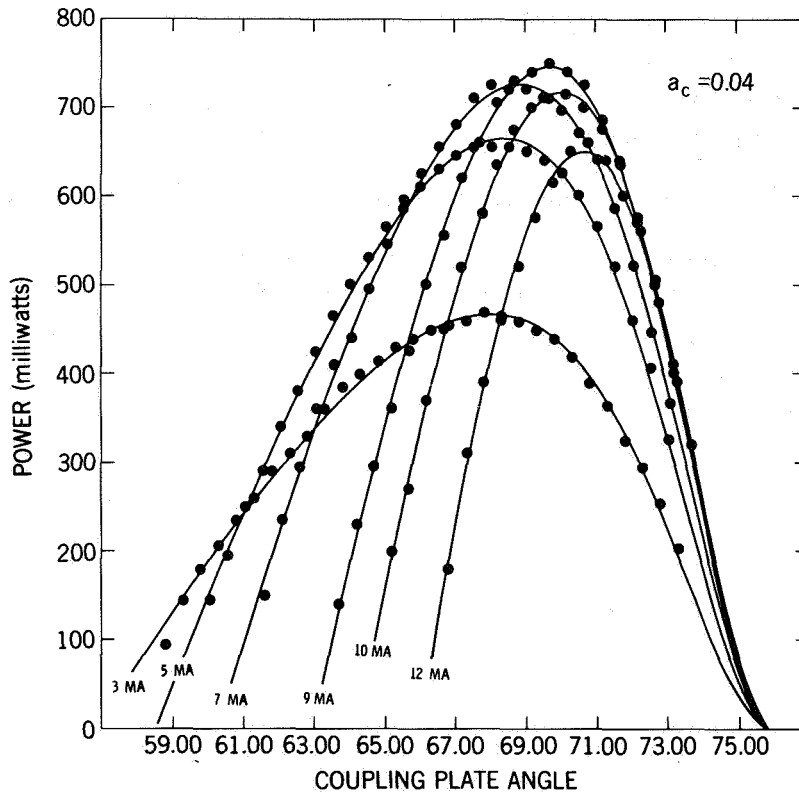


Figure 4. New experimental technique for measuring g_0 and I_s .

The data is then fitted, by a least squares method, to a theoretical curve, which depends on the two parameters of interest. Here we see a plot of the agreement between theory and experiment, where the power output is plotted versus the coupling plate angle. The Brewster angle corresponds to seventy-six degrees.

At the present time, the waveguide laser is capable of a plus or minus 200 megahertz tuning range. This is more than enough to accommodate a 300 megahertz information bandwidth. At the present time we are pursuing low loss methods of frequency selection, which will extend this range even further.

This would allow the transmission of larger information bandwidths and the relaxation of certain stringent mixer requirements.

THE CO₂ LASER FREQUENCY STABILITY MEASUREMENTS

Edward H. Johnson, Jr.

In the previous paper, one of the major problems with a laser receiver at synchronous altitude was discussed, that of Doppler shift, which can be as much as plus or minus 700 megahertz. Associated with that is also a maximum rate of Doppler change, which approaches a megahertz per second. I might add that the 10.6-micron laser frequency is 28 terahertz.

In addition to the problems imposed on receiver design that relate to maximum Doppler frequency and its rate of change, the stability of the laser is also of primary concern. Up to this date, we have had very little data on actual stability of the lasers in terms of phase noise, and in order to examine the problem and use it as an input into tracking receiver design, we implemented an experiment in the laboratory to measure and evaluate these stability effects.

Figure 1 indicates the objectives of the experiment. Primarily, we want to obtain experimental data on laser stability which affects the phase-lock loop tracking bandwidth, thus imposing minimum-bandwidth considerations. Another consideration is Doppler tracking performance. We would like to make phase-lock loop bandwidths wide for acquisition and tracking purposes; but conversely, we want to make them as narrow as stability will permit for best signal-to-noise ratios. The third effect is on a bit error rate. Our system is a coherent on-off keying system, and for that, the probability of making an error is, in general, one-half the complementary error function of the square root of the signal to four times the

EXPERIMENT OBJECTIVES

1. OBTAIN EXPERIMENTAL DATA ON LASER STABILITY FOR DESIGN OF 10.6-MICROMETER RECEIVER

- a) PHASE-LOCK LOOP TRACKING BANDWIDTH
- b) DOPPLER TRACKING PERFORMANCE
- c) EFFECT ON BIT ERROR RATE

$$P_E = \frac{1}{2} \operatorname{erfc} \sqrt{\frac{S}{4N}} \cos^2 \theta_{\text{rms}}$$

- d) FREQUENCY ACQUISITION

2. DETERMINE SOURCE OF INSTABILITIES OBSERVED

Figure 1. Quantitative CO₂ stability data required for receiver terminal design. CO₂ laser phase noise data not available.

noise. However, if there is an inability to reconstruct the carrier, you get a cosine square of theta-rms, which is caused by oscillator instability. Another concern is the problem of frequency acquisition. If it is possible to open your loop bandwidth wide, you can minimize frequency acquisition problems.

The second major purpose of the experiment was to actually look for instabilities in laser power supplies, acoustical vibrations, and other sources of instabilities.

The actual experiment configuration is shown in Figure 2. We used two CO₂ lasers, shown on the left, and with PTZ tuners, we were able to pull the frequencies of each laser until we had a nominal 20-megahertz beat frequency between the two.

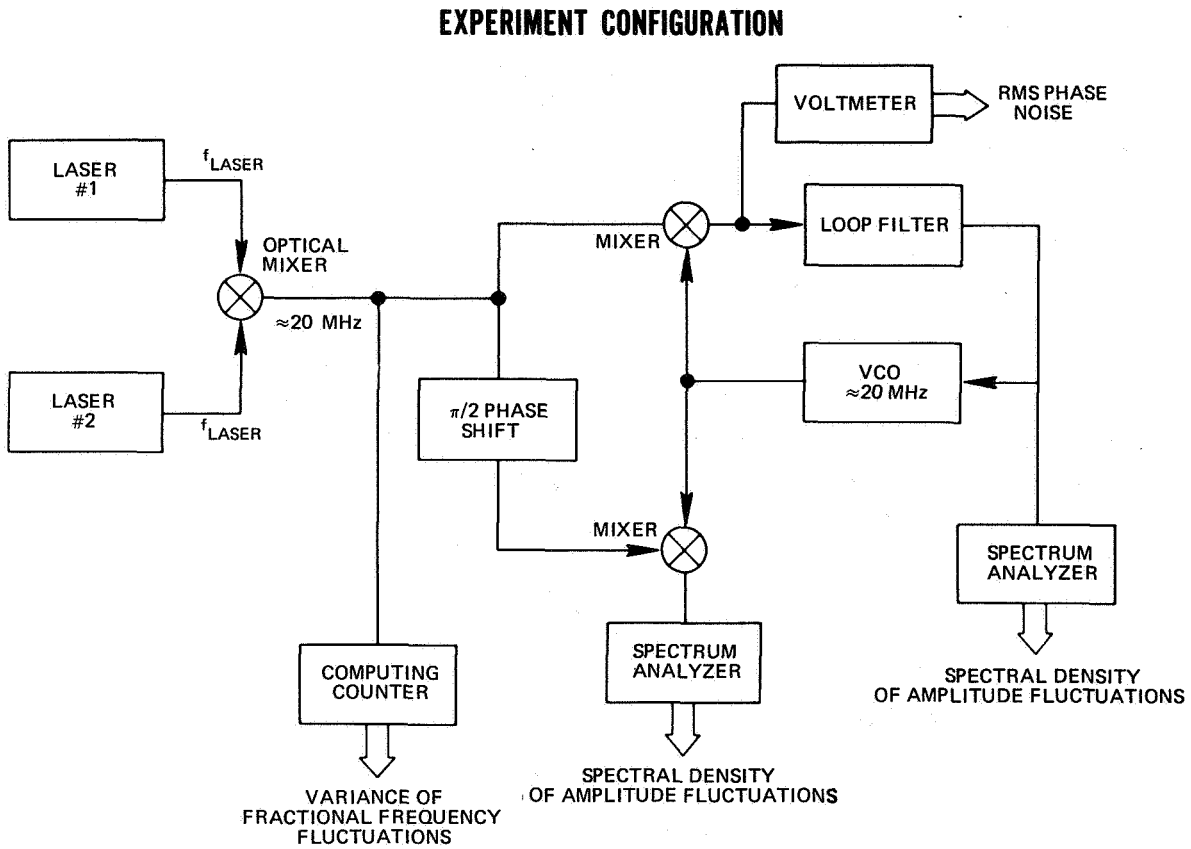


Figure 2. Experiment implemented to obtain desired data: spectral density and variance measurement.

This signal emerged from the optical mixer, and was passed to a phase-lock loop tracking receiver. At the output of this receiver, we could measure rms phase noise within a loop bandwidth, and with a spectrum analyzer, we could get a spectral density measurement of the frequency fluctuations.

A third measurement we made was down through a quadrature loop. This would be a coherent demodulation of amplitude fluctuations, and we can get the corresponding spectral density.

A fourth measurement we made was in the time domain, using a computing counter. We actually measured and plotted the variance of the fractional frequency fluctuation. This is a typical signal versus tau plot that you see in the time domain.

The result of what we're after is shown in Figure 3, in which we used the data resulting from the experiment. This plot shows the phase-lock loop tracking error, or your inability to reconstruct the carrier versus the tracking loop bandwidth. The ordinate here is the error in degrees rms versus the phase-lock loop bandwidth in kilohertz. The line running from top left to bottom right is the result of the data from the stability measurements. Basically, it implies that there is a minimum loop bandwidth that you can use.

The horizontal lines — nominally 30 degrees rms phase error — are values where the phase-lock loop will skip cycles and drop out of lock. At 20 degrees' error, some degradation of the data signal-to-noise ratio will occur. These are thus maximum values that we cannot exceed.

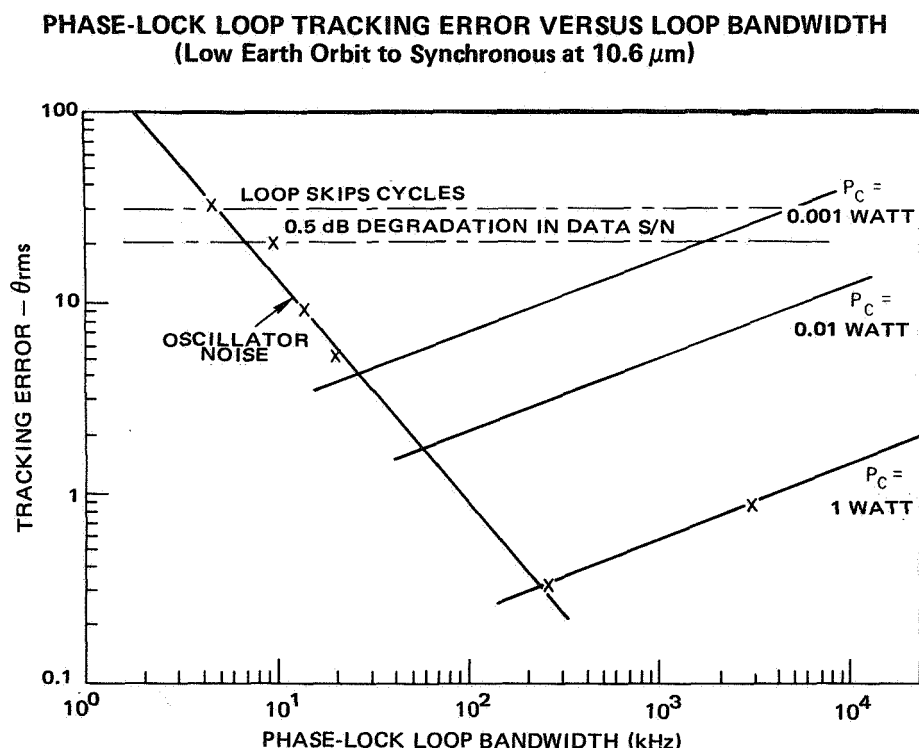


Figure 3. Data used with other receiver parameters. Adequate margin exists in terms of acquisition, Doppler tracking, and bit error rate as they relate to laser stability.

The three sloping lines on the right are for various transmitter powers on an earth orbit satellite up to synchronous altitude. As you can see, for a signal level of, say, a milliwatt in the carrier, there is an optimum loop bandwidth at which we should operate to minimize the phase error.

Corresponding to this bandwidth, there is a maximum Doppler rate associated with it. The basic result is that we have measured the data on the lasers, and there is a margin, as you can see, for these various transmitter powers.

VOICE INTELLIGIBILITY IN SATELLITE MOBILE COMMUNICATIONS

Sheldon Wishna

We have been involved in development of voice communications systems capable of operating over channels having low carrier-to-noise ratios, and giving output speech having good intelligibility.

This effort is part of the larger scope effort being conducted in the field of satellite based air traffic control systems. In this area of work, the power limitations of the satellite drastically limit the power available to the channels. In addition, because of antenna problems on the aircraft, and in general, propagation effects, these channels may be subjected to extreme amounts of fading.

It should be pointed out that the work being done in the voice communications field is directly applicable to commercial voice communication systems. Today I will talk about one of these developments, called "amplitude control technique." This method, when implemented on an analog voice communications system, improves the performance of these systems when operating over a noisy channel.

The amplitude control system has been implemented with a narrowband FM system. Now, the amplitude control system works in the following two ways with voice systems. As we know, speech consists of a series of phonemes, having various amplitudes. When the speech is transmitted over a noisy channel, the lower level phonemes tend to be masked by the noise, and therefore their contribution to the received intelligibility is nullified.

The amplitude control technique eliminates this problem by presenting at the transmitter equal amplitude phonemes. So that the low level phonemes, when they are transmitted over the noisy channel are now above the noise, and will contribute to the output intelligibility.

The second way the amplitude control technique improves voice reception is that a listener to a noisy channel over an extended period tends to get fatigued in the sense that his ability to understand what is being transmitted is greatly decreased. So, the amplitude control technique provides for squelching the noise when speech is not being transmitted.

The setup to demonstrate this technique is shown in Figure 1. Basically, we have a tape player which contains prerecorded intelligibility tapes. We have an AGC circuitry, which takes the incoming speech and makes it equal amplitude. We then send it into a typical narrowband FM transmitter, which is then sent into a channel that has a noise input, thus simulating a communication channel.

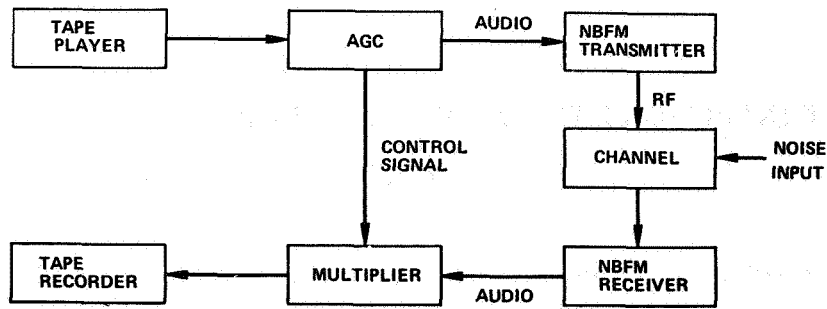


Figure 1. The laboratory test setup used to demonstrate the amplitude control technique.

From there, it is received by a typical narrowband FM receiver, which outputs into a multiplier. The control signal is then fed into the multiplier, restoring the audio to its original format. It is then recorded for later evaluation.

The proof of the pudding in any system is how well does it perform. Figure 2 shows the type of performance obtained by this amplitude control technique. These results were obtained from tests conducted in the Prince Georges County High Schools. Word intelligibility percent is plotted as a function of voice channel carrier to noise power density. We see that at 49 decibel-hertz, we have approximately equal performance for the controlled and uncontrolled situation.

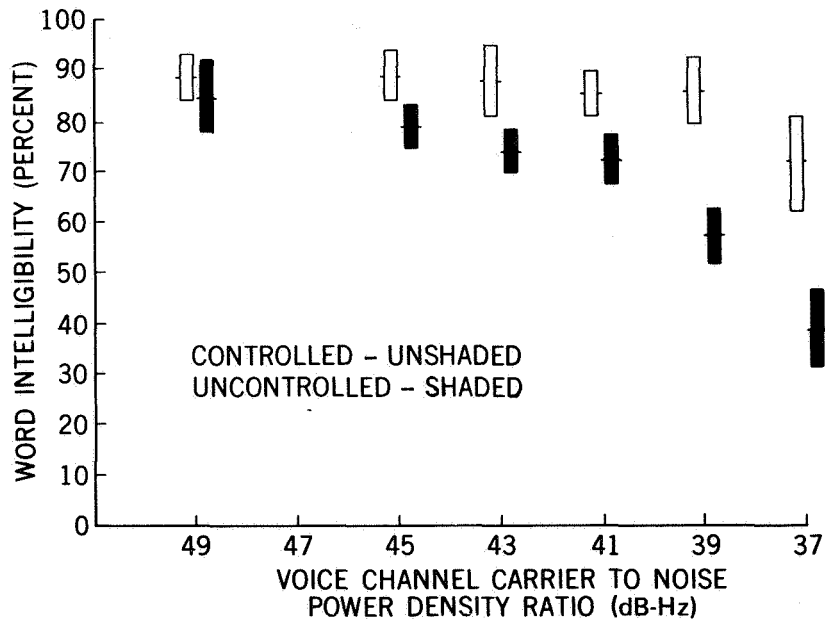


Figure 2. Graphical presentation of the received output speech intelligibility as a function of voice channel carrier-to-noise power density ratio, both with and without amplitude control.

But when we get down to extremely low carrier-to-noise power density conditions, we note that the controlled system has significant improvement over that of the uncontrolled system. In fact, we're seeing for these type of word intelligibility tests, about a 4 dB improvement. Figure 3 shows more clearly what has happened to the listener groups. Here we have the number of listener groups in percent versus the listener score in percent. We see that for the 49 decibel-hertz carrier noise range, we have approximately equal performance. However, slightly better performance results from controlled than from uncontrolled amplitude.

But if one goes down to the very low carrier-to-noise power density range of 37 decibel-hertz, we notice significant improvement in the listener groups by the use of this amplitude control technique. In fact, we even have some people for this particular word list scoring in the 90 to 100 percent range.

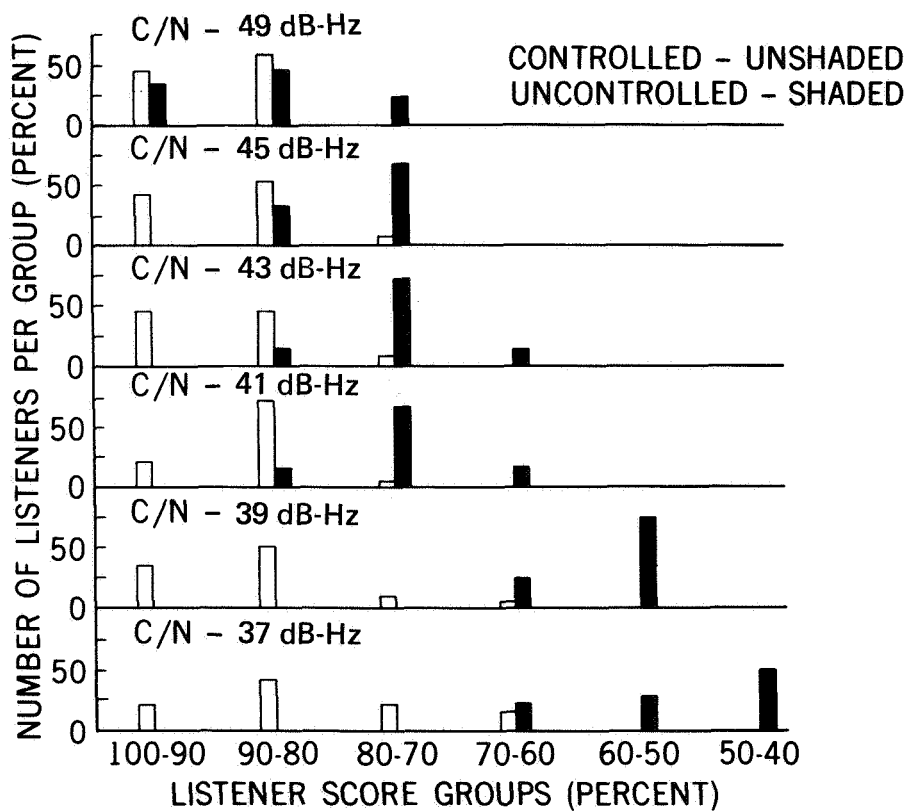


Figure 3. Graphical presentation of the distribution of the number of listeners as a function of listener score groups.

In conclusion, we have found that the amplitude control technique, when applied to analog voice systems, does lead to significant improvement of their performance. We are going to use the amplitude control technique as part of the advanced voice communications systems that we are developing at Goddard.

MEMBER OF AUDIENCE:

In a practical system, how are you going to carry along the restoration?

MR. WISHNA:

Well, it is anticipated that the control voltage will be modulated along with the audio, using a frequency multiplex system. The control voltage is contained at present in a 30-Hz bandwidth.

A ZERO-ERROR OPERATIONAL VIDEO DATA COMPRESSION SYSTEM

Richard L. Kutz

I would first like to explain the significance of "Zero Error" as used in the title. The data user is usually alarmed when any operation which is unfamiliar to him is performed upon the data before it is received at the data-user processing site. In order to minimize the concern of the data user over the possible loss of data quality due to data compression, all data was reconstructed for the data user without error with respect to the data at the input point in the communication system. So this data compression communication system is zero error or lossless since it is transparent to the data user as far as data quality is concerned. You still have to contend with channel errors, as you would with any other communication system.

This data compression system was implemented as an experiment in cooperation with the National Environmental Satellite Service (NESS) of the National Oceanic and Atmospheric Administration. The data compression system operates between the NESS command and data acquisition (CDA) station at Wallops Island, Virginia, and the NESS data processing center at Suitland, Maryland.

The data compression system has been operating since February 1972, using ATS spin-scan cloud cover data. With the launch of ITOS-D in October 1972, this data compression system has become the only source of near-realtime Very High Resolution Radiometer (VHRR) image data at the Suitland NESS data processing facility. The VHRR image data are compressed and transmitted over a 50 kilobit per second wideband ground link between Wallops Island, Virginia and Suitland, Maryland.

The goal of the GSFC/NESS data compression experiment was to send data quantized to six bits at twice the rate possible when no compression is used, while maintaining zero error between the transmitted and reconstructed data. All objectives of the data compression experiment were met, and thus a capability of doubling the data throughput of the system has been achieved.

In the first figure, to the left is a CDA station receiver feeding a 100 kilobit per second data stream into the data compression equipment. The data compression hardware consists of a programmable minicomputer with special purpose input-output interfaces designed to facilitate the data compression software algorithms. In the center of Figure 1, the compressed data is transmitted at a 50 kilobit per second rate over a wideband group phone line to the data reconstruction equipment located at Suitland, Maryland. To the right of the figure, the inverse of the data compression operation is performed on the 50 kilobit per second compressed data stream from the phone line to reconstruct a 100 kilobit per second data stream output which is identical to the 100 kilobit per second data stream

SYSTEM EQUIPMENT CONFIGURATION

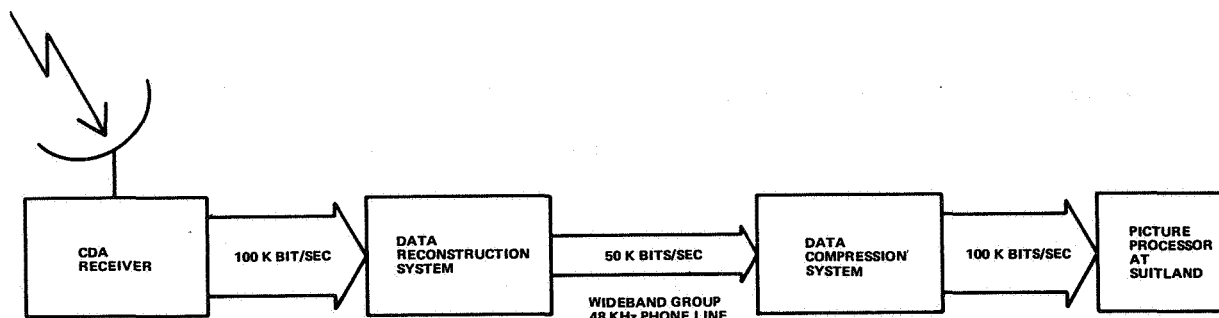


Figure 1. This data compression system provides a 100K bits/sec data transfer rate capability over a 50K bits/sec channel.

entering the data compression hardware at the Wallops CDA station. The picture processing equipment at Suitland, Maryland receives the same data quality with or without data compression, but the data rate can be doubled when data compression is used.

Before continuing, I'd like to define two terms frequently used in a discussion of data compression techniques. First, *compression ratio* is defined as the number of bits used to transmit the original or noncompressed data divided by the number of bits in the compressed data. The second term which requires definition is *entropy*: The entropy of a message is based upon its probability density function and has the units in bits. The sample entropy in bits per sample of a video image is found by summing the negative probability of a given intensity times the base-two log of the same probability over all intensities found in the empirical probability density function for the video image.

The sample entropy taken after some operation has been performed on the data tells the minimum number of bits per sample necessary to send the modified representation of the data. For example, an ATS spin-scan image quantized to six bits per sample has an entropy of 4.7 bits per sample before any other operations are performed on the data. Our goal was to achieve a two-to-one compression ratio, which implies that on the average, three bits per sample are used to encode each sample. This objective cannot be realized without employing a reversible operation on the data, which makes use of the inherent sample-to-sample dependence present in most sampled data streams. The operation selected was one which produces the difference between successive samples, because it is both easy to implement and results in a sample entropy of 2.1 bits per sample. It is now possible to construct an encoding procedure with a per scan line average of less than three bits per sample, even when synchronization and noise protection bits are added.

The algorithm used to encode the data employs the Shannon-Fano procedure. The Shannon-Fano encoding procedure shows one how to construct an encoded data stream with nearly as few bits per sample as the sample entropy for the same data. The encoding procedure produces a variable number of bits for each sample encoded. Some samples

are represented by one bit, and some by as many as ten bits. Since word synchronization is maintained by correctly decoding the previous word, one must consider the effect of channel errors on word synchronization.

Two types of synchronization words are used in each image scan line. Each scan line starts with a 32-bit line synchronization word, which establishes both line and word synchronization. The 4096 data samples in each scan line are next encoded into 16 blocks with each block representing 256 data samples. At the end of each block is a 16-bit synchronization word which ensures that word synchronization is maintained and that word synchronization can be acquired within 256 data samples. Each block of 256 encoded data samples starts with a sample from the input data. The remaining 255 samples in each block consist of the encoded successive differences between input data samples. Due to the variable length coding, the number of bits between two successive synchronization words varies from 265 to 2560. Although the data compression encoding procedure selected leads to a data

format where word synchronization depends on a low probability of channel error, experience has shown that the data compression communication system has a more robust synchronization characteristic than an image transmission system in which there is only one line synchronization word on a scan line and in which word synchronization is obtained from a fixed word length data format. The variable block length and hence variable line length data format produces a variable number of bits per image scan line; the number of bits depends on the redundancy in the scene at the scan line location.

In Figure 2, the image scan line number runs from 0 to 2000 on the abscissa, and the ordinate indicates the percentage of the original uncompressed line length remaining to be transmitted after data compression. The image data to which Figure 2 corresponds is an

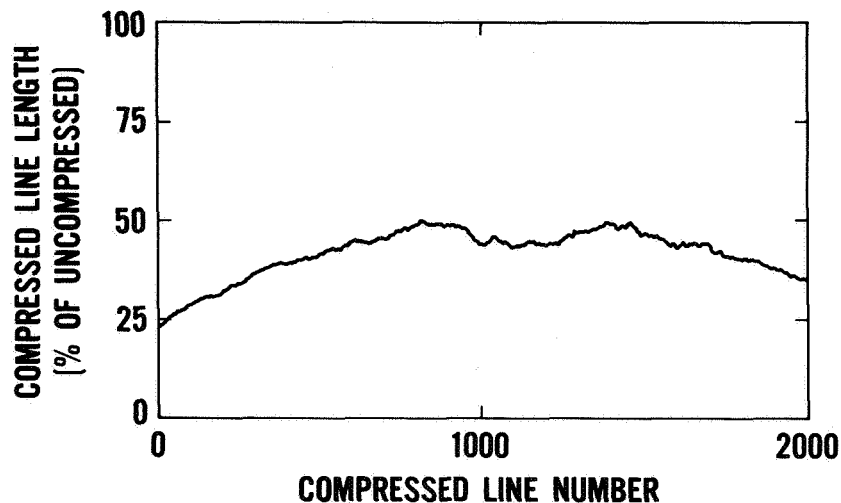


Figure 2. This graph shows the percent of data remaining after data compression on a line-by-line basis. The compression ratio varies as a function of local scene content, but on the average only half of the original number of bits need to be transmitted.

ATS spin-scan cloud cover image of the full earth disc enclosed by a black space-view surround. Figure 2 shows that more data must be transmitted in the middle of the picture than at either end, since the intersection of the scan line with the earth disc has its maximum chord length near line number 1000. However, not all of the data compression in each line is due to the constant amplitude space view, since space view accounts for only 10 percent of the uncompressed data near line 1000 and yet the compression ratio exceeds two-to-one in this area of Figure 2. The area above the curve in Figure 2 represents the increased capacity of the data compression communication system as a function of the ATS image scan line number.

Figure 3 shows a cloud cover image taken from the ITOS-D Very High Resolution Radiometer visible channel. To the left of the figure, the image is shown without data compression; to the right of the figure, the same image is shown after data compression, transmission from Wallops Island to Suitland, and reconstruction. A comparison of the data represented by these two images showed that no error was introduced into the compressed image data. In the rare cases where a channel error effect is discernible in a reconstructed compressed image, the effect shows up as a streak less than 1/16th of the image scan line length.

The results of the data compression work can be readily applied to missions where communications bandwidth or time are primary considerations. Data storage efficiency can also be increased for use onboard a spacecraft or for use with data archival systems on the ground. Data compression can also be applied to save land line costs in any spacecraft program involving a polar orbit where the Alaska CDA stations are required to send large quantities of data over great distances, as for example in the cases of ITOS, Nimbus, and ERTS. Since a 48 kilohertz wideband group from Maryland to Alaska is currently

TRANSMISSION LINK - WALLOPS TO SUITLAND

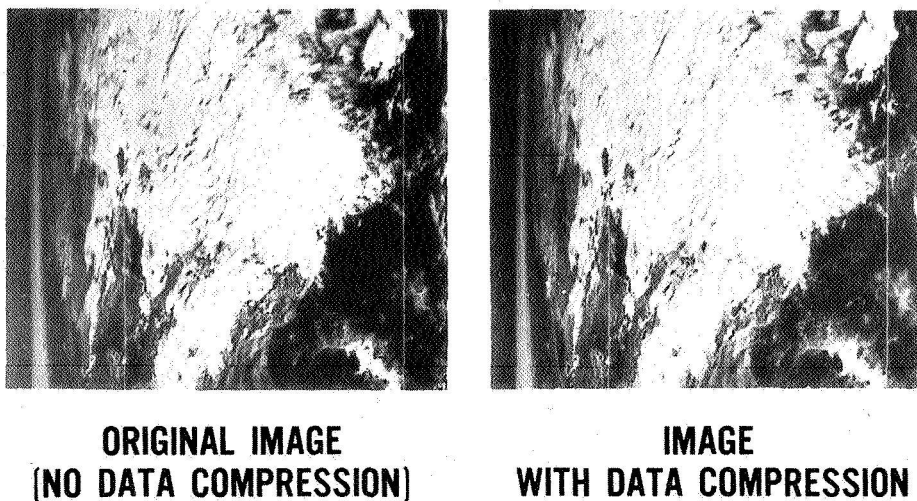


Figure 3. The original uncompressed image is the same as the compressed, transmitted, and reconstructed VHRR ITOS-D image.

rented at a cost of about \$700,000 per year, a doubling of the utilization of one of these channels would be very cost effective. The Department of the Interior is currently considering an earth observation spacecraft system requiring three CDA stations. One of the three CDA stations is necessary partially because insufficient time exists to dump the spacecraft data over the other two CDA stations. In their case, data compression could double the spacecraft data dump capacity and thus reduce the number of CDA data dump stations required from three to two, a potential savings of millions of dollars.

MR. MATHEWS:

If you tolerate small errors, couldn't you make the compression ratio very much larger?

MR. KUTZ:

Yes, I'm sure that we could get better results by allowing a small error tolerance. One reason for avoiding any error in the data up to this point in time was to help the data user gain confidence in data compression. Also, some of the image data are used to perform quantitative measurements. For example, the infrared VHRR data can be used to measure sea surface temperatures. Where there is a requirement for error-free data on the part of the user, we have shown that data compression can satisfy that requirement.

MR. MATHEWS:

We may have to encourage the data users to review their requirements for zero-error data to see if the zero-error constraint can't be relaxed in some cases.

HEALTH/EDUCATION TELECOMMUNICATIONS EXPERIMENT

Albert A. Whalen

Being criminally verbose and being restricted to only five minutes, I'm going to have to talk rather quickly.

In June of 1971, the Department of Health, Education, and Welfare, the Corporation for Public Broadcasting, and the National Aeronautics and Space Administration jointly announced the agreement to use the ATS-F spacecraft to test various educational and health delivery experimental applications of communications satellites.

The Communication and Navigation Division (CND), because of its involvement in very similar communication experiments, and because of its small ground terminal background, was selected to coordinate the technical aspects of the experiment.

CND's involvement grew to include acting as technical advisor to the various user communities, and also to providing general assistance and experiment planning. I also deal with the general system coordination among the myriad agencies involved in such bureaucracies.

The telecommunication links which are used in this experiment are shown in Figure 1. We have the master station on the left, where they generate a wideband color TV signal with its associated aural channels, transmit it up to the spacecraft (in this case, the ATS-F) and into the earth coverage horn in a wideband FM mode.

The signal is then retransmitted over the 9.1-meter (30 ft) diameter antenna at one or two of the S-band frequencies (2569.2 and 2670 megahertz) down to the user ground system complex. And today, we're going to direct our limited discussion to the small receiver-only terminal over in the extreme right of Figure 1.

Whereas this may not be advancing the state-of-the-art, it is certainly an application of the technology that has been funded and developed at NASA over the years. Such works as the Ascend study, the Edustat studies, some of the hardware work done at Washington University (in St. Louis), at Stanford, at General Electric, and some of the work done here at Goddard have demonstrated over the years that small ground terminal technology can be a reality. It does not have to be expensive or sacrifice performance. These efforts have certainly stimulated the users to propose experiments utilizing these technologies.

Figure 2 shows an artist's conception in one of our northern climes of the small ground terminal, consisting of a ten-foot diameter antenna located on a three-legged mount. The terminal is capable of 0 to 70 degrees elevation, course adjustment, and a plus or minus 5 degree elevation vernier adjustment.

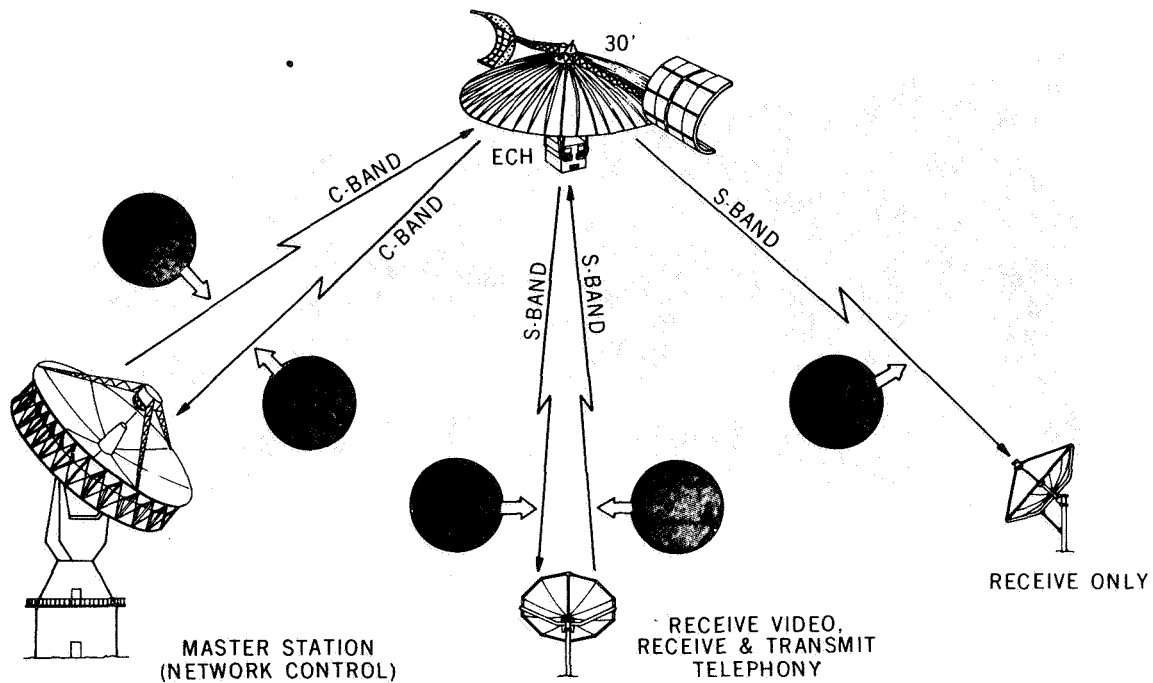


Figure 1. This general telecommunication link does not advance the state-of-the-art, but is a real application of technology.

In the azimuth, you have the capability of picking up the entire mount after loosening the guy wires, and use that for your coarse azimuth adjustment. Then there is a plus or minus five degrees vernier adjustment.

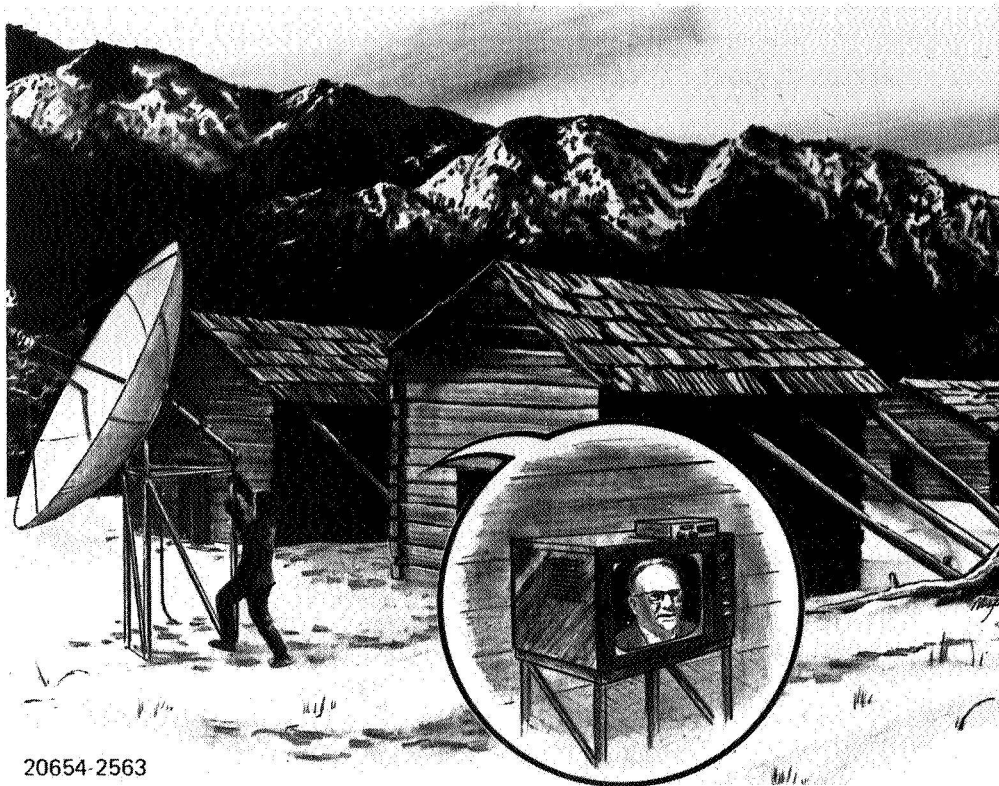
The ten-foot diameter antenna utilizes a cavity back dipole feed. Behind the cavity is located the preamplifier with 60 decibels of gain coupled through a 30.5-meter (100 ft) cable into an indoor unit.

One unique feature of this receiver, I'd like to point out, is that we have finally gone full circle again; we're back to the tuned radio frequency receiver. There is no local oscillator in this unit.

The indoor unit, mounted on top of a conventional TV set or an educational TV monitor, provides further RF gain; it drives a wideband limiter-discriminator. The entire system bandwidth without channel select filters is 190 megahertz. The channels are selected by 23 megahertz bandwidth filters prior to limiting and demodulation.

At the present time, six of these terminals are being developed under a prototype contract to Hughes Aircraft Company.

So we're now past artists' conceptions, and we're getting down to the real hardware. Figure 3 shows the first unit, which was delivered three days ago to Hughes Aircraft Company by Hewlett-Packard, subcontractor for the electronics. Note that the system is a very simple one to operate, consisting of an off-on switch, and a signal-strength meter.



20654-2563

Figure 2. NASA-funded studies and hardware development programs stimulated this experiment by proving that small, inexpensive ground terminals, such as the one sketched here, are a reality.

I might add that previous works that have been done have always been in sort of a prototype, one-of-a-kind quantity. They have been done by specialists, and here we have our first real preproduction model of something that will be built in quantities of 300 to 500 to support this experiment.

This unit currently is undergoing tests; the first test results I heard were “Wow, the pictures come through it very fine,” and now they’re getting to be a little more quantitative in their evaluation.

I might add, another concern of most people in the use of small ground terminals is not only the performance, but the cost. It turns out the cost of this ground terminal in quantities of 300 to 500 will be approximately \$2000. That includes the antenna, the pedestal, 30.5 meters of cable, the entire outdoor-indoor unit right down to base band and to interface with the TV monitor.

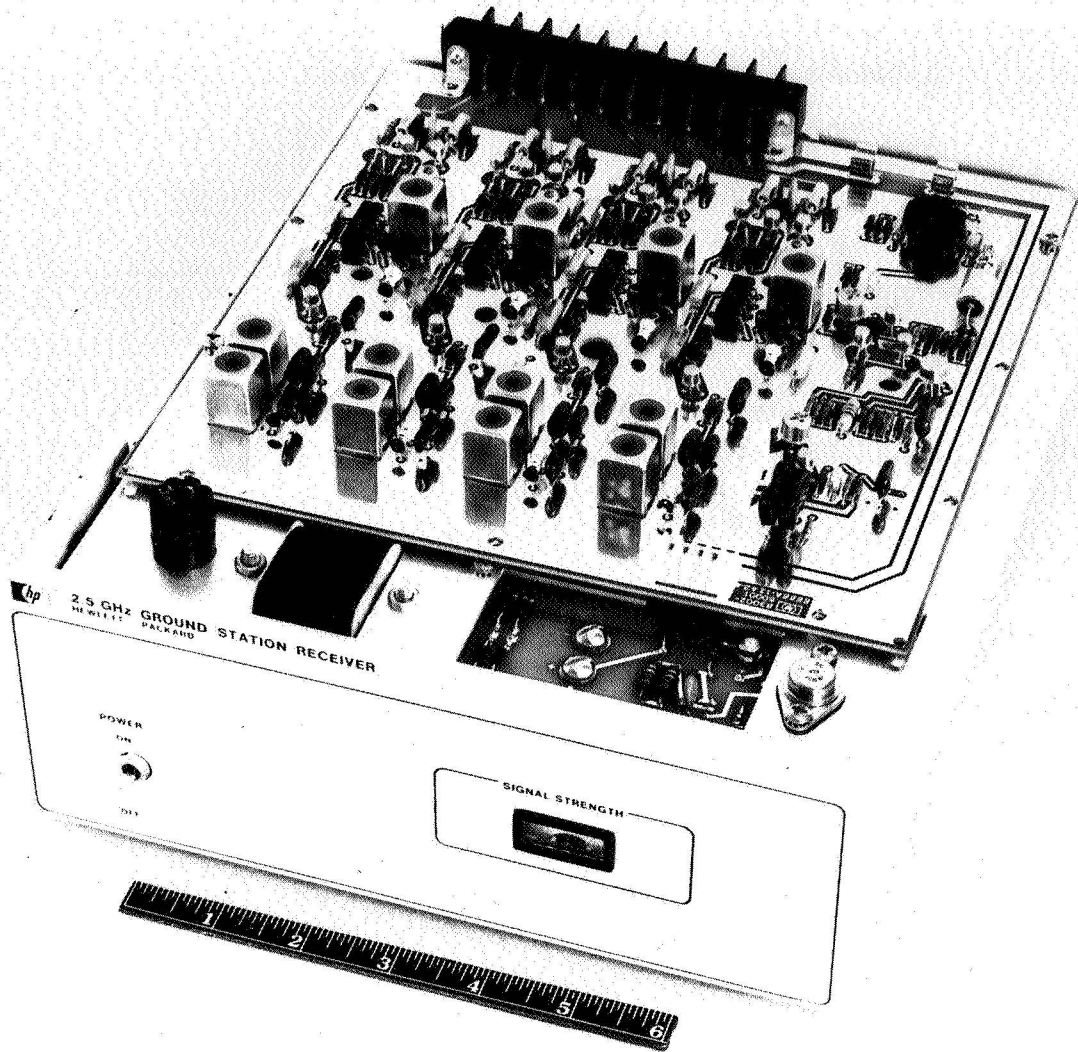


Figure 3. This prototype receiver is the first commercially built preproduction unit.



POSTMASTER: If Undeliverable (Section 158
Postal Manual) Do Not Return

"The aeronautical and space activities of the United States shall be conducted so as to contribute . . . to the expansion of human knowledge of phenomena in the atmosphere and space. The Administration shall provide for the widest practicable and appropriate dissemination of information concerning its activities and the results thereof."

—NATIONAL AERONAUTICS AND SPACE ACT OF 1958

NASA SCIENTIFIC AND TECHNICAL PUBLICATIONS

TECHNICAL REPORTS: Scientific and technical information considered important, complete, and a lasting contribution to existing knowledge.

TECHNICAL NOTES: Information less broad in scope but nevertheless of importance as a contribution to existing knowledge.

TECHNICAL MEMORANDUMS: Information receiving limited distribution because of preliminary data, security classification, or other reasons. Also includes conference proceedings with either limited or unlimited distribution.

CONTRACTOR REPORTS: Scientific and technical information generated under a NASA contract or grant and considered an important contribution to existing knowledge.

TECHNICAL TRANSLATIONS: Information published in a foreign language considered to merit NASA distribution in English.

SPECIAL PUBLICATIONS: Information derived from or of value to NASA activities. Publications include final reports of major projects, monographs, data compilations, handbooks, sourcebooks, and special bibliographies.

TECHNOLOGY UTILIZATION PUBLICATIONS: Information on technology used by NASA that may be of particular interest in commercial and other non-aerospace applications. Publications include Tech Briefs, Technology Utilization Reports and Technology Surveys.

Details on the availability of these publications may be obtained from:

SCIENTIFIC AND TECHNICAL INFORMATION OFFICE
NATIONAL AERONAUTICS AND SPACE ADMINISTRATION
Washington, D.C. 20546